WIND LOADING AND DYNAMIC RESPONSE OF AIR-SUPPORTED ROOF STRUCTURES

Submitted by Teresa L Krakowska

for the Degree of PhD

at the Department of Civil Engineering

City University, London

September 1989

To Trampik

Page No.

Contents:

Acknowledgements (vi)

Abstract (vii)

1. Introduction 1

2. Wind as a flow of fluid

2.1 Basic terms 9
2.2 Boundary layer growth (in two dimensions)
2.2.1 Flat plate in a uniform flow 15
2.2.2 Flow along a curved surface 15
2.2.3 Flow past a cylinder 18

2.3 Constitutive equations of fluid mechanics

2.3.1 Equation of continuity 21
2.3.2 Equations of motion 22

2.4 Review of solutions for potential flow 28

2.4.1 Exact analytical solutions 30
2.4.2 Appropriate solutions 31
2.4.3 Exact numerical methods 33

2.5 Solutions for flow of a real fluid

2.5.1 Laminar boundary layer 35
2.5.2. Turbulent boundary layer 36

2.6 Similitude law 38

3. Modern approach to wind engineering

3.1 Atmosphere circulations 42
3.2 Wind loading on structures, statement of the problem
3.2.1 Fundamental aspects 44
3.2.2. Division of the problem by scale 45
3.2.3 Division of the problem by frequency 46

3.3 Assessment of the problem 48
3.4 Design wind speed data 52
3.5 Assessment of wind loading 58

4. Wind response of flexible roof structures - a review

4.1 Structural response under wind loading

4.1.1 Static approach 65
4.1.2 Dynamic equation, mass and damping matrices 66

Page No.

4.1.3 Quasi-linear dynamic response 74
4.1.4 Wind loading in the non-linear time-domain method 77
4.2 Wind tunnel tests 79
4.3 Aerodynamics of flexible surfaces 87

5. Wind load modelling on an open-sided shell roof

5.1 Introduction 92
5.2 Assumption and limitations 94
5.3 Stating the problem 96
5.4 Reduction of the problem to an integral equation by Green's identity 98
5.5 Thin sections with flow on both sides 105
5.6 Vortex-lattice methods

5.6.1 Horse-shoe vortices in the plane z=0 106
5.6.2 Quadrilateral vortex-rings in the plane z=0 113
5.6.3 Quadrilateral vortex-rings on the surface 114

5.7 Numerical analysis 122

Appendix to Chapter 5 140
Two-dimensional numerical solution for a real flow

6. Wind tunnel tests on an eliptic paraboloid

6.1 Wind tunnel specification 152
6.2 Instrumentation 155
6.3 Calibration of transducers 158
6.4 Wind tunnel calibration

6.4.1 Velocity profile 166
6.4.2 Static pressure 175

6.5 Model 183
6.6 Test procedure 189
6.7 Processing experimental results 191
6.8 Discussions of the results 195
6.9 Conclusions 200

7. Review of methods of analysis for air-supported structures

7.1 Introduction 217
7.2 Linear analyses

7.2.1 Static analyses 221
7.2.2 Dynamic analyses 224

Page No.

7.3 Non-linear solutions 225

7.3.1 Shells of revolution 226
7.3.2 Finite element methods 229

7.4 Analyses of structures with strong geometric non-linearities

7.4.1 Static analyses 231
7.4.2 Dynamic analyses 235

8. Dynamic relaxation method for the static analysis of air-supported structures

8.1 Dynamic relaxation - a review

8.1.1 Formulation of the method 238
8.1.2 Dynamic relaxation with viscous damping 242
8.1.3. dynamic relaxation with kinetic damping 243
8.1.4 Stability criteria and fictitious nodal masses 246

8.2 Structural idealization and natural stiffness matrices 250
8.3 Scheme for analysis of air-supported structures 258
8.4 Numerical examples

8.4.1 Orthotropic membrane dome 263
8.4.2 Isotropic membrane dome 273

9. Explicit dynamic analysis of pneumatic structures

9.1 Explicit dynamic analysis - a review

9.1.1 Iteration schemes for explicit dynamic analysis 280
9.1.2 Modelling visco-elastic properties of the membrane 286
9.1.3 Incremental procedure allowing for for buckling 294
9.1.4 Influence of surrounding air 297

9.2 Numerical examples and discussion

9.2.1 Impulsively loaded orthotropic dome 299
9.2.2 Impulsively unloaded isotropic pneumatic dome 310

Page No.

10. Tests on impulsively loaded and unloaded pneumatic domes 322

10.1 Structural properties tests for the dome membranes

10.1.1 Introduction 323
10.1.2 Static stress-strain relations 325
10.1.3 Dynamic properties test 342

10.2 Tests on the orthotropic membrane dome

10.2.1 The model 355
10.2.2 Impulsively centrally loaded dome- static and dynamic tests 356
10.2.3 Comparison of theoretical and experimental results 360

10.3 Tests on isotropic membrane dome 373

10.3.1 Static and dynamic tests on loaded and unloaded dome 374
10.3.2 Comparison of results and conclusions 377

11. Internal air modelling

11.1 Introduction 387
11.2 Air surges within an enclosed pneumatic stressed membrane - a review 390
11.3 Iteration scheme for explicit dynamic analysis of pneumatic structures with internal air modelling

11.3.1 Numerical iteration scheme for air modelling 399
11.3.2 Numerical iteration scheme for coupled analysis 402

11.4 Numerical simulation of an impulsively unloaded pneumatic dome 405

12. Added mass effect on dynamic response of pneumatic structures

12.1 Introduction: concept of added mass 421
12.2 Numerical scheme to account for added mass

12.2.1 General assumptions 428
12.2.2 Added mass of a diaphragm embedded in a rigid bounding surface 429
12.2.3 Modelling the shallow pneumatic dome 436
12.2.4 Iteration scheme for explicit dynamic analysis of the pneumatic dome with added air mass 441

Page No.

12.3 Numerical dynamic analysis of impulsively unloaded dome 436

13. Summary, conclusions and lines of further research 456

References and bibliography 469

Acknowledgements

The author wishes to express her gratitude to all who encouraged and helped her during the studies and research at City University, and also during preparation of this thesis.

In particular the author is deeply indebted to Dr M R Barnes, whose unrelenting devotion to the art of engineering and its practical application greatly influenced her and guided her throughout the entire work.

The author owes thanks to Mr D Sykes for his valuable advice during the course of wind tunnel investigation and also to Dr B Younis for allowing her to use his version of the 'SIMPLE' program. Very sincere thanks are due to Dr S Gill for his continuing support and interest at all stages of this thesis.

The financial support of this work by the Science Research Council in the form of a Research Studentship is gratefully acknowledged.

The expert typing by Patricia Walker is greatly appreciated. The author is also grateful to all the laboratory staff of Civil Engineering and Aeronautics Departments, in particular, to Mr A Bonomini for his help and cheerful assistance throughout experimental investigation.

Abstract

This thesis is concerned with defining, theoretically, approximate values of wind loading and predicting dynamic response of air-supported structures subject to suddenly applied loads.

Wind loading on air-supported structures is a phenomenon involving significant mutual interaction between inertial, elastic and aerodynamic forces. The aerodynamic forces described by fluid mechanics equations are examined in the first part of the thesis, Chapters 2 to 6. Chapter 2 contains a brief discussion of wind as a flow of air around rigid bodies. This review is followed by an introduction to modern wind engineering, and then by discussion on the theoretical and/or experimental methods to assess wind response of flexible structures.

Under the simplifying assumption of three-dimensional potential flow of an incompressible, inviscid, steady air flow, the three-dimensional pressure coefficient distribution on an open-sided paraboloid shallow shell roof is examined in Chapter 5, employing three versions of a vortex-lattice method. The modified Hedman method with horseshoe vortices in the plane $z=0$, and a boundary condition of tangential flow applied on the body of the shell yielded the best results. In the Appendix to Chapter 5 a real flow solution based on the 'SIMPLE' algorithm is investigated for a numerical example of a thin shell submerged in steady flow - a two-dimensional approximation of the section employed in Chapter 5. For a 3D structure which cannot be adequately represented by 2D model a simple 3D potential flow solution is likely to yield more accurate pressure distributions than a sophisticated 2D real flow analysis.

The wind tunnel tests described in Chapter 6 were conducted on a thin, rigid eliptic paraboloid subject to two flow conditions: uniform flow, and in the thick turbulent boundary layer. The theoretical results predicted fairly well the mean pressure distribution on the shell in uniform flow, except on the rearmost part of the model, where separation occurred. In the case of the turbulent boundary layer flow, discrepancies in mean pressure coefficient distributions are of the same order as for uniform flow. However, as the turbulent boundary layer flow is a much more complicated phenomenon than the theoretical description of potential flow, the above conclusion cannot be generalized without further work. The vortex-lattice method, due to its simplicity, can be easily incorporated into any structure-fluid interactive scheme accounting for both static and quasi-dynamic behaviour, and an assessment of dynamic response is essential for the design of large air-supported structures.

The second part of the thesis, Chapters 7 to 12, is concerned with the structural response of air-supported structures; with special emphasis on the dynamic response following sudden release of a loading system. Chapter 7 gives a review of methods of analysis for pneumatic structures; those experiencing strong geometric non-linearities are especially focused. The dynamic relaxation method with kinetic damping is discussed in Chapter 8 with respect to the static analysis of pneumatic structures; structural idealization depending on the fabric patterning, type of loading and kind of membrane material being used.

Two series of model tests are described; both employing fairly large scale pneumatic domes. The first test model constructed using an orthotropic woven fabric is subject to centrally placed suddenly applied loading. The second test model constructed with very lightweight polythene is subject to suddenly released loading, both central and asymmetric. For this case the internal air and added mass effects become dominant.

Explicit dynamic analysis using a centred finite difference scheme is employed in Chapter 9 to analyse the response of pneumatic structures; and in particular to assess the response of the test structures. The influence of surrounding air is included as far as internal air stiffening is considered. For the suddenly unloaded dome, a revised, more efficient numerical scheme is developed, where checking for buckling is carried out at each time step, but creep strains, updated stiffness matrices and unit pressure vectors are calculated at less frequent intervals.

In Chapter 10 the tests on the impulsively loaded and unloaded pneumatic domes are described. Dome membrane properties are established from static and dynamic tests on specimens. For dynamic tests a new procedure is devised, to model more closely the state of stresses, by including two-dimensional stresses in the testing area of the specimen. Still and movie cameras were used in the static and dynamic tests on the pneumatic domes to record deflection. The results were analysed by means of photogrammetric techniques. The static results compare very well with theoretical predictions. The theoretical dynamic trace for the apex nodal deflection of the impulsively centrally loaded dome differs only slightly from experimental results. The heavy central load influences greatly the response. Discrepancies between theoretical and experimental dynamic responses of the very lightweight and suddenly unloaded dome are however large. The main area of error is caused by improper modelling behaviour of the surrounding air which should be treated as an intrinsic part of the structure.

A coupled fluid-structure explicit dynamic analysis, including membrane and air modelling, is presented in Chapter 11. The behaviour of irrotational, inviscid, compressible fluid is described from a Lagrangian point of view. Although only the simplest axisymmetric case is considered, the amount of computing is enormous, hence the procedure cannot, at present, be advocated for use in practice. In Chapter 12 the added mass effect due to vibrating air is discussed. A method to account for virtual mass in shallow pneumatic structures, based on potential incompressible flow and discrete source distributions, is presented and included in the numerical explicit dynamic procedure. The results for the centrally unloaded dome show a great improvement in terms of frequencies, with only a small increase in computing time compared with the numerical scheme of Chapter 9. The discrete source distribution method to calculate added mass effects can be easily extended to any shape of pneumatic structure, and when combined with an explicit dynamic analysis can provide a useful scheme for calculating frequencies and the approximate dynamic response of air-supported structures.

CHAPTER 1

Introduction

Air-supported structures: state of the art and problems encountered in design.

Recent advances in design techniques and the manufacture of high strength impermeable materials such as PVC coated polyester fabric, teflon coated glass cloth or silicon rubber coated glass, make it possible to construct large span air-supported and suspended membrane structures in a variety of geometrical forms. The very low mass of these fabrics (of the order .5-10 kg/m^2), their considerable tensile strengths (500 - 1500 N/cm), and their flexibility and uniform translucence are properties which enhance their popularity as a versatile material for the architectural and engineering design of wide-span structures.

An air-supported structure, the idea for which was initiated by the Engineer Frederick William Lanchester in his patent of 1917 for a field hospital, is a very elegant concept: a structural membrane is supported by a small pressure differential, usually between 15 and 25 mm of water pressure. Unlike materials used in conventional structures, the membrane is not directly resisting the applied external loads, but is containing the internal air, so that the action of air pressure forms a stable structure against external loadings.

If the external loads were uniform and normal to the surface, then an equal internal pressure differential could support these loads directly, leaving the membrane as purely a separating medium free of stresses above those required for simple stability. Since, in this instance, no additional stresses are transferred into the membrane material, anchorage forces can be kept to a minimum. This means that, unlike other structural concepts, there is no theoretical limit to the span of such an "idealized" air-supported structure. However, in practice, the external surface loadings are never uniform, and so the pressure differential must be high enough to prevent compressive (or buckling) stresses in the membrane as the fabric is capable of sustaining only tensile stresses. Furthermore, distortions under non-uniform loading can only be limited by a reasonable excess of internal pressure.

As air-supported structures can be erected or dismantled quickly, they are portable and inexpensive (from the worldwide survey, March 1984, the costs of manufacture and erection average out at £40.00 (m^2 [146]), hence they can offer a possible solution to a wide range of problems, both of social and commercial kind:-
shelters for storage, recreation arenas, production units and exhibition arenas of both a temporary and permanent nature. They are also being used increasingly as the formwork for casting rigid shells of rapid-hardening concrete or plastics. Research has been carried out concerning the possibility of using an inflatable structure

as an enclosure for a city in very cold climates (Northern Alberta [135]), and even in space projects for the construction of certain types of satellites and re-entry vehicles [120, 121, 142, 143].

The variety of possible forms of air-supported structures can be demonstrated by using analogies, such as inflated soap films over various complex plan shapes. With all these inflated soap films, the minimal surface area shapes obtained have a tendency to generate spherical, doubly curved synclastic forms. Soap bubbles conglomerate in a particular manner. They always meet at an angle of 120° to one another and the relationship between the radius of curvature of the film and the pressure differential across it is always constant. In addition to this, Frei Otto came to the conclusion that any shapes derived by revolving a linear form about an axis could be pneumatically achieved [165].

There is no generally accepted design procedure for air-supported structures [203]; their precise behaviour is very complex and there has not yet been sufficient monitoring of existing structures to predict accurately their behaviour and failure mechanisms. Figure 1 (re-printed from [203]) illustrates the problems encountered during the design of air-supported structures, in the form of inputs (sometimes feedback) from the structural analysis.

Pneumatic structures carry external loads by deforming, so the membrane has to find a new shape to balance the new loading pattern. The deformation can typically be up to 10% of the roof span in conventional airhouses [43]. This influences the load pattern, which in turn changes the deflections. The most important external forces are those resulting from extreme weather conditions such as storm winds and snowfalls.

Snow loads, although difficult to define since they depend upon a large number of factors such as ground snowfall, wind, temperature, humidity, surface condition and the temperature within the structure, are treated as static loads. Hence they present no major difficulty for analysis when using a suitable static non-linear procedure, which should account for possible build-up of snow as the structure deflects. They are, nevertheless, likely to be critical from a design point of view since they can result in dimpling of the air-supported surface structure and hence a gradual inversion and build-up of snow loading.

Many applications in hot or temperate climates will however not involve such loading, and the present work is concerned principally with the effects of wind loading on very wide span systems. Wind loading on a flexible roof structure should be regarded as an aeroelastic phenomenon, i.e. a phenomenon which involves significant mutual interaction between inertial elastic and aerodynamic forces. The relationships between them can be obtained in a theoretical

way by using dynamic equations, solid mechanics laws and theoretical fluid mechanics. Any such analysis must at the very least account for the added mass effect of the air either side of the membrane. It has been shown, for example by Irwin [97] for the case of an almost flat vibrating membrane covering an infinitely slot in wall 67m wide, that the added mass due to the surrounding air on both sides can be 37 times greater than the real mass of the membrane.

The most precise approach to wind load response is to test an aeroelastic model of an air-supported structure in a fully simulated turbulent boundary layer with the fluid (air) flow, material and structural properties scaled in accordance with the laws of similitude [97]. Attempts at complete modelling of flexible structures have been made [97] with some notable success, but without achieving the scaling of all the parameters. Only at full scale can complete aerodynamic similarity be obtained [45].

It is unlikely to be economically feasible in view of the current limitations of knowledge and computational systems to employ either a rigorous numerical aerodynamic analysis or to build and test a perfectly scaled flexible model. Therefore, an approximate approach seems desirable for design purposes.

The most common approach is to assume that aeroelastic effects are of secondary importance (i.e. that wind-structure interaction is negligible), and to obtain wind

loading as a distribution of mean plus randomly fluctuating pressure coefficients from tests on a rigid model placed in a wind tunnel with a simulated boundary layer. The subsequent numerical analysis to define structural response can be either "quasi-static" or dynamic with different degrees of sophistication.

This approach can, in some ways, be justified when high inflation pressures are employed. But there is an economic incentive to use the lowest possible inflation pressure, since this reduces membrane tension, foundation or other load supporting forces, and the cost of fans. Hence the above assumption of no wind-structure interaction becomes erroneous or uneconomic [21, 158]. For low inflation pressures, deflections due to wind loading are so large that they change the air flow pattern and hence the pressure coefficient distributions. The behaviour of the internal air, which should be considered as an integral part of the structure, can in particular be very large, especially for low rise structures.

The inefficiency and the cost of rigid model tests (a flexible model is rarely a feasible solution and always expensive) creates a need for numerical wind load analyses for air supported structures; especially those which have large spans and employ low internal pressures.

This thesis is principally concerned with the structural analysis of air-supported structures, and it is assumed that

the reader will be more familiar with structures than fluid flow. Because of the importance of the latter, however, chapter 2, which contains rather standard theory, is included to explain wind as a flow of fluid.

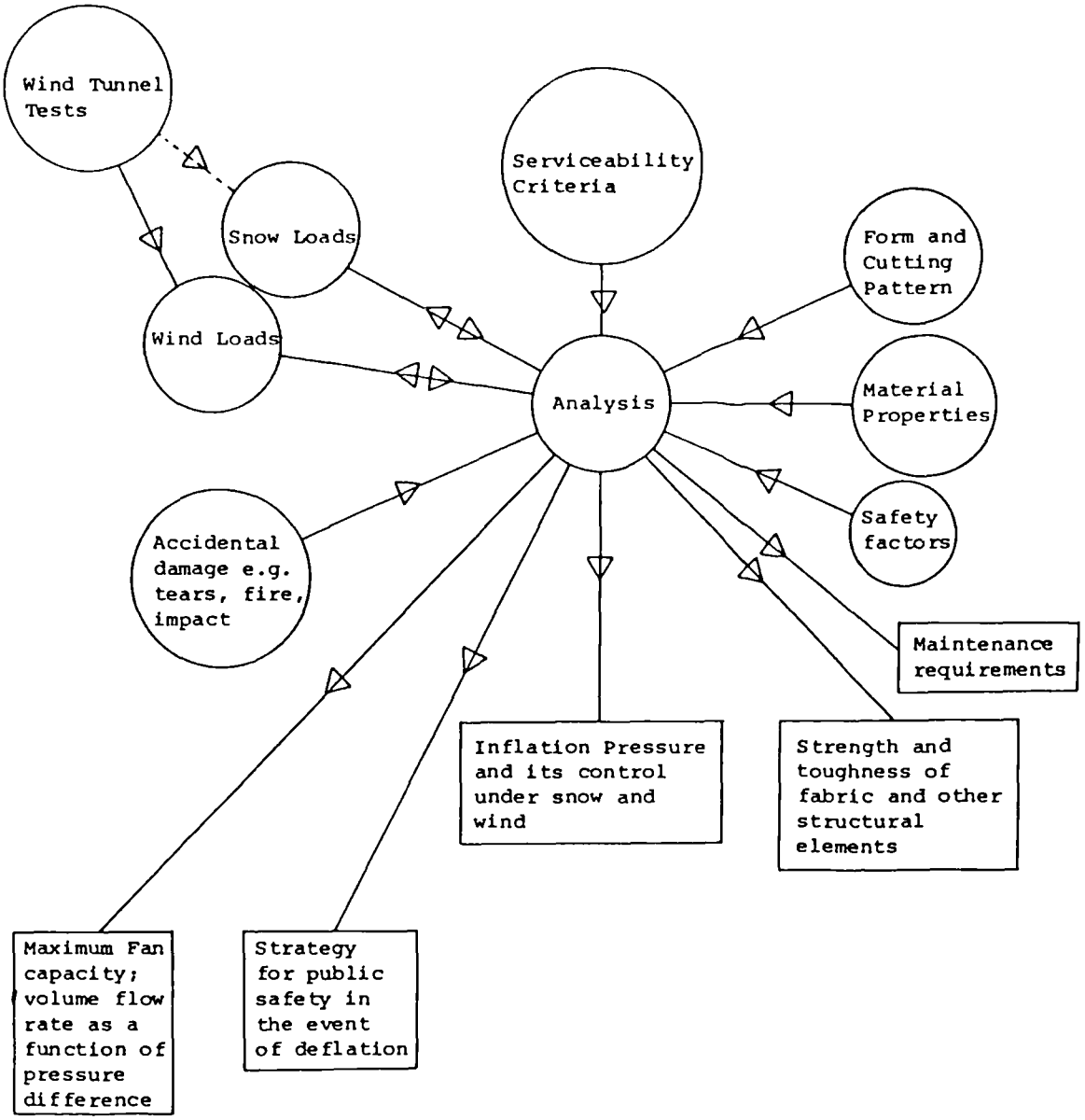
Wind Tunnel Tests
Snow Loads
Wind Loads
Serviceability Criteria
Form and Cutting Pattern
Analysis
Material Properties
Safety factors
Accidental damage e.g. tears, fire, impact
Maintenance requirements
Inflation Pressure and its control under snow and wind
Strength and toughness of fabric and other structural elements
Maximum Fan capacity; volume flow rate as a function of pressure difference
Strategy for public safety in the event of deflation

Figure 1.1

CHAPTER 2

Wind as a flow of fluid

Contents:

Basic terms - Boundary layer growth (flat plate in a uniform flow, flow along curved surface, flow past a cylinder) - Constitutive equations of fluid mechanics (equation of continuity, equations of motion) - Review of solutions for potential flow (exact analytical solutions, approximate solutions, exact numerical methods) - Solutions for flow of a real fluid (laminar boundary layer, turbulent boundary layer) - Similitude law.

2.1 Basic terms

Wind response of flexible structures should be viewed as a process involving interaction between inertial (dynamic), elastic (solid mechanics) and aerodynamic (fluid mechanics) forces. Although all three factors are very important, the movement of air (wind) is the one which starts the phenomenon, and is probably the most difficult to define. Therefore, an investigation of fluid-structure interaction should commence with a brief review of those aspects of fluid mechanics which have a direct application to wind engineering.

All materials exhibit deformation under the action of forces:-

elasticity, when a given force produces a definite deformation, which vanishes if the force is removed;

plasticity, if the removal of the forces leaves permanent deformation;

flow, if the deformation continually increases without limit under the action of forces, however small. A fluid is material which flows. A gas (air) is a fluid which is capable of filling any closed space to which it has access and is classified as a compressible fluid. The importance of compressibility is measured by the non-dimensional parameter of Mach number: the ratio of inertia to elastic forces, (which is also the ratio of the flow velocity to the speed of sound in air). For wind speeds below 50 m/s, at which the Mach number is 15, the effect of compressibility on wind pressure is less than 5% and, therefore, the air can be treated as incompressible. Another important aspect of fluid flow is viscosity. This is often regarded as the 'stickiness' of a fluid and it is its tendency to resist sliding between layers; more rigorously, the rate of change of shear strain.

The most common descriptions of fluid flow are:-

1. Steady - the velocity at each point is independent of the time and flow pattern, and is the same at each instant,
2. Unsteady - the velocity is fluctuating with time (opposite to steady),
3. Uniform - the velocity is the same at each point of the flow,
4. Non-uniform - opposite to uniform (i.e. the velocity is changing from one point in space to another),

5. Laminar - the flow movement of particles is smooth, behaving very much like laminae or layers), sliding over each other, and
6. Turbulent- the particle behaviour may be entirely random, with individual particles and groups of particles spinning and rotating and moving first in one direction, then in another, with no order or method except that the whole aggregate is proceeding in the streaming direction. This is an essentially three-dimensional phenomenon.

The quality of flow immediately adjacent to a surface is of great importance. In this region, called the boundary layer, a mean speed of flow increases from zero at the surface to the full streaming speed far away from the body. Closer experimental study of boundary-layer flows discloses that there are two different types of boundary layer:-

1. the laminar boundary layer - in which energy from the main stream is transmitted towards the slower moving fluid near the surface through the medium of viscosity alone, and only a relatively small penetration of energy to the layer close to the surface results. Consequently an appreciable proportion of the boundary-layer flow has a considerably reduced velocity.

Throughout the layer, the shearing stress, τ, is given by Newton's law of viscosity

$$\tau = \mu \frac{\partial u}{\partial y} \qquad 2.1$$

where μ is a dynamic viscosity, which can be assumed constant,

u, is the velocity in the x direction (see figure 2.1) and

$\frac{\partial u}{\partial y}$ is the velocity gradient across the streaming direction.

The laminar boundary layer can be visualised as a movement of particles in infinitesimally thin layers, with each layer having a different speed. The interface between these layers can be represented by a row of very small elemental vortices arranged as shown in figure 2.2. Each elemental vortex contributes a velocity that adds to the mean flow velocity on one side and subtracts from it on the other side. The circulation, k, is distributed along the line of the interface (or the surface in 3-D). This distribution of circulation is defined as the vorticity, ζ ,

$$\zeta = \frac{dk}{dx} \qquad 2.2$$

2. <u>the turbulent boundary layer</u> - in which there is an appreciable transport of mass between layers. The shearing stresses which occur in the flow are the result of viscous action and mass interchanges in a direction perpendicular to the surface. The total shear stress is given by:

$$\tau_t = \tau + \bar{\tau} \qquad 2.3$$

where:

τ - is viscous shear stress given by eq. 2.1,

and

$\bar{\tau}$ - is the Reynolds stress, or turbulent mean stress.

In turbulent boundary layer motion, a considerable random motion exists in the form of velocity fluctuations, both along the mean direction of flow and perpendicular to it. As a result, energy from the main stream may easily penetrate to fluid layers quite close to the surface and therefore the velocity in these layers is not much less than that of the main stream. However, in layers which are very close to the surface (here assumed smooth) it is impossible for velocities to exist perpendicular to the surface, so in a very limited region immediately adjacent to the surface the flow approximates to laminar flow creating a laminar sub-layer (shearing action becomes purely viscous).

Typical mean velocity profiles in the two types of boundary layer are shown in figure 2.1.

The shape of the turbulent boundary layer velocity profile depends very much upon Reynolds number (the ratio of inertia force to viscous force) and the surface roughness. Figure 2.3 (from [92]) shows experimental curves for the velocity profiles of turbulent boundary layers on flat walls which are smooth (a surface is considered to be aerodynamically smooth if the height of surface irregularities is less than the thickness of the laminar sub-layer) or rough, and with varying Reynolds number.

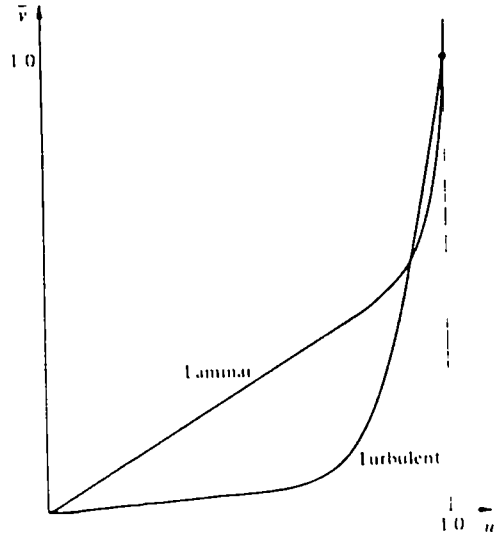

$\bar{u} = \frac{u}{u_1}$

u_1 - main stream velocity

$\bar{y} = \frac{y}{\delta}$

δ - the physical thickness of the boundary layer

Figure 2.1

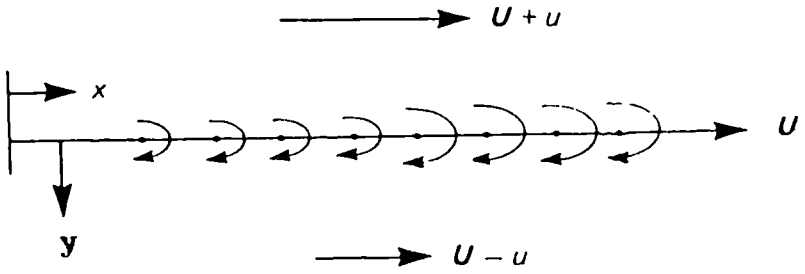

Figure 2.2

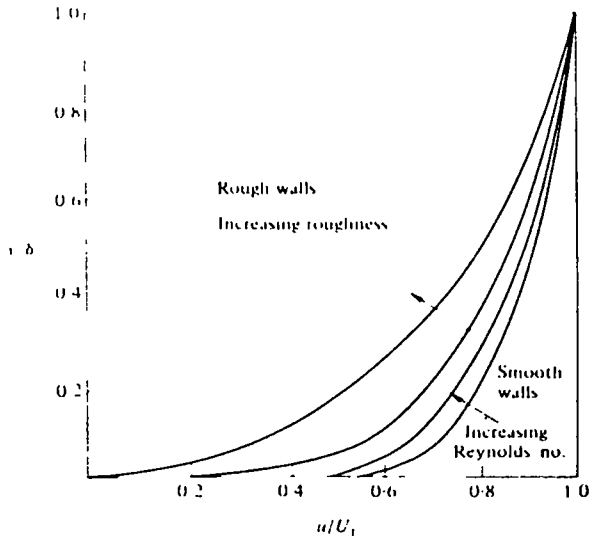

Figure 2.3

2.2 Boundary layer growth (in two dimensions)

2.2.1 Flat plate in a uniform flow (figure 2.4)

When a flat plate is placed in parallel flow at zero incidence, the static pressure remains constant in the whole field of flow. A laminar layer starts to develop from the leading edge, then grows in thickness along the surface until at some point a sudden transition to a turbulent layer occurs. Because of the greater shearing stresses within the turbulent layer, its thickness increases more rapidly than that of the laminar layer. At the trailing edge, the boundary layer joins with that from the other surface of the plate to form a wake of retarded velocity which tends to thicken as it flows away downstream.

2.2.2 Flow along a curved surface

In the case of flexible structures, their shapes, if not highly curved, at least exhibit some degree of curvature, which causes a departure from the flat-plate boundary layer growth. The major difference is that the main-stream velocity, and hence the static pressure in a streamline direction, is no longer constant. Over the leading part of the body the pressure gradient is negative; that is, the static pressure of the free stream decreases along the flow direction. This inhibits the growth of the laminar layer, which is as a rule thinner than its counterpart on the flat plate.

Over the rear portion, and in any flow situation where the pressure gradient is positive in the flow direction (figure

2.5), the boundary layer thickens rapidly and the flow may separate from the surface of the body before the rearmost point is reached.

Referring to figure 2.5, the net pressure force on a small element of fluid say ABCD, is such that it tends to retard the element's velocity. This retarding force is in addition to the viscous shear which acts along AB and CD and it continuously slows down the element as it progresses downstream. This slowing-down effect is more pronounced near the surface, where the elements are remote from the accelerating effect of the main stream.

Ultimately, at a point S on the surface, the velocity profile slope $\partial u/\partial y$ becomes zero. Apart from the change in shape of the profile, the layer must thicken rapidly under these conditions in order to satisfy continuity within the layer. Downstream of point S, the flow adjacent to the surface may well be in an upstream direction, so that a circulatory movement, in a plane normal to the surface, may take place near the surface. A line may be drawn from the point S dividing the flow into two; below the separating line a circulatory movement, and above a continuation of the mass flow of the boundary layer behind the point S. In effect, the original boundary layer is separated from the surface at point S, which is termed the separation point.

Reference to the velocity profiles for laminar and turbulent layers shows that, due to the greater extent of fluid of

lower energy near to the surface in the laminar layer, the effect of a positive pressure gradient on such a laminar layer will cause separation of the flow much more rapidly than if the layer were turbulent.

The result of separation on the rear half of a body is to increase the thickness of the wake flow, with a consequent reduction in the pressure rise, which should occur at the rear. Sometimes the separation point may be followed by a reattachment point, where the circulatory movement near the surface has disappeared.

The transition from laminar to turbulent flow usually occurs at some point along the surface. The process of transition and the factors which determine its position are still not fully understood [177]; although it is known that a shearing velocity gradient is essential to the generation of turbulence. Up to certain values of Reynolds Number $(Re)_x$, (typically 9×10^8 $((Re)_x = \frac{U\,x}{\nu}$, where U is the local mainstream velocity, ν is the kinematic viscosity in the mainstream, and x is the distance from the leading edge along the surface in a streamline direction), small turbulences in the laminar flow may be damped out, as only fluctuations with a wavelength of the order of the shear-layer thickness are amplified. At large Reynolds numbers a range of disturbances is amplified and transition is possible though not inevitable.

Free stream turbulence is a cause of early transition and low turbulence is necessary to maintain a laminar layer. Conversely, roughness of the surface will tend to initiate transition in a laminar layer, but cannot cause transition directly. It can only alter the shape of the mean-velocity profile so that the shear layer becomes unstable at a lower Reynolds Numbers and/or amplifies the existing velocity fluctuations more quickly. The velocity profile becomes unstable due to the positive streamline pressure gradient (a positive gradient tending to cause earlier transition, and a negative gradient later transition).

It should be borne in mind that a positive pressure gradient may cause either separation or transition. The positive gradient causes deceleration of the fluid particles in the boundary layer. If the particles are all moving in parallel straight lines, this will cause separation. Suppose for example, that a small lateral disturbance is imposed on a particle so that its path line becomes deflected; then the effect of the positive pressure gradient tends immediately to increase the deflection of the path line. Since this sort of process will happen throughout the layer, it is evident that general turbulence can rapidly ensue.

2.2.3 Flow past a cylinder

A circular cylinder held in a stream which is otherwise uniform and with changing velocities is shown in figure 2.6.

At very low Reynolds number (here $R_e = \frac{U_\infty D}{\nu} < 1$, where U is the free stream velocity, and D is the cylinder

diameter), the flow behaves as if it were purely viscous and the boundary layer extends to infinity. At slightly higher values of R_e (> 10) the boundary remains laminar over the whole surface and separation occurs on either side near the rear of the cylinder. A narrow turbulent wake thus develops. With further increase of the Reynolds number the separation points on either side move further apart in the upstream direction increasing the width of the wake.

At values of R_e somewhere between 60 and 140, a pair of symmetrical vortices will begin to develop on either side of the centre line behind the laminar separation points, continuously stretching downstream until a stage is reached when they become unsymmetrical ($140 < R_e < 5 \times 10^4$) and the system breaks down. The subsequent wake motion is oscillatory in character and will generate a transverse force on the cylinder. If the frequency of vortex-shedding coincides with the natural transverse frequency of the cylinder then appreciable vibration may be caused.

At a stage when R_e is between 4×10^5 and 5×10^5 the condition is reached when transition to turbulence occurs before separation. The points of separation which now occur in a turbulent layer move suddenly downstream and the wake width is very appreciably decreased.

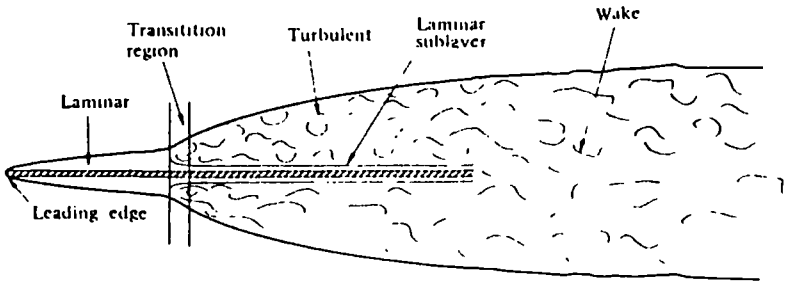

Figure 2.4

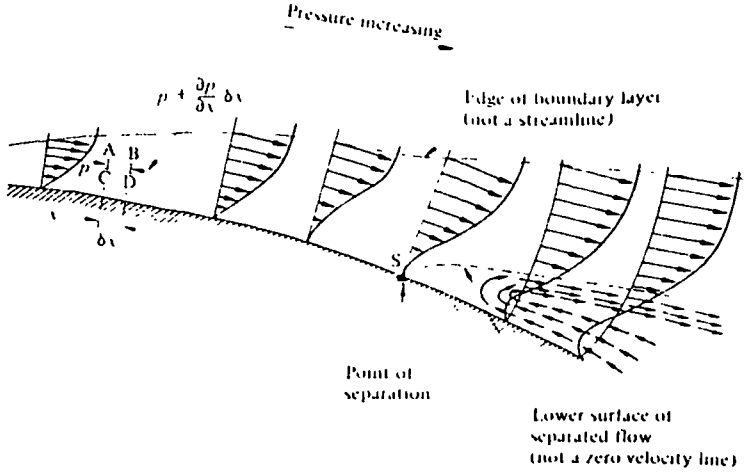

Figure 2.5

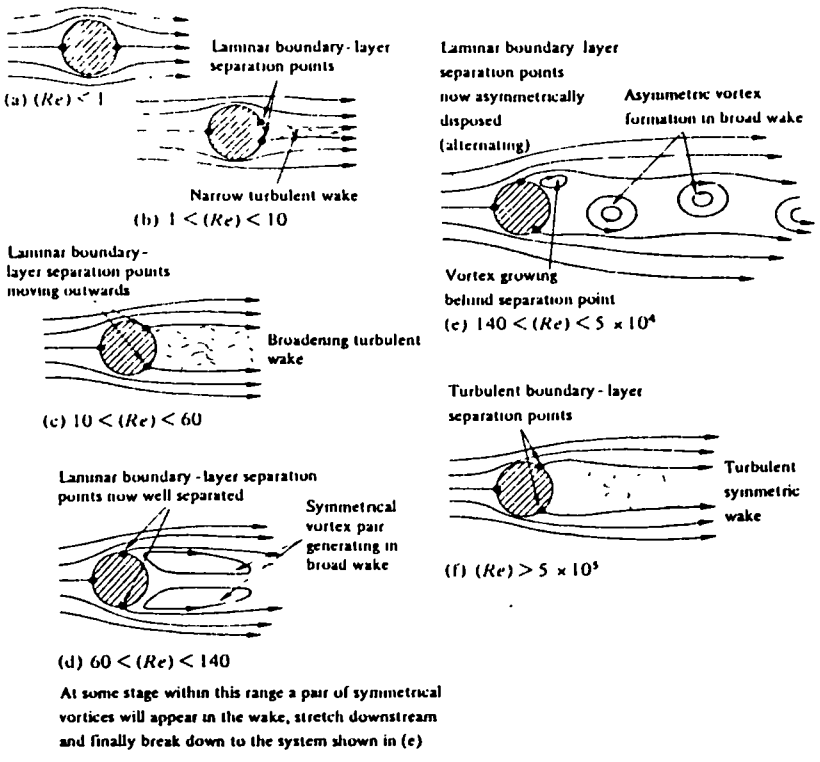

Figure 2.6

2.3 Constitutive equations of fluid mechanics

There are two basic means of describing the motion of a fluid. In the Eulerian view attention is directed to a particular point of space. As time elapses this point is occupied by a succession of fluid particles. The position of this point and time are independent variables.

From the Lagrangian or historical point of view attention is focused on a particular fluid particle and its progress is followed. The independent variables are: the initial position vector of a particle and the time.

The Eulerian view is more common in fluid mechanics and will be adopted in this chapter.

Fluids, like solids, obey the principles of conservation of mass, momentum and energy.

2.3.1. Equation of continuity

The equation of continuity (conservation of mass) expresses the fact that for a unit volume there is a balance between masses entering and leaving per unit time, and the change in density.

$$\frac{\partial \rho}{\partial t} = \nabla (\rho \vec{q}) = 0 \qquad 2.4$$

where:

ρ is density,

$\vec{q}$ is a velocity, $q = \vec{\imath}u + j\vec{v} + \vec{k}w$, and

$$\nabla(\rho \vec{q}) = \frac{\partial \rho u}{\partial x} + \frac{\partial \rho v}{\partial y} + \frac{\partial \rho w}{\partial z}$$

In the case of an incompressible fluid, $d\rho/dt = 0$, and equation 2.4 takes the form:

$$\nabla \vec{q} = 0 \qquad 2.5$$

or, using cartesian co-ordinates:

$$\frac{\partial u}{\partial x} + \frac{\partial v}{\partial y} + \frac{\partial w}{\partial z} = 0 \qquad 2.5a$$

2.3.2 Equations of motion

The equations of motion for a fluid are derived from Newton's second law, which states that the product of mass and acceleration is equal to the sum of the external forces acting on a body. In fluid motion it is necessary to consider two classes of forces: those acting throughout the mass of the body (like gravitational forces), and those forces which act on the boundary (pressure and friction).

The equation of motion can be written:

$$\rho \frac{dq}{dt} = \vec{F} + \vec{P} \qquad 2.6$$

where:

$\bar{F} = \bar{i} X + \vec{jK} + kZ$ is a body force,

$\bar{P} = \vec{i} p_x + \vec{j} p_y + \vec{k} p_z$ is a surface force, and

$\frac{dq}{dt}$ presented in cartesian co-ordinates is:

$$\frac{du}{dt} = \frac{\partial u}{\partial t} + u\frac{\partial u}{\partial x} + v\frac{\partial u}{\partial y} + w\frac{\partial u}{\partial z}$$

$$\frac{dv}{dt} = \frac{\partial v}{\partial t} + u\frac{\partial v}{\partial x} + v\frac{\partial v}{\partial y} + w\frac{\partial v}{\partial z} \qquad 2.7$$

$$\frac{dw}{dt} = \frac{\partial w}{\partial t} + u\frac{\partial w}{\partial x} + v\frac{\partial w}{\partial y} + w\frac{\partial w}{\partial z}$$

The body forces do not present any problem as they are generally known, but the surface forces depend on the rate at which the fluid is strained by the velocity field present in it.

The stress in a constant density fluid acting on x, y, z planes can be represented as:

$$\begin{aligned} p_x &= i\,(\sigma_x - p) + j\,\tau_{xy} + k\,\tau_{xz} \\ p_y &= i\,\tau_{yx} + j\,(\sigma_y - p) + k\tau_{yz} \\ p_z &= i\,\tau_{zx} + j\,\tau_{zy} + k(\sigma_z - p) \end{aligned} \qquad 2.8$$

where

σ_x, σ_y, σ_z are internal normal stresses,

τ_{xy}, τ_{xz} are internal shear stresses,

and p is a pressure

By analysing a small parallelepiped of volume dv = dx dy dz, the resultant surface force P per unit can be found to be [38]:

$$p = i\,\frac{\partial p_x}{\partial x} + j\,\frac{\partial p_y}{\partial y} + k\,\frac{\partial p_z}{\partial z} \qquad 2.9$$

Substituting equation 2.8 into 2.9 and then into 2.6, the following equations are obtained:

$$\begin{aligned} \rho\,\frac{du}{dt} &= X + \left(\frac{\partial \sigma_x}{\partial x} + \frac{\partial \tau_{xy}}{\partial y} + \frac{\partial \tau_{xz}}{\partial z}\right) - \frac{\partial p}{\partial x} \\ \rho\,\frac{dv}{dt} &= Y + \left(\frac{\partial \tau_{xy}}{\partial x} + \frac{\partial \sigma_y}{\partial y} + \frac{\partial \tau_{yz}}{\partial z}\right) - \frac{\partial p}{\partial x} \\ \rho\,\frac{dw}{dt} &= Z + \left(\frac{\partial \tau_{xz}}{\partial x} + \frac{\partial \tau_{yz}}{\partial y} + \frac{\partial \sigma_z}{\partial z}\right) - \frac{\partial p}{\partial z} \end{aligned} \qquad 2.10$$

Stoke's law, which is empirical, like Hooke's law, gives for the surface stresses:

stress = 2 μ (rate of strain)

for example

$$\sigma_x = 2\,\mu\,(\frac{\partial u}{\partial x}) \qquad 2.11$$

$$\tau_{xy} = \mu\,(\frac{\partial u}{\partial y} + \frac{\partial v}{\partial x})$$

If μ (the viscosity) is constant and the flow is incompressible, $\Delta \vec{q} = 0$, and substituting 2.11 into 2.10 results in one form of the Navier-Stoke's equations:

$$\frac{d\bar{q}}{dt} = \bar{F} - \frac{1}{\rho}\nabla p + \frac{\mu}{\rho}\nabla^2 \bar{q}^2 \qquad 2.12$$

In cartesian co-ordinates, for the x direction, equation 2.12 takes the form:

$$\frac{\partial u}{\partial t} + u\frac{\partial u}{\partial x} + v\frac{\partial u}{\partial y} + w\frac{\partial u}{\partial z} = X - \frac{1}{\rho}\frac{\partial p}{\partial x} + \frac{\mu}{\rho}(\frac{\partial^2 u}{\partial x^2} + \frac{\partial^2 u}{\partial y^2} + \frac{\partial^2 u}{\partial z^2}) \qquad 2.12a$$

The unsteady Navier-Stoke's equations (2.12) and the continuity equation (2.4) are instantaneously valid in turbulent flow. Because the equations are nonlinear, however, the time-mean velocity components and the pressure do not obey the Navier-Stoke's equations.

The time mean of a quantity ϕ, denoted by $\bar{\phi}$ is defined as:

$$\bar{\phi} = \lim_{T\to\infty} \frac{1}{T} \int_0^T \phi\, dt \qquad 2.13$$

Expressing all the instantaneous quantities, u, v, w, p and X (equations in the y and z directions can be transformed in a similar way) as the sum of time mean-values (with the overbar omitted for simplicity) and fluctuating parts u', v', w', p', X', equation 2.12a becomes [38]:

$$u\frac{\partial u}{\partial x} + v\frac{\partial u}{\partial y} + w\frac{\partial u}{\partial z} = X - \frac{1}{\rho}\frac{\partial p}{\partial x} + \frac{\mu}{\rho}\left(\frac{\partial^2}{\partial x^2} + \frac{\partial^2}{\partial y^2} + \frac{\partial^2}{\partial z^2}\right) u$$

$$- \frac{\partial \overline{u'w}}{\partial x} - \frac{\partial \overline{u'v}}{\partial y} - \frac{\partial \overline{u'w'}}{\partial z} \qquad 2.14$$

The first line in the above equation is the equation for steady viscous (laminar) flow and the second line contains the gradients of the extra turbulent quantities divided by density.

The quantities $\rho\overline{u'u'}$, $\rho\overline{u'v'}$ and $\rho\overline{u'w'}$ are mean rates of transfer, by turbulence, of the u component of moment through the faces of the small parallelepiped of volume dxdydz, perpendicular to x, y and z respectively. The extra turbulent stresses (the Reynolds stresses) can be summarized by the following array:

$$\begin{vmatrix} q_x & \tau_{xy} & \tau_{xz} \\ \tau_{yx} & \sigma_y & \tau_{yz} \\ \tau_{zx} & \tau_{zy} & \sigma_z \end{vmatrix} \equiv -\rho \begin{vmatrix} \overline{u}'^2 & \overline{u'v'} & \overline{u'w'} \\ \overline{u'v'} & \overline{v}'^2 & \overline{v'w'} \\ \overline{u'w'} & \overline{v'w'} & \overline{w}'^2 \end{vmatrix} \qquad 2.15$$

In tensor notation the total stress (viscous term added to turbulent stress) is:

$$\sigma_{ij} = -\rho\overline{u}'_i\ \overline{u}'_j + \mu\left(\frac{\partial u_i}{\partial x_j} + \frac{\partial u_j}{\partial x_i}\right) \qquad 2.16$$

For i = j = 1 it takes the form:

$$\sigma_x = -\rho \overline{u'^2} + 2\mu \left(\frac{\partial u}{\partial x}\right) \qquad 2.16a$$

and, as an example, for i = 1 and j = 2

$$\tau_{xy} = -\rho \overline{u'v'} + \mu \left(\frac{\partial u}{\partial y} + \frac{\partial v}{\partial x}\right) \qquad 2.16b$$

The continuity equation, 2.5, is linear, hence its mean is $\nabla\bar{q} = 0$, as well as $\nabla\bar{q}' = 0$.

The Reynolds stresses appear as extra unknowns in the mean-motion equations (equation 2.14 and similar equations for the y and z directions). The central problem of turbulent flow is to find empirical expressions for them.

Boussinesq (1877) attacked the problem by assuming that the turbulent stresses are proportional to the velocity gradient (similar to viscous stresses). The coefficient of proportionality, ε_m, was called the eddy viscosity and was defined by:

$$-\rho \overline{u'v'} = \rho \varepsilon_m \frac{\partial u}{\partial y} \qquad 2.17$$

Here, ε_m, can be thought of as the product of a velocity and a length.

Prandtl (1925) developed a theory called the mixings - length theory, where he proposed that the Reynolds stress should be calculated from:

$$- \rho \overline{u'v'} = \rho l^2 \left| \frac{\partial u}{\partial y} \right| \frac{\partial u}{\partial y} \qquad 2.18$$

Using equation 2.17 we can write the following relation between viscosity and mixing length:

$$\varepsilon_m = l^2 \left| \frac{\partial u}{\partial y} \right| \qquad 2.19$$

According to Von Karman's hypothesis, the length l defined by equation 2.18 is given by:

$$l = k \left| \frac{\partial u/\partial y}{\partial^2 u/\partial y^2} \right| \qquad 2.20$$

Where k is an empirical constant known as Von Karman's constant.

In the case of an ideal fluid (incompressible with no viscosity) equation 2.12 takes the form known as Euler's equation of motion:

$$\frac{d\bar{q}}{dt} = \bar{F} - \frac{1}{\rho} \nabla p \qquad 2.21$$

2.4 Review of solutions for potential flow

In the absence of viscous and other rotational forces, an assumed irrotational flow upstream will remain so in the region in consideration. Letting $\bar{q}$ denote the velocity field in this region, the irrotationality condition states that the velocity vanishes; that is

$$\bar{\nabla} \times \bar{q} = 0 \qquad 2.22$$

The preceding equation is automatically satisfied, if a velocity potential ϕ is introduced such that

$$\bar{q} = \bar{\nabla} \phi \qquad 2.23$$

For this reason, irrotational flows are also called potential flows.

As a result of introducing the velocity potential, the velocity vector (generally having three components) is replaced by a single scalar quantity ϕ.

Substituting equation 2.23 into 2.22 yields the continuity equation for incompressible potential flow as follows:

$$\nabla^2 \phi = 0 \qquad 2.24$$

Where $\nabla^2 = \nabla \cdot \nabla$ is the Laplacian operator, and equation 2.24 is called the Laplace equation.

The equation of motion 2.21 for potential and incompressible flow can be presented in integrated form:

$$\rho \frac{\partial \phi}{\partial t} + p + \frac{1}{2} \rho q^2 = H \qquad 2.25$$

which is known as Bernoulli's equation, with H being a constant of integration.

The problem of incompressible potential flow past a streamline body is commonly solved in two steps [39]:

1. A velocity potential is found by solving the Laplace equation 2.24, which satisfies both the boundary condition prescribed far upstream and the requirement that the fluid velocity be tangent to the body surface. The latter condition is justified by the fact that the boundary layer around the body is assumed to be thin.

2. Then the pressure field can be computed from Bernoulli's equation and expressed as a distribution of pressure coefficients. The pressure coefficients, C_p, are defined as:

$$C_p = \frac{p-p_\infty}{\frac{1}{2}\rho|\bar{q}_\infty|^2} \qquad 2.26$$

Where p_∞ and q_∞ are respectively the pressure and velocity at infinity;
and for steady flow, by employing equation 2.25, C_p is expressed as:

$$C_p = 1 - \frac{|\bar{q}|^2}{|\bar{q}_\infty|^2} \qquad 2.27$$

2.4.1. Exact analytical solutions

Despite the fact that Laplace's equation is one of the simplest and best known of all partial differential equations, the number of useful exact analytical solutions satisfying the boundary conditions is quite small, and valid only for an extremely limited class of boundary surfaces.

In axisymmetric and three-dimensional cases the direct problem of potential flow can be solved analytically only by the technique of separation of variables. For this technique to be applicable, the boundary must be a co-ordinate surface of one of the special orthogonal co-ordinate systems for which Laplace's equation can be separated into ordinary differential equations. The only exact analytic solution of the direct problem of potential flow about a closed axisymmetric or three-dimensional body is that for the general ellipsoid and its specialisations [90].

In two-dimensional cases Laplace's equation is simply separable in all orthogonal co-ordinate systems. This technique is not commonly used, because in two dimensions the direct problem of potential flow can be replaced by the problem of finding a suitable conformal transformation of the boundary. The use of this latter method has resulted in a considerable number of useful potential flow solutions [41].

There is also a fairly large number of two-dimensional and axisymmetric solutions available from indirect methods. In such approaches, first suggested by Rankine in 1871, a set of known singularities is hypothesised to exist in the fluid; usually in the presence of an onset flow. The singularities most often used are: point sources, line sources, doublets and vortices. For these, the fluid velocity and pressure at any point can easily be obtained. For two-dimensional and axisymmetric flows, the total stream function of the singularities and the onset flow may be utilised to calculate streamlines, any one of which may then be considered to be a boundary surface [41]. A similar procedure could be followed in three dimensions, but it would be considerably more difficult because of the absence of a simple stream function.

It is clear that the variety of boundary shapes for which exact analytic solutions can be obtained is far too limited to be of much use in practical applications, especially in the case of flow about bodies of irregular shape.

2.4.2. Approximate solutions

Because exact analytic solutions are scarce and exact numerical methods had been (up to the nineteen-sixties) beyond the capability of hand computation, approximate solutions in the past received most of the attention of investigators of potential flow problems. Many approaches have been formulated. Some are analytic, in that the general solution can be written in a simple closed form, and

other are numerical in that considerable computation is required to obtain a solution for each specific case.

A large and well-known class of approximate solutions uses one or both of the following assumptions:

a) the body is slender, with small local surface slope,

b) the perturbation-velocity components due to the presence of the body are small with respect to the uniform stream (i.e. the onset flow).

Another type of approximate solution utilises a distribution of singularities interior to the body surface. For example, the singularities are normally placed along the chord or camber line for two-dimensional aerofoils, along the axis of symmetry for axisymmetric bodies, and on the surface for three-dimensional shapes. Various types of singularities are used, for example: sources, dipoles, vortices etc., both discrete and distributed. The locations and general properties of the singularities are assumed, and their strengths are determined so that boundary conditions are satisfied in some sense on the body surface.

Some of these methods, although they yield only approximate solutions, are well suited for particular cases. A prolate spheroid in a uniform stream parallel to the axis of symmetry can be exactly represented by a source distribution of linearly varying strength located along the axis of symmetry between the focii [90].

Other examples are vortex-lattice methods, which use a distribution of vortices in the form of horse-shoes. These methods are particularly well suited to analyse lifting surfaces like, for example, thin wings. Typical among these is the method of reference 175, which provides general nonplanar capability, uses nonlinear boundary conditions, and computes forces and surface pressures without the small-disturbance assumptions common to classical planar wing theories.

2.4.3. Exact numerical methods

The exact numerical methods approach to solving arbitrary subsonic potential flow problems involves the mating of classical potential theory with contemporary numerical techniques. Classical theory is used to reduce an arbitrary flow problem to a surface integral equation relating boundary conditions to an unknown singularity distribution. Contemporary numerical techniques are then used to calculate an approximate solution to the integral equation. This involves representing flow boundaries by surface panels on which potential flow singularities are distributed. The problem is then to determine their strengths to produce a flow field satisfying the boundary conditions.

Whereas there is no limit to the number of different singularity distributions that can induce a given flow field, the type of singularity plays an important role in determining the success of a numerical solution method. The advantages of using the combined source-doublet

distribution, corresponding to the classical third identity of Green, are described and demonstrated in reference 30.

Green's third identity shows [149] that any solution of Laplace's equation may be expressed as the perturbation potential induced by a combination of source singularities of strength σ, and doublet singularities of strength μ, distributed on the surface of the body:

$$\phi(p) = \iint_B \sigma(Q) \left(-\frac{1}{4\pi r}\right) ds + \iint_B \mu(Q) \frac{\partial}{\partial n_Q} \left(\frac{1}{4\pi r}\right) ds \quad 2.28$$

Where

r - is the distance from the field point P to the boundary (surface of the body) point Q, and $\frac{\partial}{\partial n_Q}$ is the derivative in the direction of the surface normal.

There are varieties of different methods depending upon the way singularities are located [176]; for example: constant-strength source panel method, constant-strength doublet panel method, doublet column panel method, or doublet network panel method. When the idea was first conceived by Hess and Smith [90], the surface of the body was approximated by flat panels, but there soon followed more sophisticated methods which used curved panels with varying strength of singularities [30, 31, 72, 139, 176].

Some efforts have been made to simulate phenomena such as separation [3], or rolled tip vortex sheets [199] - caused by viscosity, and thus not directly obtainable from pure potential flow.

2.5 Solutions for flow of a real fluid

2.5.1 Laminar boundary layer

The motion of fluid in a laminar boundary layer is described by equations 2.5 and 2.12 together with appropriate boundary conditions. Generally speaking, the process of obtaining analytical solutions of the boundary layer equations encounters considerable mathematical difficulties. The differential equations are non-linear in most cases, so they can be solved only by power-series expansions or by numerical methods.

There are in existence comparatively few exact analytical solutions [41], and they are for very simple geometric boundary conditions.

For two-dimensional cases it is convenient to represent the governing equations in terms of the vorticity vector $\bar{\Omega}$, the velocity vector $\bar{U}$, and the stream function Ψ. This has the advantage of eliminating the pressure. These equations are [77]:

$$\frac{d}{dt} = (\bar{\Omega} - \nabla) \bar{U} + \frac{\mu}{\rho} \nabla^2 \bar{\Omega}$$

$$\nabla^2 \Psi = - \bar{\Omega} \qquad 2.29$$

$$\bar{U} = \nabla \times \Psi$$

For three-dimensional flows, it is necessary to define multiple stream functions and therefore the problem becomes somewhat more complex. For this reason, there have been relatively few calculations in 3D using equations 2.29 [80].

Numerical methods to solve equations 2.5 and 2.12 require mapping the surface of the body and the surrounding fluid so far as there is any interference of the body into the fluid. In three dimensions the task can be enormous. A wide variety of basic techniques have been used, for example, finite-difference, finite element, spectral or pseudo-spectral and vortex or integral methods. Each has to be integrated into a mesh. In general the computation of viscous phenomena, with any useful degree of practical resolution, leads to systems of equations that for efficiency, have to be solved using some form of an implicit numerical method.

2.5.2 Turbulent boundary layer

Most flows which occur in practical applications are turbulent and they are usually defined in terms of quantities representing the mean and fluctuating parts of a variable, as shown when Navier-Stokes equations were discussed. The turbulent boundary layer is described by a combination of the Navier-Stoke equations 2.14, the Reynolds stresses 2.16, the continuity equation 2.5, and the boundary conditions which require that the mean velocity components and all turbulent fluctuations vanish at solid boundary walls.

The numerical solutions in a turbulent flow are even more difficult than in pure viscous flow, because we face the additional problem that there is no reliable general formula for the extra turbulent (Reynolds) stresses. Therefore the

problem cannot be solved unless the extended Navier-Stokes equations are 'closed' by replacing the unknown turbulent quantities, involving Reynolds stresses, by empirical combinations of the existing variables.

Two approaches have been used to model turbulence [80]: the so-called first-order approach, in which the Reynolds stress tensor is modelled in terms of the mean flow quantities; and the second-order approach, in which the terms in the tensor are carried along in the computations as dependent variables expressed in terms of a higher order tensor, which must be modelled.

The first approach forms the basis for the conventional zero-equation (or algebraic), one equation and two equation models. Most of these models are expressed in terms of a turbulence velocity scale, v, and a turbulence length scale, l. On dimensional grounds, a combination of these scales determines the value of the kinetic eddy viscosity

$$\nu_t = C_t \, v l \qquad 2.30$$

where C_t is a constant.
Algebraic models relate ν_t directly to averaged field quantities, but both the one-and two-equation models contain additional partial differential equations for the turbulence scales.

The simplest models use, for the turbulence velocity and length scales, equations that apply uniformly throughout the flow. More elaborately, the distributions of v and l are

prescribed by different expressions for so-called "inner" and "outer" layers.

For the simplest models of Reynolds stresses, the general numerical techniques for turbulent flow are basically the same as in laminar flow. More sophisticated models require a finer mesh than those employed in laminar boundary layer solutions.

2.6 Similitude law

Most real fluid flow problems can be solved, at best, only approximately by analytical or numerical methods. Thus, experiments play a critical role in verifying solutions, in suggesting which approximations are valid, or in providing results that cannot be obtained by theoretical analysis or numerical simulation. Unfortunately most real flow situations are far too large for conventional experiment at their true size. The field conditions are so uncontrolled as to make systematic study tedious and very expensive, so in many cases are impossible to model. When testing of the real system (that is, the prototype) is not feasible, a model (that is to say, a scale version of the prototype) can be constructed and the performance of the prototype determined from that of the model.

Similitude of flow phenomena should not only occur between a prototype and its model but also between the various natural phenomena. There are three basic types of similitude [193], all of which must be obtained if complete similarity is to

exist between fluid phenomena. They are:

1. Geometric similarity, which states that the flow fields and boundary geometry of the model and *prototype have* the same shape and therefore that the ratios, λ, between corresponding lengths, areas and volumes in the model and prototype are the same;
2. Kinematical similarity - the ratios of corresponding velocities and accelerations of the model and prototype are the same throughout the flow, and equal to λ ;
3. Dynamic similarity - the ratio of all forces acting on any fluid mass should be maintained on all the corresponding fluid masses throughout the flow fields, and equal to λ.

The above types of similitude can be expressed as scale factors between the model and the prototype in each of the three primary dimensions of mass, length and time, hence:

Length scale factor $\mathcal{L}$ = model length/prototype length

Mass scale factor $\mathcal{M}$ = model mass/prototype mass

Time scale factor $\mathcal{T}$ = model time/prototype time

The similitude law is presented here in very general terms; each particular situation requires listing all physical quantities which have potential roles in determining the behaviour of the prototype. Then, by applying the Buckingham's (PI) Theorem [193], the physical quantities are transferred to non-dimensional parameters, which number is k less than the number of the physical quantities, where k is the number of independent dimensions (equal to three, if all principal dimensions are involved).

In the case of wind loading on structures this procedure yields [45] the following typical set of non-dimensional parameters:

z/D - height above ground (typical length variable)

$V(z)/\bar{V}$ - wind speed coefficient (typical velocity variable)

z_o/D - roughness number (ground roughness/structure rise)

ρ_s/ρ_a - density number (inertia of structure/inertia of air)

$nD/\bar{V}$ - Strouhal number (reduced frequency)

$\rho_a\bar{V}D/\mu$ - Reynolds number (inertia of air/viscous forces)

$gD/\bar{V}^2$ - gravity number (gravity forces of structure/inertia of air)

$E/\rho_s V^2$ - elasticity number/elastic forces/inertia of structure)

ζ - structural damping ratio

where

D - is a structural length dimension (the size of a building)

$\bar{V}$ - the mean wind speed at a reference height

ρ_s - the density of structural components

ρ_a - the density of air

z - height above the ground

$V(z)$ - the wind speed at height Z

z_o - the aerodynamic roughness of the ground

n - frequency of the structure

g - acceleration due to gravity

E - the elastic modulus of the structure

ζ - the damping ratio of the structure

Close examination of these non-dimensional parameters leads

to the conclusion that the only scale factor at which complete dynamic similarity is obtained is when $\mathcal{L} = \mathcal{M} = \mathcal{T} = 1$ [45] that is at full scale, and that no 'model' can be completely accurate. The accuracy of a given model depends on which non-dimensional parameters have been matched, and on the significance of those excluded from the matching. These aspects are discussed in more detail in chapter 4.

CHAPTER 3

Modern Approach to Wind Engineering

Contents:

Atmospheric circulations - Wind loading on structures statement of the problem (Fundamental aspects, Division of the problem by scale, Division of the problem by frequency) - Assessment of the problem - Design wind speed data - Assessment of wind loading.

3.1 Atmospheric circulations

Wind, or the motion of air with respect to the surface of the earth, is caused by atmospheric pressure difference which arise from differences in the amount of heat received from the sun. Other forces acting on a given mass of air are due to curvature and rotation of the earth - the Coriolis Forces. At large heights above the earth's surface, where the effects of surface friction can be ignored, and in quasi-steady conditions (i.e. when the weather map is not changing rapidly), the resultant of these forces produces a steady motion, parallel to isobars, which is the so-called gradient wind speed.

The lowest height at which the wind velocity is equal to the gradient velocity lies between 300 m and 3000 m above ground level [84]. Below this height, in what is known as the planetary boundary layer, the wind is retarded by surface friction, so that the total kinetic energy of the flow is reduced. The surface friction also generates fluctuations in the flow (i.e. turbulence), so that there is a transfer

of kinetic energy from the mean flow into these fluctuations. The result is that within this layer the mean wind direction is no longer parallel to the isobars, (the Ekmann Spiral), and its value decreases from the gradient speed at the gradient height to zero at the earth's surface.

At a given height above ground level, the atmospheric pressure is proportional to the mass of the column of air lying above that height. If a mass of air is suddenly transported upwards, it will undergo a rapid adiabatic expansion and consequently its temperature will decrease. Such a rising mass of air can only be in thermal equilibrium with its new surroundings if the air temperature in the atmosphere decreases with increasing height above ground level at a rate equal to the decrease in temperature obtained in the adiabatic movement of the mass of air upwards. If the decrease of atmospheric temperature with height satisfies this condition, the atmosphere is said to be naturally stable, and the temperature to have an adiabatic lapse rate. If the temperature decreases more rapidly than the adiabatic rate, then a vertically rising mass of air will remain hotter and therefore lighter than its surroundings and will continue to rise. Such an atmosphere is said to be unstable. Conversely, if the temperature decreases less rapidly than the adiabatic rate or even increases with height, then a rising mass of air will become heavier, than its new surrounding, and so will tend to sink back again. Such an atmosphere is said to be stable.

In general, the fluctuations in the new flow arise both from mechanical stirring of the mean flow by surface friction and from convection caused by the thermal gradient in the atmosphere. However, most structural wind loading problems are concerned with high wind conditions with (basic hourly-mean wind speeds exceeding 10 m/s). In high winds, surface friction causes so much mechanical stirring of the atmosphere that the thermal effects giving rise to the convection process are destroyed, [84] and the lapse rate is always approximately adiabatic and the stability neutral.

Careful observations of the wind and of chart records from meteorological stations reveal that the variations in wind speeds are not regular, but are highly complex and irregular [82]. This implies that the occurrence of a particular value of wind speed can only be discussed in terms of a probability. Thus, at any instant, a complete description of the flow field is never likely to be available and any useful description of the flow has to be obtained by employing statistical theory.

3.2 Wind loading on structures, statement of the problem

3.2.1 Fundamental aspects

The starting point for any rational consideration of the way wind acts to produce loads on a structure must be an appreciation of three fundamental aspects of the problem [45]. These are:

1. the wind climate, comprising the weather systems that produce strong winds.

2. the atmospheric boundary layer, comprising the lower layer of the atmosphere in which the wind is modified by the rough surface terrain; and
3. the structure, which is immersed in the boundary layer and is itself a single element of the terrain.

In order to estimate the extent of any interaction between the three aspects, the problem has been viewed as a whole by Cook [45] and each aspect presented in terms of its overall scale or by frequency.

3.2.2 Division of the problem by scale

The scale parameters characterising the three fundamental aspects are assumed [45] as:

1. 600 km - a measure for the scale of a typical weather system producing strong winds in temperate latitudes,
2. 2500 m - the scale of the boundary layer. This value is typical for the gradient height in strong wind, and for the 'fetch' (the distance of the terrain upwind of a structure, which influences the wind incident on that structure)
3. 60 m, as a scale of a typical structure (most of the major buildings in the UK are this size or smaller)

Comparing the scales leads to two conclusions:

1. There is negligible interaction between the wind climate and the boundary layer; and
2. Interaction between the boundary layer and the structure is insignificant in terms of scale. The extent of this interaction will depend on the physical properties of the structure in question.

3.2.3 Division of the problem by frequency

The majority of data on the characteristics of wind comes from anemometers mounted near the ground (usually at a standard height of 10 m), and thus contain contributions from the weather systems and from the boundary layer. One method to break down the record into components by frequency is to form the spectrum [45, 92, 153].

The first comprehensive spectrum of this type was compiled by Van der Hoven at Brookhaven, Long Island, NY, USA and is reproduced in Figure 3.1. This spectrum shows three distinct features [45]:

1. A major peak at a centre-frequency of 0.01 cycles/hour, which corresponds to the typical 4-day transit period of fully developed systems, usually called the macrometeorological peak.
2. A second major peak comprising a range of higher frequencies which are associated with the turbulence of the boundary layer and which range in period from about 10 minutes to less than 3 seconds. This is usually called the micrometeorological peak.
3. The well defined gap between these two peaks, in which there is little wind fluctuation over a range of frequency of about one order of magnitude.

Other spectra compiled since this one have all confirmed these three features to be typical of temperate latitudes [45, 92, 182]. The existence of the spectral gap, which separates the spectral components of the wind climate and

the boundary layer, confirms that there is negligible interaction between the wind climate and the boundary layer; hence permitting the separate and independent assessment of these two aspects.

Acquisition of data on the characteristics of wind loads on real full-scale structures is a long and expensive process, hence it is usually only attempted by government research organisations such as the US National Bureau of Standards, the National Research Council of Canada or the UK Buildings Research Establishment (BRE) [45].

A spectrum of pressure measured on the roof of a two-storey house from the BRE full scale experiment at Aylesbury, Buckinghamshire, is presented in Figure 3.2. The spectrum shows a characteristic double-humped form, with the peaks of each hump separated by an order of magnitude in frequency. The lower frequency peak corresponds to the micrometeorological peak in the Van der Hoven spectrum (Figure 3.1), and is the contribution from the boundary-layer turbulence. The higher frequency peak is caused by turbulence generated by the building itself and is of a scale approximately equal to that of the building. Each contribution is of a similar magnitude, but this balance can vary with location over the building. The width of each peak is sufficiently great for the two contributions to overlap each other. Although this does not necessarily indicate an interaction, it is not possible to separate the two contributions.

Clearly the characteristics of the boundary layer over different types of terrain can be assessed without reference to any particular structure [45]. Assessment of the flow around a structure and the loads imposed on it by the wind should be made in a manner which accounts for the additional fluctuations introduced by the structure, and ideally also for any interaction with the boundary layer.

3.3 Assessment of the problem

Wind effects on structures have been stated in subclause 3.2 in terms of three fundamental aspects: the wind climate, the boundary layer and the structure. In practice there are many different methods of assessment and prediction of wind loads.

Cook in [45] gives six ways in which the problem is or has been approached. The most common are those shown diagramatically in Figure 3.4. The three aspects are shown as individual ellipses, but those representing the boundary layer and the structure are drawn overlapping to represent the overlap and possible interaction. Boxes have been drawn around the blocks to indicate the way in which the aspects are grouped for assessment

a) Static Assessment

The design method derived from this approach was simply to combine a design mean wind speed with a design static loading coefficient to produce a full design load. Buildings were tested in wind tunnels assuming wind as a smooth uniform air flow. This is generally no longer used.

b) Quasi-static Assessment - Time Domain -
(Current Code of Practice for wind loadings on structures in UK, CP3: 1972, France and Australia)

This approach is a compromise which assumes that all the fluctuations of load are due to the gusts in the boundary layer; thus the contribution from building generated turbulence is suppressed by this method. The structure is assumed to respond in exactly the same manner to gusts as it does to the mean flow (quasi-static) It is implied that the maximum load on a structure occurs at the same instant of time as the maximum incident gust. This leads to a design approach called the equivalent-static-gust-method. In situations where the contribution from the building is not large (for overall forces and movement) the accuracy of this approach is quite good. For local forces on cladding, particularly in regions of separated flow near the periphery of a roof, the accuracy of this approach is, however, poor. The equivalent-static-gust design method combines a design gust wind speed with a design mean loading coefficient (given in CP 3: 1972 only for very simple shapes of buildings) to produce a design load. The design wind speed is assessed as the maximum gust speed likely to occur in the lifetime of the structure. The gust duration is usually taken as 1 second; hence, from Figure 3.1, most of the fluctuations of the

micrometeorological peak are included in this assessment.

c) Quasi-static Assessment-Frequency Domain - (Current Code of Practice for Wind Loading on Structures in Canada, Australia and USA)

If the structure is sufficiently stiff enough that its response follows the quasi-static loading, then the previous approach is adequate [45]. However, when the structure is sufficiently flexible for it to respond dynamically, the approach must be modified. In this modified method, assessment of the boundary layer is made separately from the wind climate and is made in the frequency domain in terms of the spectrum of the micrometeorological peak. The action of the turbulence in producing loads on the structure is quantified in terms of an admittance function, and the response of the structure to the loads is quantified by a frequency response function. The design method using this approach is the admittance method, advocated by Davenport [49-52], which works entirely in the frequency domain in the following manner. A design mean wind speed determines the turbulence spectrum over any given terrain; the admittance function corresponding to the aerodynamic shape of the structure acts on this turbulence spectrum to produce a quasi-static load spectrum; and the frequency response function

of the structure operates on the quasi-static load spectrum to produce the dynamic response spectrum. It is worth noting that the quasi-static assumption, that all the fluctuations of load are due to the turbulences of the boundary layer, is retained in this approach. The structure does not respond equally to each loading frequency.

The accuracy of this method is reasonable, and can be used for the design of structures with linear dynamic characteristics [45].

d) Individual Assessment -
(Calculations of local pressures in the current Code of Practice in the UK., Australia, Canada and the USA).

Contrary to the previous approaches the fluctuations contributed by the structure are assessed; the contributions from the boundary layer and from the building being assessed together as separating them would cause difficulties. This approach, largely empirical, is used as a correction to an otherwise quasi-static method.

e) Overall Assessment. [45]
In overall assessment, the performance of a structure exposed to the wind conditions prevailing at a particular site is assessed over a long period of time, and no attempt is made to

divide the problem into its individual aspects.

This approach was employed by BRE to perform a damage survey of the entire range of building types in the UK over 20 years, from 1962 to 1982, and is presented in Chapter 3 of Reference 45. The performance of the existing stock of buildings and structures when exposed to strong wind was assessed, without any instrumentation, in terms of actual damage sustained. Thus the results obtained are only qualitative.

f) Ideal Assessment

This form of assessment ideally fits the observed behaviour of the three fundamental aspects of the problem. Only the design methods for stiff structures, which respond statically to the fluctuations of load, have been developed from this form of assessment (c). No suitable design methods have yet been developed for dynamic structures to replace the quasi-static admittance other than ad-hoc modelling [45].

3.4 Design wind speed data

Until the 1960s wind speed data was very simple, as it was assumed that buildings were subjected to smooth uniform wind. The first international conference on wind effects on buildings and structures held in London in 1963 brought about the transition from steady deterministic aerodynamics

to turbulent statistical aerodynamics. At this conference Franck presented Jensen's Scaling Law (discussed in Chapter 2.6), Davenport presented his statistical approach to wind loading [49] and Newberry presented the BRE's first data from full-scale measurements on tall buildings in London. More intensified work followed, directed at improving the collection of meteorological data, and interpreting this data, in terms of roundly-based probabilistic models, in a manner suitable for use in the analyses of structures subject to wind loading.

The quantities which are employed to define design wind speeds are: the mean wind speed, the maximum gust speed and turbulence intensity. They can be explained by looking at Figure 3.3 which shows typical wind speed records taken at height z [63, 64, 66, 67]. The instantaneous wind speed, $V_z(t)$, varies with time as illustrated in Figure 3.3. The mean wind speed, $\bar{V}_z$, is the average of $V_z(t)$ at height z over a relatively long time period, T_o, (usually 1 hour). At any time, t, the instantaneous wind speed is given by:

$$V_z(t) = \bar{V}_z + u_z(t) \qquad 3.1$$

Where $u_z(t)$ is the component in the direction of the mean wind of the fluctuations due to turbulence. The mean value of $u_z(t)$ over the period, T_o, is zero. But an overall measure of the degree of turbulence is given by the mean square or variance:

$$\sigma_u^2 = \frac{1}{T_o} \int_0^{T_o} [u_z(t)]^2 \, dt \qquad 3.2$$

The quantity $\delta u/\bar{V}_z$ is called the intensity of turbulence. The instantaneous wind speed can be averaged over much shorter periods of time than 1 hour. From the wind speed record illustrated in Figure 3.3 it is possible to obtain a continuous series of values of τ second gust speeds, $V_{z\tau}$, averaged over a period of τ. (τ varies from 4 second for low wind speeds down to about 1 second or less for extreme winds); $\hat{V}_z$ is then the expected maximum of these values occurring in the period T_o

The ratio $\hat{V}_z/\bar{V}_z$, the ratio of expected maximum τ-second gust to the mean wind speed for the period T_o within which V_z occurs, is called the gust factor, K_τ.

The most convenient way of presenting the mean speed data is as follows [45]:

$$\bar{V} = \bar{V}_b \, S_a \, S_b \, \ldots \, S_z \qquad 3.3$$

Where

$\bar{V}_b$ is the basic hourly-mean wind speed, the gradient wind speed

As most wind engineering applications are concerned with strong wind data, Cook and Mayne [45, 130] recommend using for $\bar{V}_b$ the gradient wind speed, which is an extreme value obtained by applying a statistical analysis, namely the theory of extreme values, to the complete hourly-mean speed data collected over a long period of time at a particular site.

S_a, S_b ... S_z are the parameters which affect the determination of the strong-wind speed and they are as follows:

1. statistical factor, which depends upon the average return period, T, and probability, P_N, that the actual maximum wind speed will equal or exceed a given value; most commonly [45, 66] T = 50 years and P_N = .636;
2. altitude factor, which accounts for the effect of large-scale slowly changing topography on the gradient wind speed;
3. directional factor, which is a function of wind direction (in UK);
4. seasonal factor, which expresses the variation of extreme winds with seasons;
5. exposure factor, is based on the equilibrium effect of surface roughness and depends upon wind speed, latitude and surface roughness;
6. height factor, expresses the most important feature of the atmospheric boundary layer, namely an increasing value of velocity with increasing height above ground level. Its assessment is based on a power law approximation or, more accurately, a log-linear-law approximation [45, 66, 140]. It is mainly influenced by surface roughness and height;
7. fetch factor, expresses the influence of surface roughness changes upwind of the site in question;
8. topography factor, expresses the effect of sudden changes in topography like escarpments, ridges, cliffs or hills.

The expected maximum value of the τ second gust occurring in any one hour within the atmospheric boundary layer is given by [67];

$$\hat{V}_{zx} = \hat{V}\,\hat{K}_x = V_z\,K_\tau\,\hat{K}_x \qquad 3.4$$

Where V_z is the corresponding mean-hourly wind speed with the same probability of exceedance as the gust, and is calculated as above assuming that equilibrium conditions exist.

K_τ - is the gust factor for uniform terrain (no changes in roughness) and is defined by:

$$K_\tau = \hat{V}_z/V_z = 1 + gI_n \qquad 3.5$$

It is primarily dependent on duration, time of the gust and the intensity of turbulence, I_n. Both g and I_n are given in ESDU data [67] and

$\hat{K}_x$ accounts for roughness changes.

Although gust wind speeds respond to changes of surface roughness in an exactly similar manner as the hourly-mean wind speed , the energy balance tends to minimise changes of gust profile [67].

Any change in mean wind speed tends to be offset by an opposing change in turbulence intensity. The kinetic energy lost from the mean wind speed profile approaching the ground appears as turbulences, u, v, w, which vary in both: time and space. Since the mean of any of u, v, w is zero, hence their values are expressed in terms of intensity of turbulence, i.e. $\frac{u'}{V'}\ \frac{v'}{V'}\ \frac{w'}{V'}$ where u', v' and w' are root

mean square or variance values, and $\bar{V}$ is the mean wind speed at the same height.

Development of the Deaves and Harris model gives the upwind component intensity $\frac{u'}{V}$ over uniform flat terrain [67, 45]. The remaining two components are obtained from observations that, near the ground, the three intensities tend to remain in the fixed proportions: $v'/u' = 0.68$, $w'/u' = 0.45$. The turbulence components alter in response to a change in surface roughness. As in the transition region, a balance is expected between kinetic energy lost from the mean wind speed, $\bar{V}$, and gained by the turbulences u', v', w', hence the rms value of turbulence in a transition region can be estimated [63, 64]. For sufficient accuracy in design, no corrections are required for the effect of topography on the atmospheric turbulence [45].

The most valuable descriptions of atmospheric turbulence are in terms of their spectra [63, 45]. The spectral functions of atmospheric turbulence provide information on the frequency distribution of the kinetic energy of the various fluctuating velocity components. Used in conjunction with certain transfer functions they provide information about the dynamic loading on, and response of, buildings in the atmospheric wind. [6].

By employing Fourrier analysis, the spectral functions of atmospheric turbulence can be determined from the amplitudes

of time-varying functions, here variances, which are easier to formulate for three turbulence components, u, v, w varying in time and in space [82].

A complete description of the average spatial and temporal properties of u, v and w would require a knowledge of the relationship of each of the three turbulence velocity components at one point (x_1, y_1, z_1) in space, to the corresponding components at some other point (x_2, y_2, x_2). This implies the specification of nine different functions [82], each of which, in general, depend upon the same variables: x_1, x_2, y_1, y_2, z_1, z_2 and time. The majority of practical wind loading problems allow disregard of some of the functions.

3.5 Assessment of wind loadings

The choice of the most suitable way of assessing wind loading on a structure is strongly dependent on the characteristics of the structure itself. The principal characteristics are: the natural frequencies of each of the first few normal modes of the structure and their effective amplitudes [45].

When a structure is small, the whole structure will be loaded by quite small gusts, and the full range of frequencies in the boundary-layer turbulence and the building generated turbulence will be significant. When a structure is large, the smaller gusts will not act simultaneously on the structure, and they will tend to

cancel each other, so that only the lower frequencies are significant.

When a structure is stiff it will have a high value of natural frequency in each of its first few normal modes and will tend to follow the fluctuations of load without significant amplification or attenuation. Conversely, when a structure is flexible it will have low values of natural frequency in each of its first few normal modes and will follow, without amplification or attenuation, only those components of the load at frequencies below the dominant natural frequencies. At wind load frequencies above these natural frequencies the response of the structure to the fluctuations of load will be attenuated. In all cases the response to wind frequencies near a natural frequency of the structure will be amplified.

When a structure becomes very flexible, the deflection due to wind loading may induce additional aerodynamic forces. These additional forces may produce further structural deformations which may induce new aerodynamic forces. Such interaction may tend to become smaller until a condition of stable equilibrium is reached or may conversely tend to instability. Such responses are called aeroelastic.

There are four types of structural instabilty associated with wind action [45, 58, 59, 203]:

1. vortex-capture - when a vortex shedding frequency coincides with the natural frequency of a transverse

mode of vibration of the structure, the structure moves across the wind in phase with this vortex shedding. When the movement is greater than typically 5% of the structure width or depth, the vortex shedding frequency may remain locked to the modal frequency over a range of wind speeds.

2. divergence - this is loss of static stability of the structure due to the flow over it. If, for example, an initially flat membrane is deflected, the air flow will speed up over any peaks and slow down over any troughs. Thus the pressure will be reduced over the peaks and increased over the troughs tending to reinforce the deflection.

3. galloping - is a dynamic instability which may typically occur in slender structures having cross-sectional shapes such as rectangular or 'D' section. It is generally caused by a negative increase of the aerodynamic side force with increasing incidence. This can be an effect of, for example, the flow around a square section being separated and reattached on one side and simply separated on the other.

4. flutter - a dynamic instability, which involves at least two degrees of freedom of the structure. Each degree of freedom may, itself, be positively damped aerodynamically, but sufficient energy to promote instability is extracted from the airstream because of coupling between the degrees of freedom.

Cook proposed dividing all structures or structural elements into five main groups and for each of these groups suggests

a different method of assessing wind loadings [45].

Class A - small static structures

Structures and/or elements of structures which are stiff enough for wind effects to be determined by static methods, and small enough for the relevant wind information to be specified as a wind speed at a single point in space [64].

Class B - moderate static structures

Structures which are stiff enough for wind effects to be determined by static methods, but where at least one dimension is large enough to require the relevant wind information to be specified in the form of multi-point data [65].

Class C - large static structures

Structures which are stiff enough for wind effects to be determined by static methods, but for which the shape of the individual structure/load influence functions has to be considered in conjunction with the multi-point wind data.

Class D - dynamic structures

Structures, or parts of structures, which are not stiff enough to be assessed by static methods, yet remain sufficiently stiff to prevent aeroelastic instabilities. Assessment of these structural systems generally requires a full dynamic approach.

Class E - aeroelastic structures

Structures, or parts of structures, that are so flexible that their motion interacts with their aerodynamics in an inherently complicated, inseparable and possibly unstable manner. Cook and BRE [45] do not give any guidance for assessing wind loadings on such structures, but conclude that redesign may be necessary to avoid possibilities of aeroelastic instabilities.

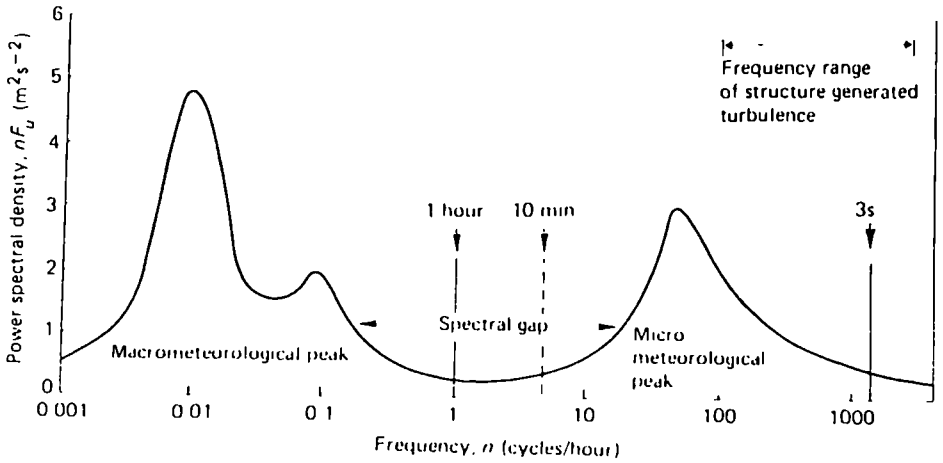

Figure 3.1

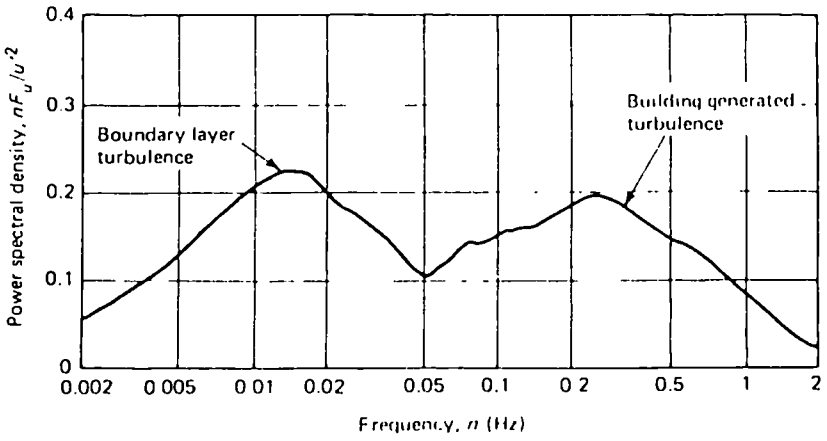

Figure 3.2

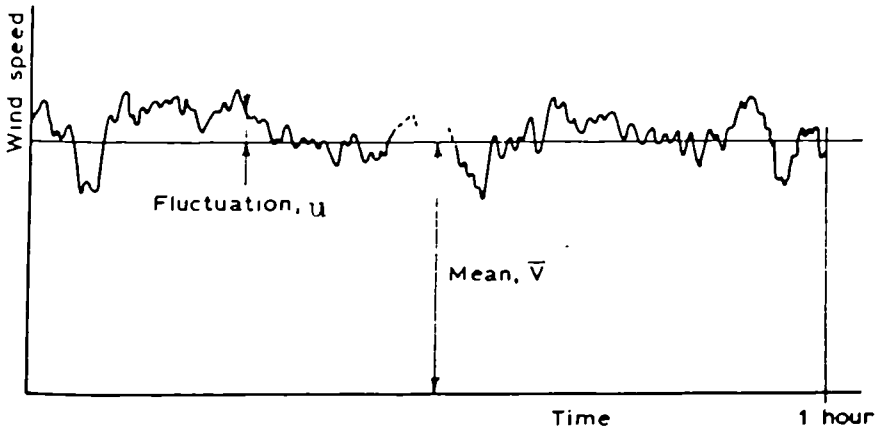

Figure 3.3

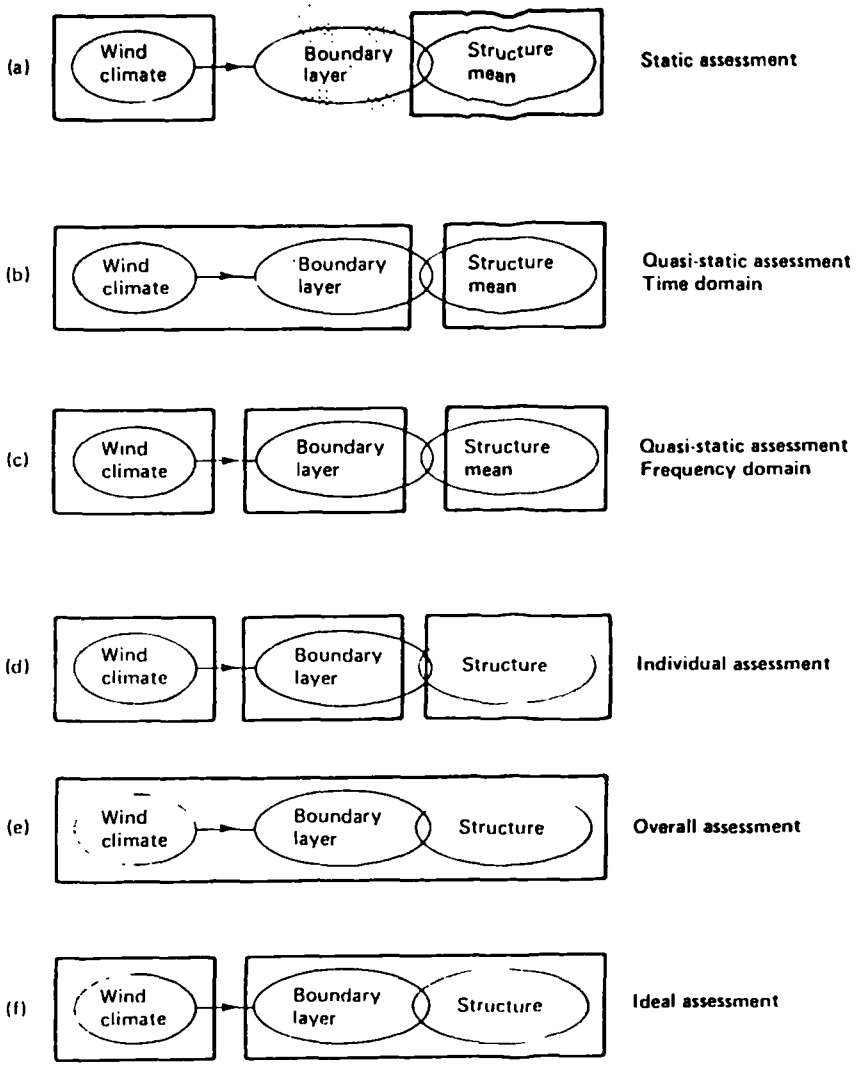
(a)
Wind climate
Boundary layer
Structure mean
Static assessment
(b)
Wind climate
Boundary layer
Structure mean
Quasi-static assessment
Time domain
(c)
Wind climate
Boundary layer
Structure mean
Quasi-static assessment
Frequency domain
(d)
Wind climate
Boundary layer
Structure
Individual assessment
(e)
Wind climate
Boundary layer
Structure
Overall assessment
(f)
Wind climate
Boundary layer
Structure
Ideal assessment

Figure 3.4

CHAPTER 4

Wind response of flexible roof structures - a review

Contents:

Structural response under wind loading (Static approach; Dynamic equation, mass and damping matrices; Quasi-linear dynamic response; Wind loading in non-linear time-domain method) - Wind tunnel tests - Aerodynamics of flexible surfaces.

4.1 Structural response under wind loading

4.1.1 Static approach

The highly complicated nature of wind flow and the consequent loads imposed on structures is widely appreciated. Yet in the case of many small conventional airhouses, and even for the approximate analysis of larger and more sophisticated pneumatic structures, treating wind loads in terms of equivalent static forces is very common. The static wind pressure is then expressed as:

$$p_w = \tfrac{1}{2} \rho_{ar} C_p V^2 \qquad 4.1$$

where

ρ - is the air density

V - is the wind velocity (given by the Code of Practice)

C_p - non-dimensional wind pressure coefficients which are given in Codes of Practice, or other publications, for the most common shapes of roof.

Because of the great variety of geometric shapes of membrane or pneumatic structures it is, in most cases, necessary to undertake wind tunnel tests in order to establish the required values of pressure coefficients. For structures

which do not deform excessively, in the case of air-supported structures, those with high internal pressure, models for wind tunnel testing can be made rigid to give meaningful C_p distributions.

When however the internal pressure is lower, which may be necessary to achieve a more economical solution, wind loading can cause large deflections which change the geometry of the structure and hence influence the wind pressure coefficients. Therefore, it is advisable to obtain pressure coefficient distributions from wind tunnel tests on flexible models.

In the simple static approach it is assumed that the same velocity, V, acts on all points of a structure simultaneously. This method can be justified for smaller structures with a high level of damping and/or where the natural frequencies are much higher than the frequencies at which any considerable wind energy is experienced. For larger flexible structures, however, with low natural frequencies, a more precise analysis may be necessary to ensure economy.

4.1.2 Dynamic equation, mass and damping matrices

Wind loading on structures has recently been better understood and more precisely described; and therefore the dynamic response of flexible structures has received greater emphasis.

In general, the equation of motion may be written in the following matrix form [42]:

$$M\ddot{r} + C\dot{r} + Kr = P(r, \dot{r}, \ddot{r}, t) \qquad 4.2$$

where

M, C and K are the mass, damping and stiffness matrices respectively;

$P(r, \dot{r}, \ddot{r}, t)$ is the external time-dependent loading; and $\ddot{r}$, $\dot{r}$ an r are respectively the acceleration, velocity and displacement vectors.

The evaluation of the stiffness matrices for tension members, whether cables or membrane elements, is a standard operation given in references 107, 108 for cable elements and in reference 9, 161 for membrane elements.

In general, quasi-elastic material behaviour is assumed as shown in figure 4.1. A membrane and/or a cable responds in an elastic manner when it is in tension, but the stiffness becomes zero for any negative strain, as the material is not capable of sustaining compression.

The response of flexible roof structures is a geometrically non-linear problem, hence the stiffness matrix is not constant but depends on the displacement vector.

With regard to the mass matrix, it can be formulated either as a consistent mass, or as a lumped mass matrix. In general, a lumped mass matrix approach is more commonly used because of the advantages both for the solution of the

eigen-value problem and in the direct interaction of the equations of motion. [107, 34, 9].

When a membrane roof vibrates it undergoes alternate accelerations and decelerations and so also does the adjacent surrounding air. The total effective mass undergoing acceleration is therefore not just that of the membrane but also an additional amount, the added mass, due to this surrounding air. In equation 4.2 the mass matrix should therefore include the structural mass (here mass of membrane and/or cables) and the additional mass due to the vibrating attached air mass.

Jensen [99, 100] conducted a series of tests on suspended cable structures with and without membrane cladding and concluded that this additional mass is of great importance for nets clad with a membrane. He proposed that the additional mass, m", could approximately be calculated as [100].

$$m'' = C_m \rho_a a^3 \qquad 4.3$$

where

ρ_a is the density of air,

a is a dimension of the structure and

C_m is a coefficient dependent on the shape and vibration mode of the structure.

For actual tension structures, the above coefficient for C_m had to be set between 2.5 and 7.5. The influence of the added mass is illustrated in figure 4.2 [100], showing a

plot of frequency against mass. The theoretical values of frequencies were calculated by Jensen without accounting for added mass. It is worth noting that, with decreasing structural mass, the influence of vibrating air becomes more significant.

For lightweight construction such as membranes, or nets covered only by a membrane, the added mass may be of sufficient magnitude to substantially reduce the natural frequencies compared with those based upon the mass of the structure alone.

Irwin et al [97] performed simplified two-dimensional calculations of the Montreal Olympic Stadium roof and concluded that added mass due to the attached vibrating air could be 37 times greater than the structural mass.

The first amplitude of vibration of a structure subject to a sudden wind gust or shock loading may be only marginally affected by the magnitude of the damping forces, although the rate of decay of the subsequent oscillatory motion and the amplitudes of response due to regularly pulsating forces are very much a function of the level of damping. The energy loss in vibration is due to work done by forces resisting the motion and is caused by hysteresis in the members, friction in joints and resistance by the surrounding mass of air.

Buchholdt [34] concludes that the inclusion of these forces

separately is not a practicable proposition and suggests, for cable roof structures, the calculation of damping coefficients from a knowledge of the modal damping ratios of similar structures.

Although damping results from many different and complicated energy loss mechanisms, Jensen, after several tests on suspended structures (with and without membranes), split the damping capacity into the following components [99, 100:

1. Structural damping: which consists of the damping capacity of the structural system.

   For tents or membrane structures using sailcloth, polyester fabric or nylon membranes, the damping logarithmic decrement, δ , (δ = ln (An/A_{n+1}), where A_n and A_{n+1} denote two successive amplitudes) is of 4 to 10%. In general damping decreases with increasing pretension of the membrane.

2. For cable network structures, the magnitude of damping depends on the design and construction of the cladding. The damping is due to the energy loss in joints and nodal points. Its value varies between 5 to 20%

3. Aerodynamic damping: should only be considered in lightweight structures and is primarily dependent on the vibrating air mass and the size and shape of the structure. As given in reference (100), the aerodynamic damping of actual structures can be approximately expressed as:

$$\delta = \frac{1}{2} C_d \frac{m''}{A_o} \frac{A}{m} \qquad 4.4$$

where

$\frac{m''}{A_o}$ expresses a mean added mass of vibrating air per unit area of the membrane,

$\frac{m}{A}$ - the mass of membrane per unit area of the structure,

and

C_d is a coefficient, which value varies between

0.03 - 0.07

As is the case with added mass effects, the aerodynamic damping capacity increases with a decrease of structural mass.

In works by: Irwin et al [97], Kind [105] and Barnes [9, 12], it has been shown that the response of air supported structures is highly influenced by pneumatic effects: the pneumatic stiffness (an internal pressure increase being directly proportional to volume decrease), and the pneumatic damping (the decay of overpressure being dependent on the porosity of the structure - escape of air through boundary connections and openings). For ideal air-houses for which the building cavity can be assumed as essentially sealed, as considered by Tryggrason and Isyumor (reference 1 and 2 in [106]), the pneumatic stiffness is the only important pneumatic effect. However, as real air houses are usually quite porous, because of the needs of ventilation, the

pneumatic damping can play a very important part.

In [106] Kind presents an approximate analysis of pneumatic effects for volume displacing modes of motion in air-supported structures considering only free vibrations of the structure. The leakiness of the building and the fans providing air for ventilation and pressurisation were modelled, but elastic effects were not included. Kind concluded that both pneumatic stiffness and pneumatic damping can be expected to be important in air supported structures.

For a quasi-static loading acting on a small structure, stiffness is more likely to be the dominant pneumatic effect, although damping will often remain significant. Pneumatic damping tends to assume greater importance as the size of the structure increases.

In the case of a short duration loading, such as a 1 second gust load, even the response of a large air structure will be greatly affected by pneumatic stiffness.

Acoustic damping is another potentially important damping mechanism in air supported structures [97, 106]. Irwin et al [97] related this energy loss mechanism to low frequency acoustic waves being radiated from air supported structures during their volume-displacing type of motion. The term acoustic is used for convenience as the lengths of transmitted waves by a real structure is, in general, much

larger than those normally associated with acoustic waves. Irwin [97], estimated the acoustic damping ratio to be

$$\xi_A = 10\ \omega_n\ \sqrt{A/C} \qquad 4.5$$

where

A is the area of roof

C is the speed of sound, and

ω_n is the natural circular frequency of the structure.

Expression 4.5 is applicable in the case of a well sealed membrane roof which acts essentially as an acoustic source. This expression indicates that acoustic damping can be of comparable magnitude to pneumatic damping [106]. It also shows that acoustic damping becomes progressively less important as the frequency decreases. Furthermore, increased building leakiness results in more pneumatic damping and reduces acoustic damping.

The damping matrix can be obtained from the damping ratios of a structure in different ways. One of the approaches [42, 34] results in damping forces at different points in a structure being proportional to the distribution of mass. A second way of constructing a damping matrix with orthogonal properties, from the damping ratios, is to assume that the damping is a linear function of both the mass and the stiffness [42, 34]. Alternatively, the damping can be taken as a certain percentage of critical damping.

4.1.3 Quasi-linear dynamic response

For the purpose of calculating structural response due to wind loading, the vector P in equation 4.2 is formed from the effect of the dynamic wind pressure P_D (x, y, z, t). The dynamic wind response, in works by Knudson [107, 108] and Morris [150] is restricted to the case of buffeting by wind and the total wind pressure is given by:

$$p(x, y, z, t) = 1/2\ \rho\ C_p(x, y, z)[\bar{V}(x, y, z) + \nu\ (x, y, z, t)]^2 \qquad 4.6$$

where

p(x, y, z, t) is the pressure per unit surface area,

ρ - mass density of air

C_p (x, y, z) the pressure coefficient, which value depends on the direction of the wind. Strictly it will be time dependent, but it is customary to approximate C_p by static wind test values [150]

$\bar{V}$ - mean velocity component

ν - the randomly fluctuating component of the wind velocity about its mean value

Jansen [100] proposes including the influence of the surrounding air in the expression for the total wind pressure by adding to it an additional term, namely

$$C_m\ \rho\ \frac{A_o}{D}\ \frac{dV}{dt}$$

The term expresses the inertial reaction associated with the acceleration of the surrounding air. A_o is a reference area for a virtual mass, D is the diameter of the object, while C_m is a coefficient for the additional mass term.

In determining the quasi-linear dynamic response to wind loading, the total pressure given by equation 4.6 is separated into the pressure $\bar{p}$ caused by the mean velocity, and the fluctuating wind pressure component

The mean pressure

$$\bar{p}(x, y, z) = 1/2\ \rho\ C_p\ (x, y, z)\ \bar{V}^2\ (x, y, z) \quad 4.7$$

is added to the live and the dead loads acting on the structure to form a quasi-static load vector. The quasi static equilibrium configuration is then found by a nonlinear iterative method such as: the Newton-Raphson method, conjugate gradient method or dynamic relaxation [14].

The fluctuating wind pressure is given by

$$p_d(x,y,z,t)=1/2\ \rho\ C_p(x,y,z)[2\bar{V}(x,y,z)\ v\ (x,y,z,t) + v^2\ x,y,z,t)] \quad 4.8$$

Knudson [107], using a deterministic approach to wind loading, developed a method to deal with p_d based on Taylor's Hypothesis. This assumes that the velocity fluctuations recorded at a point travel unchanged in the direction of the mean wind at the mean wind velocity. A wind record is assumed to be incident upon the structure as a 'plane' wave and is then moved across the structure in the direction of the mean wind at the mean wind velocity as a series of strips (with the same velocity across each strip) with the different velocities indicated by the wind record. The variation in wind velocity in the lateral direction could be accounted for by employing a second assumption, of homogeneous isotropic turbulence, to describe the nature of wind [82].

By assuming that oscillations due to the fluctuating wind pressure are small and hence that the stiffness matrix is effectively constant, the equation of motion (4.2) is reduced to a linear problem, which is then solved by a mode superposition technique or one of the direct integration methods [14].

Since the wind is a random phenomenon, it is more properly dealt with in a nondeterministic analysis based on the theory of random vibration. Analyses used by Knudson [107] and Morris [150] are based on works by Davenport [49] and by Harris [82] dealing with the random description of wind on structures.

Once again the oscillations are assumed to be linear, but this time the p_d function, equation 4.8, is made linear by neglecting the last term, involving $v^2(x,y,z,t)$. Hence the process becomes Gaussian.

The response, or the maximum expected deflection due to wind, is then computed in a frequency domain analysis with the aid of random vibration theory. The procedure may be represented in a schematic way as follows:

turbulence spectrum	+	aerodynamic admittance function	——>	aerodynamic force spectrum
aerodynamic force spectrum	+	mechanical admittance	——>	response spectrum
response spectrum	+	gust response factor	——>	expected peak response

4.1.4 Wind loading in the non-linear time-domain method

There is evidence which indicates that some pneumatic structures, especially of high rise to span ratio, normally considered to act linearly in their dynamic response, do in fact behave nonlinearly when excited in one of their fundamental modes, especially when the level of damping is low. For such structures, as Buchholdt suggests, time integration methods need to be adopted [34].

The fluctuating pressures caused by wind are then given by:

$$p_d = \tfrac{1}{2} \rho C_p (V(t) - \dot{x})^2 \qquad 4.9$$

where

$\dot{x}$ - is the velocity of the structure at a given point and in the direction of the wind

C_p - the pressure coefficient for the same point, and

$V(t)$ - is the wind speed vector at time t, and is expressed as:

$$V(t) = \bar{V} + w(t) + \varepsilon(t) = \bar{V} + v(t) \qquad 4.10$$

where

$\bar{V}$ - is the mean velocity,

$w(t)$ - all the elements in this vector have the same power spectrum and are correlated to each other in accordance with the assumed coherence function (given in [34]),

$\varepsilon(t)$ - the elements in this vector are uncorrelated and take into account the variation of the power spectrum with height above ground level [34]

In the structural analysis, the response is predicted by forward integration (in the time domain), using a step-by-

step method in which equilibrium of dynamic forces at the end of each time increment is established by minimization of the total potential work [34].

However, in shallow large span pneumatics (the main concern of this thesis), for which the velocities of the structure movements in the direction of wind are small compared with the wind velocity ($\dot{x} << V(t)$), equation 4.9 is reduced to equation 4.6.

For very large air-supported structures any load acting on the structure causes not only membrane deformation to balance external forces but also sets into motion the enclosed air. Neglecting internal air mass momentum by employing only static analysis may result in erroneous prediction of the overall structural behaviour. On the other hand, for such large span air structures the design gust wind speed might be significantly reduced (compared with smaller span structures) especially if their rise/span ratio is low. In this case they will have less mechanical freedom for lateral movements and thus there will be less mobilization of internal air momentum compared with traditional air-houses with high rise/span ratios. A low rise/span ratio is also likely to ensure more uniform suction loading over the whole surface with little or no pressure indentation areas on the windward side. The effect of this is that displacements are more symmetric and thus volume displacing, which will induce more effectively the internal air stiffening effects [16].

4.2 Wind tunnel tests

Tests on aeroelastic models of air-supported structures in a fully simulated boundary layer are considered to provide the closest approximation to full scale behaviour of a prototype. It was mentioned in chapter 2.6 that scaling all modelling parameters is only possible in a full scale model. The scales of tested models range from 1/20 to 1/100 or even more, hence relaxing some of the parameters becomes a standard procedure.

The first more comprehensive tests in wind tunnels on air-supported structures started in the sixties. The early models used were: spheres (three-quarter-, hemisphere) or rectangular based structures with spherical or non-spherical ends. Tests were carried out on smooth flexible models in smooth flow conditions. In some of them [43] the steady deflections were measured by photogrammetry. In others, pressure coefficients were determined from rows of conventional pressure taps fitted along circumferential centre lines of the models [158]. The works conducted by Beger [21] and Niemann [158] focused on defining pressure coefficient distributions with respect to wind directions and different pi/q ratios (internal pressure/stagnation pressure of the oncoming flow). The velocities used were up to 35 m/s.

Figure 4.3 shows Berger's results from his tests on a hemisphere. The distributions of pressure coefficients are presented only for a cross-section in the wind direction.

The pressure distributions of a hemisphere obtained by Niemann are given in figure 4.4 for two different values of internal pressure. The main feature of these two figures is that the peak value of function, C_{ps}, varies considerably with pi/q ratios. For small values of pi/q, C_{ps} is much larger than for higher pi/q ratios. As there is an economic incentive to reduce inflation pressure, cases of lower pi/q ratios can be of great importance. In such cases values of C_p distribution obtained from rigid model wind tunnel tests can underestimate the wind loading.

Recently much work has been done in attempting to scale not only models in more realistic terms but also the flow conditions, namely by simulating more closely the atmospheric boundary layer [39, 44, 54, 97]. For the design of the Montreal Olympic Stadium roof [97], very thorough studies were carried out in an attempt to model completely the flexible structure. The importance of allowing for stiffening effects due to the compression of the internal air, added mass effects and acoustic damping was emphasised.

The accuracy with which the modelling parameters must be scaled depends on the information sought from the test. To establish pressure distributions and the power spectra of fluctuating pressures Cook [43] employs rigid models. In such an approach it is assumed that the structural motion does not affect the wind loading on the structure. The actual modes of unstable behaviour are then investigated on flexible models in a wind tunnel under smooth flow, preceded

by the determination of natural frequencies for the first few modes of vibration using simplified linear theory.

Similar types of tests, namely tests on rigid models to establish the pressure coefficient distribution, followed by flexible model tests to detect instability, were conducted on spherical inflated models by Newman [156].

Non-Dimensional Parameters

The following non-dimensional parameters are required to describe the full behaviour of prototype air-supported structures subject to wind loading [43]:

1. $\frac{m}{\rho D}$ - ratio of membrane mass, m, to air mass (ρ-air density, D-a representative dimension of the structure). When the structure is in motion, a large mass of air is mobilised which can become more important than the membrane mass itself.

2. $\frac{k}{\Delta pD}$ - stiffness of membrane (k - is the stiffness of the membrane per unit width and Δp - is the pressure difference across the membrane). This condition would require producing a membrane model material with warp and weft stiffness appropriately scaled.

3. $\frac{C^3D^3}{U^2V_i}$ - enclosed air stiffness (C is the speed of sound in air, U is the speed of flow of external fluid, V_i - is internal volume of the structure). As the structure is at least partially sealed, there may be substantial stiffness imparted to the structure due to the compression of the air when the enclosed volume is changed. If C/U cannot be modelled (which is very often the case), it is possible to make a volume adjustment to the model by adding a secondary chamber [43, 97]. The stiffness due to air is likely to be most significant for displacements where large volume changes occur. This is not likely for aerodynamic instabilities, but can be important for large scale buffeting at low internal pressure, where the stiffening effect is accompanied by 'sloshing' of the internal air. The behaviour of this latter effect is not properly modelled by adding a chamber.

4. $\frac{\Delta p}{\rho U^2}$ - pressurisation - this parameter must be (and can easily be) modelled to ensure that the ratio of internal to external loading is maintained.

5. τ - damping factor (τ - damping of the membrane/unit width).

a) membrane damping.

This would require producing a material with damping properties appropriately scaled to those of the prototype. On the other hand, the aerodynamic damping is usually dominant, therefore no particular pains need normally be taken to match the mechanical damping parameter [97].

b) $\frac{\Delta p}{\rho c^2}$ acoustic damping (damping due to radiation of sound waves to surrounding air).

This term can also be written $\frac{\rho U^2}{\rho c^2}$ thus reducing to U/C and indicating a need for wind speeds for modelling to equal those at full scale.

6. $C_i D^2 \sqrt{\frac{\rho}{\Delta \rho}}$ - damping due to leakage of air through the seams, section joints, edge connections and air-lock doors.

(C_i - is a coefficient of leakage).

The coefficient C_i can only be satisfactorily determined by full scale measurements or estimates based on these measurements.

7. $\frac{\rho UD}{\mu}$ - Reynolds Number, ratio of internal to viscous forces (μ is viscosity of fluid)

For a continuously curved body, such as an airhouse, the point at which the flow separates from the surface is highly dependent on Reynolds Number. It is very important to correctly model the separation position as the surface pressure distribution will be significantly affected. Another factor which influences flow separation is roughness.

Directly scaling Reynolds number would require a very high wind speed, therefore recently an indirect method has been employed, namely artificial roughening of the model surface.

8. $\frac{U^2}{Dg}$ - Froude Number, ratio of inertia force in fluid to gravity force in the structure (g - is acceleration due to gravity)

It is not necessary to achieve this similarity as in the case of an air-supported structure the weight of the membrane is resisted at all points by the internal pressure.

The above parameters should be supplemented with those necessary to simulate a turbulent boundary layer: the roughness length and the length scale of the turbulence.

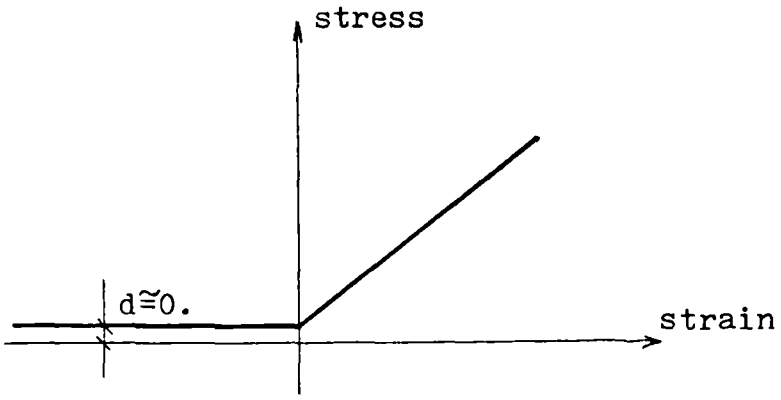

Figure 4.1

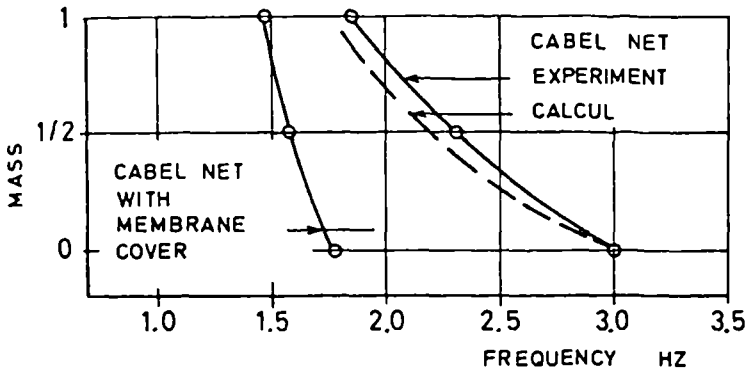

Figure 4.2

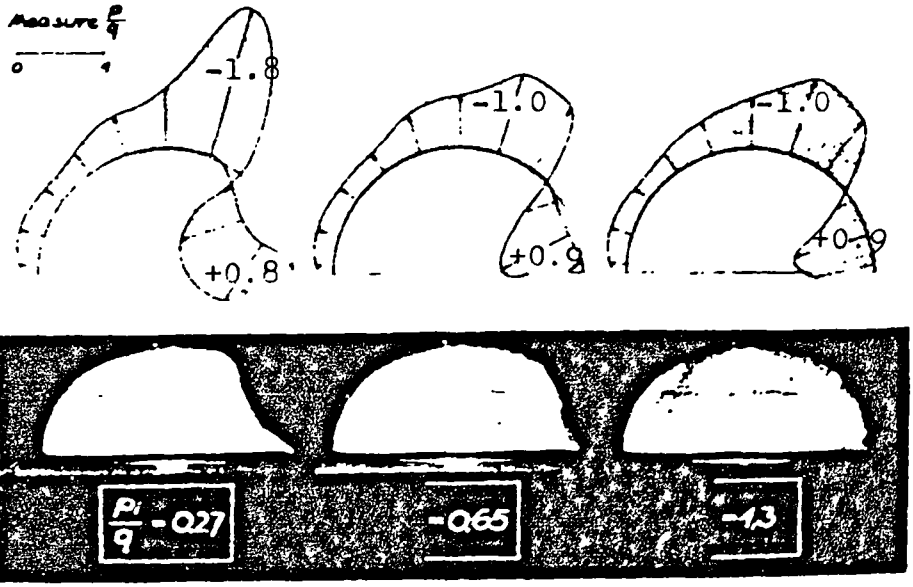

Figure 4.3

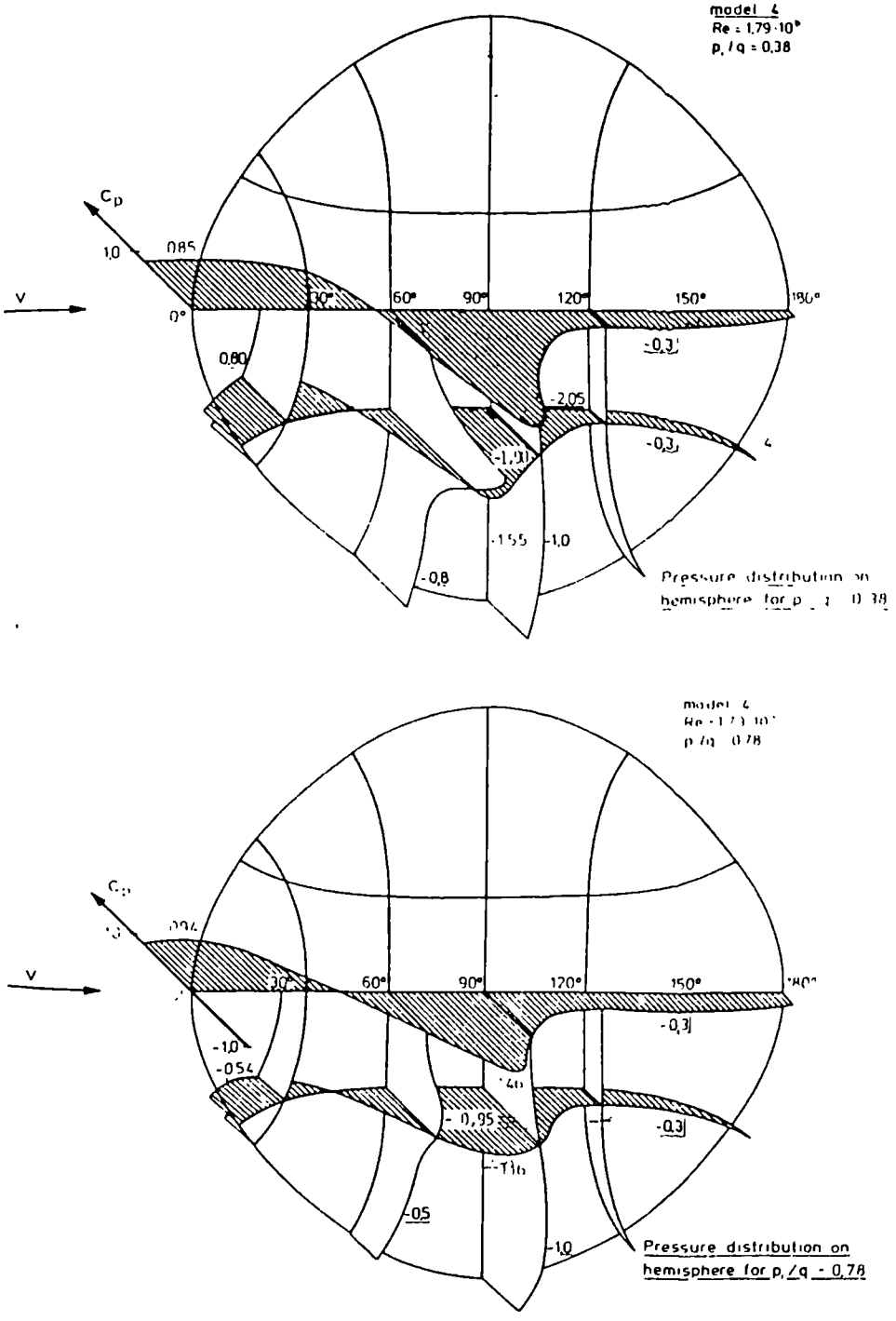
model 4
Re = 1,79·10⁶
p_l/q = 0,38
Cp
1,0
0,85
V
0°
30°
60°
90°
120°
150°
180°
0,80
-0,3
-2,05
-0,3
-1,21
-1,55
-1,0
-0,8
Pressure distribution on hemisphere for p_l/q = 0,38
model 4
Cp
V
-1,0
-0,54
-0,95
-0,3
-0,3
-0,5
-1,0
Pressure distribution on hemisphere for p_l/q = 0,78

Figure 4.4

4.3 Aerodynamics of flexible surfaces

In chapter 4.1 wind response of flexible roof structures was presented as a static or dynamic reaction of cables and/or membrane to externally applied load. This approach does not properly represent the behaviour of air-supported structures, where the surrounding air should be treated as an integral part of the structure. Some attempts have been made to model closely the behaviour of air houses by including in dynamic analyses the added mass effect and aerodynamic damping. Representing wind turbulence in a spectral form makes it possible to predict the amplified response to those wind frequencies which are close to the natural frequency of the structure, and whose spectra contain high energy. Although the statistical approach to wind represents the phenomenon in a more realistic way than in deterministic analyses, unfortunately, the methods of chapter 4.1 fail to predict instabilities; either divergence (static) or flutter (dynamic).

The approaches which can be adopted here are those used in classical aerodynamics, i.e. those which take into account mutual iteraction between inertia, fluid and elastic forces. Equations describing the phenomenon are:

1. elasticity - the relationship between deflection and elastic forces of structures.
2. dynamic - relationship between inertia and applied loads.
3. fluid mechanic - equations of motion and continuity and
4. boundary conditions

The equations are, in general, differential and highly nonlinear, and therefore it is difficult to produce results unless certain simplifications are made. The most common are:

1. flow is irrotational (potential)
2. fluid and elastic equilibrium equations are linearised by small disturbance concepts
3. boundary conditions are linearised and expressed in terms of velocity normal to the surface of the structure (velocity of the fluid normal to the surface is equal to the normal velocity of the structure on the boundary).

There are many investigations employing the above assumptions, but mainly with regard to the vibration of aerofoils, flat or near flat panels and membranes. This topic is also covered in classical books on aeroelasticity such as Bisplinghoff [27] or more modern texts like Dowell [58, 59].

Very interesting theoretical work on the aerodynamic instability of these panels has been done by Miles [145], and extended through mainly experimental work by Dugundji [60]. Miles formulated the problem in two dimensions using a wind generated wave analogy and assuming deflections in a travelling wave form. Unfortunately his work is mainly concerned with isolated or periodically supported two dimensional panels submerged in high wind and therefore his work cannot be directly applied to wind response of flexible

structures. The same can be said about the vast amount of cases presented by Bisplinghoff.

Two dimensional panels in uniform incompressible flow on one side, embedded in an infinite rigid plane were studied by Kornecki [109], Dowell [58] and Shahrokh [179]. Simply supported damped panels in subsonic flow lose their instability by divergence, hence instability can be predicted from steady aerodynamic theory. However post-divergence flutter is not ruled out.

Williams [204] presents analytical investigation into the behaviour of pretension membranes subject to incompressible uniform flow, confining his work to travelling wave solutions in two dimensions. He concludes that for a low profile two dimensional air-supported structure, travelling wave type instability (flutter) can occur only when the membrane is at the point of losing static stability.

The experimental study carried out by Siev [181] in uniform flow on a model 40 x 40 cm in plan and 20 to 24 cm in height, covered by a soft hyper-shaped rubber membrane, led to the conclusion that there is a danger of flutter which is more likely to happen in membrane structures which are not fully sealed than in closed air-houses. Siev intimates that flutter (or vibrations of increasing amplitude) induced at a certain air speed, is associated with the appearance of vortices inducing pressure variations coupled to movements of the structure. Following these conclusions Kunieda [109]

tried to analytically predict flutter of hanging roofs and curved membrane roofs by introducing infinitesimally thin vortex sheets between the wind flow and the roof, and in the wake from the trailing edge. By doing so he concluded that flutter of such roofs occurs at a wind velocity which is lower than the divergence critical wind velocity. In the development of his theory Kunieda assumed travelling wave type deflections.

A study by Newman [154] was concerned with predicting the shape and the pressure coefficient distribution on a thin symmetrical lenticular aerofoil subjected to low speed flow. The aerofoil was anchored at both its leading and trailing edges and inclined at zero incidence to the wind flow. This configuration was assumed to idealise the flow past a long low inflated building, when the effect of turbulence is neglected. The analysis was based on steady inviscid theory for a thin aerofoil [27]. The aerofoil shape was established by distribution sources along the axis of symmetry and by applying linearised boundary conditions.

The equations were solved simultaneously by assuming C_p values in the form of a Fourier series. The theoretical analysis was supported by experiments conducted on a lenticular aerofoil submerged in uniform flow. The comparison of pressure coefficient and tension, between theory and experiment, was satisfactory for small values of the thickness/length ratio. Further tests have been conducted on a two dimensional inflated building, with a

height to width ratio of 0.18, immersed in an artificially thickened boundary layer, about 20 times as thick as the height of the building [75]. The Newman theory predicted the membrane tensions fairly well, underestimating them by only about 10%.

In his latter theoretical work, Newman [155] investigates two dimensional inflated buildings with height to width ratios ranging from 0.19 to 0.33 and submerged in a more realistic representation of the atmospheric boundary layer, namely inviscid flow with uniform vorticity. The simulated flow is chosen to match both the velocity and the velocity gradient of the wind (here, in a wind tunnel) at the maximum height of the building. The shape of the building is replaced by a many-sided polygon with a uniform source distribution on each straight-line. Then the original method given by Hess and Smith [90] for pressure distribution on a rigid body, is applied iteratively to find the final shape of the flexible building. The results thus obtained were compared with experimental values. The tension in the membrane was found to be quite close to that predicted by the theory, but the external pressure was, in general, too low owing to the presence of separation bubbles at the leading and trailing edges.

CHAPTER 5

Wind load modelling on an open sided shell roof

Contents:

In this chapter wind loading on a shallow open sided eliptic-parabaloid shell roof is examined under the approximation of potential flow. The limitations and simplicity of potential flow are discussed. The problem is reduced to an integral equation representing a distribution of sources and doublets over the body surface. Three vortex-lattice methods differing in the distribution of vortices are presented. The Hedman horse-shoe and the quadrilateral vortex-rings methods, with singularities placed in the plane z=0 are all applied in a modified form. The numerical procedures based on the methods are outlined, and applied to the eliptic-paraboloid shell. The number of panels essential to model the flow, and the standard procedure of setting back the leading element vortices are investigated. The modified Hedman method with horse-shoe vortices in the plane z=0 and a boundary condition of tangential flow applied on the body surface of the shell is found to give the best result.

5.1 Introduction

Wind loading treated, even in the simplest way, as a set of static single point data, requires knowledge of the pressure coefficient distribution on a structure. For some simple or very common shapes the information is given in available literature [45].

When a roof is of more irregular shape, or undergoes large deformations, as in the case of pneumatic structures, the determination of wind load pressure coefficients may require model testing in a wind tunnel. For a very thin and flexible structure it is, however, difficult to measure pressure or deflection directly. When the prototype is properly scaled, the stiffness of material is very small, and even attaching very small and light devices to measure pressures or deflections can alter the response of the model; and the alternative indirect way of measuring the value of reaction in supports, requires very precise scaling of the stiffness of all structural elements. For air-supported structures this may mean producing specially designed material. Even if this is successfully done there is a further problem of matching the Reynolds Number which, for a smooth structure, greatly influences the point (or line) of separation. A method which avoids the need for excessively high wind tunnel speeds is to roughen the model surface, but this in turn changes the membrane properties.

In such circumstances it is desirable to investigate whether any numerical method is able to give sufficiently accurate information concerning the distribution of pressure coefficients. Bearing in mind that we are dealing with a two domain problem (structure-fluid), with the structure being flexible, it is advisable to find a numerical method which is as simple as possible. Hence as a first approach it is reasonable to examine the suitability of methods which assume time-independent potential flow. This is assessed in

the present chapter in isolation from any structure deformation effects.

5.2 Assumptions and limitations

In the lower parts of the atmospheric boundary layer, where the majority of structures are situated, the air flow is turbulent (a flow in which the particles or groups of particles, while moving randomly, spinning and rotating, proceed in the streaming direction). The intensity of the random motion depends mainly upon the roughness of the terrain and its height. In an open, nearly flat or gently undulating countryside, or in low rise residential suburbs, the intensity of turbulence at a height of 10 m above ground level is smaller than 0.35 [82]. For a city centre its value is 0.58.

In the simplified analysis of the present chapter the influence of turbulence and of mean velocity variations with height are neglected. The structure to be considered is assumed to be submerged in a uniform steady flow. Additional assumptions are of potential flow of an incompressible inviscid fluid.

Compressibility is normally considered to be significant only when the wind speed is more than half the speed of sound in air [147]. With the values of wind speed at the height of typical structure being below 50 m/sec (the speed of sound in air is approximately 340 m/sec) the neglect of compressibility is therefore justified. Viscosity is a very

important factor in predicting the point of separation for continuously curved bodies such as airhouses. In very large shallow pneumatic structures, however, the separation of flow is much further downstream than in high rise domes. Hence, disregarding viscosity in the approximate analysis of very long shallow structures may still allow to obtain meaningful values of pressure coefficients to be obtained.

The existence of a velocity potential depends on the condition of irrotationality of the flow, which means physically that all fluid particles have zero angular momentum about their own centre of gravity axes. This condition is expressed mathematically by the disappearance of the curl of vector V ($\bar{V} = u\bar{i} + v\bar{j} + w\bar{k}$; where V is the velocity vector), or in component form:

$$\frac{\partial v}{\partial x} - \frac{\partial u}{\partial y} = 0, \quad \frac{\partial w}{\partial y} - \frac{\partial v}{\partial z} = 0, \quad \frac{\partial u}{\partial z} - \frac{\partial w}{\partial x} = 0 \qquad 5.1$$

Vanishing of the curl in a vector field is necessary and sufficient to assure that the vector is the gradient of some scalar function [169]. This function in the present case is the velocity potential, ϕ. The scalar components of:

$$\bar{V} = \text{grad } \phi \qquad 5.2$$

are the familiar relations:

$$u = \frac{\partial \phi}{\partial x}, \quad v = \frac{\partial \phi}{\partial y}, \quad w = \frac{\partial \phi}{\partial z} \qquad 5.3$$

which reduces the number of dependent variables in an aerodynamic problem by two.

The main implication of the assumption of steady flow is that the analysis cannot be used directly to predict a

dynamic instability, namely flutter. This type of instability is related to the excessive negative damping of external wind flow. (the energy is input rather than removed from a structure).

It should be borne in mind that most of the assumptions discussed above have been made primarily in order to simplify the mathematical description of a highly complicated phenomenon, thus enabling a numerical scheme which may be employed in the approximate prediction of structural response to wind loadings of long span flexible pneumatic structures. Such structures may interact fairly strongly with the wind flow, and thus changes of shape need to be accounted for during the process of non-linear dynamic structural analysis.

5.3 Stating the problem

The velocity field $\bar{V}$ is expressed as the sum of two velocities:

$$\bar{V} = \bar{V}_{\infty} + \bar{q} \qquad 5.4$$

The vector $\bar{V}_{\infty}$ is the velocity of the onset flow, which is defined as the velocity field that would exist in the fluid if all boundaries ceased to exist. The vector $\bar{q}$ is the disturbance velocity field due to the boundaries.

If p is the fluid pressure and ρ is the constant fluid density, the general Navier-Stokes equations are reduced, for steady potential flow, to:

$$(\bar{V} * \text{grad})\ \bar{V} = -\frac{1}{\rho}\ \text{grad}\ (p) \qquad 5.5$$

and the equation of continuity becomes:

$$\text{div } (\bar{V}) = 0 \qquad 5.6$$

or, from equation 5.2:

$$\nabla^2 \phi = 0 \qquad 5.7$$

For irrotational and barotropic (possessing a unique pressure-density relation) flow, equation 5.5 can be integrated to give one of the forms of the Bernoulli equation:

$$\frac{p}{\rho} = P - \tfrac{1}{2} |\bar{V}|^2 \qquad 5.8$$

where P is the constant of integration.

In most applications the onset of flow is a uniform stream that is, $\bar{V}$ is a constant vector. Under these circumstances, equation 5.8 can be written in terms of the pressure coefficient C_p, as

$$C_p = \frac{p - p_\infty}{\tfrac{1}{2} \rho |V_\infty|^2} = 1 - \frac{|\bar{V}|^2}{|V_\infty|^2} \qquad 5.9$$

where p_∞ is the pressure at infinity.

To complete the mathematical description of flow problems the boundary conditions must be considered. When the fluid mass is unbounded, these ordinarily comprise two types: conditions at infinity, and conditions arising from the presence of a body submerged in the fluid. The former requires only that the fluid be at rest or in some specified uniform motion at remote points. The condition at the boundary of a typical body states simply that over its surface, the perpendicular component of fluid velocity, $\partial \phi / \partial n$, is fixed by the body's motion. In the particular case of a body which does not move this condition requires the disappearance of the velocity normal to the surface:

$$\bar{V} \times \bar{n} \,|_S = 0 \qquad 5.10$$

where $\bar{n}$ is the unit outward normal vector at a point S of the body.

The essential simplicity of potential flow derives from the fact that the velocity field is determined by the equation of continuity (equation 5.7) and the condition of irrotationality (equation 5.2). Thus the equation of motion is not used, and the velocity may be determined independently of the pressure. Once the velocity field is known, the pressure is calculated from equation 5.9. Hence the problem is reduced to solving equation 5.7, which is known as the Laplace equation, subject to the boundary conditions. Different approaches to obtaining a solution have been discussed in chapter 2. The exact analytical solutions in three dimensions yield good results, but they are limited to a narrow class of boundary conditions; for arbitrary bodies numerical methods are more suitable.

5.4 Reduction of the problem to an integral equation by Green's identity

The most common numerical methods are based on the theory that any continuous acyclic irrotational motion of a liquid mass may be regarded as associated with a distribution of doublets and sources over the boundary [116]. The proof rests on the divergence theorem (Gauss's theorem), which states that the volume integral of the divergence of a vector field $\bar{U}$ taken over any volume, τ, is equal to the surface integral of $\bar{U}$ taken over the closed surface

surrounding the volume τ (see figure 5.1), that is:

$$\int_{\tau} \nabla . \bar{U} \, d V = - \int_{S} \bar{n} . \bar{U} \, d s \qquad 5.11$$

$$\iiint_{\tau} \left(\frac{\partial U_x}{\partial x} + \frac{\partial U_y}{\partial y} + \frac{\partial U_z}{\partial z} \right) d x \, dy dz = - \iint_{S} (U_x ds_x + U_y ds_y + U_z ds_z)$$

In mathematics texts, the unit normal is directed out of τ. Aerodynamicists prefer to use a unit normal directed outward from solid surfaces, which necessitates the minus sign in the equation.

Terms in equation 5.11 are:

τ - is a region in space (a flow field in our case)

s - is the surface which bounds τ

$\bar{n}$ - is a unit vector normal to S and directed into τ

U - is a continuous function of position inside τ

The vector $\bar{U}$ to which equation 5.11 will be applied is defined by:

$$U = \phi \nabla \phi_s - \phi_s \nabla \phi \qquad 5.12$$

Where ϕ is the velocity potential of the flow in τ, so that:

$$V = \nabla \phi \qquad 5.13$$

is the fluid velocity in τ; whereas ϕ_s is the potential of a source of unit strength at some arbitrary point P in τ.

$$\phi_s = \frac{1}{2\pi} \ln r \text{ in two dimensions}$$

$$\phi_s = - \frac{1}{4\pi} \frac{1}{r} \text{ in three dimensions} \qquad 5.14$$

Where r is the distance from P to the point at which U is to be evaluated (see figure 5.2)

If the function U defined by equation 5.12 is to be continuous in $\mathcal{V}$, so must also be continuous ϕ, $\nabla\phi$, ϕ_s, and $\Delta\phi_s$. As ϕ_s and its derivatives are singular at P, before integrating over $\mathcal{V}$, we have to curve out a small circle (in 2D) or sphere (in 3D) centered at P and of radius ε (see figure 5.2). Let $\mathcal{V}_\varepsilon$ be the part of $\mathcal{V}$ outside that excluded region and S_ε be the surface of the circle or sphere. For the same reason, such entities as the vortex sheet shed by a surface should be excluded from $\mathcal{V}$, since the velocity $\nabla\phi$ is discontinuous across such a sheet.

The surface, S, generally has three components:

1. S_B, the surface of the body immersed in the flow,
2. S_∞, a surface far from S_B
3. S_C, a two-sided surface that runs between S_B and S and which sandwiches discontinuities in ϕ and/or $\Delta\phi$.

The source potential ϕ_s and ϕ satisfy Laplace's equation everywhere in $\mathcal{V}_\varepsilon$ and therefore it can be proved that $\nabla . U = 0$ [149]. Thus applying equation 5.11 to the region $\mathcal{V}_\varepsilon$ gives:

$$\int_{\mathcal{V}_\varepsilon} \nabla . U d\mathcal{V} = 0 = - \int_{S+S_\varepsilon} \bar{n} (\phi \nabla\phi_s - \phi_s \nabla\phi) ds \qquad 5.15$$

Separating the integrals over the surfaces S and S_ε gives:

$$\int_{S_\varepsilon} \bar{n} (\phi \nabla\phi_s - \phi_s \Delta\phi) ds = - \int_S n (\phi \Delta\phi_s - \phi_s \Delta\phi) ds \qquad 5.16$$

If ε tends to zero, ϕ and $\Delta\phi$ approach their values at P, ϕ_p and V_p respectively, and the left hand side of equation 5.16 becomes:

$$\int_{S_\varepsilon} \bar{n} (\phi \nabla\phi_s - \phi_s \nabla\phi) ds \approx \phi_p \int_{S_\varepsilon} n \nabla\phi_s ds - V_p \int_{S_\varepsilon} \bar{n} \phi_s ds \qquad 5.17$$

The first integral on the RHS of equation 5.17 is the strength of the source inside, here unity. In the second integral ϕ_S is constant on S_ε , hence:

$$\int_{S_\varepsilon} \bar{n}\, \phi_S ds = \phi_S \int_{S_\varepsilon} n d\bar{s} = 0 \qquad 5.18$$

The above reduces equation 5.15 to a form known as Green's identity:

$$\phi_p = \int_S (n^- . \nabla\phi)\, \phi_S - \phi\, (n \,.\, \Delta\phi_S)\ \ ds \qquad 5.19$$

This formula gives the value of ϕ, at any point P in $\mathcal{V}$, in terms of the value of ϕ and $n .\nabla\phi$ on the boundary of $\mathcal{V}$ [143]

The derivation of equation 5.19 is rather mathematical but the result has an important physical meaning. The first integral $\int_S (\bar{n} \nabla\phi)\, \phi_S\, ds$ contains the quantity ϕ_S, which depends only on the distance between P and the ds, whose contribution to the integral is under consideration. Thus although introduced as the potential of a source of unit strength at point P, evaluated at a point on S that is a distance r away, it could also be taken as the potential of a source of unit strength at ds, evaluated at P. With this interpretation, the integral can be called the potential of a source distribution on S whose strength per unit area is $\bar{n}. \nabla\phi$, the component to S of the local fluid velocity.

The integral $\int_S \phi\, (n. \phi_S)\, ds$ has similar interpretations.

The term $\bar{n}.\nabla\phi_s$ is the rate of change of ϕ_s in the direction of $\bar{n}$ at the element ds. This can be viewed as follows: As shown in figure 5.3, let Q_1 and Q_2 be points a distance δ apart, on either side of ds, and arranged so that $Q_2\ Q_1 = \delta\ \bar{n}$. Let ϕ_1 and ϕ_2 be the values at Q_1 and Q_2 respectively of the potential of a unit strength source at P. Then:

$$n\ .\ \nabla\phi_s = \lim_{\delta\ \longrightarrow 0} \frac{\phi_1-\phi_2}{\delta} \qquad 5.20$$

However, ϕ_1 and ϕ_2 can be regarded as the values at P of the potentials due to unit strength sources at Q_1 and Q_2. Then $\phi_1/\delta\ -\ \phi_2/\delta$ is the difference between the potentials at P of two sources of strength $1/\delta$ at Q_1 and Q_2. As $\delta\ \longrightarrow 0$, they coalesce into what is called a doublet, whose strength is defined to be the product of the source strength and the distance between the sources or, in this case, unity. From the viewpoint of an observer at P, the second part of the integral in equation 5.19 is, therefore, the potential of a doublet distribution over the surface S. The axes of the doublets are normal to S and the strength per unit area of the distribution is ϕ, the local velocity potential.

In three dimensions equation 5.19 is more commonly presented in a different form. Equation 5.14 is substituted into 5.15 and by tensor analysis:

$$\bar{n}\ .\ \nabla\phi = \frac{\partial\phi}{\partial n}$$

$$n\ .\ \nabla\phi_s = -\frac{1}{4\pi}\ x\ \frac{\partial}{\partial n}\left(\frac{1}{r}\right) \qquad 5.21$$

hence, the new form is:

$$\phi_p = -\frac{1}{4\pi}\int_S \frac{1}{r}\frac{\partial\phi}{\partial n}\,ds + \frac{1}{4\pi}\int_S \phi\,\frac{\partial}{\partial n}\left(\frac{1}{r}\right)\,ds \qquad 5.22$$

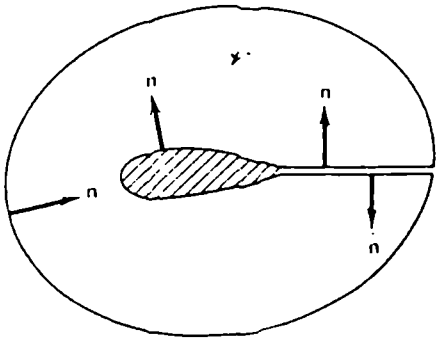

Figure 5.1

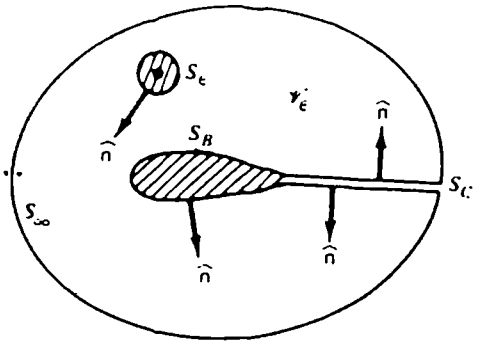

Figure 5.2

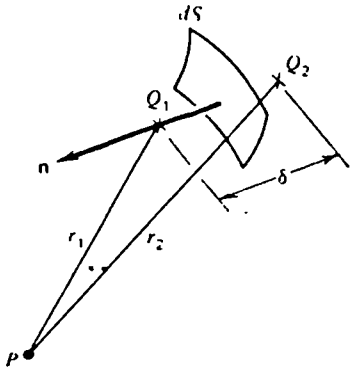

Figure 5.3

5.5 Thin sections with flow on both sides

For a surface having both sides exposed to the flow, such as an infinitesimally thin section, only one type of singularity may be used [116]. If the tangential velocities on the two sides of the boundary are continuous, but the normal velocities are discontinuous only sources are required. If, on the other hand, the normal velocities are continuous but tangential velocities are discontinuous, the motion can be imagined to be generated by a distribution of doublets.

In the case of an open thin section submerged in a uniform flow with the boundary condition of zero normal velocities on both sides, the surface can be viewed as a layer (sheet in 3D) of doublets. The velocity field of a doublet is more complicated than that of sources and vortices, hence it is useful to recognise that, to every doublet distribution, there corresponds an equivalent vortex distribution [116]. Lamb showed that a uniform distribution of doublets over any surface is, in a sense, equivalent to a vortex. The axes of the doublets must be supposed to be everywhere normal to the surface, and the density of the distribution must be equal to the strength of the vortex.

In view of the above a thin section can be represented as a mass of liquid at rest, separated top and bottom from the external flow by narrow shear regions. These boundary layers resemble very closely surfaces of tangential velocity discontinuity, obtained by replacing the surface with two (three) dimensional vortex sheets.

Our investigation is confined to the case of irrotational motion. In order to ensure that the introduction of vortices does not violate this condition, it is necessary to comply with the Helmholtz's vortex theorem, which states that a vortex cannot end in the fluid. Any vortex lines which exist must either form closed curves, or else traverse the fluid beginning and ending on its boundary [116, 27].

The simplest representation of the vortex sheet in the three dimensional case is obtained by concentrating vorticity into a lattice of line vortex elements. Falkner's method for the calculation of aerodynamic loads on wings of arbitrary shape was the first to use discrete vortices in this way: unswept horseshoe vortex elements were used to represent the spanwise and chordwise vorticity [68]. Computation was minimized for hand calculations by the use of loading functions. Hedman [88] developed the vortex -lattice method for planar wing problems using swept vortex elements; the strengths of which were solved directly on a high speed computer without the aid of loading functions. Hedman's method can be extended to non-planar cases [175] or to panel methods [139] which use a surface distribution of quadrilateral vortex rings.

5.6 Vortex-lattice methods

5.6.1 Horse-shoe vortices in the plane z = 0

The present method makes use of some aspects of the vortex-lattice method developed by Hedman [88].

The continuous vortex distribution, which represents the continuous loading on the open sided shell roof is replaced by a system of discrete vortices, or so-called horseshoe vortices. The strengths of the vortices are determined by the requirement of tangential flow in as many points (control points) as there are vortices. The system can be thought of as a collection of horseshoe vortices with each horseshoe vortex inducing the same flow field as an elemental area of the roof does.

The configuration of the roof is idealised by dividing the surface into trapesoidal elements in the xy plane arranged in strips parallel to the free stream velocity so that the surface edges and the fold lines (if there are any) lie on box (panel) boundaries (see figures 5.4 and 5.5). Throughout this chapter direct reference is made to the open sided shell roof of eliptic paraboloid shape, as shown in figure 5.5, as it is easier to explain the concept of the method in relation to a particular shape.

The load carried by one panel element induces a flow field that can be calculated with the aid of a horseshoe vortex. The horseshoe vortex will be positioned in the plane z=0 (here the plane which contains the four corners of the eliptic-paraboloid) on each element, in such a way that the bound vortex will coincide with the quarter-length line of the panel, and trailing vortices will continue into the wake as two semi-infinite filaments parallel to the free stream direction. The control points, where the conditions of

tangential flow are satisfied, will be positioned on the roof surface at the three quarter length line and halfway between that line's inboard and outboard points (see figures 5.4 and 5.5).

Reasons for the positioning of the horseshoe vortices and the collocation points can be found in discussions relating to two dimensional thin aerofoil theory [27]. If the vortex-lattice method is applied in two dimensions, a lift and a pitching moment obtained from this configuration will be the same as appropriate values calculated from the thin aerofoil theory [88].

The method is not very sensitive to the pattern of panels chosen to represent the surface, except that panels behind each other should be in streamwise columns [88]. Otherwise a control point of one panel may lie very close to the trailing vortex of another panel, where the induced velocity is high and not representative of the average induced velocities in the range between the trailing vortices.

The expression for the vortex induced flow field is derived with the aid of the Biot-Savart's law [27]. As utilized in fluid mechanics, this law states that an elementary length ds of vortex line of circulation Γ induces a velocity:

$$d\bar{q} = \frac{\Gamma d\bar{s} \times \bar{R}}{4 \pi R^3} \qquad 5.23$$

at a point P located a vector distance R from ds (see figure 5.6). The scalar form of this law reads:

$$dq = \frac{\sin \alpha}{4 \pi R^2} \Gamma \, ds = \frac{r}{4 \pi R^3} \Gamma \, ds \qquad 5.24$$

Where

α and r are as shown in figure 5.6.

Some useful applications of the Biot-Savart's law are listed below:

1) A linear vortex of finite length (figure 5.7)

$$q = \frac{\Gamma}{4\pi h} (\cos \alpha + \cos \beta) \qquad 5.25$$

2) A semi-infinite vortex (figure 5.8)

$$q = \frac{\Gamma}{4\pi h} (\cos \alpha + 1) \qquad 5.26$$

3) An infinite vortex

$$q = \frac{\Gamma}{2\pi h} \qquad 5.27$$

The three disturbance velocity components (u, v, w) at the collocation point P (x_c, y_c, z_c) on a panel n due to a horseshoe vortex, placed in a box k, of intensity Γ_k can be derived as follows:

1. Velocity components due to the bound vortex (figure 5.9)

$$u_{CB} = q_{CB} \cos \gamma$$
$$v_{CB} = 0 \qquad 5.28$$
$$w_{CB} = - q_{CB} \sin \gamma$$

where

$$q_{CB} = \frac{\Gamma_k}{4\pi h} (\cos \alpha + \cos \beta)$$

$$\cos \alpha = \frac{|y_c - y_i|}{\sqrt{(x_c - x_i)^2 + (y_c - y_i)^2 + z_c^2}}$$

$$\cos \beta = \frac{|y_c - y_{i+1}|}{\sqrt{(x_c - x_{i+1})^2 + (y_c - y_{i+1})^2 + z_c^2}}$$

$$\cos \gamma = \frac{|x_c - x_i|}{h}$$

$$\sin \gamma = \frac{z_c}{h}$$

$$h = \sqrt{z_c^2 + (y_c - y_i)^2}$$

and

$$x_i = x_{i+1} \quad ; \quad y_{i+1} = y_i + b$$

2. Velocity components due to port free vortex (figure 5.10)

$$u_{cp} = 0$$

$$v_{cp} = q_{cp} \cos \gamma \qquad 5.29$$

$$w_{cp} = - q_{cp} \sin \gamma$$

Where

$$q_{cp} = \frac{\Gamma_k}{4\pi h} (\cos \alpha + 1)$$

$$\alpha = 180 - \beta = 180 - \sin^{-1} \frac{h}{\sqrt{(x_c - x_i)^2 + (y_c - y_i)^2 + z_c^2}} \quad \text{for } x_c < x_i$$

or

$$\alpha = \sin^{-1} \frac{h}{\sqrt{(x_c - x_i)^2 + (y_c - y_i)^2 + z_c^2}} \quad \text{for } x_c > x_i$$

$$\gamma = \sin^{-1} \frac{z_c}{h}$$

$$h = \sqrt{(y_c - y_i)^2 + z_c^2}$$

3. Velocity components due to starboard free vortex (figure 5.11)

$$u_{cs} = 0$$

$$v_{cs} = q_{cs} \cos \gamma$$

$$w_{cs} = q_{cs} \sin \gamma$$

where

$$q_{cs} = \frac{\Gamma_k}{4\ h} (\cos \alpha + 1)$$

$$\alpha = 180 - \beta = 180 - \sin^{-1} \frac{h}{\sqrt{(x_c - x_{i+1})^2 + (y_c - y_{i+1})^2 + z_c^2}} \quad \text{for } x_c < x_{i+1}$$

or

$$\alpha = \sin^{-1} \frac{h}{\sqrt{(x_c - x_{i+1})^2 + (y_c - y_{i+1})^2 + z_c^2}} \quad \text{for } x_c > x_{i+1}$$

$$\gamma = \sin^{-1} \frac{z_c}{h} \qquad \text{and}$$

$$h = \sqrt{(y_c - y_{i+1})^2 + z_c^2}$$

The complete horseshoe vortex placed in the panel k causes a disturbance velocity, in the collocation point on the panel n, with components:

$$\begin{aligned} u_{cnk} &= u_{cb} \\ v_{cnk} &= v_{cp} + v_{cs} \\ w_{cnk} &= w_{cb} + w_{cp} + w_{cs} \end{aligned} \qquad 5.31$$

The total induced velocity components in the collocation point on the panel n are obtained through summation over all the horseshoe vortices:

$$u_{cn} = \sum_{k=1}^{\iota} u_{cnk} = \sum_{k=1}^{\iota} R_{unk}\, \Gamma_k$$

$$v_{cn} = \sum_{k=1}^{l} v_{cnk} = \sum_{k=1}^{l} R_{vnk}\,\Gamma_k \qquad 5.32$$

$$w_{cn} = \sum_{k=1}^{l} w_{cnk} = \sum_{k=1}^{l} R_{wnk}\,\Gamma_k$$

where

l is the total number of panels,

and R_{unk}, R_{vnk}, R_{wnk} are the coefficients of the disturbance velocity components obtained from equations 5.29 to 5.31.

Then, the conditions of tangential flow are applied to give:

$$u_{cn} \times C_{xn} + v_{cn} \times C_{yn} + w_{cn}\ C_{zn} = V \times C_{xn} \qquad 5.33$$

where

V is the free stream velocity,

and C_{xn}, C_{yn}, C_{zn} are the components of the normal vector to the surface at the collocation point on the panel n.

In the original Hedman method, the vortices and the control points were positioned on a wing chord line (here equivalent to the plane z = 0). The slope of the wing was used only on the RHS of equation 5.33. For the present application this is inadequate.

In matrix notation equation 5.33 can be written as:

$$[T]\ \{\Gamma\} = \{VN\} \qquad 5.34$$

where

$$T\ (n,k) = R_{unk} \times C_{xn} + R_{vnk} \times C_{yn} + R_{wnk} \times C_{zn}$$

$$VN(n) = V \times C_{xn}$$

Equation 5.34 represents l linear equations in terms of the l unknown vortex intensities. The set of linear equations can be solved by any direct or iterative method.

After all values of Γ_k are known, the total velocities (i.e. free stream plus disturbance velocities) are calculated at each collocation point. And finally, pressure coefficients are evaluated from equation 5.9.

5.6.2 Quadrilateral vortex-rings in the plane z = 0

In section 5.5 it was shown that in the case of a thin section submerged in a uniform flow with the flow on both sides and with normal velocities continuous on the two sides, the surface can be viewed as a layer of doublets. Hence, this time, by more direct application of Green's identity, we will investigate pressure coefficient distributions, where instead of horseshoe vortices, doublets are used. The singularities will be positioned, as in section 5.6.1, in the plane z = 0, and the control points will be situated on the surface of the section.

As a surface made up of a network of the constant-strength doublet panels is the same as the surface represented by a lattice of ring vortices, the latter will be used to define the velocity field since it is easier to apply. The general pattern of vortices will be as shown in figure 5.12, namely: the load of each panel, but the last row will be approximated by quadrilateral vortex-rings. In the last row, vortices will be of the horseshoe form, to allow for

trailing vortices extending from the rear section. The control points will be placed at the mean of the four corner points of each quadrilateral vortex-ring, as shown in figure 5.12. The coordinates of a control point are thus:

$$x_c = \frac{x_1 + x_2 + x_3 + x_4}{4}$$

$$y_c = \frac{y_1 + y_2 + y_3 + y_4}{4} \qquad 5.35$$

$$z_c = f(x_c, y_c)$$

The induced velocity components will be calculated in a similar way to that outlined in section 5.6.1 by applying the Biot-Savart's law, but accounting for a different shape of the basic building block, the quadrilateral vortex ring.

5.6.3 Quadrilateral vortex-rings on the surface

In the methods of sections 5.6.1 and 5.6.2 vortices in the form of horseshoe or quadrilateral vortex-rings were distributed in the plane z = 0. The methods belong to the group of approximate numerical methods. Since 1962 aerodynamicists have used exact numerical methods, which are directly based on the Green's identity. In these applications singularities are placed on the surface of a body. This implies that a body of arbitrary shape can be modelled.

In a third attempt to calculate the pressure coefficient distribution on an open sided shell roof, the quadrilateral vortex-rings will be distributed on the surface of a model.

The eliptic paraboloid section will be divided into trapezoidal elements, and the load on each of them, except the last row, will be represented by the quadrilateral vortex-ring. The last row, in a similar way to section 5.6.2, will be represented by horseshoe vortices (see figure 5.13).

The presence of the trailing vortex sheet makes the problem non-linear, since two basic unknowns: the geometric shape of the trailing sheet, and the overall distribution of vorticity, are interdependent. The linearised solution [139] which is employed here, assumes that the trailing sheet lies in the plane of the roof and then, when it leaves the surface, extends to infinity in the mean plane (here the plane $z = 0$).

As before, the collocation points are found as the mean of the four corner points of each quadrilateral vortex-ring. In the case of a rectangular element the geometrically mean point is also the interior point at which the velocity induced by the vortex-ring is a minimum. More generally, the minimum induced velocity point seems to be a better criterion for the control point location than the mean of the corner points [139]. In the case of the shallow, symmetrical, eliptic paraboloid shell, however, the shape of elements does not greatly deviate from rectangular. Hence for simplicity of calculation the geometric criterion is used.

The velocity coefficients, R_{unk}, R_{vnk}, R_{wnk}, in equation 5.32 for the present method, take more complicated forms than those of section 5.6.1. They can be found as follows: The velocity at point P of figure 5.14, due to the vortex line 1-2 is defined as

$$q_{p12} = \frac{\Gamma}{4\pi h} (\cos \alpha + \cos \beta) \qquad 5.36$$

where

$$\cos \alpha = \frac{d_1^2 + d_3^2 - d_2^2}{2\, d_1\, d_3}$$

$$\cos \beta = \frac{d_3^2 + d_2^2 - d_1^2}{2\, d_3\, d_2}$$

d_1, d_2, d_3, - are the distances between points 1-P, 2-P and 1-2 respectively, and

$$h = |\sin \alpha|\, d_1.$$

The x, y z velocity components are given by:

$$u_{p12} = q_{p12} \times C_x \qquad 5.37$$

$$v_{p12} = q_{p12} \times C_y$$

$$w_{p12} = q_{p12} \times C_z$$

where

C_x, C_y, C_z are direction cosines

The values of these direction cosines can be obtained from the Biot-Savart law, which states that the vector q_{p12} is perpendicular to the plane defined by points 1, 2 and P (see figure 5.14)

Therefore

$$C_x = \frac{a_2 \times b_3 - a_3 \times b_2}{|\bar{a}| \times |\bar{b}|} \qquad 5.38$$

$$C_y = \frac{a_3 \times b_2 - a_2 \times b_3}{|\bar{a}| \times |\bar{b}|}$$

$$C_z = \frac{a_1 \times b_2 - a_2 \times b_1}{|\bar{a}| \times |\bar{b}|}$$

where

$$\bar{a} = \bar{i}a_1 + \bar{j}a_2 + \bar{k}a_3$$

$$\bar{b} = \bar{i}b_1 + \bar{j}b_2 + \bar{k}b_3$$

and

$$a_1 = x_1 - x_p \qquad b_1 = x_2 - x_p$$

$$a_2 = y_1 - y_p \qquad b_2 = y_2 - y_p$$

$$a_3 = z_1 - z_p \qquad b_3 = z_2 - z_p$$

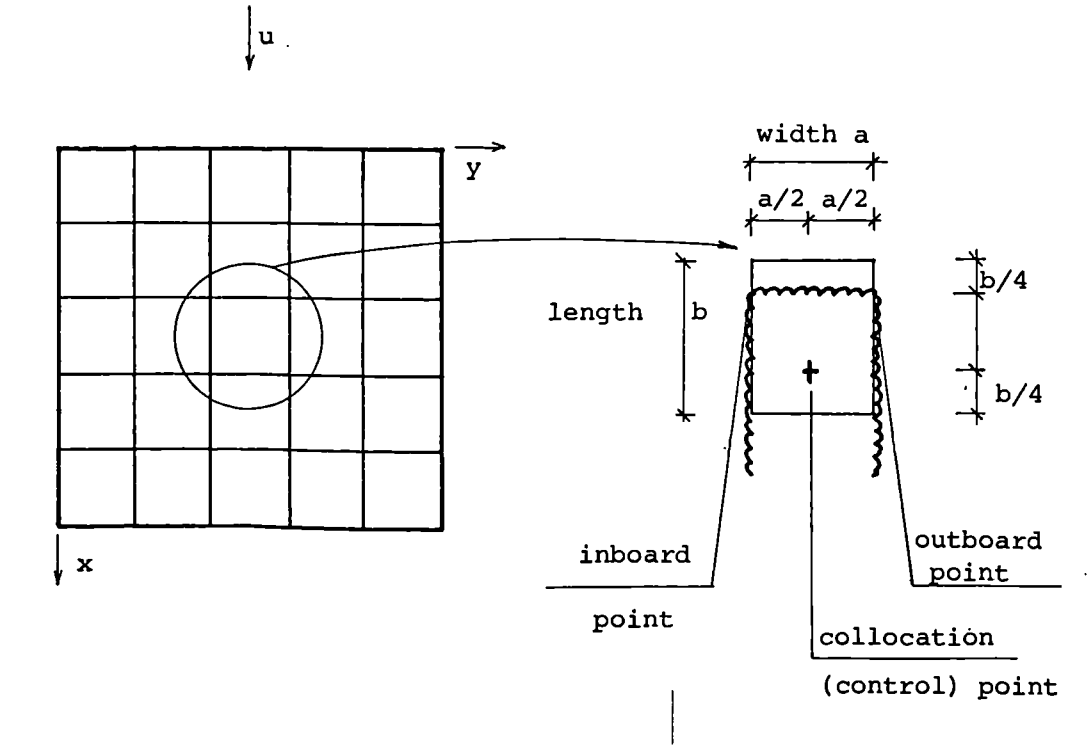

Figure 5.4

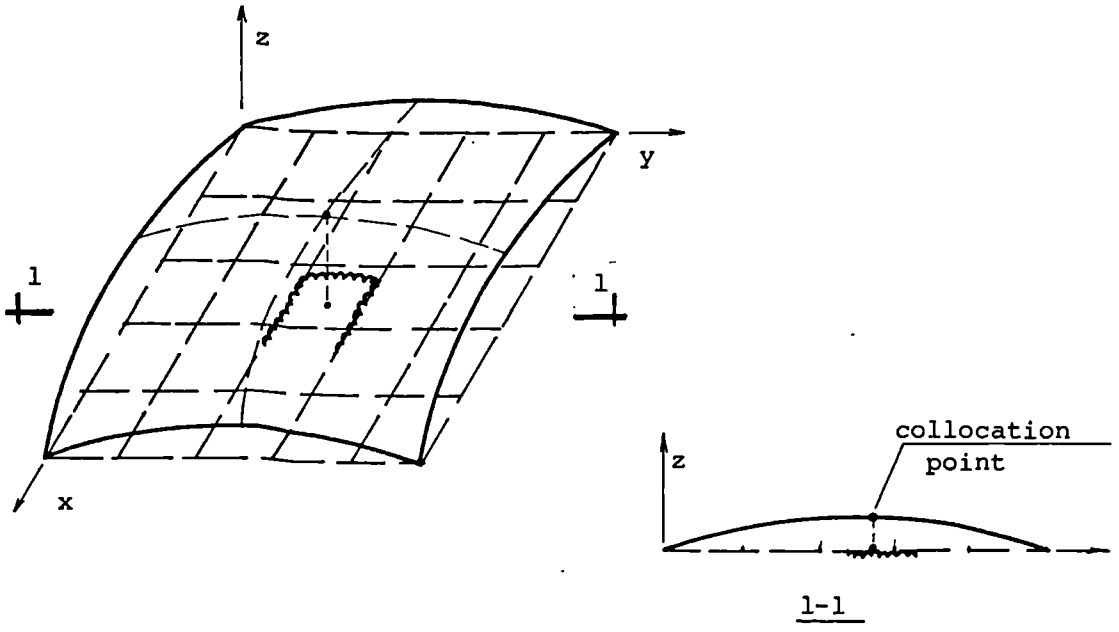

Figure 5.5

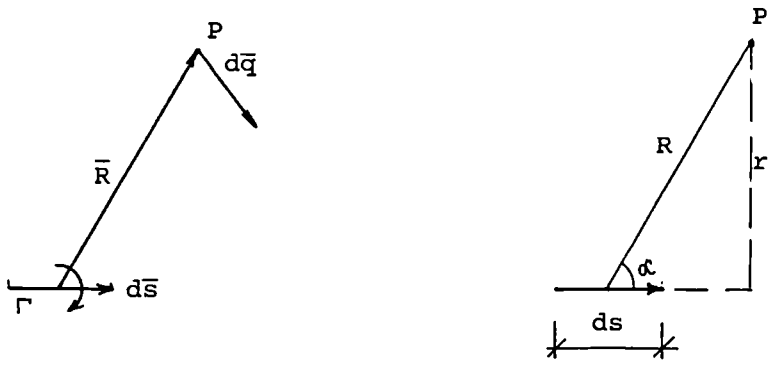

Figure 5.6

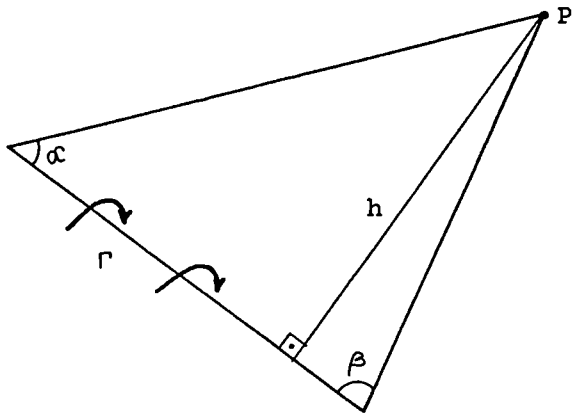

Figure 5.7

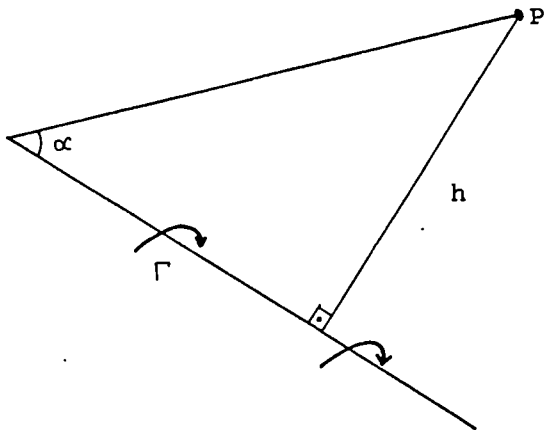

Figure 5.8

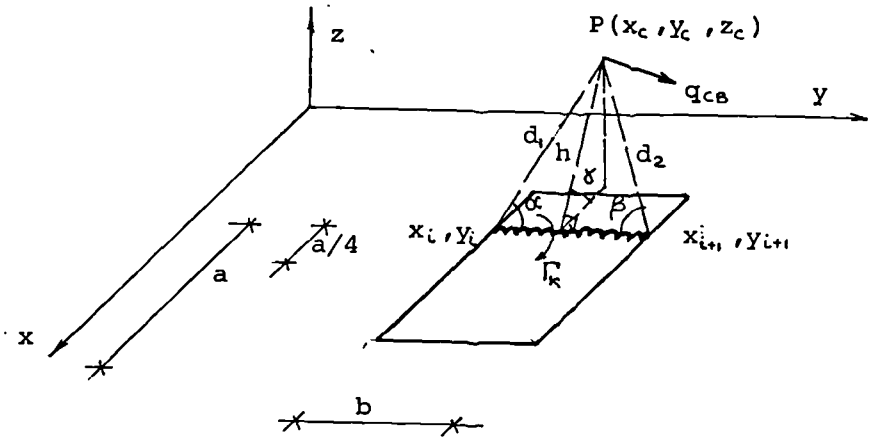

Figure 5.9

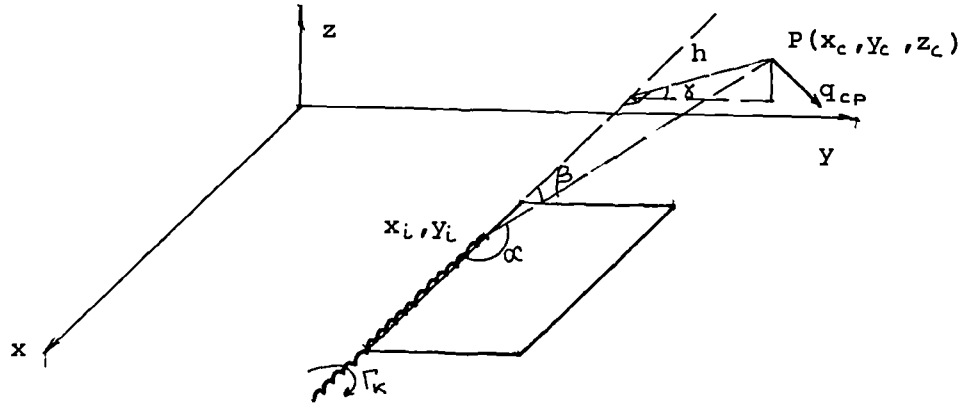

Figure 5.10

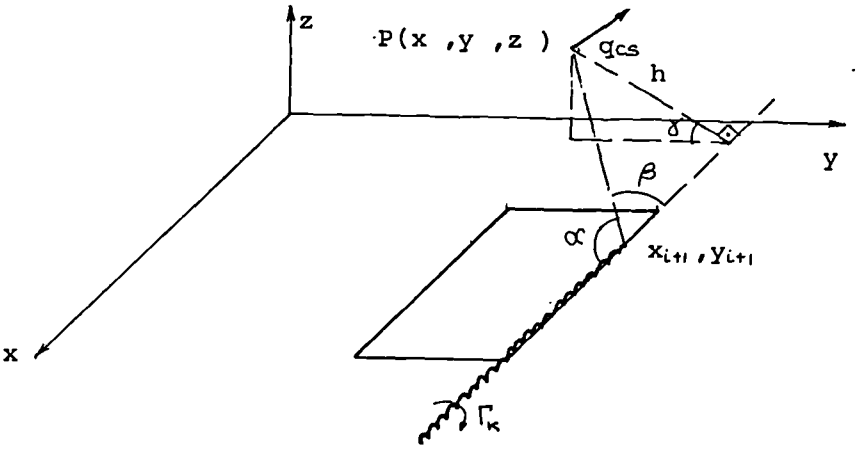

Figure 5.11

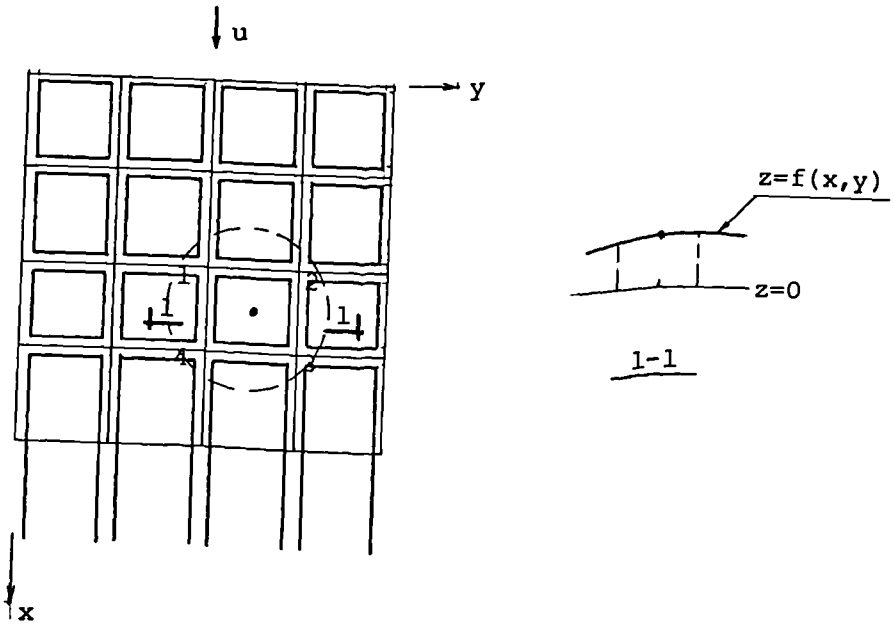

Figure 5.12

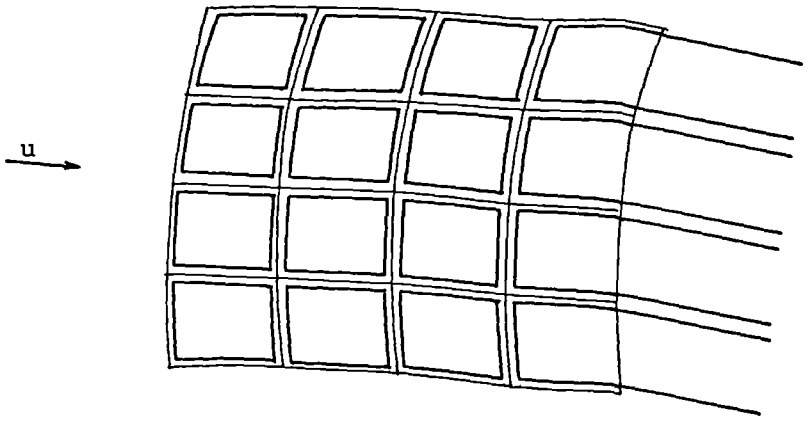

Figure 5.13

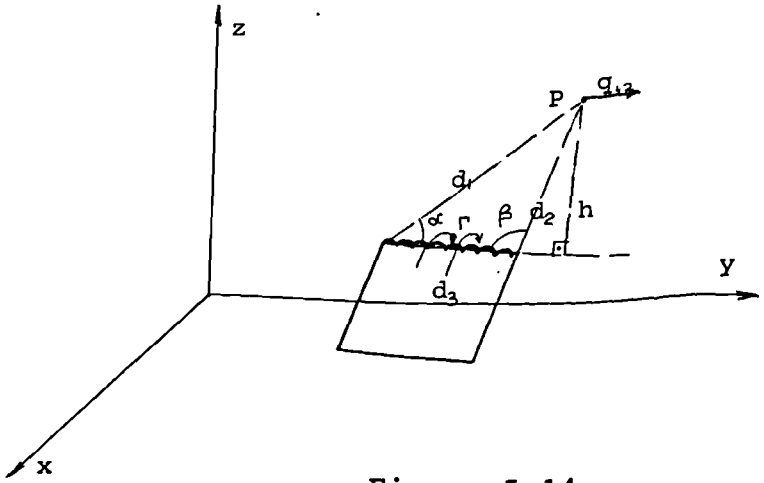

Figure 5.14

5.7 Numerical analyses

The main steps in the vortex-lattice methods can be represented by the flow chart given in figure 5.15. The approaches described in the subclauses of section 5.6 can be applied to any shallow, open-sided, shell roof of arbitrary shape. The methods have been coded in standard Fortran for the Gould minicomputer with application to the doubly symmetric eliptic paraboloid shell roof. Therefore, the discussion below will be mainly concerned with this shape, with some remarks of a more general nature.

In more general cases, the input of geometry may be rather lengthy, but here the problem is largely reduced due to the fact that the shape of the roof can be described by a single mathematical equation, namely:

$$Z(x, y) = f_1 + f_2 - 4f_1 \frac{(x - \frac{a}{2})^2}{a^2} - 4f_2 \frac{(y - \frac{b}{2})^2}{b^2} \qquad 5.39$$

where

f_1, f_2, a, b are shown in figure 5.16

The actual values of f_1, f_2, a and b, which were used in the numerical analyses are:

f_1 = 12.5 mm

f_2 = 56.5 mm

a = 450 mm

b = 350 mm

The parameters were chosen to coincide with those of the model which was tested in the wind tunnel and which is described in Chapter 6.

Two directions of wind were considered:

1. parallel to the longitudinal edge of the shell
2. perpendicular to the longitudinal edge

The vortex lattice methods which were used can be divided into three categories:

1. horseshoe vortices in the plane z = 0
2. quadrilateral vortex-rings in the plane z = 0
3. quadrilateral vortex-rings on the surface of the shell

In each of the categories 2 and 3, two cases are examined:

a. with a quadrilateral vortex-ring distribution as shown in figures 5.12 and 5.13
b. with the leading element vortices set back one quarter of each element width from the leading edge, and the last row of control points placed a quarter element width upstream of the trailing edge (see figure 5.17). This arrangement was used in order to investigate the influence of the standard vortex-lattice practice for shell roofs.

In the first step the projection of the surface on the xy plane is divided into equal size rectangular elements. The category 3 requires additional information i.e. the z coordinates. The input of surface coordination for each panel contains 3 points for category 1 (the inboard and outboard points, and the control point) and 5 for the remaining two categories, namely: 4 corner points (x, y coordinates for category 2) and the control point.

In the case of the eliptic paraboloid defined by equation 5.39 and shown in figure 5.16, the vector normals to the surface at the control points are obtained from the vector product of two vectors $\bar{u}$ and $\bar{v}$ tangential to the curve at these points. At any point $P(x_1, y_1, z_1)$ on the shell two parabolds lying in mutually perpendicular planes (parallel to x and y axes) can be defined:

$$Z(x)_{y=y1} = C_1 - 4f_1 \frac{(x - \frac{a}{2})^2}{a^2} \qquad 5.40$$

$$Z(y)_{x=x1} = C_2 - 4f_2 \frac{(y - \frac{b}{2})^2}{b^2}$$

where C_1, C_2 are constants.

The derivatives, $\frac{dz(x)_{y=y1}}{dx}$, $\frac{dz(y)_{x=x1}}{dy}$, at point P give the gradients of the curves $z(x)_{y=y1}$ and $z(y)_{x=x1}$ respectively, from which the components of vectors tangential to the shell can be derived.

Calculations for the coefficients of the disturbance velocity components can be greatly shortened by noticing two facts:

1. some parts of the vortex-rings or the trailing vortices of horseshoe vortices are common to two adjacent elements; the appropriate coefficients need not be calculated twice, they differ only in their sign.

2. due to the symmetry of the problem (of the geometry and of the flow) about the plane $y = \frac{b}{2}$, only half of the problem need be modelled. The coefficients of the image panels (symmetry can be viewed as a mirror reflection) are obtained from the corresponding real panel coefficients by observing that the x and z components are the same and the y components differ only in their sign. The coefficients of disturbance velocities of corresponding real and image elements are added together since the vortex strengths are equal.

The vortex strengths are found from the set of linear equations (5.34) giving the tangential flow conditions at all control points. The equations are solved by a standard matrix inversion scheme, namely the Gaussian elimination method. In the case when a smaller computer is used and/or the problem requires more elements, storage space in the computer may become a major problem. In such cases matrix partitioning methods may be required.

Substituting the vortex strengths into equation 5.32 gives the velocity at each control point due to vortex-ring/horseshoe vortices. The total tangential velocities are obtained by adding the free stream velocity to the disturbance velocities. The pressure coefficients on the top side of the shell are then found from equation 5.9.

The accuracy of numerical methods depends greatly upon the size and number of elements used to model the problem. This

aspect was investigated by dividing the shell into 5x5, 9x9 and 17x17 panels and considering the C_p distributions along the axes of symmetry. Graphs in figure 5.18 show the results obtained using horseshoe vortices distributed in the plane z = 0 for the two wind flow cases:

1. wind parallel to the longitudinal edge. The ratio of rise to span of the shell in this longitudinal direction is 1/36.
2. wind perpendicular to the longitudinal edge, (or wind in the traverse direction). The ratio of rise to span of the shell for this direction is 1/6.

Similar comparisons were made for the method using quadrilateral vortex-rings placed on the surface of the shell, and the results are shown in figure 5.19. The method of category 2, namely quadrilateral vortex-rings placed in the plane z = 0, was not tested since the factor influencing the number of divisions are similar to those for the category 1 method.

Conclusions which can be drawn from the graphs in figures 5.18 and 5.19 are as follows:

1. All the graphs show a convergence trend i.e. the difference in results between: 17x17 panels and 9x9 panels are smaller than between 9x9 and 5x5 panels.
2. The maximum discrepancies in the values of C_p coefficients between the various divisions are:

   5x5 and 17x17 - 0.07 (figure 5.18b)

   9x9 and 17x17 - 0.01 (figure 5.18b) (except the leading edge of figure 5.18a)

(Note that different C_p scales have been used for clarity). For the purpose of wind loading on structures the above discrepancies are both small.

3. In the method using horseshoe vortices in the plane z = 0, for wind parallel to the longitudinal direction, the results at the leading edge show greater differences than at other points. This may imply that a fine division in this area is required. On the other hand, Hedman [88] showed that this method tends to over-estimate C_p values near leading edges; therefore using a course division throughout a roof and taking the control point C_p value as the average in each panel may result in a move realistic loading.
4. The method with quadrilateral vortex-rings distributed on the surface of the shell, for wind parallel to the longitudinal direction shows the greatest discrepancy.

For further discussion of results the division with 9x9 panels will be considered. To investigate how the set back of the leading element vortices (a standard practice for vortex-lattice methods) influences the prediction of wind loading on the open sided shell roof, the C_p distributions along the axis of symmetry can be examined. These C_p distributions were obtained from the vortex-lattice methods using the same pattern of vortices but placed in two different manners (cases a and b). The comparison is carried out for categories 2 and 3, namely quadrilateral vortex-rings placed in the plane z = 0 (figure 5.20), and on the surface (figure 5.21). The differences are small.

It is worth noting that the C_p values calculated using the two methods (horseshoe vortices distribution (figure 5.18), and set back quadrilateral vortex-rings (figure. 5.20) case b) are almost identical. In the case of singularity distribution in the plane z = 0, the first method is preferable because of its simplicity. However, when vortices are distributed over curved surfaces, quadrilateral vortex-rings are simpler (see figure 5.22b), as the number of disturbance velocity coefficients to be calculated is much greater in the horseshoe vortex distribution method (see figure 5.22a).

Figure 5.24 shows a comparison of the non-dimensional pressure coefficient distributions obtained from the methods of category 1 and category 3 case b. The C_p values are given as numbers corresponding to the control points on the top of the shell. The presentation of these C_p values as continuous functions along the axis of symmetry is given in figure 5.25. The results from the two approaches vary greatly.

Conclusions

Due to the great discrepancies in C_p distributions, on the top surface of the open sided eliptic paraboloid shell, obtained from the methods:

i) Using horseshoe distribution in the plane z = 0, and

ii) Using swept quadrilateral vortex-rings on the surface of the curved body,

it is necessary to examine the two approaches more closely.

From the graphs of figures 5.18 and 5.20 it can be concluded that the two methods: i) the horseshoe vortices and ii) the swept quadrilateral vortex rings, yield identical results when singularities are distributed in the same place.

The panel method employing constant strength quadrilateral vortex-rings placed on a curved body is equivalent in two dimensions to concentrated vortices at every node excepting the last (figure 5.23a). The velocity field due to one of these vortices has little effect on the tangential velocity at the control point nearby. When the section is shallow, the conditions are even more critical, as not only the nearest vortex, but also the vortices in near proximity have small effects on C_p values at the control points. It appears to be that the velocity field on the surface of a shallow structure, due to point vortices placed on the body of the structure, is too singular to be relied upon.

In the case of vortices in the plane $z = 0$ this problem almost disappears in all areas except the leading and the trailing edges (figure 5.23b). Hence, under the assumption of potential flow, this approach is more likely to give reasonable results for shallow sections except near the leading and trailing edges.

The theoretical results obtained by the methods:

a) Using horseshoe distribution in the pane $z = 0$, and

b) Employing swept quadrilateral vortex-rings on the surface of the curved body

will be compared in chapter 6 with experimentally obtained non-dimensional pressure coefficients.

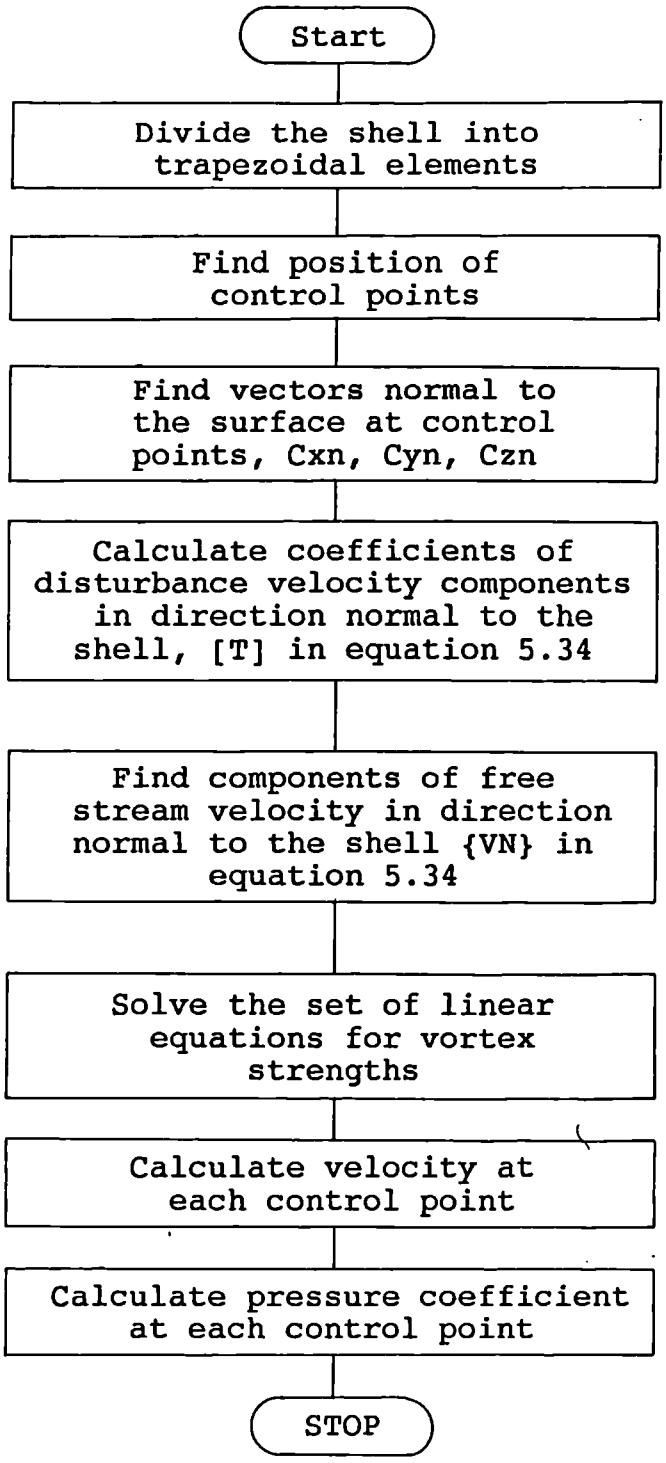
Start
Divide the shell into trapezoidal elements
Find position of control points
Find vectors normal to the surface at control points, Cxn, Cyn, Czn
Calculate coefficients of disturbance velocity components in direction normal to the shell, [T] in equation 5.34
Find components of free stream velocity in direction normal to the shell {VN} in equation 5.34
Solve the set of linear equations for vortex strengths
Calculate velocity at each control point
Calculate pressure coefficient at each control point
STOP

Figure 5.15

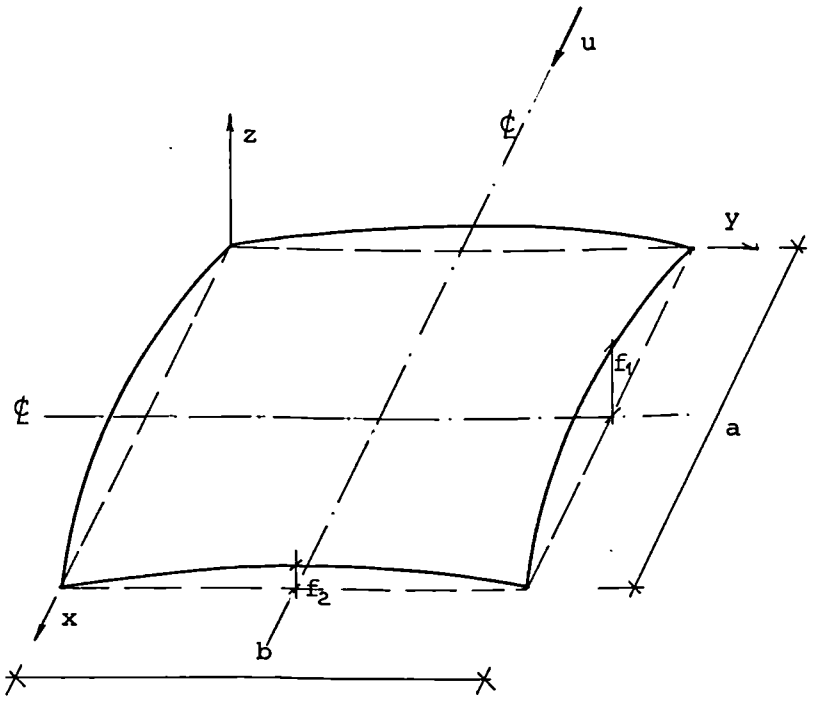

Figure 5.16

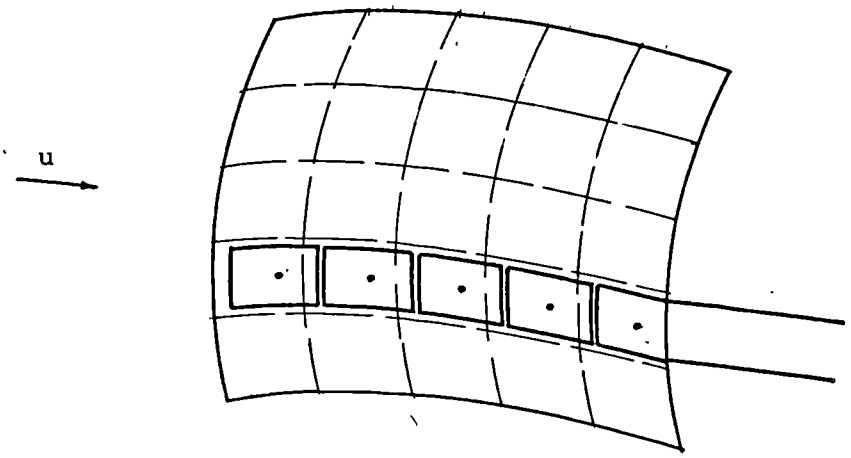

Figure 5.17

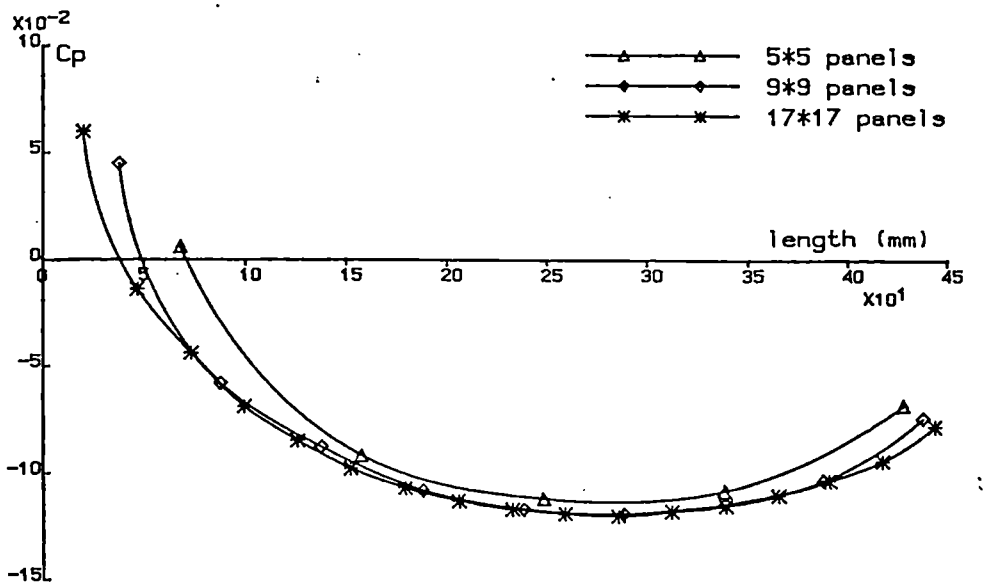

a.wind in longitudinal direction

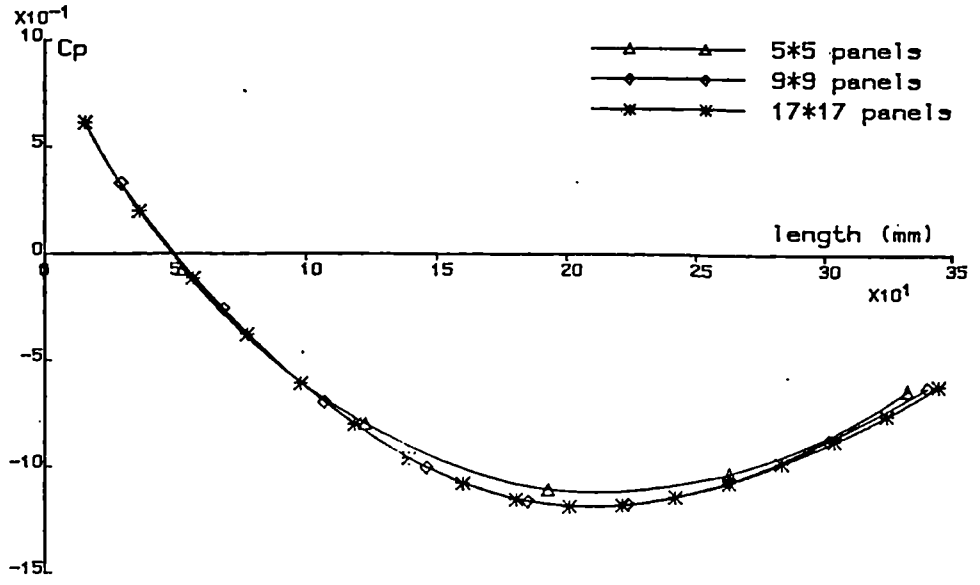

b.wind in traverse direction

Figure 5.18 Horseshoe vortices in the plane Z = 0

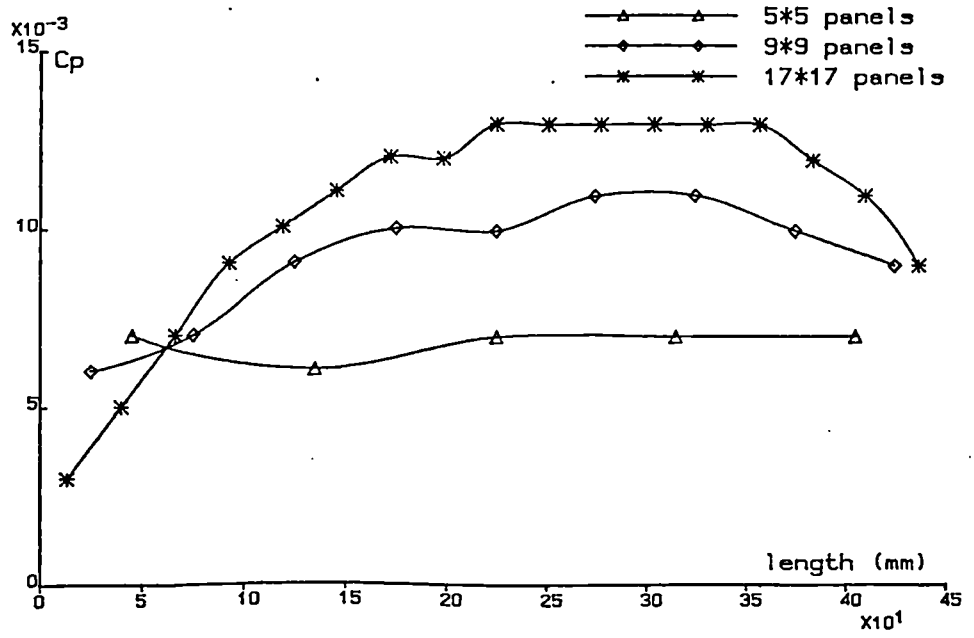

a.wind in longitudinal direction

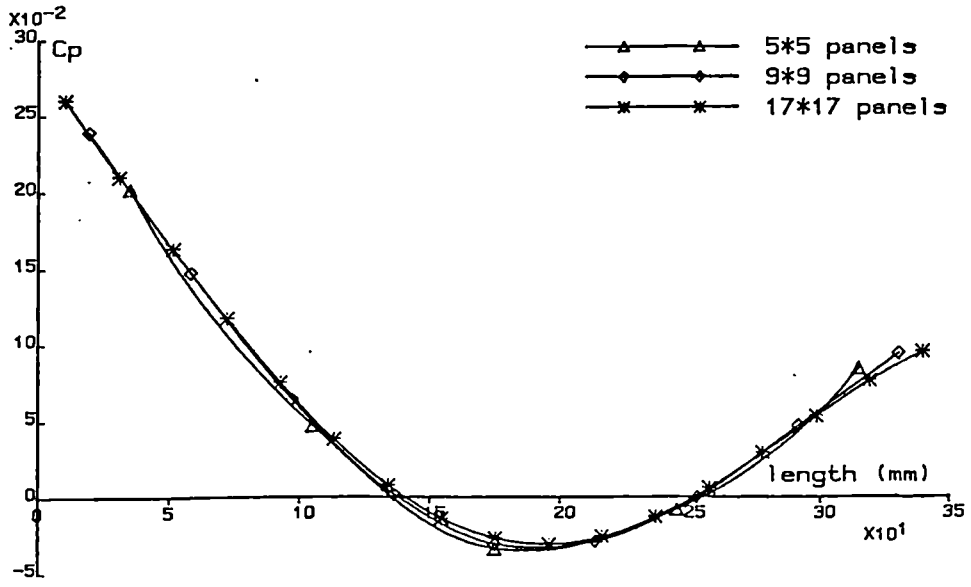

b.wind in traverse direction

Figure 5.19 Quadrilateral vortex-rings on the surface

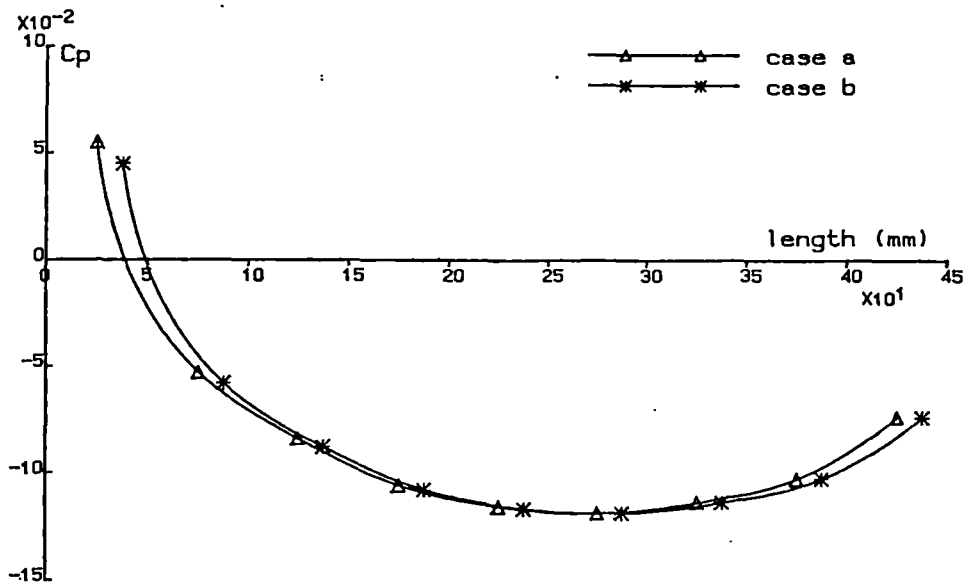

a.wind in longitudinal direction

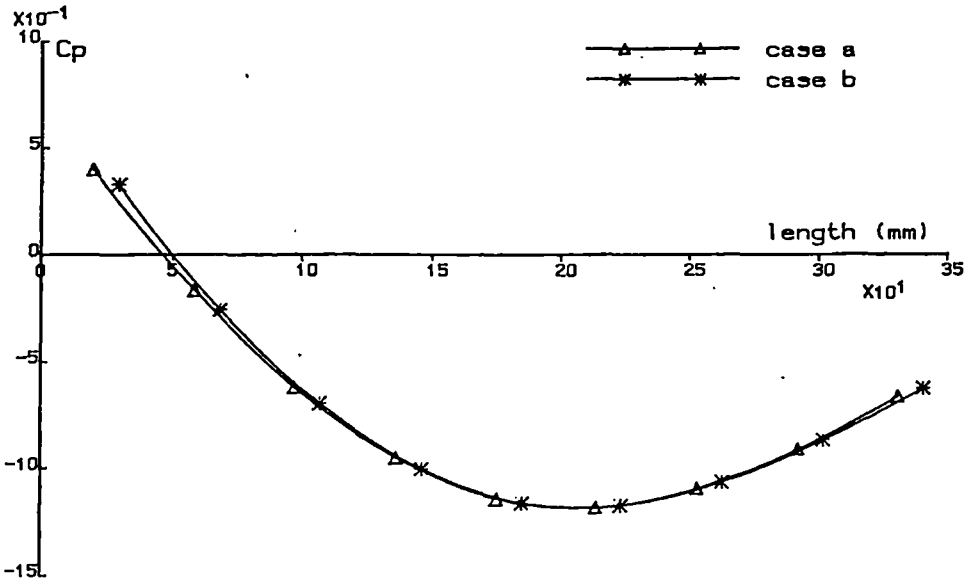

b.wind in traverse direction

Figure 5.20 Quadrilateral vortex-rings in the plane Z = 0

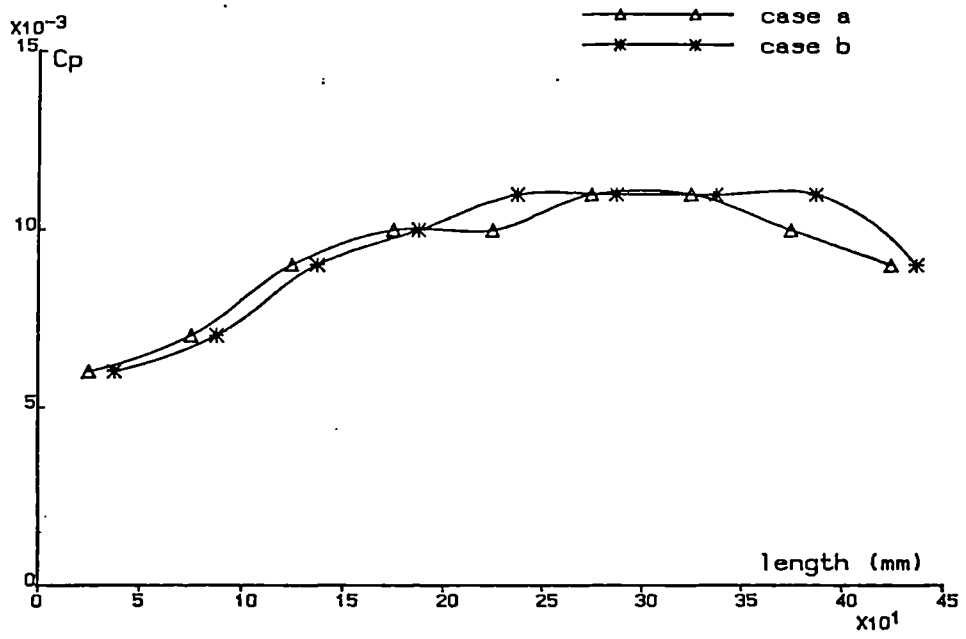

a.wind in longitudinal direction

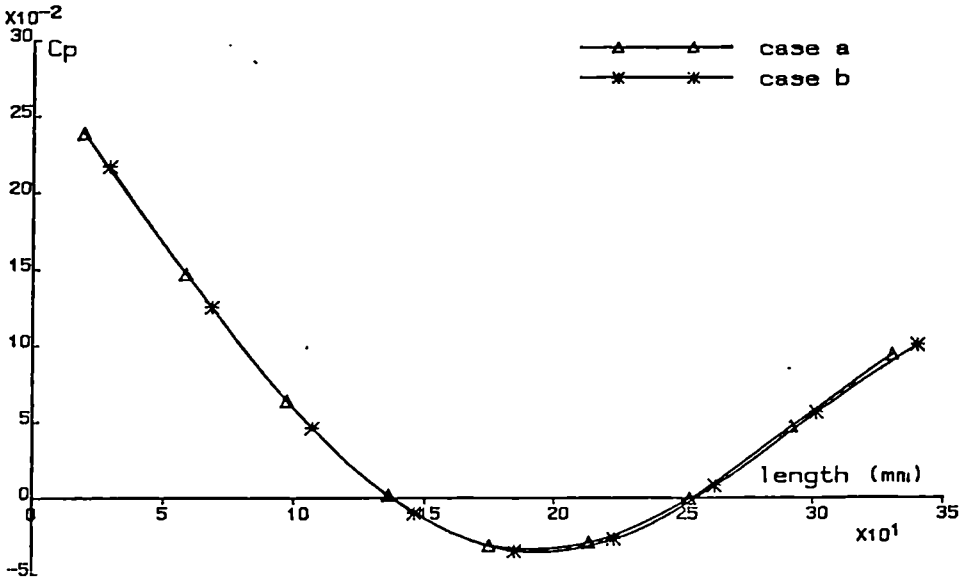

b.wind in traverse direction

Figure 5.21 Quadrilateral vortex-rings on the surface

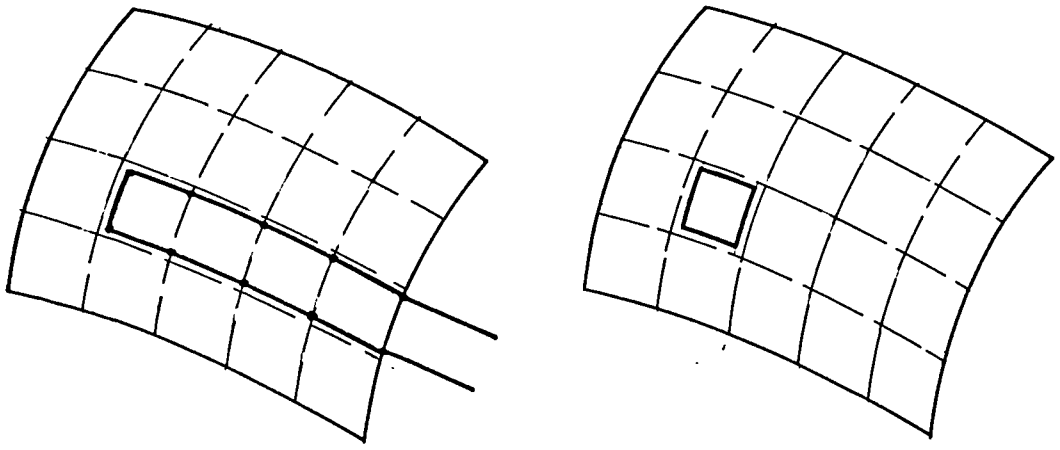

a. b.

Figure 5.22

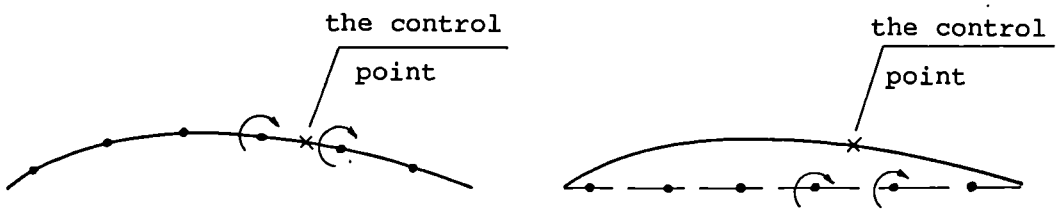

a. b.

Figure 5.23

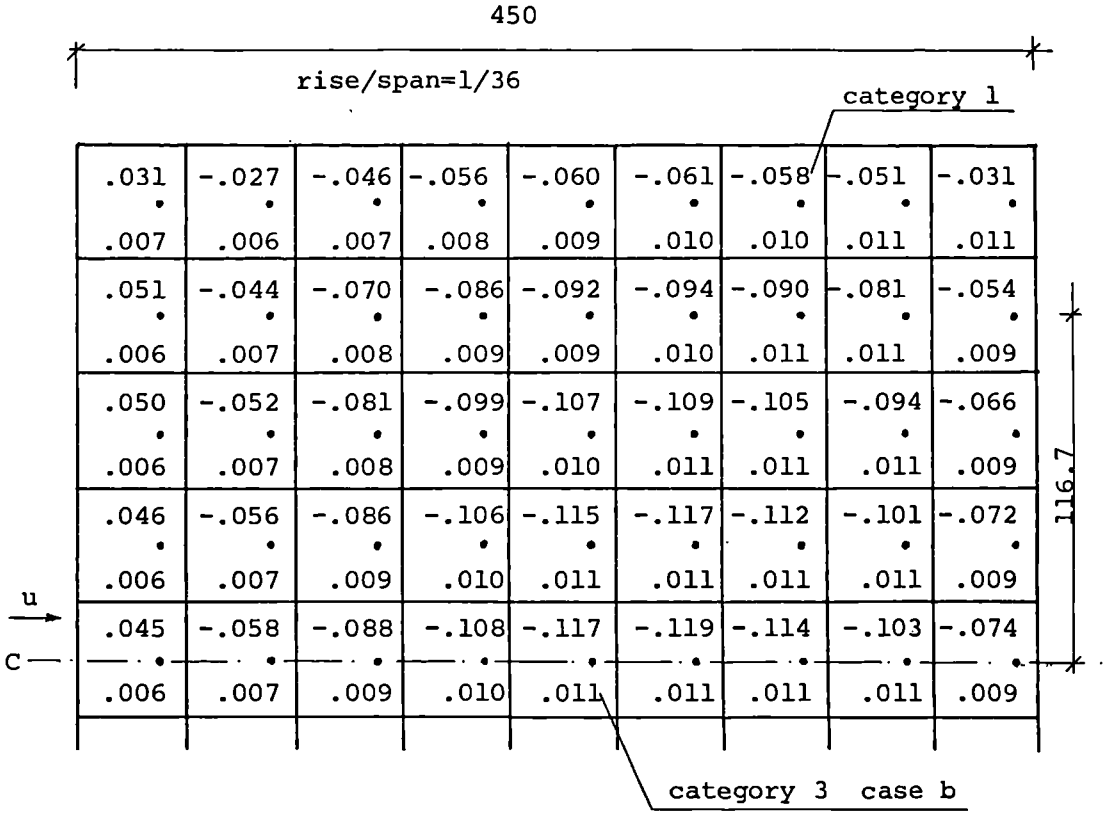

a.wind in longitudinal direction

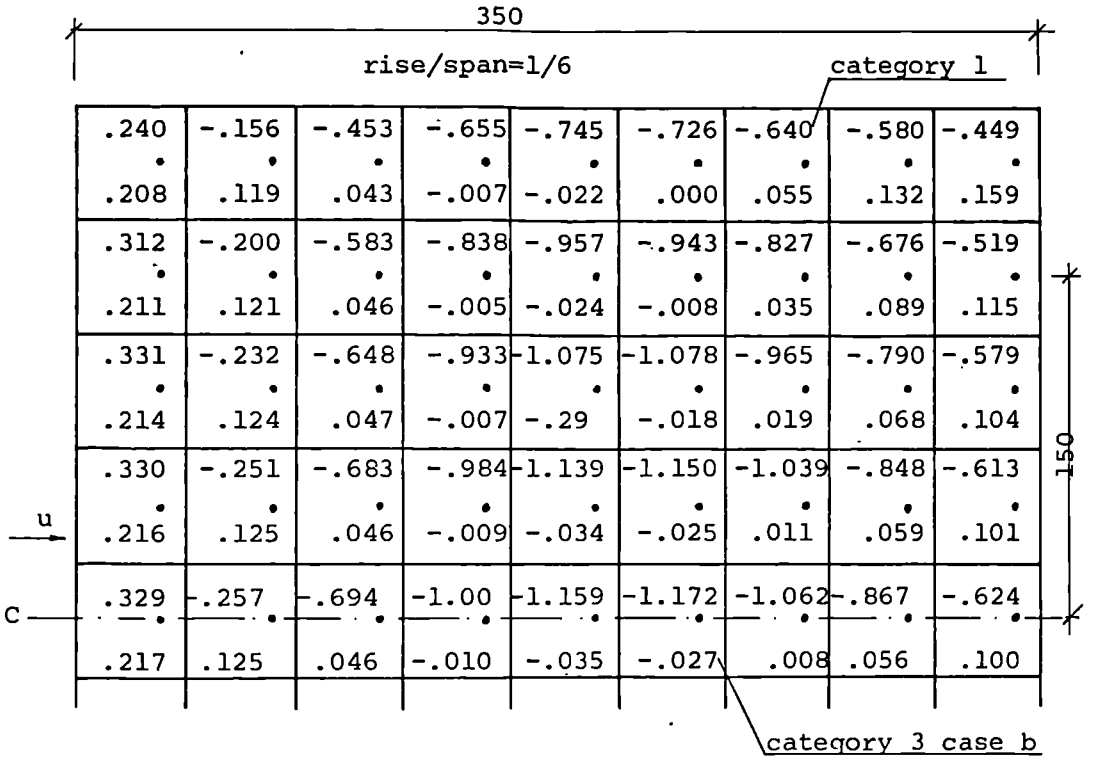

b. wind in traverse direction

Figure 5.24

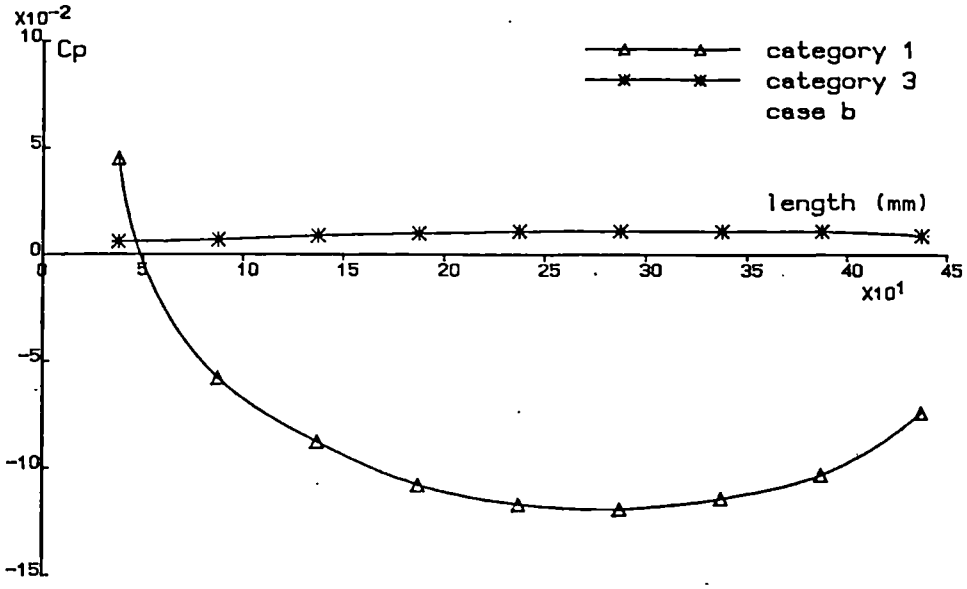

a.wind in longitudinal direction

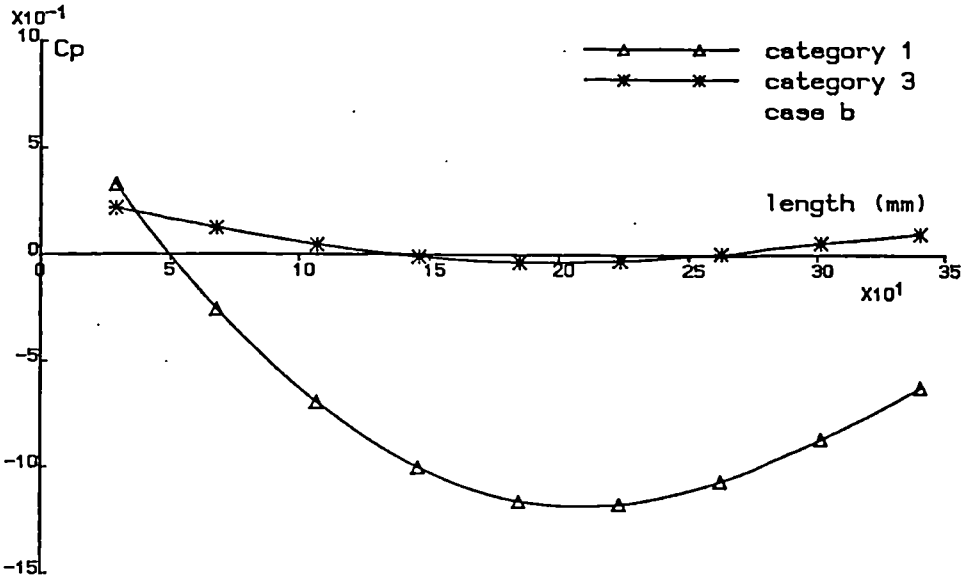

b.wind in traverse direction

Figure 5.25 C_p distribution along axis of symmetry

Appendix to Chapter 5

Two dimensional numerical solution for a real flow

Wind response of air-supported structures is a two-domain problem. This means that the equations describing the behaviour of both the fluid and the structure should be solved together. The type of coupling depends upon the problem under consideration.

The common approaches used in fluid mechanics were briefly reviewed in Chapter 2 and it was concluded that the potential flow approximation is, at the present stage, the most practicable method from the point of view of the amount of computation involved in the numerical modelling of wind action on highly deformable structures. The vortex-lattice methods, based on this theory, were examined for a thin open sided shallow shell. The main weakness of these approaches lies in their incapability of predicting the point of separation and consequently the sudden drop in pressure that would occur on a structure. Hence attempts have been made to model air flow more accurately, and to reassess by means of a numerical example the conclusions of Chapter 2 which were based on a literature review.

The numerical code quoted in this appendix is based on the Navier-Stokes equations extended to turbulent flow, and the continuity equation subject to appropriate boundary conditions. In the approach proposed by Patankar [168] and adopted in this program, the finite difference equations are derived from non-linear fluid differential equations by

means of the control volume formulation. The control volume technique which is a variant of the weighted residual method, can be explained briefly by a simple example as follows:

If a differential equation is represented as

$$L(\phi) = 0 \qquad \text{A1}$$

and $\bar{\phi}$ is an approximate solution expressed in terms of a number of undetermined parameters; a_o, a_1, ... a_m, as for example

$$\bar{\phi} = a_o + a_1 x + a_2 x^2 + ... + a_m x^m \qquad \text{A2}$$

the substitution of ϕ into the differential equation A1 leaves a residual R, defined as

$$R = L(\bar{\phi}) \qquad \text{A3}$$

In order to make the residual small the following integration is performed over the domain of interest:

$$\int W R \, dx = 0 \qquad \text{A4}$$

where W is a weighting function.

By choosing a succession of weighting functions, as many equations can be generated as are required for evaluating the parameters.

The simplest weighting function is W = 1. From this, a number of weighted-residual equations can be generated by dividing the calculation domain into subdomains (control volumes) and setting the weighting function to be unity over one subdomain at a time and zero everywhere else. This variant of the method of weighted residuals is called the control-volume formulation. In this method the calculation

domain, here fluid surrounding the body is divided into a number of non-overlapping control volumes (in two dimensional cases, quadrilaterals are most common). For each control volume one grid point is assigned. The differential equation is integrated over each element. Piecewise profiles expressing the variation of ϕ between the grid points are then used to evaluate the required integrals. The result is a set of discretization equations containing the values of ϕ for a group of grid points. When the discretinzation equations are solved to obtain the grid-point values of the dependent variable, only the grid-point values of ϕ are considered to constitute the solution, without any explicit reference to how ϕ varies between the grid points. This viewpoint permits complete freedom of choice in employing different profile assumptions for integrating different terms in the differential equation.

The mathematical representation of the flow field is more complicated than equation A1, namely the problem is nonlinear and involves two unknowns: the velocity and the pressure fields. The procedure developed for the calculation of the flow field by Patankar, Spalding, Caretto, Gosman [references in 168] has the name SIMPLE (Semi-Implicit Method for Pressure-Linked Equations). The important operations, in order of their execution are:

1. assume the pressure field p*
2. solve the momentum equations to obtain u*, v* and w*
3. calculate the pressure correction, p', from the equation derived by combining continuity and momentum equations, and the total pressure is p = p* + p'

4. calculate velocity corrections u', v' and w' due to the pressure correction p' (a formula obtained by subtracting the momentum equations) and the total velocities u = u* + u', v = v* + v' and w = w* + w'
5. solve the discretization equation for other ϕ's (such as turbulence quantities) if they influence the flow field enough through fluid properties
6. treat the corrected pressure, p, as a new guessed pressure p*, return to step 2 and repeat the whole procedure until a converged solution is obtained.

Thus formulated, the procedure described in [168] is capable of solving a variety of problems; from potential steady flow around an axisymmetric body to the prediction of fluid behaviour around an arbitrary body submerged in time averaged turbulent flow.

The computer code (in Fortran 77) used in this work is a two dimensional version of the 'SIMPLE' program used since 1972 at Imperial College for Boundary Layer Calculations and amended by Younis [207] to suit this particular case.

The whole procedure consists of three steps:

1. grid generation

The decision on grid spacing in the x and y directions, its inclination, and the extremities of the mesh with respect to the body is made by the user. The computer program is used to verify this grid graphically and numerically, and to smooth the data, as well as to prepare the input file for stage 2.

2. the actual analysis

The input data comprises: the geometric input generated in step 1 and the data describing fluid properties. These consist of type of flow to be considered, boundary conditions, and the accuracy required by stating the value of terminal residuals.

The output contains a full description of the resulting flow field; the most important information, in the present application, being pressure and velocity distribution, and the stream function.

3. plotting the output data

When necessary the grid is refined and/or altered, and steps one to three are repeated.

A numerical example

The numerical analysis was performed for an open sided thin shell, infinitely long of section shape as shown in figure A1. The shape and dimensions are those of the cross section along the shorter (or transverse) axis of symmetry of the shell tested in the wind tunnel (see Chapter 6). This transverse direction is that for which separation of flow was found to occur. The approaching flow was assumed to be steady, laminar and with a uniform velocity of 15 m/s.

Two different grids were used in the numerical calculations [207]:

1. test 1 used a course grid, as shown in figure A.2a; with the shell represented by 8 elements (for clarity the y direction is 3 times exaggerated with respect to the x direction in figure A2)

2. test 2 used a finer grid; the grid being refined by a factor of 2 compared with the grid used in test 1. The grid is shown in figure A.3a (for clarity the y direction is 3.5 times exaggerated with respect to the x direction). The shell is idealized consequently by 16 elements.

In test 1 the program converged to reasonably small residuals after 30 cycles, and the resulting stream lines are shown in figure A.2b.

In test 2 convergence did not proceed as quickly and 200 cycles were necessary to obtain results of similar accuracy to that of test 2. The stream lines are shown in figure A.3b.

The pressures on the shell, p_m, obtained from both test 1 and test 2 were nondimensionalised by applying the standard formula:

$$C_p = \frac{p(x,y,z) - p_{ref}}{\frac{1}{2} \cdot \rho_a V^2} \qquad A5$$

where p(x, y, z) is the actual pressure at a grid point on a model;

p_{ref} - a reference pressure, here, the pressure of the approaching flow;

ρ_a - is the air density, and

V - is the free stream velocity.

These Cp distributions, together with the results obtained from the two dimensional vortex-lattice method with vortices distributed in the plane y = 0, were plotted as shown in figure A4. In the latter technique the shell was divided into 8 and 16 elements for direct comparison with test 1 and 2.

By examining figures A.2b and A.3b, showing the stream lines, in conjunction with the plots representing the grids used in tests 1 and 2 respectively, the following conclusions can be drawn:

1. the mesh is extended into too long distances, both upwind and downwind, with respect to the shell such that, at the extremes of the grid, the streamlines are not affected by the presence of the body. A decrease in the area covered by the mesh, in these parts, reduces the number of grid points and hence would speed up the whole procedure.

2. the lower level streamlines are influenced by the presence of the shell. This implies that the distance from the body to the bottom line should have been made larger to exclude boundary effects.

Although the 'SIMPLE' program is not based on the streamline technique, it was felt that by changing the shape and inclining the grid lines more smoothly, especially in the areas just before and after the shell, the number of cycles required to get convergence could be reduced.

The distributions of pressure coefficients from tests 1 and 2 show greater discrepancy than those obtained from the vortex-lattice method for the same idealisation of the shell. This implies that the former method is more dependent on size of mesh.

The plot of C_p values from test 2 is close to the potential flow results, which were compared for the 3D case with the experimental results (the numerical prediction compares fairly well with the experimental results, except in the area of separation). Positive pressure obtained from the SIMPLE program, but not predicted by the vortex-lattice method, occurs in the area where the grid refinement causes the greatest changes in C_p values. Further refinement could be needed to find the final C_p distribution for the real flow solution.

The curve representing the C_p distribution from test 2 for a distance along the shell centreline greater than 300 mm shows slight contraflexure, which may indicate the start of separation. In order to examine the occurrence of this phenomenon, a smaller mesh is needed in this area. It should be noted that although for the three dimensional case

the separation of flow in the rearmost part of the shell was traced experimentally, this does not imply that the same feature should occur in the two dimensional case.

When a three dimensional problem, the open sided, shallow eliptic paraboloid shell, is approximated by the two dimensional case of an infinitely long parabolic shell of the same centreline section shape, the results obtained from the real flow analysis differ from the 3D experimental results much more (for max C_p above 150%), than the simple 3D potential flow results. The computer and the human time required to prepare the data and to run the numerical program based on the potential flow theory is only a small fraction of that which is necessary for obtaining the real flow solution.

The computations were carried out on a minicomputer Gould 6000 and c.p.u. times were: less than a minute and 43 minutes for potential (16 elements) and real flow (test 2) respectively. This excluded the time for pre and post processing.

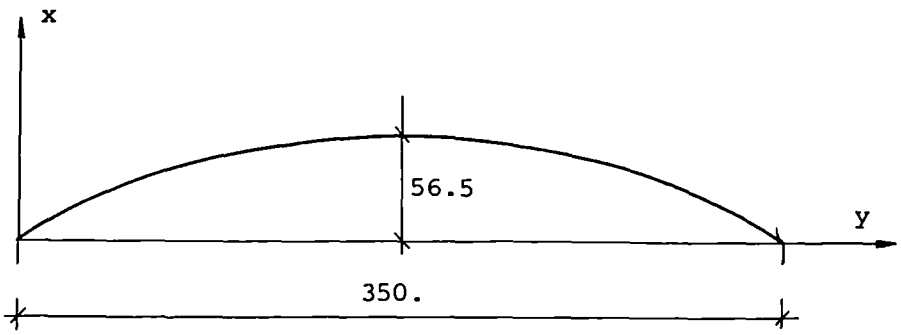

Figure A.1 A Shell section

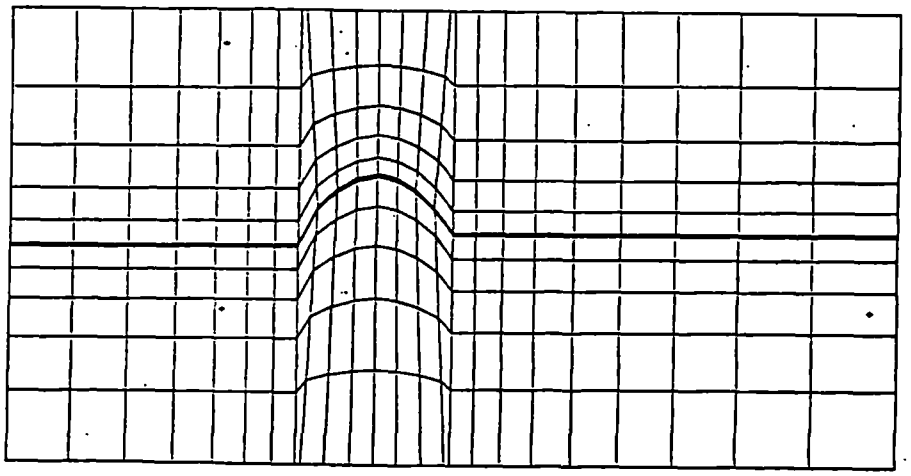

a. Grid

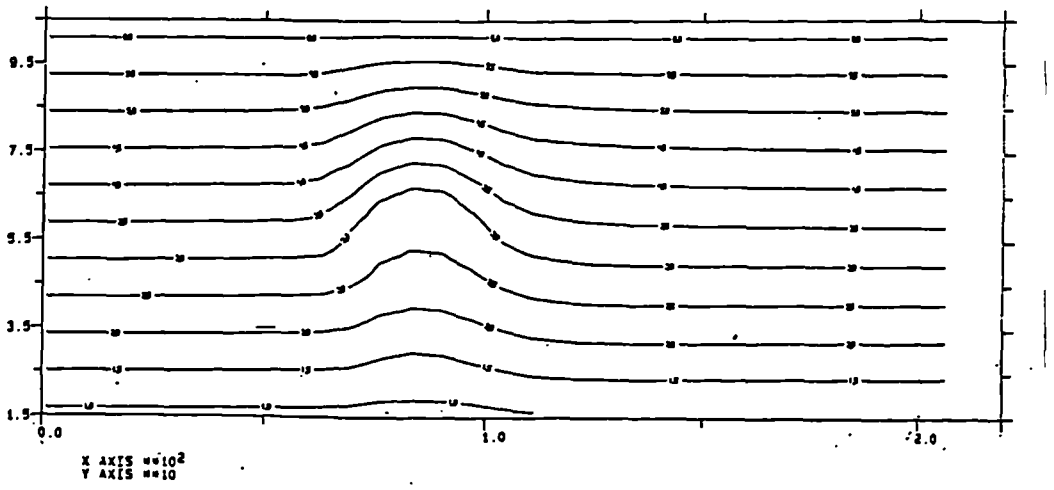

b. Stream lines
Figure A.2 Test 1

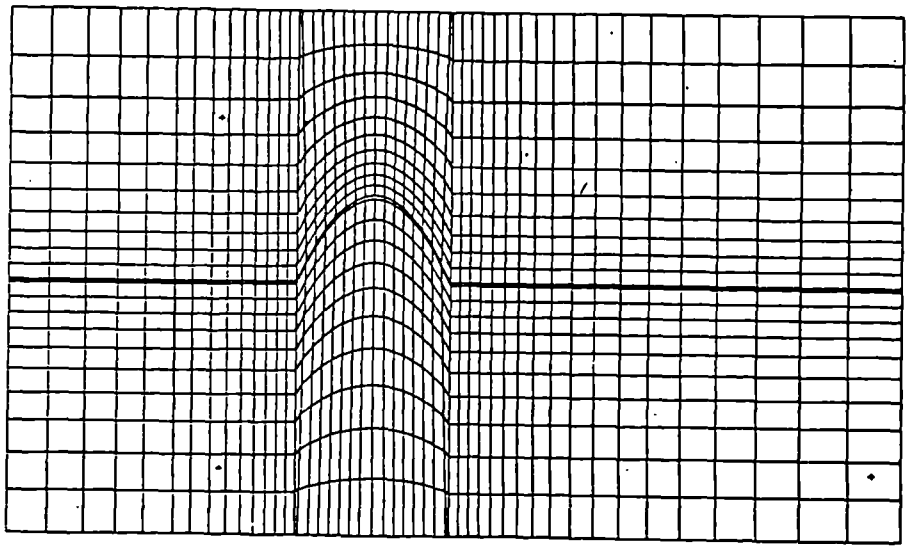

a. Grid

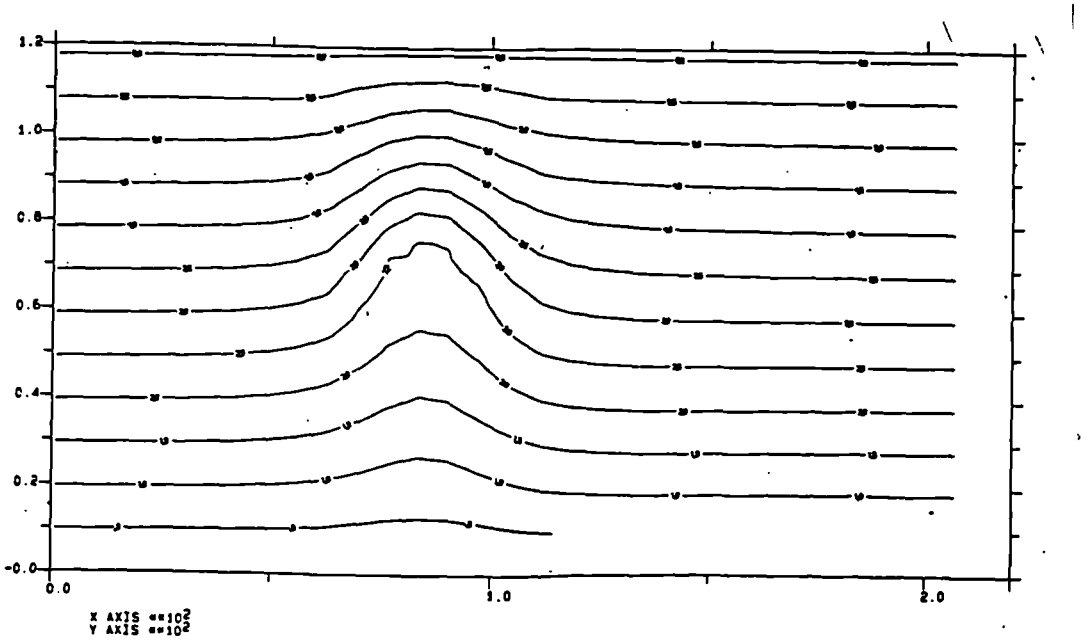

b. Stream lines
Figure A.3 Test 2

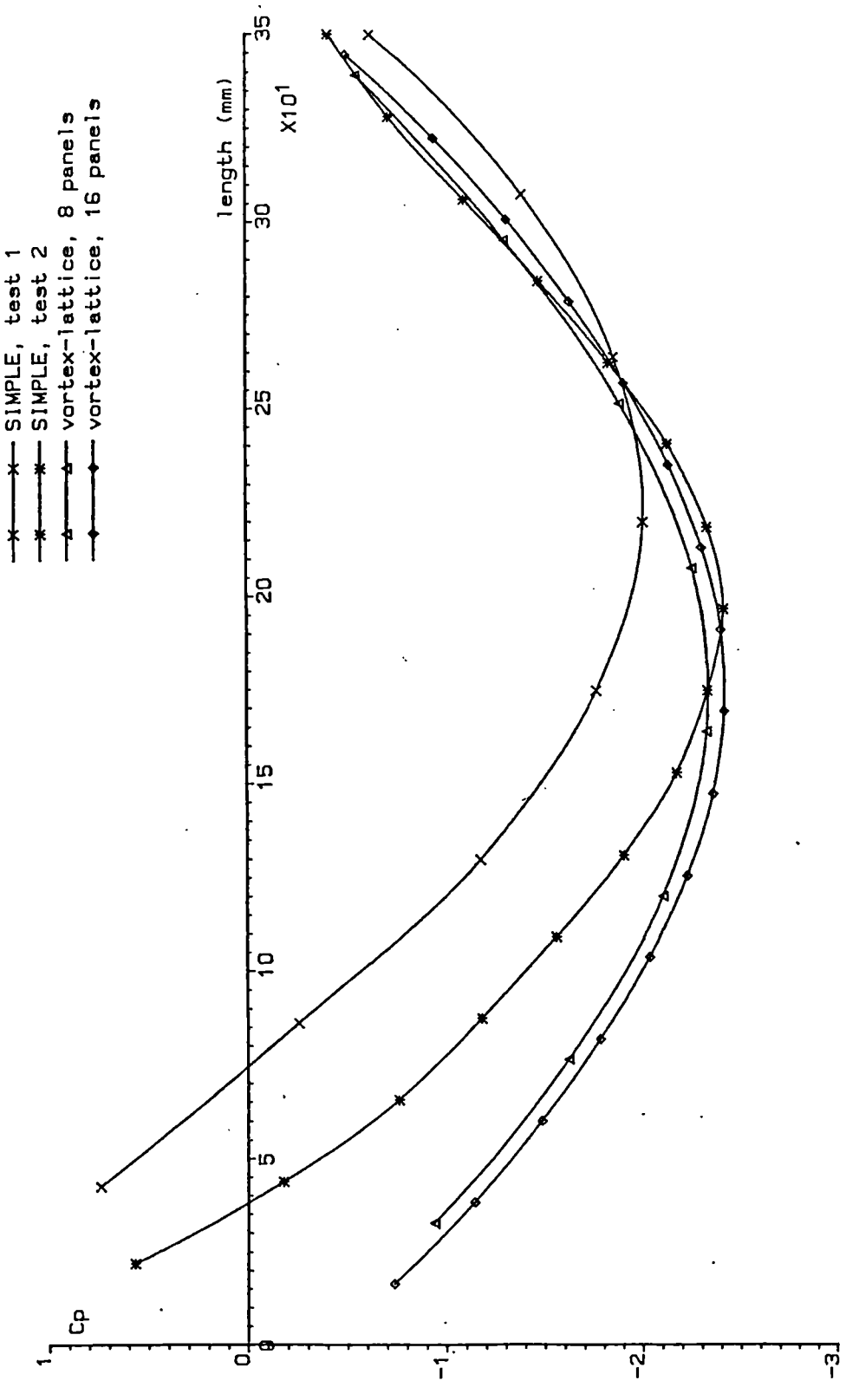

Figure A.4 Cp distribution

CHAPTER 6

Wind tunnel tests on an eliptic paraboloid

Contents:

In this chapter wind tunnel tests on an open sided shallow eliptic paraboloid shell are described, and the results are discussed. The characteristics of the wind tunnel and instrumentation are briefly discussed together with the computing equipment, calibration methods for transducers, velocity profiles (laminar and turbulent boundary layers) and the tunnel static pressure calibration. To provide a comparison with the theoretical results obtained in chapter 5 for the eliptic paraboloid open sided shell, an appropriate model was built and tested in an industrial wind tunnel. A description of the model construction and pressure tapping is given. The tests on the shell, in the longitudinal and the traverse directions, submerged in a uniform flow and in a turbulent boundary layer are then described. The results for non-dimensional pressure coefficients are compared with the theoretical C_p values. The modified Hedman method is found to predict fairly well the pressure distribution on the shell in the uniform flow, except on the rearmost part where separation occurs.

6.1 Wind tunnel specification

The first wind tunnels were designed for testing aircraft models and many early tests conducted on building models were made in these tunnels. Since the 1960s, when theory and experimental practice were sufficiently developed to allow for a new appreciation of the problems of wind loading

on structures, purpose designed industrial wind tunnels have been built.

The model was tested in an industrial wind tunnel at the City University Aeronautics Department. Four basic parts can be distinguished in the wind tunnel:

1. A duct to control the passage of the air through the test section, where the model is mounted. The City University tunnel is of closed, vertical, single return type. In this type the air follows a continuous path in the vertical plane defined by the wind tunnel walls, as shown diagramatically in figure 6.1. The test section is enclosed by solid boundaries (closed test section).
2. A drive system to move the air through the duct. In the tunnel under consideration the drive system consists of two fans located as far as possible from the working section.
3. A model of the test object, which is usually a reduced-scale model, and
4. Instrumentation, which may either be quite simple such as a manometer to measure pressure, or extremely complex, such as modern pressure transducers fitted into scanivalves and feeding output to a relatively large digital computer.

The cross-sectional area of the wind tunnel is a very important parameter, as it defines the maximum size of models which can be tested in the tunnel. Any model placed in a wind tunnel should not be greatly

influenced by the constraining effects of the tunnel walls. Hunt suggested [reference 6.5 in 92], that for the most common scale models of buildings, the optimum industrial aerodynamic tunnel should have a working section of about 1.5 - 2 m by 2 - 3 m. The working section of the City University tunnel being 1.5 x 3 m lies in this range.

The main objective of the test conducted on the eliptic shell roof was to establish pressure coefficient distributions. Therefore, to obtain the best results, the air speeds chosen for the purpose of the tests were in the upper range of safe air speeds obtainable in this tunnel. They varied from 12 m/s to 21 m/s.

The model was tested under two different conditions:

1. In approximately uniform flow; the floor upstream was left smooth and the shell was situated above the natural boundary layer. These conditions were created in order to match as closely as possible the assumptions of the theoretical analysis.
2. In a turbulent boundary layer, which was generated by expanded polystyrene cubes 50 x 50 x 50 mm thick placed upstream of the model. However, to generate a boundary layer of sufficient depth for practical purposes using roughness alone would require a test section length of approximately 28 m [39].

   Hence, in order to accelerate the growth of a uniform boundary layer by prompting early separation and ensuring mixing of the flow, a specially shaped barrier

was placed across the floor of the wind tunnel [see figure 6.2]. The complete set up to create the turbulent boundary layer had been already available in the Aeronautics Department [211]. The model was tested in this simulated atmospheric boundary layer in order to compare the potential flow solution with more realistic wind action.

6.2 Instrumentation

Before the model was placed in the wind tunnel, certain flow characteristics: such as distribution of static pressure and variation in velocity, were determined. Subsequently the roof model was submerged in an air stream to establish the forces acting on it. In all cases interest was centred on determining the total and static pressures; velocities when required being calculated from these two pressure values. The pressures were measured by a combination of the following devices:

1. Pitot and Pitot-static tubes,
2. inclined manometer,
3. Furness manometer and
4. scani-valve system.

Pitot-static tubes (see figure 6.3)

A Pitot-static tube is a device used for determining the total head and the static pressure of an airstream when connected to pressure measuring equipment like a manometer or scani-valve. A Pitot tube is employed to measure only the total pressure.

When a Pitot-static tube (figure 6.3) is placed in an air stream and points A and B are connected to a pressure measuring device, the pressure thus measured gives:

At point A $p_A = p + \frac{1}{2} q^2 \rho_a$ (total pressure, or very often, total pressure minus atmospheric pressure),

At point B $p_B = p$ (static pressure, or very often static minus atmospheric pressure)

where

p is the static pressure

q is the stream velocity, and

ρ_a is the air density

The difference between these two pressure gives:

$$p_A - p_B = \frac{1}{2} q^2 \rho_a$$

Hence the velocity can be found to be:

$$q = \sqrt{\frac{2(p_A - p_B)}{\rho_a}} \qquad 6.1$$

Inclined manometer

An inclined manometer is built from a series of straight glass-tubing of the same diameter connected by tubing at the bottom. The tubing is filled with a fluid, and the difference in fluid height, between the reference tube and the tube connected to a device such as a Pitot tube, is measured usually by an attached scale. The density or specific gravity of the fluid is known, and thus the change in pressure is calculated as follows:

$$\Delta p = \Delta h \times g \times \rho_m \times \sin \alpha \qquad 6.2$$

where

Δh is the difference in height of fluid between the reference tube and the tube in question,

ρ_m is the density of manometer fluid,

g 9.81 m/s (in SI units) and

α is the angle between the horizontal and the manometer tubes.

With the advent of digital-data-acquisition systems the use of manometers has declined. However, there are still a few cases where a manometer is useful. An example of this was the test which was conducted in order to establish the thickness of the natural boundary layer at the working section of the wind tunnel.

Furness manometer and scani-valve

A Furness manometer and a scani-valve both contain diaphragm type pressure transducers; devices which for the purpose of measurements turn physical input quantities such as pressure (or more often difference in pressure) into electrical output signals. Pressure transducers require a bridge power supply and the output-voltage varies with pressure. Their output (voltage) - input (pressure) relationship is predictable to a known degree of accuracy at specified environmental condition. Very often this relation is linear.

A Furness manometer is an example of equipment where a single transducer is used to measure only one difference in pressure at a time.

A series of diaphragm type pressure transducers are made to fit into scani-valves. The stepping motor of the scani-valve, which was used during the wind tunnel tests was connected to a single 48 port valve. The motor, by rotating one of the two ground plates, connected each input tube in sequence to a plenum and thus to the transducer. Through its control, the scani-valve was made to step to each inlet port and hold for a predetermined time and then step to the next port. The hold time, required to allow the plenum pressure to stabilize, was adjusted but had to be constant for each port. This time is a function of the tubing length and pressure.

6.3 Calibrations of transducers

When an inclined manometer is employed, a difference in pressure can be worked out directly from equation 6.2. Both the Furness manometer and the scani-valve require an additional operation to establish their characteristics i.e. the output-input relationship. During calibrations, a series of known pressures is applied, and the pressure and output voltage are recorded. These data are then fed into a curve-fitting routine to determine the calibration curve.

Furness manometer calibration

A Furness manometer can operate in different ranges. Its pressure transducer is fixed permanently in position and encased in a metal box. This makes it more stable and not easily influenced by small environmental changes. Therefore the calibration of the Furness manometer need be performed only once for a whole series of tests.

The Furness manometer calibration was carried out on the 30 mm range, the range to be used during the wind tunnel tests, using the Cassela manometer. The calibration equipment was arranged as shown in figure 6.4a. A series of pressures was applied by a syringe which was connected in parallel with the Cassela manometer and the Furness manometer. Both devices were arranged in such a way that they measured the difference between applied and atmospheric pressure. The differential pressure was expressed in terms of mm of water in the Cassela manometer, and in milivolts in the Furness manometer. Digital output was obtained from a d.c. voltometer connected to the Furness manometer. Both results were plotted to give the linear relationship between electrical output in milivolts and mm of water (see figure 6.4b). The relationship obtained, 17.53 mv/mm H_2O confirmed the previous results.

Setra transducer calibration

A Setra transducer, model 237, a low range sensor of .7 kN/m (.1 psid) to 35 kN/m (5 psid), was calibrated while mounted into the scani-valve.

The transducer had a flush mounting configuration to fit the scani-valve. The model 237 combines a rugged capacitance-type pressure sensing element and a high output electronic circuit in a small transducer to enable accurate low pressure measurements.

The transducer was mounted into the scani-valve, model D (see figure 6.5) and calibrated in the arrangement shown in

figure 6.7a and in the photograph of figure 6.6, under positive and negative pressures. The results were plotted on a graph to give an almost straight gradient of .0346 V/mm H_2O (see figure 6.7b).

The Setra transducer was found to be very sensitive, hence three calibrations were carried out before each series of tests and, additionally, a check was performed during each test. This was possible due to the special arrangement of pressure points on the manifold. Figure 6.7b shows one of the graphs obtained during calibration. It should be noted that the differences in the calibration ratio, from various calibrations were within 3.5%.

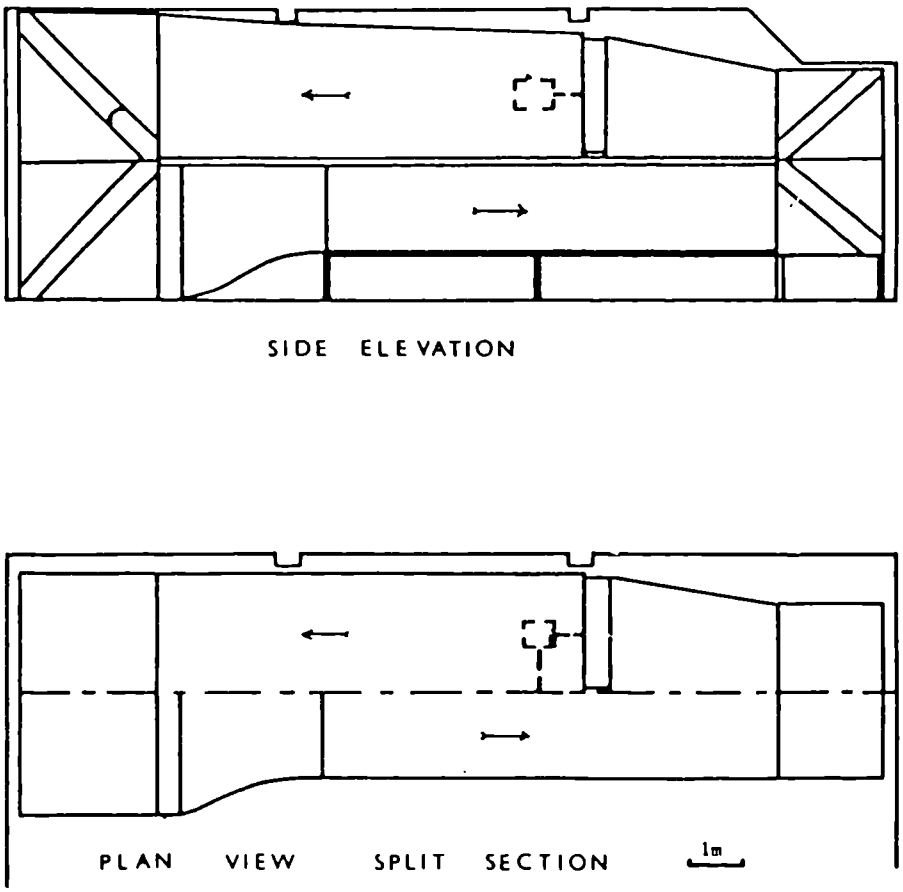

Wind tunnel layout.

Figure 6.1

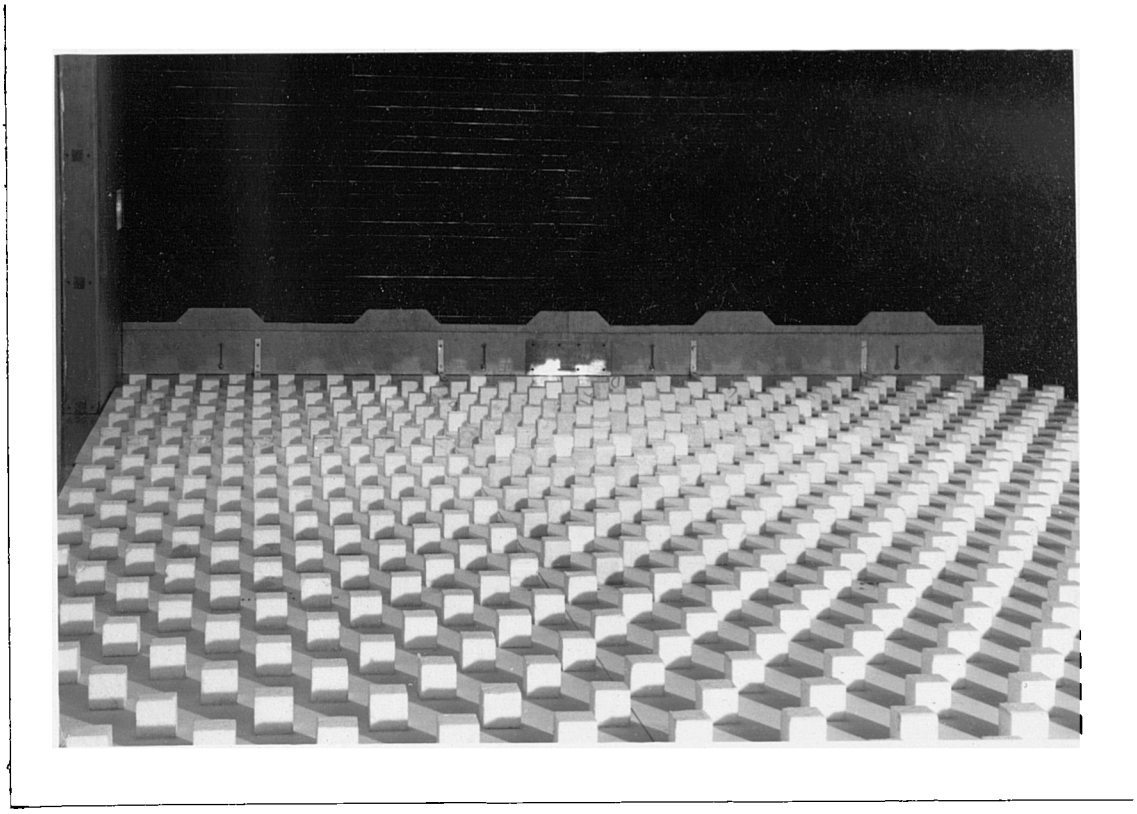

Figure 6.2

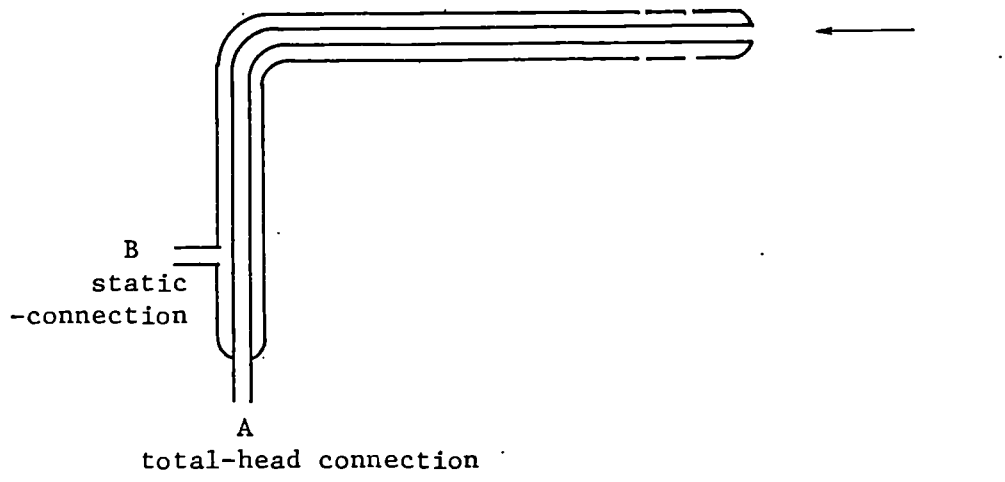

Figure 6.3

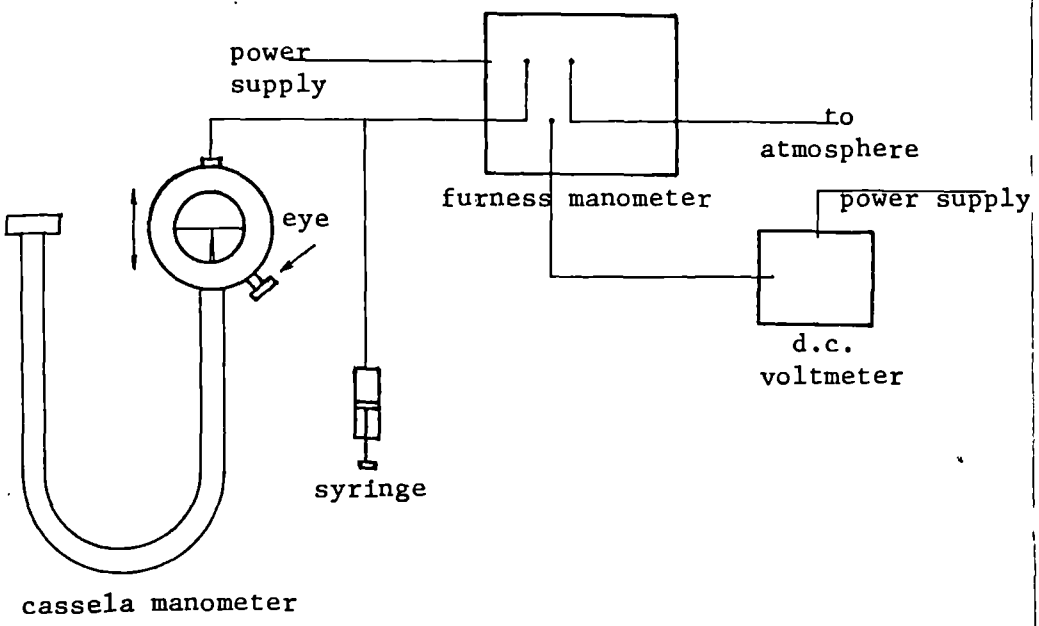

a.calibration equipment

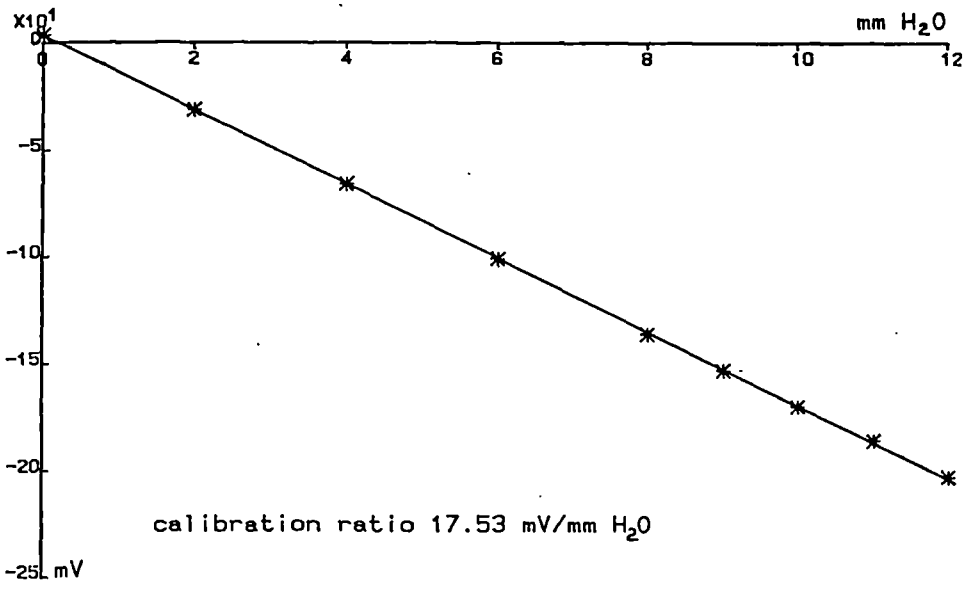

b.calibration plot

Figure 6.4 Furness manometer calibration

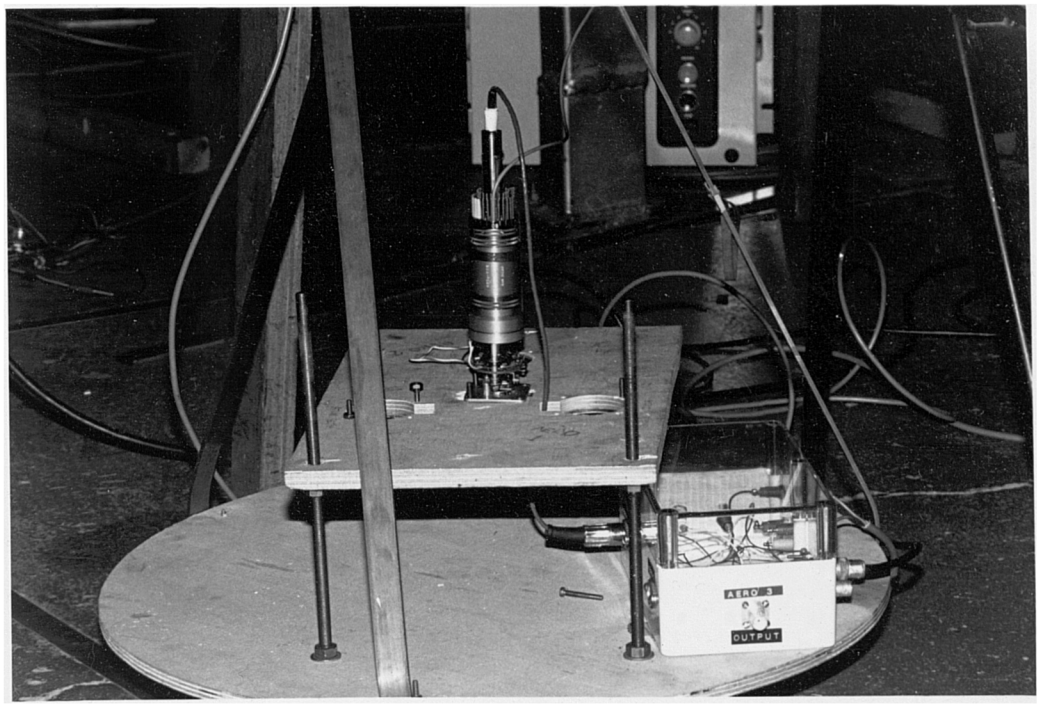

Figure 6.5

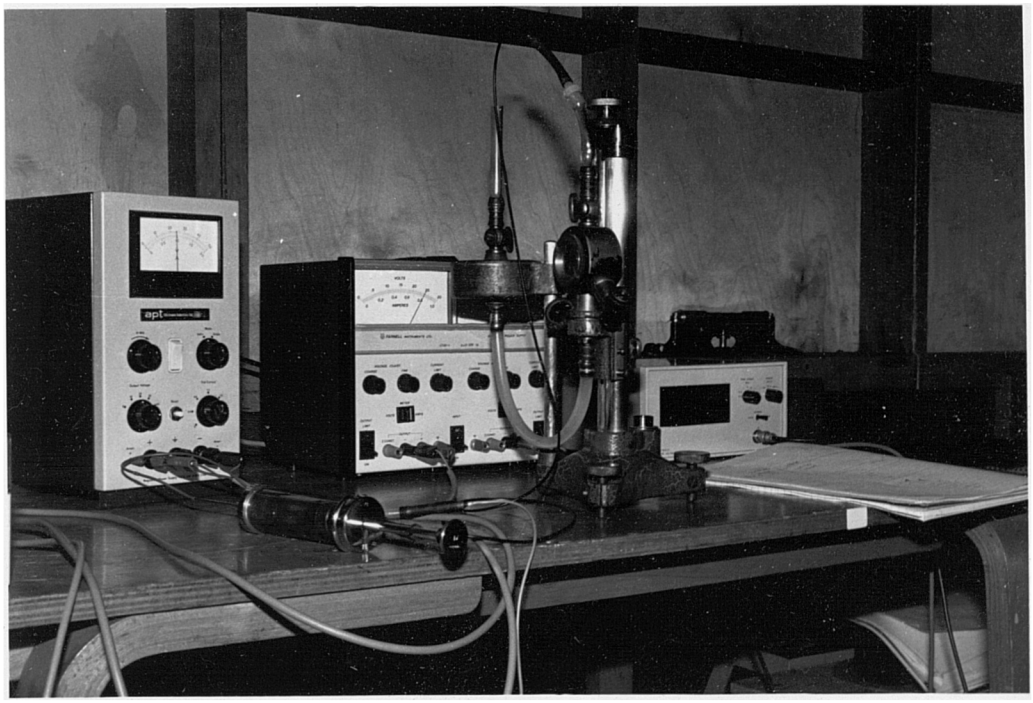

Figure 6.6

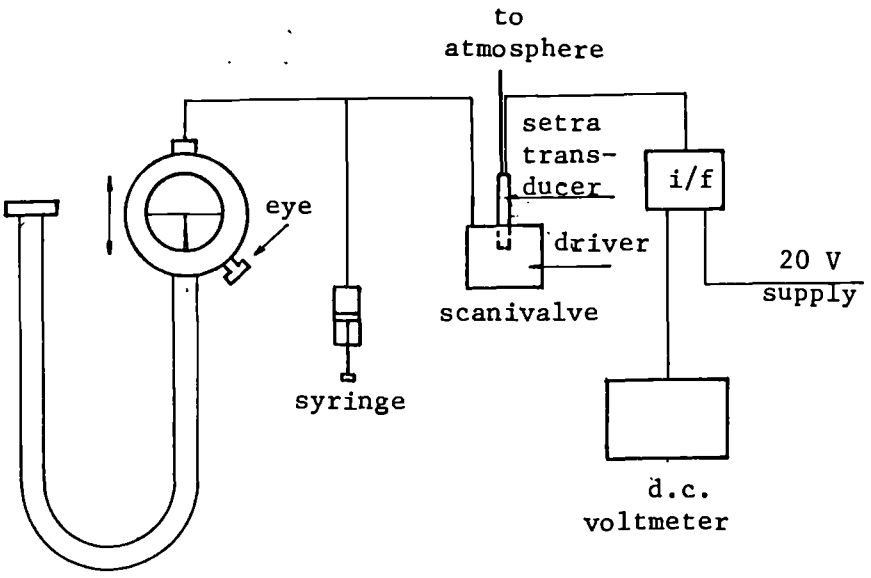

a.calibration equipment

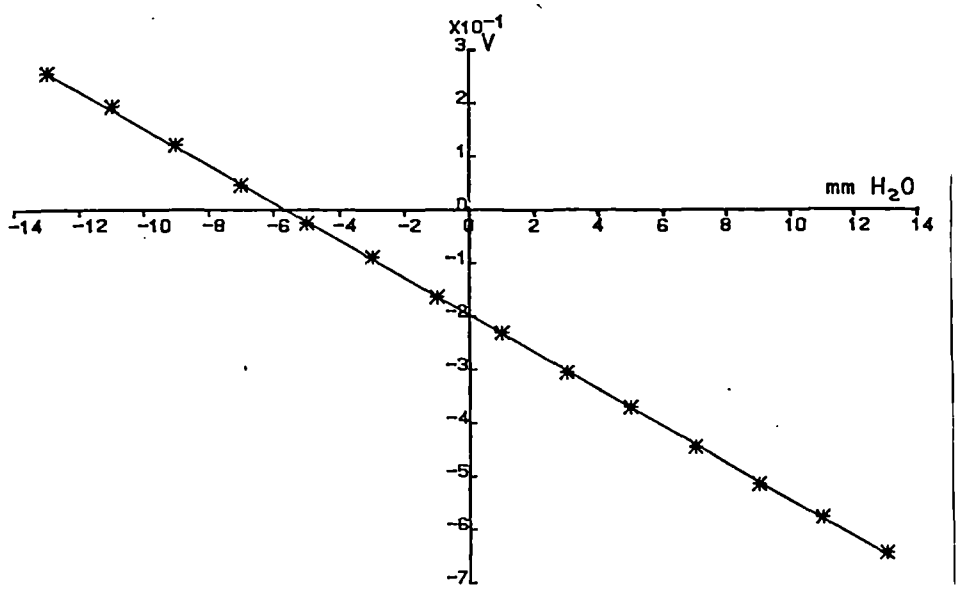

calibration ratio .0346 V/mm H_2O

b.calibration plot

Figure 6.7 Setra transducer calibration

6.4 Wind tunnel calibration

Before the model was placed and tested, the wind tunnel had to be calibrated. This consisted of two procedures:

1. investigation of velocity profile and
2. investigation of static pressure distribution

6.4.1 Velocity profile

a. Laminar boundary layer

The numerical analyses described in chapter 5 were concerned with structures submerged in a uniform air stream. Therefore in order to correlate the theoretical results with experimental, the model was tested in conditions as close as possible to those assumed in deriving the numerical solution.

In a wind tunnel, even without any roughness upstream (a smooth floor), the velocity profile is not uniform throughout the section. In the areas close to the walls and floor, laminar boundary layers will develop. In a tunnel with a working section 1.5 x 3 m and a model size 350 x 450 x 287 mm high placed in the centre, the boundary layer velocity gradient which develops due to the presence of vertical walls and the ceiling will be a long distance away from the shell. Only the thickness of the floor boundary layer will be of interest to us. Hence the following calibration was performed in order to establish that the lowest point of the shell, 21.8 cm above the floor level, was above the floor velocity gradient.

The test section entrance (upstream) was left empty (smooth floor) and a vertical rake of pitot tubes and, separately, a pitot-static tube were positioned on the floor of the working section where the structure was to be sited. Additionally, a pitot-static tube which is permanently fixed to the wall of the wind tunnel, 20 cm below the ceiling and about 5 m upstream from the centre of the working section was incorporated into the test to give the total and static pressure of the free stream. Accurate measurements of the vertical spacing of the pitot tubes on the rake were taken using a cathetometer, a vertically movable telescope. All pitot tube outlets, thirty of the rake and four of the pitot-static type, were connected to an adjustable-angle multiple manometer. The first and the last tube of the manometer were open to the atmosphere.

The tunnel was run at four different speeds: 11.4 m/s, 15.7 m/s, 19.5 m/s and 22.5 m/s (velocities obtained from the wall pitot-static tubes) and each time the heights of liquid in the manometer tubes were recorded. For each run the critical height, i.e. the height above which the velocity stays constant, was found to be approximately the same - 13 cm.

Velocities were obtained from equations 6.1 and 6.2 as follows:

$$u = \sqrt{\frac{2(p_A - p_B)}{\rho_a}}$$

where

ρ_a = 1.2256 kg/m (the density of air)

$\Delta P_a - \Delta P_B = k\ (\Delta h_a - \Delta h_B) \times g \times \rho_m \times \sin \alpha$

k = 25.4×10^{-3} (the constant for dimensional homogenity)

ρ_m = $.808 \times 10^3$ kg/m^3 (the density of fluid)

d = 15.9

hence

$$u = \sqrt{90.01 \times (\Delta h_A - \Delta h_B)} \qquad 6.3$$

An example of the velocity profile, the plot height against non-dimensional velocity (the ratio of velocity at height z to the free stream velocity recorded by the wall pitot-static tube), is given in figure 6.8. It can be seen that the lowest point of the shell is well above the floor laminar boundary layer. The natural floor boundary layer is very thin, approximately 100 mm. The free stream velocity at the working section is slightly higher than the reference velocity measured by the wall pitot-static tube; the ratio for four different wind tunnel speeds remained approximately constant at 1.05.

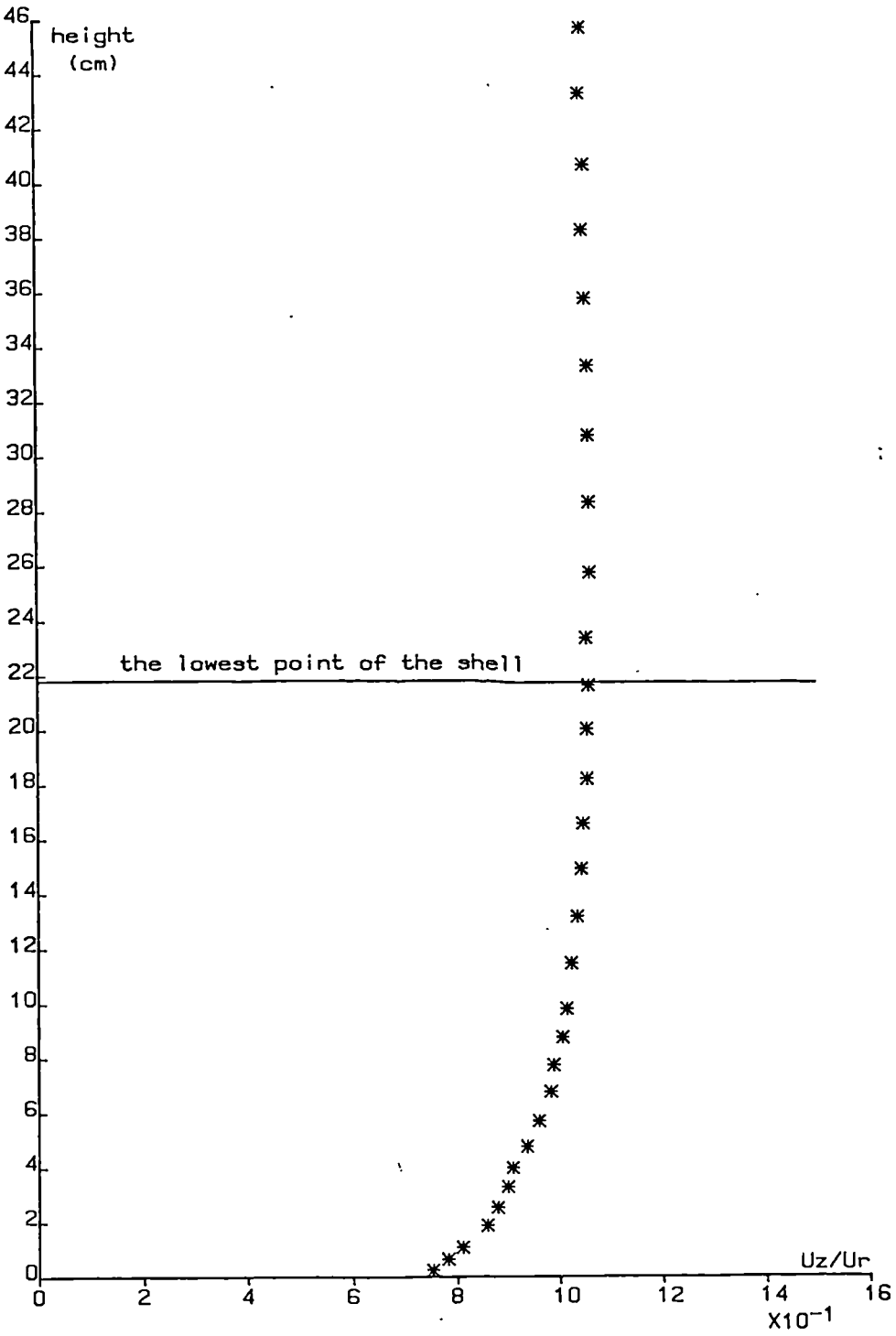

Figure 6.8 Velocity profile, 'smooth' floor

b. Turbulent boundary layer

The numerical analyses of chapter 5 were based on potential flow theory, hence the uniform flow is the closest approximation. But this does not prevent a comparison of the theoretical results for C_p distributions, with those obtained for a more realistic situation, namely pressure distributions on the shell submerged in a simulated atmospheric boundary layer in the wind tunnel.

In his paper 'The Nature of Wind', Harris [82] discusses a simplified approach to variations in the hourly mean wind speed with height in the atmospheric boundary layer. All terrains are divided, as a function of their roughness, into 3 categories:

A - an open terrain with very few obstacles

B - a terrain uniformly covered with obstacles 10 to 15 m in height, and

C - a terrain with large and irregular objects;

the power law exponent , a, and the gradient height, z_G, for each type are given with the velocity profile being assumed as defined by a simple power low of the form:

$$\frac{\bar{V}(z)}{\bar{V}_G} = \left(\frac{z}{z_G}\right)^a$$

where

$\bar{V}_G$ - is the mean velocity at the gradient height

$\bar{V}(z)$ - is the mean velocity at a point of height z above the ground level

For the purpose of this investigation, a turbulent boundary layer is deemed to be defined, when $\bar{V}_G$, z_G and a are known.

Due to large discrepancies between the theoretical assumptions of the numerical analysis and the test conditions in a turbulent boundary layer, a thorough investigation, involving testing of the model in different types of simulated terrain was not undertaken. The tests conducted in the turbulent boundary layer were carried out only to give some indication of the order of errors resulting from simplifying the problem by assuming potential flow.

Bearing in mind the above, terrain B, which is a middle one in terms of ground roughness conditions, was chosen. This type of terrain represents areas such as residential suburbs, small towns, woodland and shrub, small fields with bushes, tree and hedges. The terrain was simulated, as described earlier, by expanded polystyrene cubes and a specially shaped barrier (this set up had been previously used and checked in this wind tunnel).

As for the previous laminar flow measurements, the rake of pitot tubes and the separate pitot-static tube were placed in the working section of the wind tunnel, and their heights were measured. This time, however, the tubes were connected to a scanivalve which had 48 ports. The arrangement of manifolds is shown in figure 6.9. One pressure point, here the total pressure outlet from the pitot-static tube fixed

to the wall of the tunnel, was connected in parallel with the furness manometer and the scanivalve system to enable recalibration of the setra transducer during tests and to measure instantaneous values of free stream velocity, which was to be used as a reference value. The setra transducer was found to be very sensitive. Hence in order to eliminate any shift in calibration, after every 6 or 7 pressure points, one port on the manifold was left open to the atmospheric pressure. The eventual shift was assumed to vary linearly. This arrangement of manifolds enabled also a check on whether the scanivalve stepped properly.

A scanivalve can be controlled manually, i.e. stepping, homing and taking reading of electrical output from the transducer can be performed by an operator, or all those functions can be done by a computer equipped with an analog to digital and digital to analog converter. Before testing, all electrical connections between various devices and mechanical fixings of tubes were checked by running the wind tunnel and operating the scanivalve driver manually; taking readings from a digital d.c. meter. During the actual runs the computer facility Gen-Rad, on a PDP-11, was used; the arrangement of equipment is shown in figure 6.10. The existing program had to be modified to deal with this case. The flow chart of the modified program is shown in figure 6.11.

It should be noted that although during the tests rms (root mean square) values were calculated, they were only

approximate values as proper calibration of the frequency response was not performed.

The aim of the turbulent boundary layer calibration was to establish whether the power law exponent, a, and the scale gradient, z_G, complied with the values given in [82] for the terrain type B in the range of velocities under consideration. Four tests were carried out under different velocities: 20.4 m/s, 18.8 m/s, 17.4 m/s and 14.4 m/s.

In order to find a and z_G, the power law (equation 6.4) is rewritten in a different form. By taking logs of both sides of equation 6.4 and rearranging, the following equation is obtained:

$$\lg z = \frac{1}{a} \lg \bar{V} + (\lg z_G - \frac{1}{a} \lg V_G) \qquad 6.5$$

The above equation represents a straight line with slope 1/a and intersection $\lg z_G - \frac{1}{a} \lg V_G$.

Values of velocity were obtained from equation 6.1 as follows:

$$\bar{V} = \sqrt{\frac{2(\Delta P_A - \Delta P_B)}{\rho_a}}$$

where

$$\Delta P_A - \Delta P_B = \frac{S_t - S_s}{C_t} \times g \times \rho_m \times k$$

$\rho_m = 10^3$ kg/m^3

$k = 10^{-3}$ constant for dimensional homogenity

$g = 9.81$

C_t - is the calibration factor of the transducer, approx., C_t = .00346 V/mm H_2O (the precise value is obtained from calibrating the transducer against the furness manometer before each run)

S_t - is the mean value in volts of the signal obtained either from the pitot tube of the rake, or from the total outlet of the pitot-static tube, when V_G is calculated.

S_s - is the value of signal obtained from the static outlet of the pitot-static tube; either from the tube fixed to the wall, when free stream velocity V_G is calculated, or from the tube placed on the floor of the testing section.

hence

$$\bar{V} = \sqrt{\frac{16.008(S_t - S_s)}{C_t}} \qquad 6.6$$

The values of log (z) and log (V) for the thirty rake tubes were plotted on graphs for each case separately. As an example figure 6.12 shows the results obtained from the run with 14.4 m/s free stream velocity. They do not represent as a whole (even approximately) one straight line. But it can be noticed that points with $z \geq 18.4$ cm (the lowest point of the shell is 21.3 cm) tend to form a straight line from which a and z_G can be obtained. Figure 6.13 shows the velocity profile for the same case. The theoretical results based on equation 6.4, with a and z_G, from figure 6.12, are superimposed on the experimental data. Values of a and z_G obtained from the runs with different free stream velocity

varied slightly; the discrepancies however were fairly small. For further application their average values were employed, namely a = .24 and z_G = .95 m. The values given in [82], describing the terrain type B are: a = .28 and z_G = 430 m, and for terrain A: a = .16 and z_G = 300 m. From the above we can conclude that the terrain simulated in the wind tunnel is of a type between terrain A (open terrain with very few obstacles) and B: (being closer to B) and the scale is approximately 1:450.

It was not of primary importance to scale properly the terrain type B. The results for wind loading on the shell submerged in the turbulent boundary layer were to be used to give some indication of the influence of turbulences present in the flow on the pressure coefficient distributions for the open sided roof. Therefore no further work aimed at improving the velocity profile was carried out.

6.4.2 Static pressure

When a Pitot-static tube is situated next to a model in the working section of the wind tunnel, the value of static pressure measured is influenced by the disturbance velocity (V_y or V_z). This means that $p + \frac{1}{2} V_y^2 \rho_a - p_{atm}$ (or $p + \frac{1}{2} V_z^2 \rho_a - p_{atm}$) is measured (rather than $p_{stat} - p_{atm}$).

In order to eliminate this discrepancy and to account for any static pressure variation caused by the presence of the model, calibration of the working section is essential. This is accomplished by running the tunnel at various

speeds, while measuring the static pressure both at the place to be occupied by the model and at a long distance away, where the presence of the model should not influence the static pressure.

Separate calibrations were performed for the uniform flow and the turbulent boundary layer, as the presence of obstacles (cubes and the barrier) influences the static pressure distribution in the wind tunnel. The tunnel was run at different speeds, and the values of static pressure were measured using the arrangement shown in figure 6.10. The static outlet of the pitot-static tube fixed to the wall was used as the reference pressure. Then the values $p_{statfloor} - p_{atm}$ (p_{sf}) were plotted against $p_{statwall} - p_{atm}$ (p_{sw}) to give approximately a straight line (see figure 6.14).

Location on Manifold	Pressure pipe identification	Location on Manifold	Pressure point identification
8	wall,total pres	29	18
9	atm	30	atm
10	1	31	19
11	2	32	20
12	3	33	21
13	4	34	22
14	5	35	22
15	6	36	24
16	atm	37	atm
17	7	38	25
18	8	39	26
19	9	40	27
20	10	41	28
21	11	42	28
22	12	43	30
23	atm	44	atm
24	13	45	wall static pres.
25	14	46	floor, static pres
26	15	47	floor, total pres
27	16	48	atm
28	17		

Pressure pipes 1 to 30 are connected to the rake

Figure 6.9

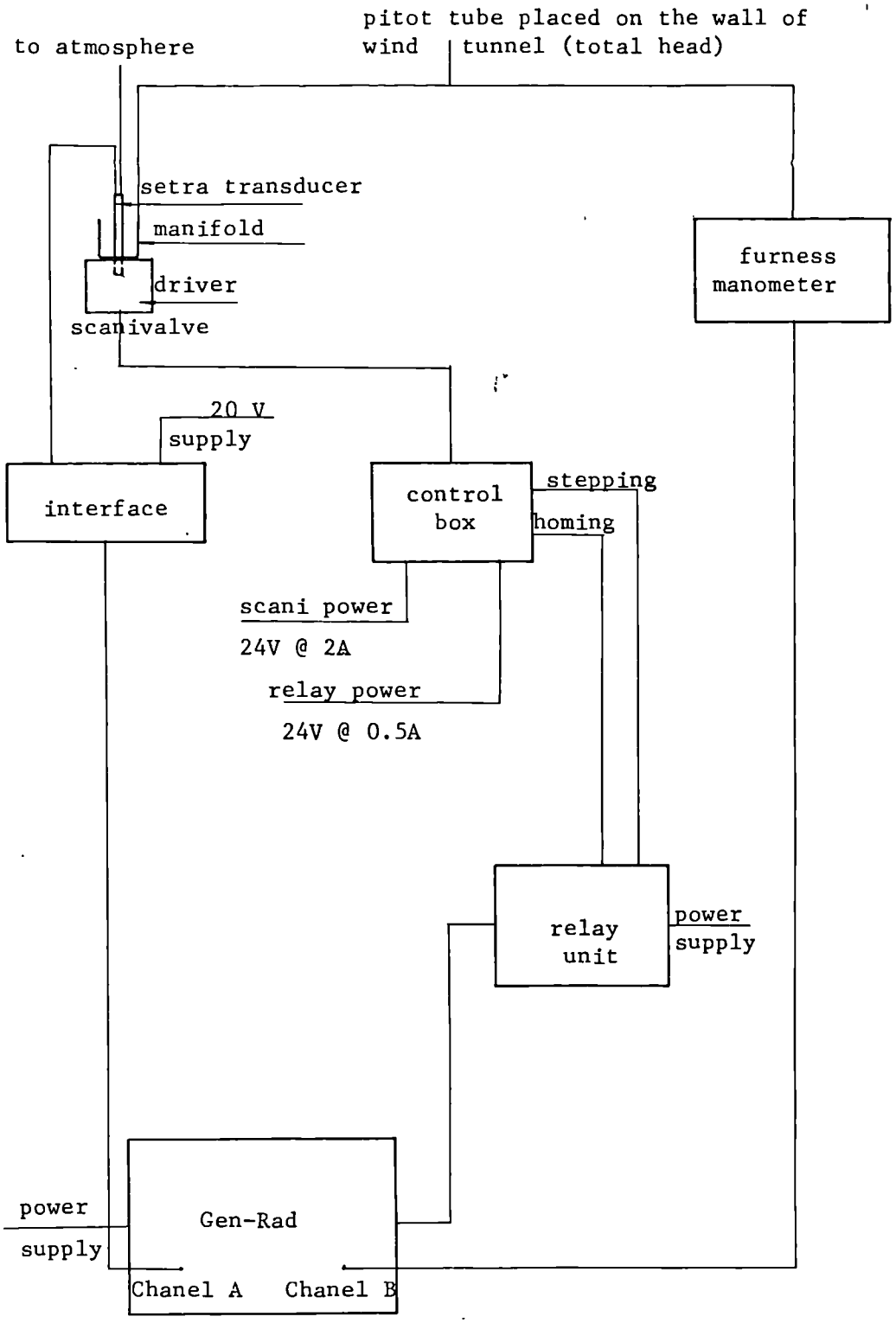
pitot tube placed on the wall of
wind tunnel (total head)
to atmosphere
setra transducer
manifold
driver
scanivalve
furness
manometer
20 V
supply
interface
control
box
stepping
homing
scani power
24V @ 2A
relay power
24V @ 0.5A
relay
unit
power
supply
power
supply
Gen-Rad
Chanel A
Chanel B

Figure 6.10

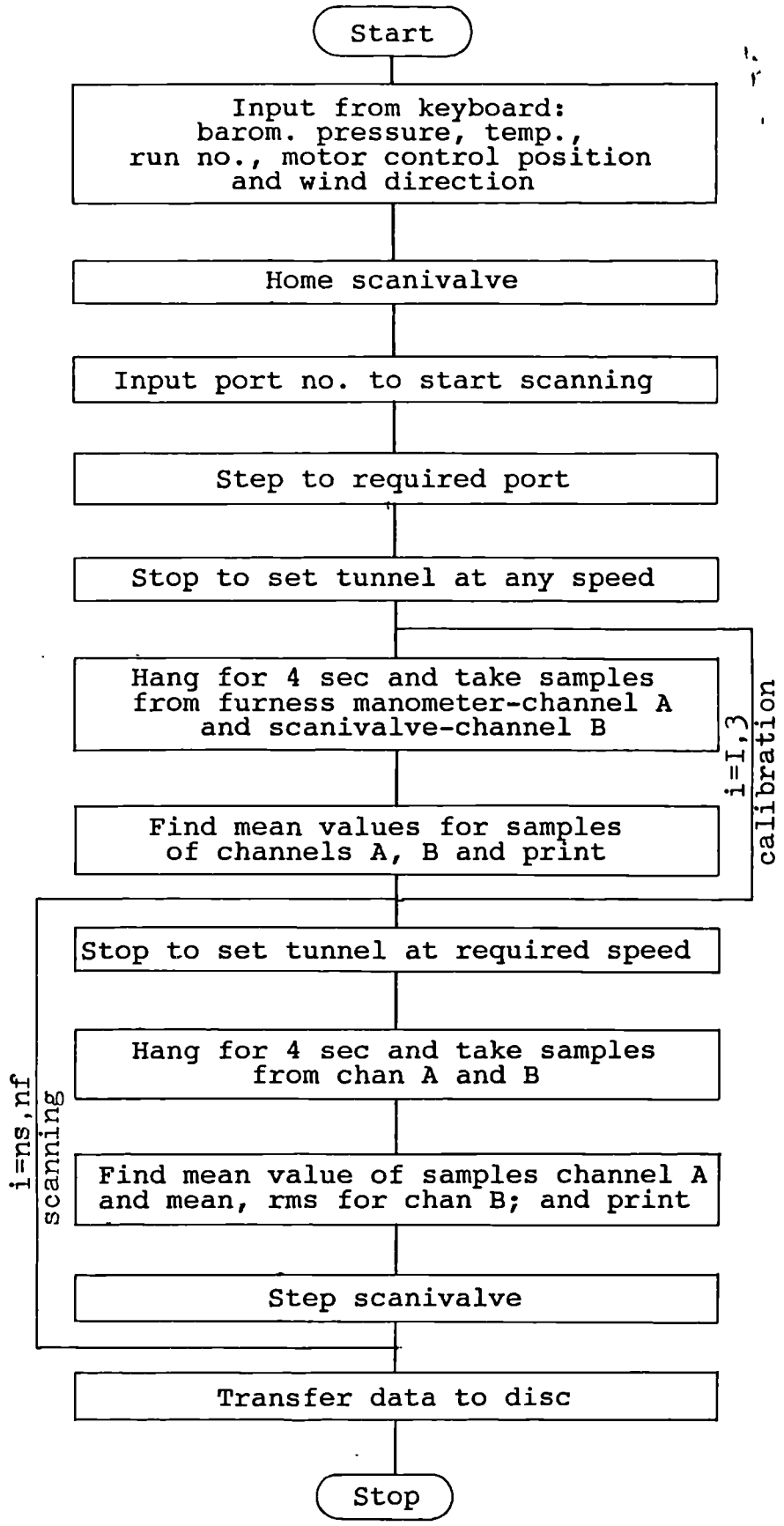
Start
Input from keyboard:
barom. pressure, temp.,
run no., motor control position
and wind direction
Home scanivalve
Input port no. to start scanning
Step to required port
Stop to set tunnel at any speed
Hang for 4 sec and take samples
from furness manometer-channel A
and scanivalve-channel B
Find mean values for samples
of channels A, B and print
i=1,3
calibration
Stop to set tunnel at required speed
Hang for 4 sec and take samples
from chan A and B
Find mean value of samples channel A
and mean, rms for chan B; and print
Step scanivalve
i=ns,nf
scanning
Transfer data to disc
Stop

Figure 6.11

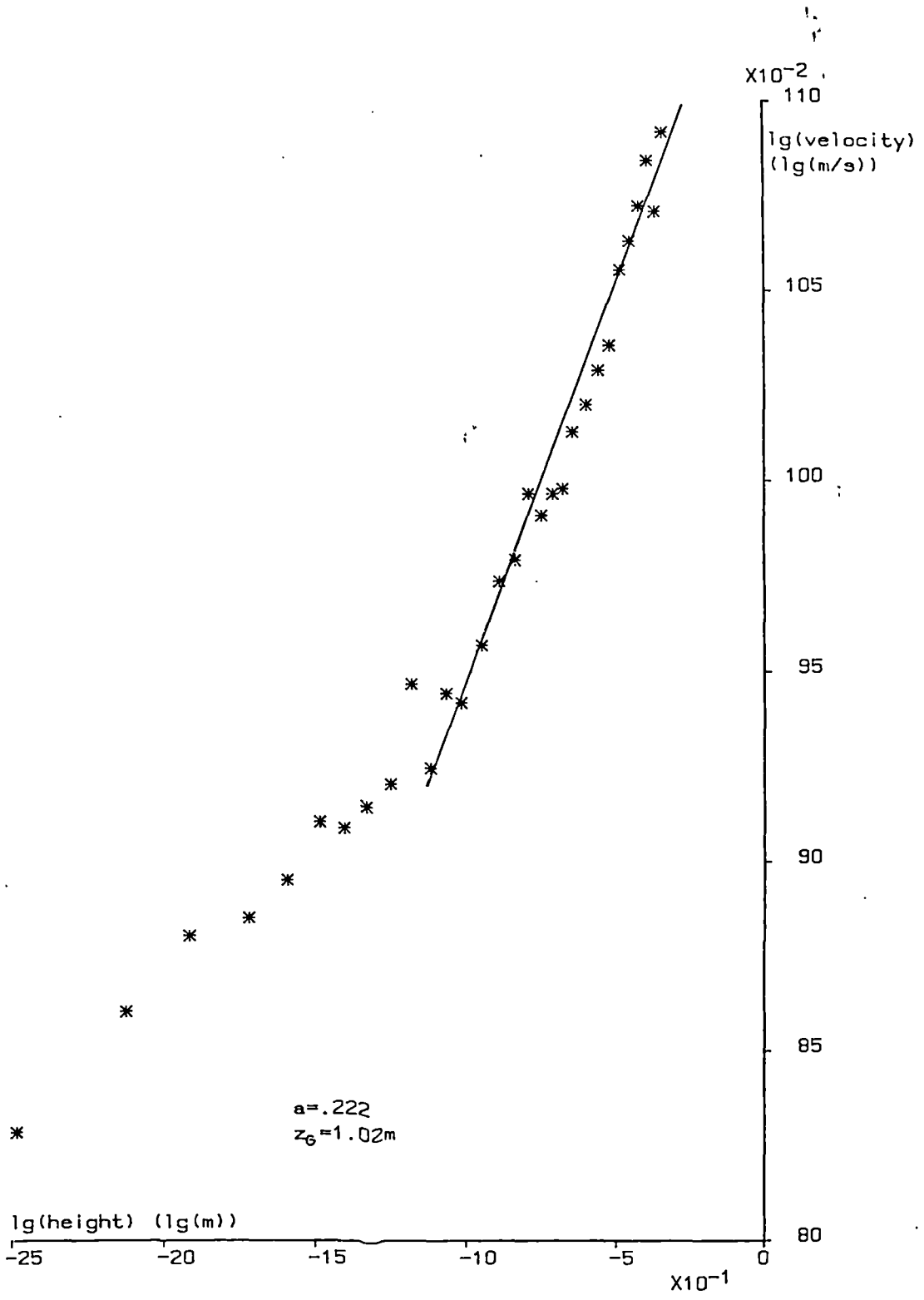

Figure 6.12 Turbulent boundary layer, the plot lg(z) against lg(V)

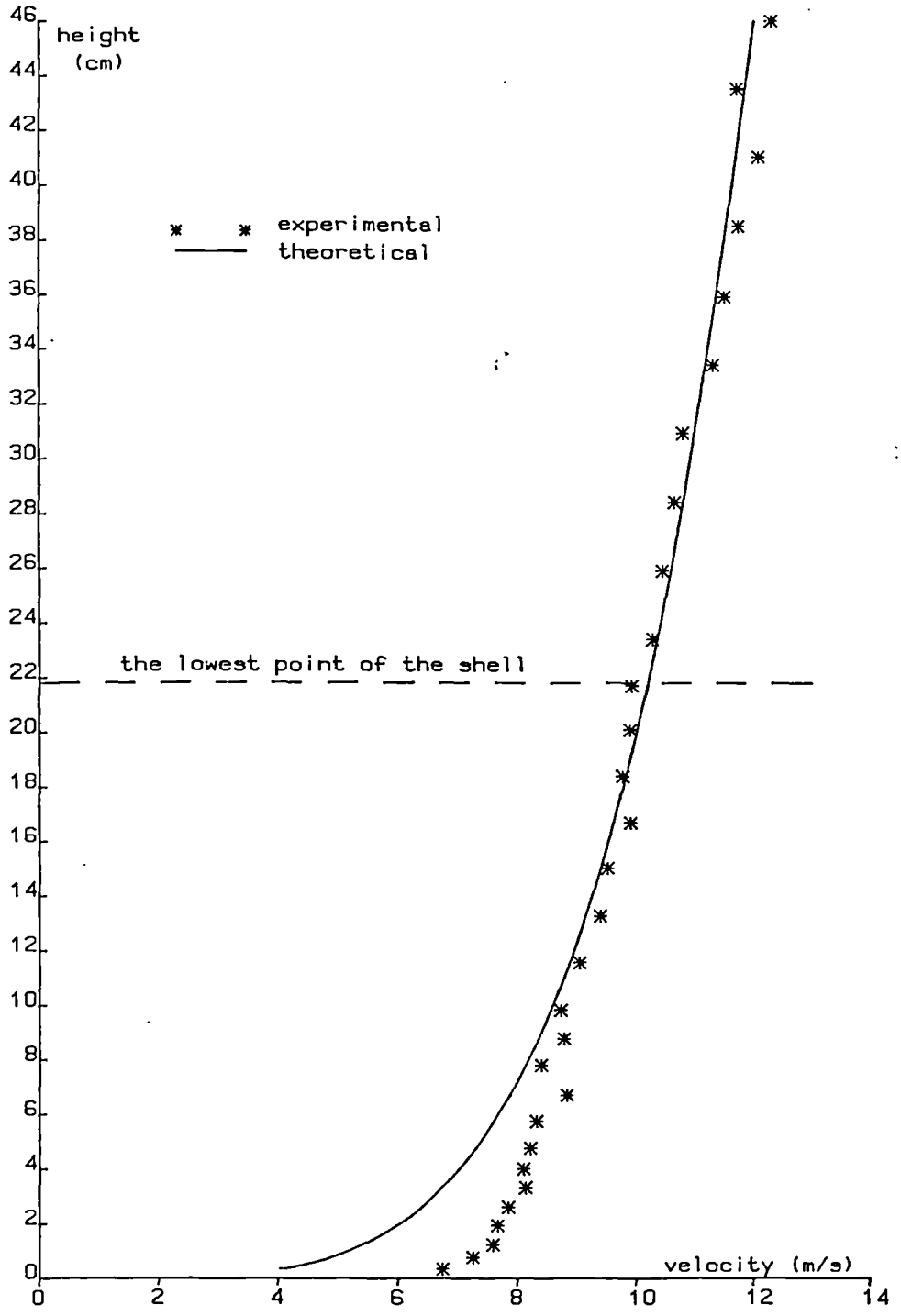

Figure 6.13 Turbulent boundary layer, velocity profile

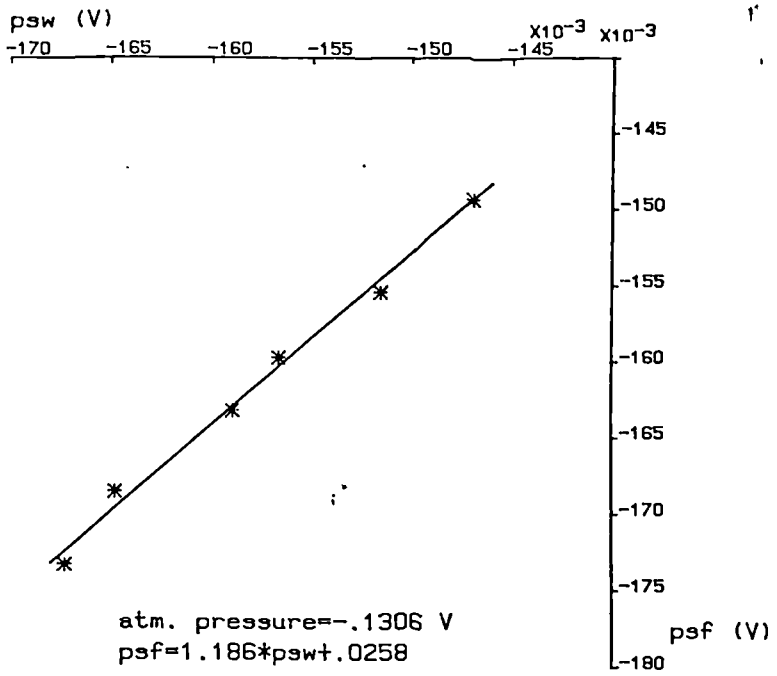

a.uniform flow

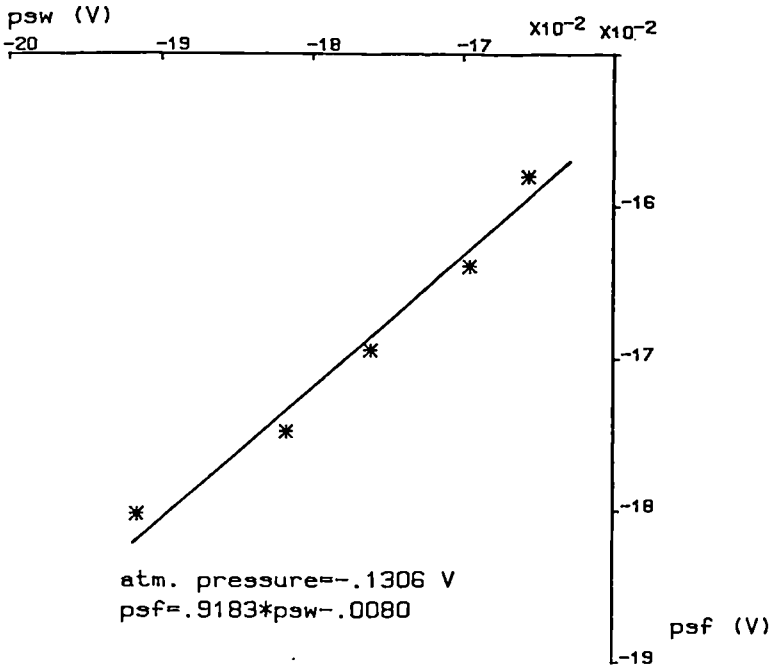

b.turbulent flow

Figure 6.14 Static pressure calibration

6.5 Model

The model, a general view of which is shown in the photograph of figure 6.15, was constructed from an aluminium shell supported on four aluminium rods fixed to a steel base. The shell was of eliptic paraboloid shape, 2 mm thick, 450 x 350 mm in plan, with rises of 12.5 mm and 56.5 mm in the x and the y directions respectively (see figure 6.22). In each corner of the shell a 7 mm diameter hole was drilled to allow for supporting bars (see figure 6.21).

On the surface of the shell lines were drawn dividing the shell into 36 panels (6 x 6), of equal sizes in the xy plane. On each panel the positions of two control points were marked (one for the longitudinal and one for transverse wind direction) (see figure 6.20) to coincide with those of the collocation points defined by the horseshoe vortex-lattice method. A total of 72 small holes were drilled as marked on the shell. The size of the holes was chosen to allow for close fitting brass tubes, approximately 19 mm long and of 1.5 mm external diameter (1.0 mm internal diameter). The brass tubes were fixed into the holes and additionally glued by means of Superglue, with the ends protruding on the concave side of the shell (see picture in figure 6.16). On each of the brass tube tips, a plastic tube of length 1.1 m was firmly positioned and then attached to the underside of the shell in such a way that half of the plastic tubes were gathered in each of two opposite corners (see figure 6.17).

The aluminium shell was supported on four 10 mm diameter aluminium rods which were fixed by means of steel collars to the steel base plate 510 x 410 x 8 mm thick (see figure 6.18). The collars were screwed down to the plate. The collar-rod connections were such that in the final stage, vertical adjustments of up to 5 mm could be made by means of small screws. The top 15 mm of the 4 rods were filed off to 7 mm diameter, to ensure the proper positioning of the shell. When the shell was threaded on to its supports, and permanently fixed by means of Superglue, the protruding parts of the rods were filed off to the shell surface (see figure 6.19). The top surface of the model was then made smooth and sprayed with a matt aerosol paint.

The base plate was designed to prevent uplifting of the model, when placed in the wind tunnel, under the most severe conditions, and to stabilise the entire model.

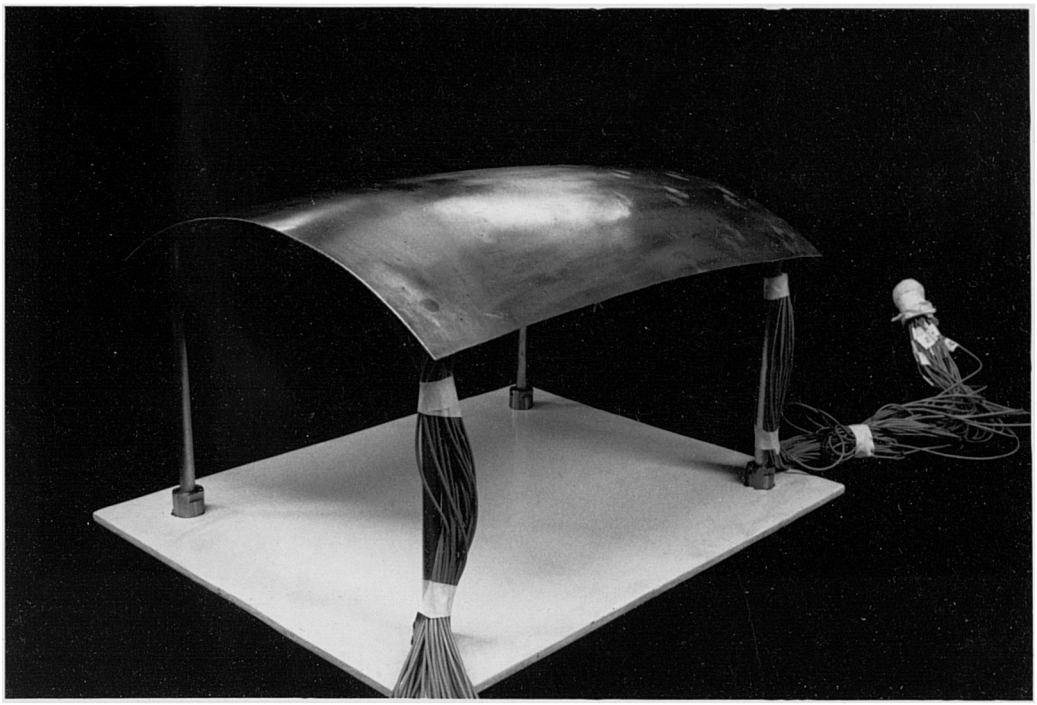

Figure 6.15

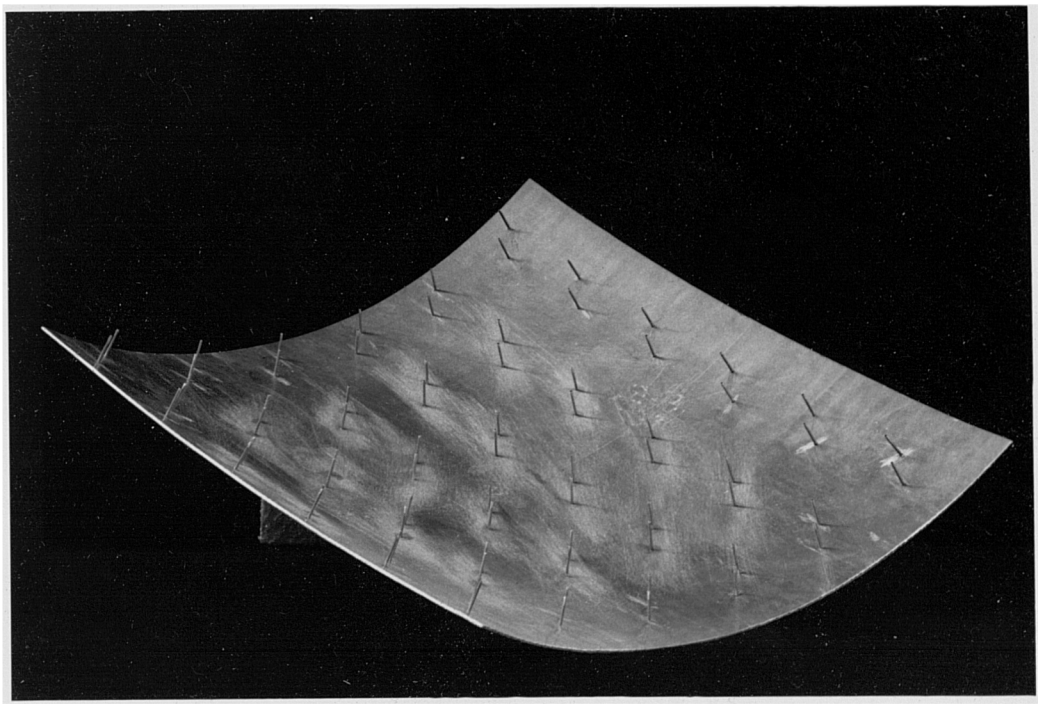

Figure 6.16

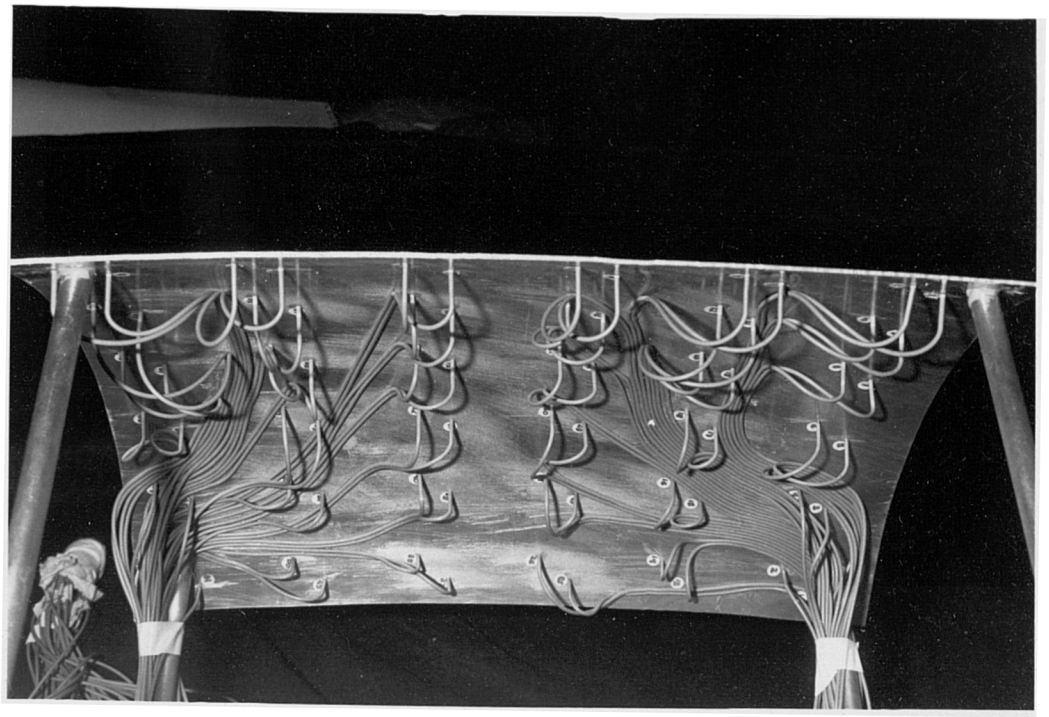

Figure 6.17

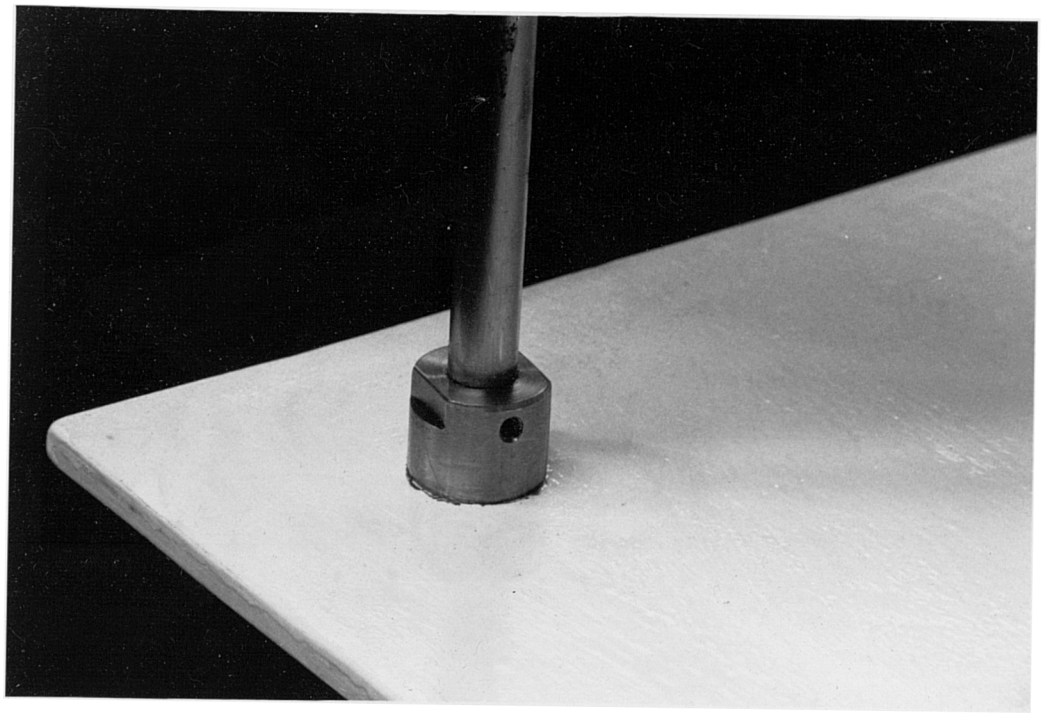

Figure 6.18

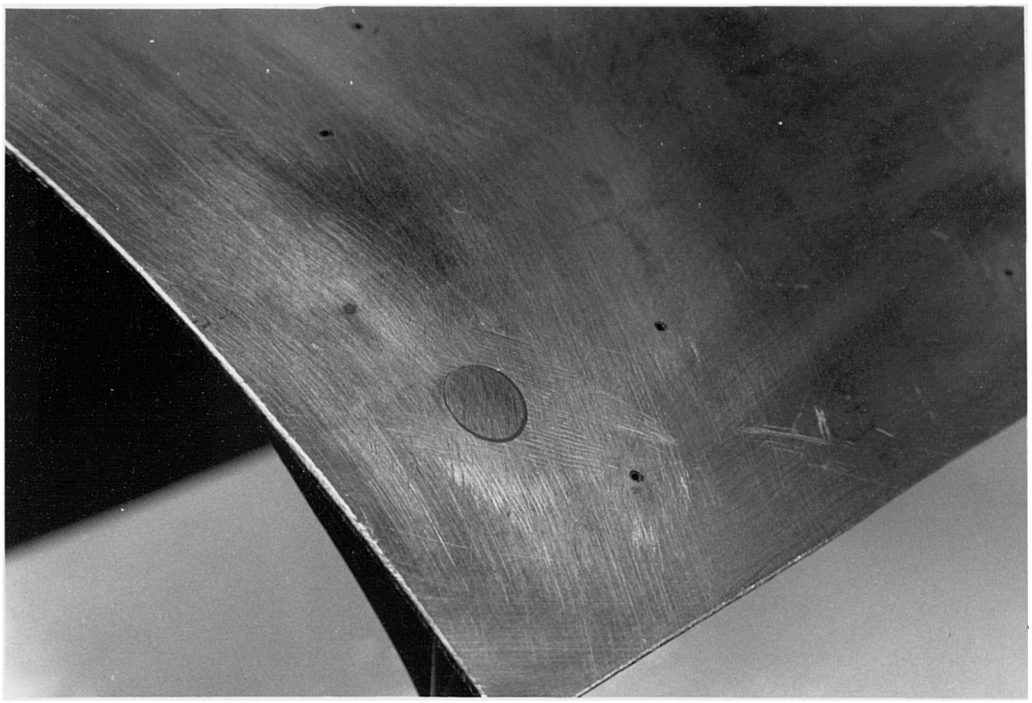

Figure 6.19

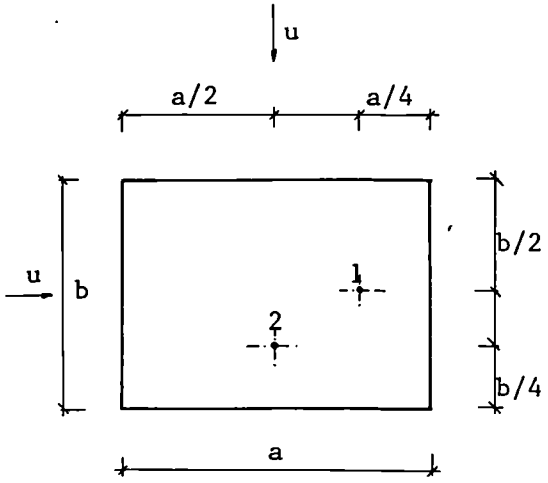

Figure 6.20

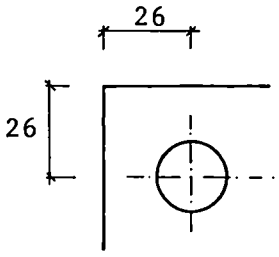

Figure 6.21

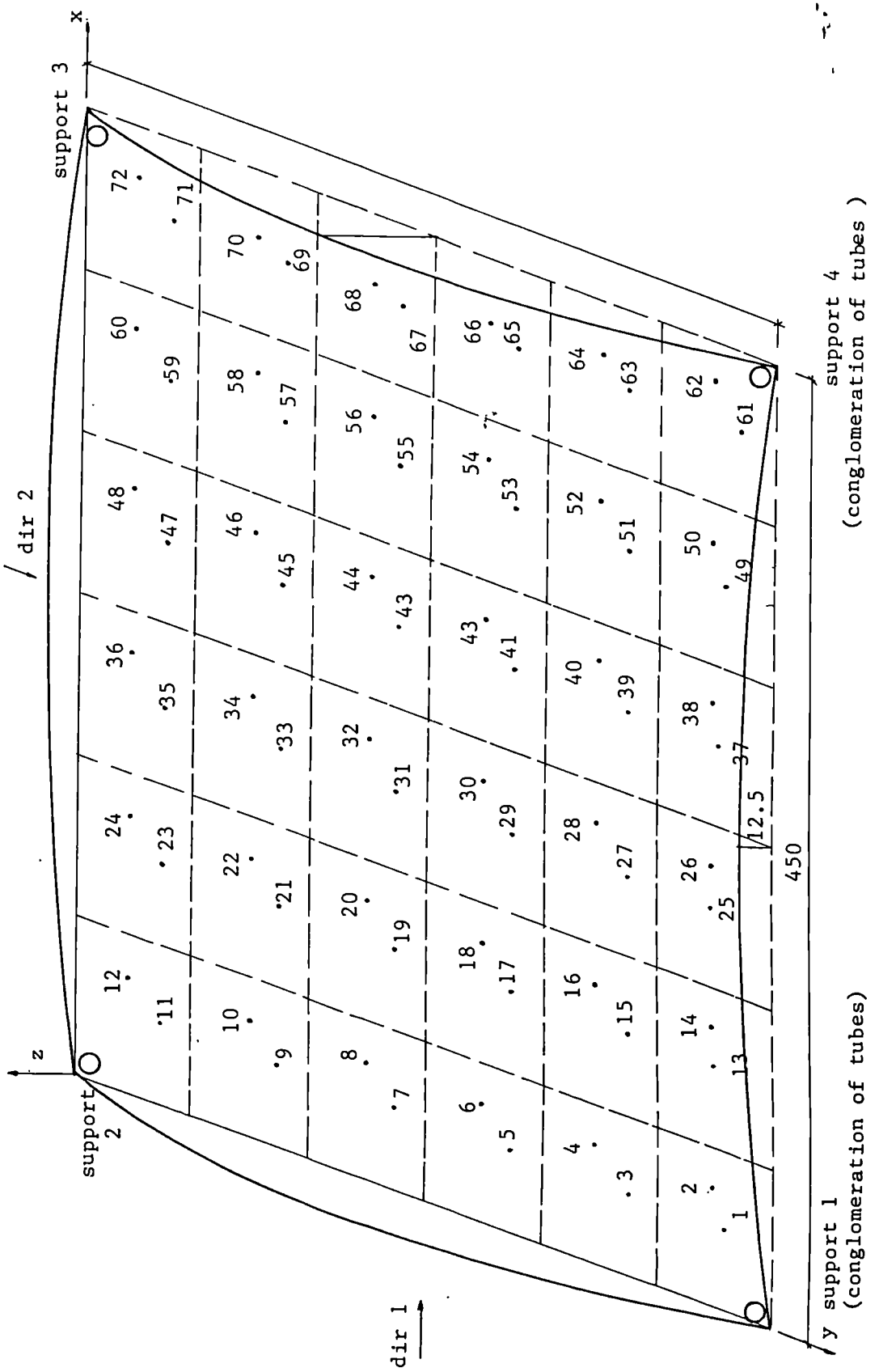
x
support 3
dir 2
z
support 2
dir 1
y support 1
(conglomeration of tubes)
support 4
(conglomeration of tubes)
12.5
450

Figure 6.22

6.6 Test procedure

As described in subclause 6.5, the pressure tappings were drilled in the shell and connected with pressure-tight fittings to brass stub tubes on the underside of the model; these in turn provided the connection to plastic pressure tubes.

At this stage the plastic tubes were firmly fitted onto the ports of two manifolds. The arrangement is shown in figures 6.23 and 6.24 for manifolds 1 and 2 respectively. The model was positioned in the centre of the wind tunnel turntable, and the plastic tubes together with the manifolds were passed through holes, specially prepared in a replaceable central part of the turntable. All remaining small openings were scaled up by means of blocking pieces and P.V.C. adhesive tape. One of the manifolds was connected to the scanivalve pressure switching device.

The model was tested as follows:

I. In the uniform flow, without obstacles in the test section entrance of the wind tunnel

   a) With wind in the longitudinal direction (dir 1), using manifold nr 1 (see figures 6.22 and 6.23), under three different free stream velocities: 18.8 m/s 17.2 m/s and 15.7 m/s

   b) With wind in the transverse direction (dir 2), using manifold nr 2 (see figures 6.22 and 6.24), under three different free stream velocities as above.

II. In the turbulent boundary layer - with obstacles in the upwind region

a) With wind in the longitudinal direction (dir 1), using manifold nr 1, under four different free stream velocities: 20.6, 18.9, 17.7 and 14.5 m/s

b) With wind in the transverse direction (dir 2), using manifold nr 2, under four different free stream velocities, as above.

The pressures on the model and the total and static pressures in the wind tunnel were measured by the arrangement of equipment shown in figure 6.10.

In chapter 5 it was emphasised that the numerical analysis based on potential flow assumptions is not capable of predicting the points of flow separation hence significant discrepancies in pressure distributions between experimental and theoretical results in these areas are expected. In order to locate these positions and to gain a better understanding of the flow patterns around the open sided shell, flow visualisation tests were performed.

Off surface techniques such as smoke, soap bubbles or streamers give a better overall picture of flow than surface methods, but in general they require more time for preparation and testing. The simplest technique to apply seemed to be the tufts method. The main disadvantage of this method is that all tests have to be re-run since tufts (can block pressure points and/or influence pressure

distributions on a model. Thus separate runs are required for pressure measurements and for flow visualisation. The tufts used, were of thin wool, approximately 25 mm long and fixed to the shell by means of Scotch tape in a grid 8 x 6.

6.7 Processing experimental results

Pressures on buildings are most usefully dealt with in a non-dimensional form as follows: [92, 97, 201]

$$C_p = \frac{p_m - p_{st}}{0.5\ \rho_a\ V_G^2} = \frac{p_m - p_{st}}{p_G} \qquad 6.6$$

where

p_m is the pressure measured on a model,

p_{st} is the static pressure in the working section of the wind tunnel,

p_G is the separate dynamic pressure

V_G is the gradient or free stream velocity and

ρ_a is the density of air.

The above parameters were obtained from experimental data as follows:

$$p_m - p_{st} = \frac{S_m - S_{fst}}{C_f}\ g \cdot \rho_m \cdot k \qquad 6.7$$

$$0.5\ \rho_a\ V_G^2 = \frac{S_{wt} - S_{wst}}{C_f}\ g \cdot \rho_m \cdot k \qquad 6.8$$

where

C_f is the calibration factor for the setra transducer approximately C_f = 00346 V/mm H_2O (the precise value is obtained from calibration performed before each run)

S_m - is the mean value of the signal in volts obtained from a pressure point on the shell through the scanivalve ($\frac{S_m}{C_f} = p_m - p_{atm}$)

S_{wt} - is the mean value of the signal in volts obtained from the total outlet of the reference pitot-static tube fixed to the wall of the wind tunnel, through the furness manometer ($\frac{S_{wt}}{C_f} = p_{wt} - p_{atm}$; where p_{wt} is the total pressure of the free stream)

S_{wst} - is the value of the signal in volts obtained from the static outlet of the pitot-static tube at the same reference point ($\frac{S_{wst}}{C_f} = p_{sw} - p_{atm}$; where p_{sw} is the static pressure of free stream)

S_{fst} - is the value of the signal in volts obtained from calibration of the wind tunnel (see figure 6.14)

$\frac{S_{fst}}{C_f} = p_{sf} - p_{atm}$; where p_{sf} is the static pressure in the working section of wind tunnel)

Substituting equations 6.7 and 6.8 into equation 6.6 gives:

$$C_p = \frac{S_m - S_{fst}}{S_{wt} - S_{wst}} \qquad 6.9$$

Analogously to equation 6.9, the approximate non-dimensional RMS values of C_p are calculated as follows:

$$RMS_{C_p} = \frac{S_{RMS}}{S_{wt} - S_{wst}} \qquad 6.10$$

where

S_{RMS} - is the RMS value of the signal obtained from the pressure point on the model.

S_{wt} values were varying during the tests with a turbulent boundary layer; hence for each pressure point, which was measured at different instants of time, the S_{wt} value recorded in the same instant was used. The values of S_{wt} were available due to the fact that the samples from the total pressure outlet of the reference pitot-static tube were continuously collected through the furness manometer into channel A of the computer, and the means were stored on a disc.

More appropriately, the reference dynamic pressure in equation 6.6 should be that measured at some height in the working section, near the place occupied by the model, but not affected by its presence. In the case of the shell roof submerged in uniform flow, the dynamic pressure in the area to be occupied by the model remains approximately constant. Its value is derived from the known dynamic wall pressure by multiplying the latter by the square of the corresponding velocities ratio (here the ratio is 1.05; see 6.4.1)

In the majority of practical applications, where a model is tested in a turbulent boundary layer, pressures are made non-dimensional by dividing the pressure at each point on the model by the dynamic pressure of the free stream. Thus obtained, C_p values are very convenient, both for calculation and application. When processing the data from a test in a wind tunnel two sets of information can be kept separately; those defining the boundary layer and those giving the pressure coefficient distribution. A designer,

in order to assess wind loading on a structure, needs to know the C_p values and the gradient wind velocity; velocity profile is not directly required.

But in order to obtain meaningful comparisons between theoretical (potential flow), uniform flow experimental and turbulent boundary experimental pressure coefficient distributions, pressures on the model from the turbulent boundary test should be made non-dimensional by dividing them by the dynamic pressure, p_H, of the approaching stream at the height of the shell. Hence, for the shell submerged in a turbulent boundary layer, the non-dimensional pressure coefficients, C_{pH}, were obtained in the following manner:
C_{pH} is defined as;

$$C_{pH} = \frac{p_m - p_{st}}{p_H} \qquad 6.11$$

Where

$p_m - p_{st}$ is expressed by equation 6.7, but

$$p_H = 0.5 \quad \rho_a \cdot V^2 \qquad 6.12$$

The velocity, V, is obtained from the power law, equation 6.4, as

$$V = V_G \left(\frac{z}{z_G}\right)^a \qquad 6.13$$

hence equation 6.12 takes the form:

$$p_H = 0.5 \cdot \rho_a \cdot V_G^2 \cdot \left(\left(\frac{z}{z_G}\right)^a\right)^2 \qquad 6.14$$

By substituting equation 6.8 the following equation results:

$$p_H = \frac{S_{wt} - S_{wst}}{C_f} \quad g \cdot \rho_m \quad k \left(\left(\frac{z}{z_G}\right)^a\right)^2 \qquad 6.15$$

Now by equations 6.15 and 6.7, equation 6.11 takes the form:

$$C_{pH} = \frac{S_m - S_{fst}}{S_{wt} \quad S_{wst}} \left(\left(\frac{z}{z_G} \right)^a \right)^{\frac{1}{2}} = C_p \times A$$

Where z is the height of the point mid-way between the lowest and the highest point of the shell, a = 0.24 and z_G = 0.95 m. The value of A was 1.889.

The results for C_p distributions obtained from all cases did not show any discernible dependence upon velocity for the range of velocities used in the tests; therefore only average values are listed in figures 6.25 to 6.28.

6.8 Discussion of the results

When a model is tested in a wind tunnel, streamlines and wakes are prevented from expanding in the way they would in full scale unconstrained freestream flows. These constraining effects of the wind tunnel walls start having a significant influence on model pressures when the model occupies more than 10% of the tunnel cross-section [92]. The cross-section area of the shell is smaller than 0.45 · (.056 + .0125) = .031 m^2 which is less than 1% of the wind tunnel working section. Hence the blockage effects are not likely to have any noticeable influence on C_p values.

The main attention during tests in the wind tunnel was focused on the convex side of the shell. Pressure was measured on this side, and therefore the top surface of the model was kept as smooth as possible, and without any obstacles. All the connections (the brass and plastic

tubes) between pressure points and the pressure measuring device were carried out on the opposite side of the shell. Although they were arranged as neatly as possible (see figure 6.17), they influenced to some degree the directions of streamlines around the shell which, in turn, led to some changes in the loading pattern.

The areas where these effects are most clearly visible are those near the supporting rods: nr 1 and 4 (see figure 6.22), where the plastic tubes were brought to the bars. The effects can be clearly observed at the pressure points: 2, 4 and 62, 64 - for wind in the longitudinal direction; and at points 1 and 61 for wind in the traverse direction. The problem is discernible (right bottom corner) on a picture (figure 6.29) taken when the shell with tufts on was tested in uniform flow with wind in the longitudinal direction. The results at the pressure point 47 (for wind in the lateral direction) seem to be rather unrealistic and this pressure point was probably blocked.

The shape of the shell and the flow are symmetrical and therefore one would expect to obtain symmetrical results (excluding points very close to the supports: 1 and 4). The C_p values, as given in the tables of figures 6.25 to 6.28 are however not exactly symmetrical. The reasons for this could be the small deviations in the shape of the shell and/or the plastic tubes attached to the underside of the shell. This illustrates the sensitivity of wind loading to slight aberations in shape.

Uniform flow tests

For the longitudinal wind direction, for which the ratio rise to span of the shell is 1/36, the streamlines stayed attached to the shell; no catastrophic separation of flow can be detected (see figures 6.25 and 6.29). Examining the results row by row it may be observed that the C_p values for one side of the shell (2, 4, 6 and 14, 16, 18) are more affected by the presence of tubes than the other. Pressure coefficients are reasonably regular, with greater suction in the middle, decreasing in value towards edges (except the last row). The sudden increase in suction at the point 72 can be explained by the presence of the supporting bar, which forces streamlines to come closer together thus causing an increase in loading.

The irregular behaviour of the tuft near point 72, during the flow visualisation tests, suggests the occurrence of rolling-up vortices; (see figure 6.31) a feature which causes an increase in the value of local pressure. The suction due to edge vortices is of small value and cannot be detected in the first five rows. In the last row, however, the presence of supporting bars seems to reinforce this action and gives noticeable results.

In the case of flow in the lateral direction, where the rise to span ratio of the shell is greater (1/16) separation of flow can be observed both from the flow visualisation technique (see figure 6.30), and by examining the numerical results, which show a sudden increase in the value of the

fluctuating (RMS) component. The separation starts from edges (pressure point 7, 67) and at the beginning is very mild (not visible on the picture), and then grows (pressure points 5, 65 and 3, 63) until it extends across the whole shell (the last row of pressure points (see figure 6.32).

The higher rise to span ratio of the shell leads to closer and more curved streamlines; a flow pattern which is more sensitive to any irregularities in shape or presence of any obstacles, like for example the supports. This probably explains why, at the first row, (points 11 and 71) there are proportionally higher RMS_{C_P} values and why, in the flow visualisation tests, tufts at these points are deviated. The sudden increase in suction at the points 1 and 61 seems to be due to superposition of two effects; the conglomeration of tubes at the supporting bars and the occurrence of rolling-up vortices.

Turbulent boundary layer tests

Pictures taken during the flow visualisation tests are presented in figures 6.33 and 6.34 for wind in the longitudinal and lateral directions respectively. Generally the tufts, which indicate the direction of streamlines, are less aligned in this case, and due to the turbulence behave in an irregular manner.

The turbulence of the approaching flow is visible in the first row of numerical results (see figures 6.27 and 6.28) and in the pictures. The flow in contact with the shell at its top surface loses some of the fluctuations, but these

values still remain high, the tufts become more aligned and RMS_{C_p} values are smaller (as a proportion of mean C_p values).

Due to the presence of fluctuations in the approaching flow, the start of separation in the case of wind in the traverse direction is not easily traced. A clear indication cannot be found until the last row of pressure points, where it is detectable both in the numerical results and from the photographic evidence.

6.9 Conclusions

In figures 6.35, 6.36, 6.37 and 6.38, the theoretical results obtained from the analyses based on vortex-lattice methods with

(a) horseshoe vortices distributed in the plane z = 0 and

(b) quadrilateral vortex rings placed on the surface of the model,

are compared with the experimental C_p values from the uniform flow tests and the turbulent boundary layer tests. Due to symmetry only half of the results are presented. In general, the experimental C_p values are obtained as a mean of the pressure coefficients at two corresponding points: from the right and the left hand sides of the shell, except when wind is in the longitudinal direction, where the values quoted are those taken from the side of the shell less affected by the underside tubes.

The theoretical procedures of Chapter 5 based on the potential flow theory are confined to flows which remain attached to the surface of a model (structure). This implies that the theoretical analyses are not capable of predicting correct values of pressure coefficients in the areas of separation.

As discussed in Chapter 5, the two theoretical approaches give results which differ significantly. It was expected that the method using horseshoe vortices distributed in the plane z = 0 was likely to give better results and this

appears to be the case, though the results are unreliable near the loading and trailing edges.

In the case of wind blowing in the longitudinal direction (rise to span ratio 1:36) the theoretical analysis based on the modified Hedman method tends to underestimate values of suction by approximately 30% compared with the uniform flow test results. At edge points of the last row differences are greater since the theory does not account for the occurrence of rolling-up edge vortices. The turbulent boundary test coefficients are smaller on average by 20% than the theoretical, except at edge points of the last row of panels where their values are closer to the theoretical prediction than the uniform flow results.

For the lateral wind direction, (rise to span ratio 1:6) the horseshoe vortex method overestimates the values of suction in the central part of the shell by, on average, 18% for the uniform flow and 30% for the turbulent flow. In the leading edge area the uniform flow suction coefficients are slightly larger than those theoretically predicted. The leading edge drag obtained from the theory is very close to that measured in the turbulent boundary layer tests. The trailing edge, where separation occurs is, as expected, the area of greatest discrepancy between the theory and the experiments.

The case with wind in the longitudinal direction is closer to the theoretical assumptions. The shell is shallower, hence separation should occur at a later stage, further

downstream from the leading edge, than in a steeper model. But, because pressure coefficients are rather small, the presence of the underside tubes and other effects are likely to have a greater influence on measured wind loading on the shell for this direction. This could explain why the relative differences in the non-dimensional pressure coefficients, between theory and experiments are generally larger for the longitudinal wind direction.

The test results show that the $\bar{C}_p$ values obtained from the turbulent boundary layer tests are smaller than both the uniform flow and the theoretically predicted results (except at the rear edge points). Only one type of terrain was, however, simulated in the wind tunnel (relatively smooth) and only one model was tested.

In the theoretical analysis a 6 x 6 panel idealisation was used; this division coinciding with the pressure tapping on the model. On the other hand an increase in the number of elements used for the horseshoe vortex-lattice method, as shown in Chapter 5, is likely to yield a C_p distribution differing by only about 5% from the present.

The modified Hedman method is not very dependent on the number of elements and, in general, is very simple to apply compared with real flow solutions (see Appendix to Chapter 5). It can therefore be easily incorporated into any structure - fluid interaction scheme accounting for both static and quasi-dynamic behaviour.

However, it should be borne in mind that the method is based on potential ideal flow assumptions, and consequently such features as flow separation, rolling up vortices or turbulence cannot be modelled properly. However, when the modified Hedman method is employed to examine a static or quasi-dynamic behaviour of a shallow tensile membrane structure, the inefficiency of the method (resulting in unreliable prediction in pressure coefficients near the leading and trailing edges) is rather unlikely to cause gross errors in the predicted structural response. This is due to the fact that the areas of likely greatest under or over estimation in C_p coefficients occur near supports; the parts of the structure where external loads have the smallest effect on deflections and stresses in the membrane.

Location on Manifold	Pressure pipe identification	Location on Manifold	Pressure point identification
1	wall, total	25	40
2	atm	26	42
3	2	27	44
4	4	28	46
5	6	29	48
6	8	30	atm
7	10	31	50
8	12	32	52
9	atm	33	54
10	14	34	56
11	16	35	58
12	18	36	60
13	20	37	atm
14	22	38	62
15	24	39	64
16	atm	40	66
17	26	41	68
18	28	42	70
19	30	43	atm
20	32	44	72
21	34	45	wall, static
22	36	46	floor, static
23	atm	47	floor, static
24	38	48	atm

Pressure pipes 2 to 72 are connected to the shell

Figure 6.23 Manifold No. 1 arrangement

Location on Manifold	Pressure pipe identification	Location on Manifold	Pressure point identification
1	wall, total	25	39
2	atm	26	41
3	1	27	43
4	3	28	45
5	5	29	47
6	7	30	atm
7	9	31	49
8	11	32	51
9	atm	33	53
10	13	34	55
11	15	35	57
12	17	36	59
13	19	37	atm
14	21	38	61
15	23	39	63
16	atm	40	65
17	25	41	67
18	27	42	69
19	29	43	atm
20	31	44	71
21	33	45	wall, static
22	35	46	floor, static
23	atm	47	floor, static
24	37	48	atm

Pressure pipes 1 to 71 are connected to the shell

Figure 6.24 Manifold No. 2 arrangement

Pressure Point (See fig. 6.22)	Average Cp	Approx. RMS Cp	Pressure point	Average Cp	Approx RMS Cp
2	- .08	.02	38	- .11	.02
4	- .08	.02	40	- .15	.01
6	- .08	.03	42	- .16	.01
8	- .06	.03	44	- .16	.01
10	- .05	.02	46	- .15	.01
12	- .04	.02	48	- .13	.02
14	- .10	.02	50	- .16	.02
16	- .13	.02	52	- .16	.02
18	- .13	.02	54	- .16	.02
20	- .12	.02	56	- .16	.01
22	- .11	.02	58	- .16	.01
24	- .09	.02	60	- .15	.02
26	- .09	.02	62	- .26	.03
28	- .14	.01	64	- .17	.02
30	- .16	.01	66	- .12	.02
32	- .15	.01	68	- .10	.01
34	- .14	.01	70	- .11	.01
36	- .10	.01	72	- .14	.02

Figure 6.25 Uniform flow, longitudinal dir.

Pressure Point (See fig. 6.22)	Average Cp	Approx. RMS Cp	Pressure point	Average Cp	Approx RMS Cp
11	- .05	.04	5	- .73	.08
23	- .07	.04	17	- .91	.04
35	- .09	.04	29	- .96	.03
47	- .37	.02	41	- .94	.03
59	- .06	.04	53	- .85	.04
71	- .04	.03	65	- .62	.10
9	- .48	.03	3	- .75	.12
21	- .63	.03	15	- .77	.05
33	- .70	.02	27	- .81	.05
45	- .72	.03	39	- .79	.05
57	- .66	.03	51	- .75	.06
69	- .49	.03	63	- .63	.15
7	- .66	.04	1	- .48	.10
19	- .89	.03	13	- .11	.06
31	- .96	.03	25	- .02	.07
43	- .96	.03	37	+ .003	.08
55	- .85	.03	49	- .09	.08
67	- .62	.05	61	- .35	.11

Figure 6.26 Uniform flow, traverse dir.

Pressure Point (See fig. 6.22)	Average Cp	Approx. RMS Cp	Pressure point	Average Cp	Approx RMS Cp
2	-.006	.15	38	- .06	.09
4	+.002	.21	40	- .09	.08
6	+ .02	.19	42	- .09	.08
8	+ .04	.17	44	- .09	.08
10	+ .04	.19	46	- .08	.08
12	+ .04	.13	48	- .06	.09
14	- .02	.10	50	- .09	.09
16	- .04	.10	52	- .09	.08
18	- .06	.10	54	- .09	.08
20	- .06	.10	56	- .09	.08
22	- .04	.10	58	- .09	.08
24	- .02	.10	60	- .07	.09
26	- .04	.09	62	- .17	.08
28	- .08	.01	64	- .11	.08
30	- .08	.08	66	- .04	.06
32	- .08	.09	68	- .04	.06
34	- .08	.08	70	- .04	.06
36	- .04	.09	72	- .07	.08

Figure 6.27 Turbulent boundary layer, longitudinal dir.

Pressure Point (See fig. 6.22)	Average Cp	Approx. RMS Cp	Pressure point	Average Cp	Approx RMS Cp
11	.09	.23	5	- .66	.19
23	.08	.24	17	- .83	.23
35	.06	.26	29	- .83	.24
47	- .03	.02	41	- .87	.24
59	.09	.26	53	- .77	.20
71	.15	.22	65	- .64	.18
9	- .34	.14	3	- .66	.22
21	- .47	.15	15	- .67	.21
33	- .53	.15	27	- .68	.23
45	- .53	.16	39	- .68	.23
57	- .49	.15	51	- .68	.21
69	- .34	.14	63	- .68	.23
7	- .57	.15	1	- .34	.18
19	- .77	.19	13	- .11	.11
31	- .79	.19	25	- .06	.11
43	- .83	.21	37	- .04	.11
55	- .72	.17	49	- .09	.10
67	- .55	.15	61	- .30	.17

Figure 6.28 Turbulent boundary layer, traverse dir.

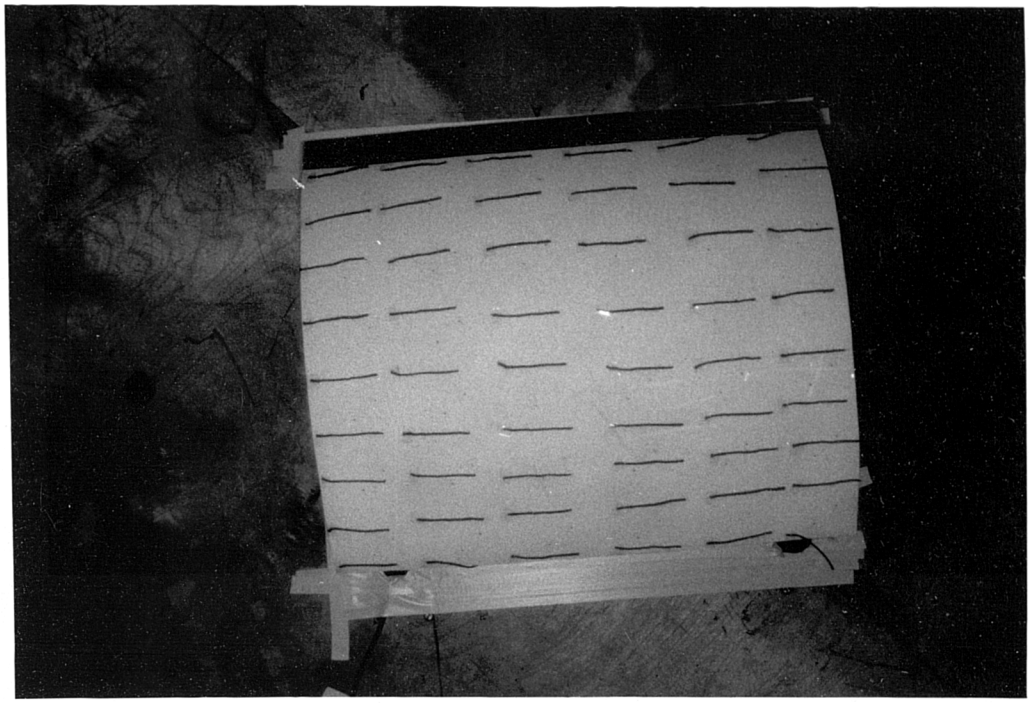

Figure 6.29 Uniform flow, wind in dir. 1

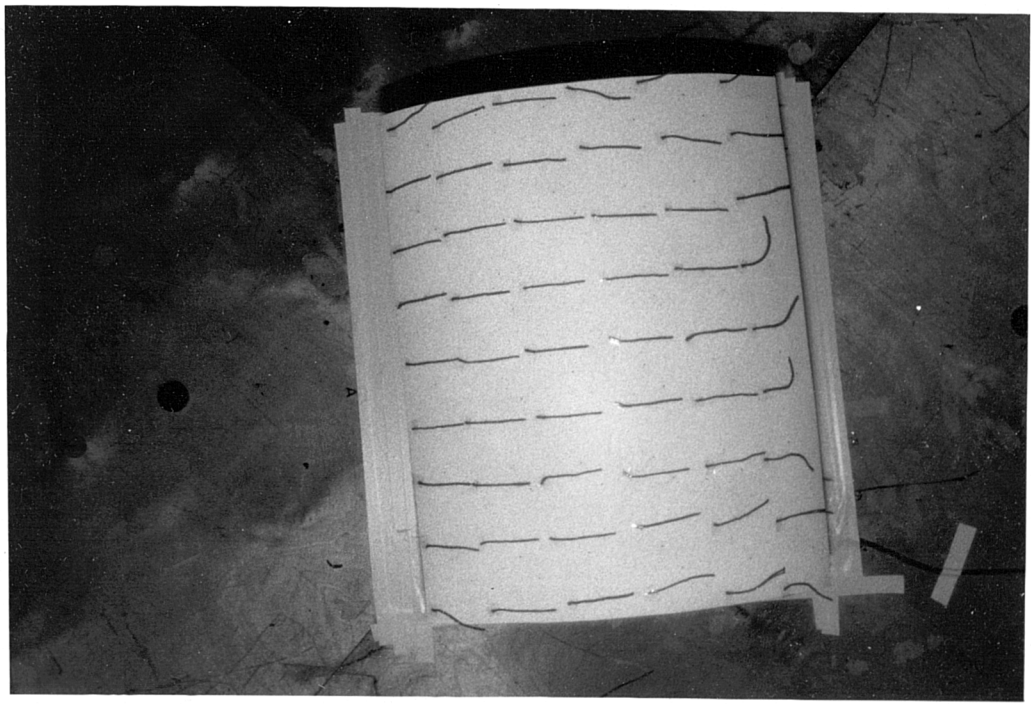

Figure 6.30 Uniform flow, wind in dir. 2

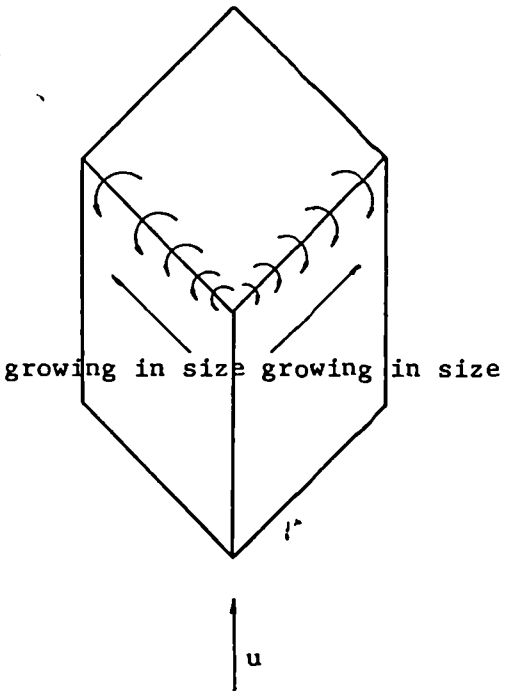

Figure 6.31

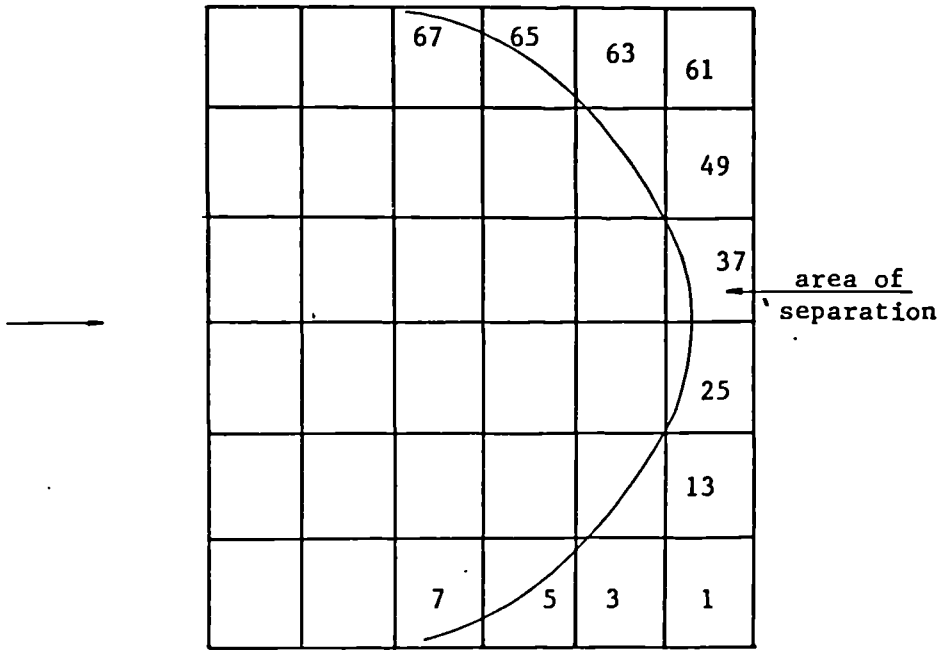

Figure 6.32

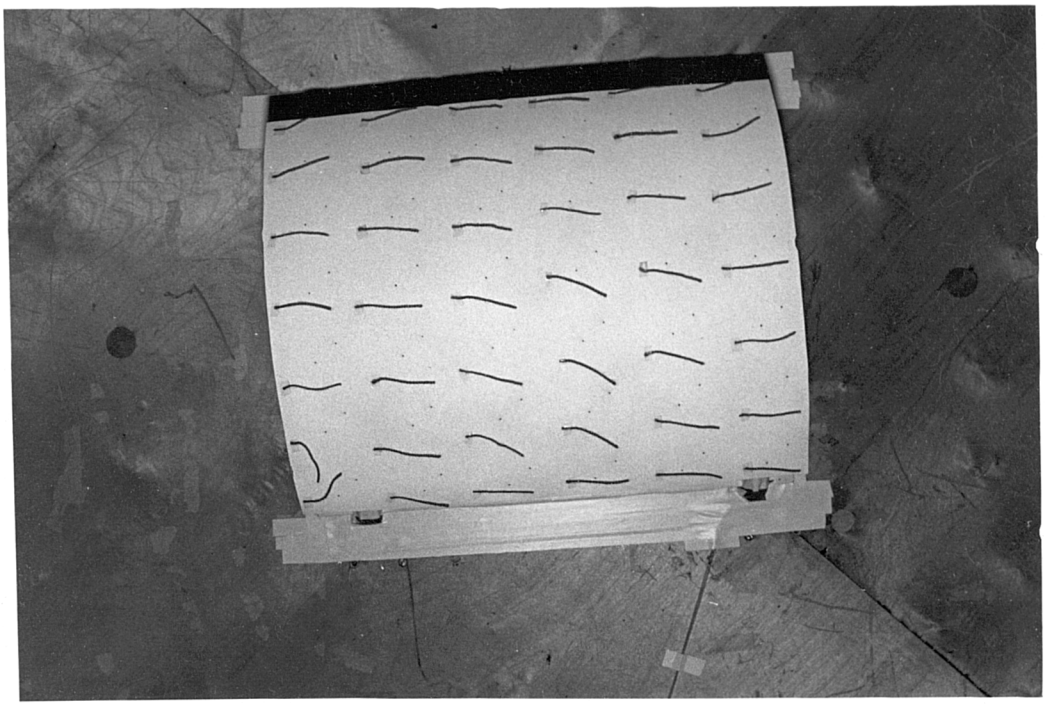

Figure 6.33

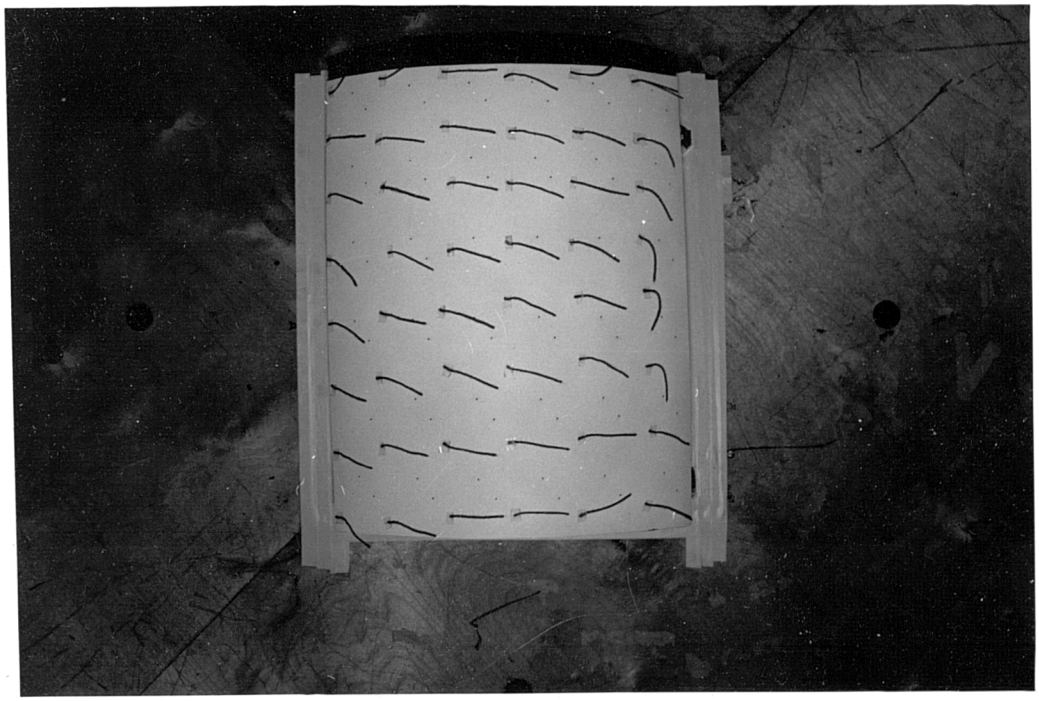

Figure 6.34

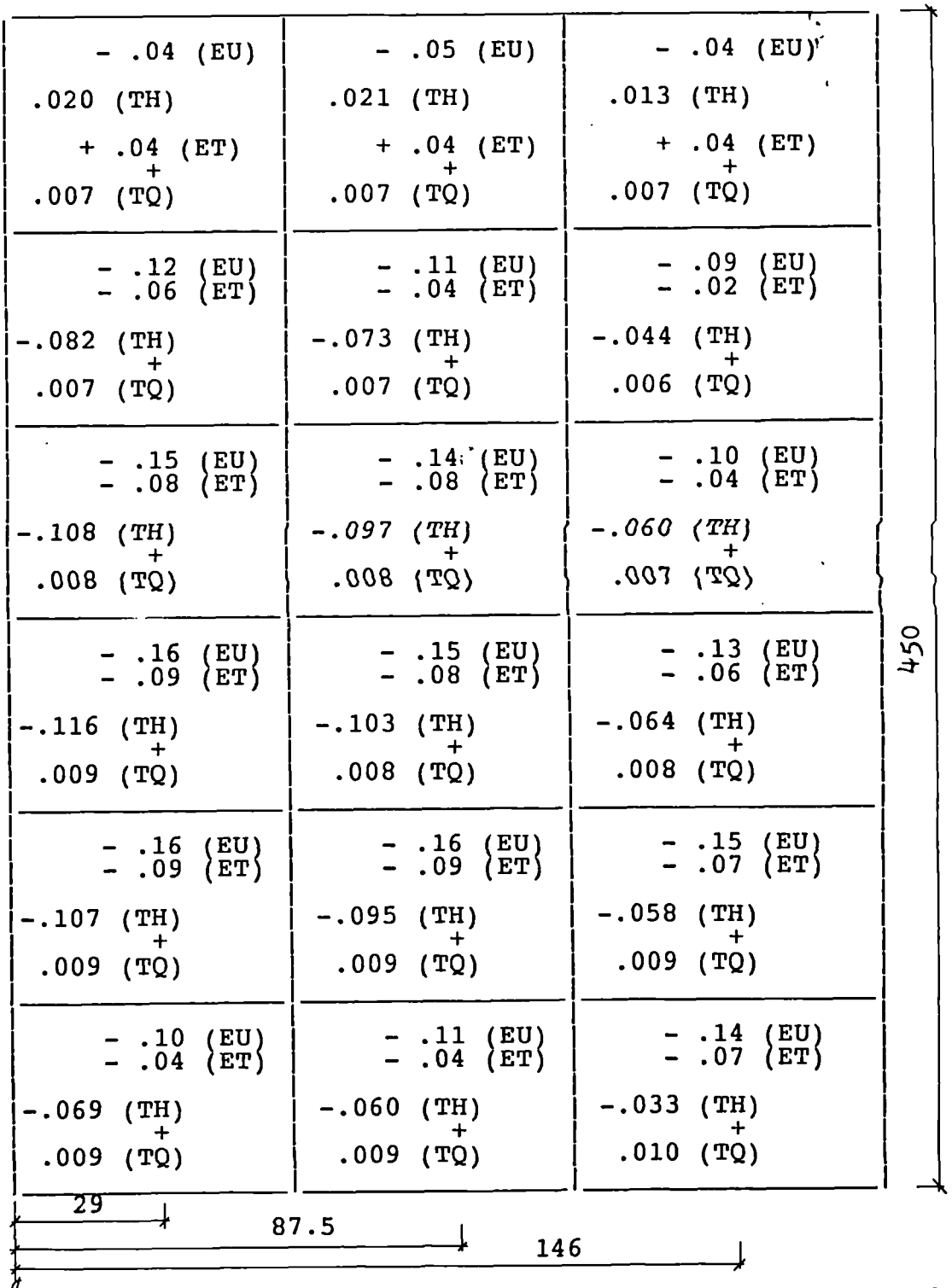

TH - theoretical results, horseshoe vortices in the plane z=0
TQ - theoretical results quadrilateral vortices on the surface
EU - experimental results, uniform flow
ET - experimental results, turbulent boundary layer

Figure 6.35 Cp distribution, wind in the longitudinal direction

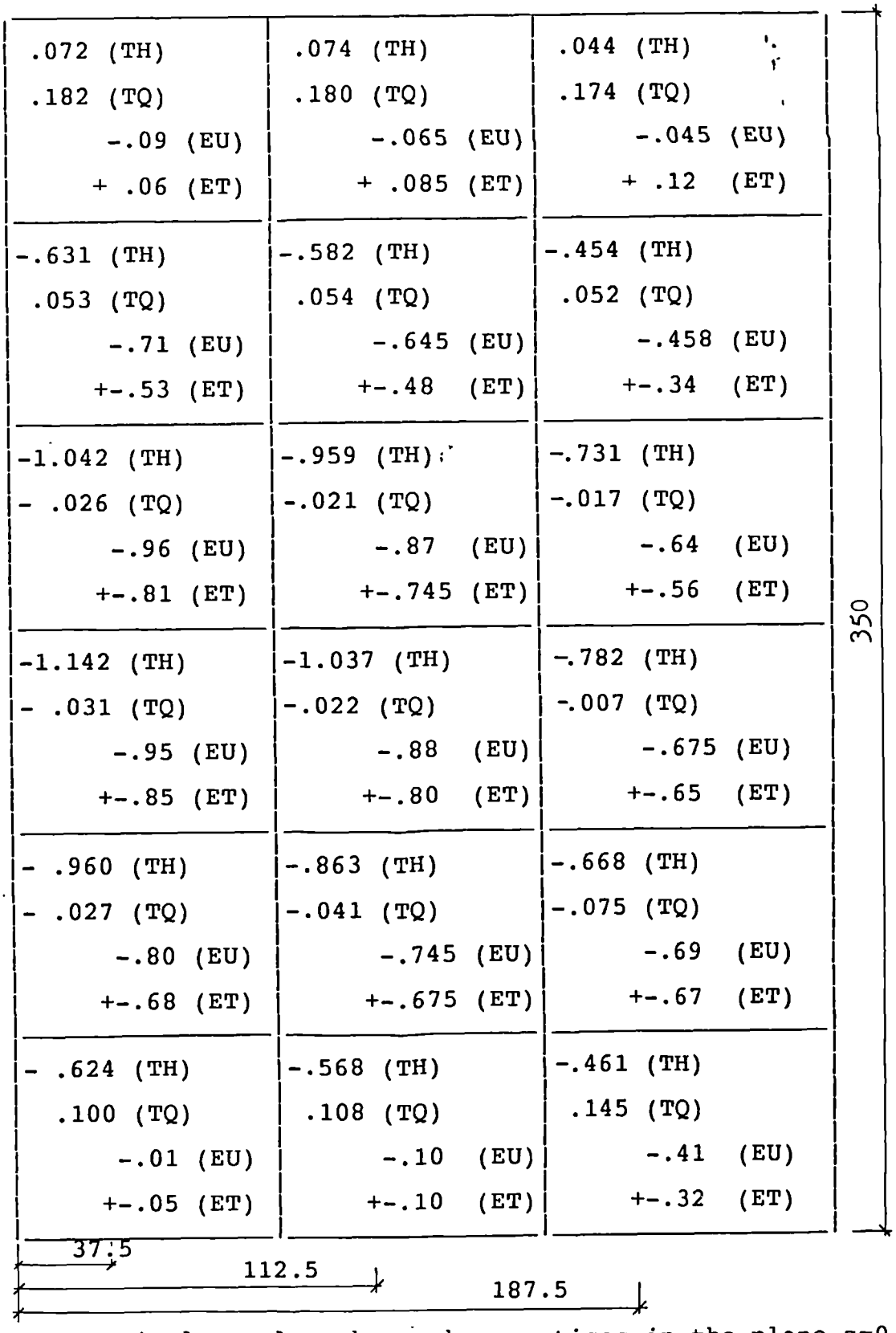

TH - theoretical results, horseshoe vortices in the plane z=0
TQ - theoretical results quadrilateral vortices on the surface
EU - experimental results, uniform flow
ET - experimental results, turbulent boundary layer

Figure 6.36 Cp distribution, wind in the traverse direction

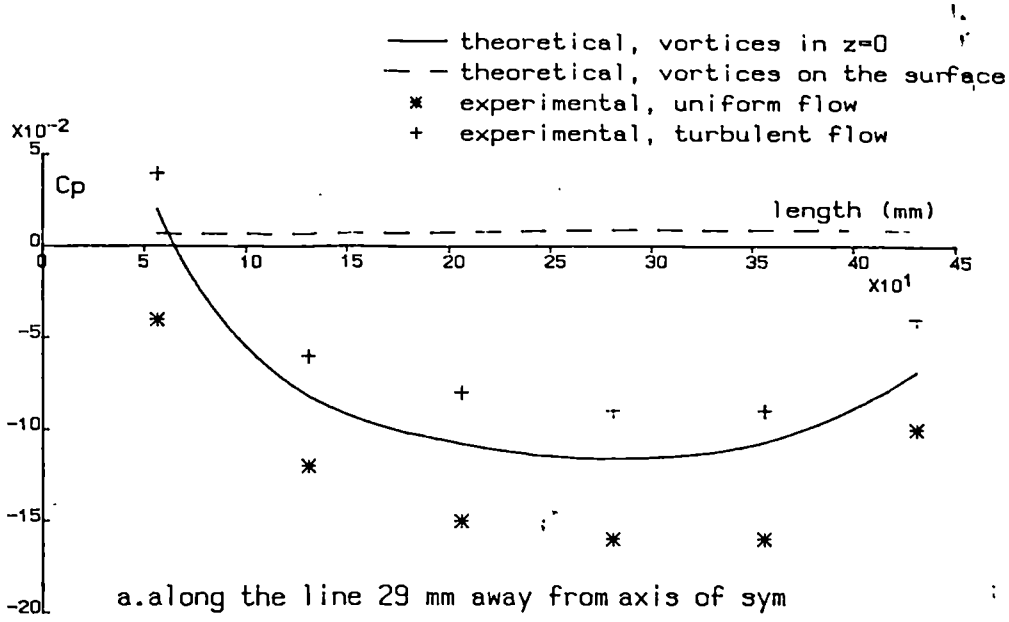

a.along the line 29 mm away from axis of sym

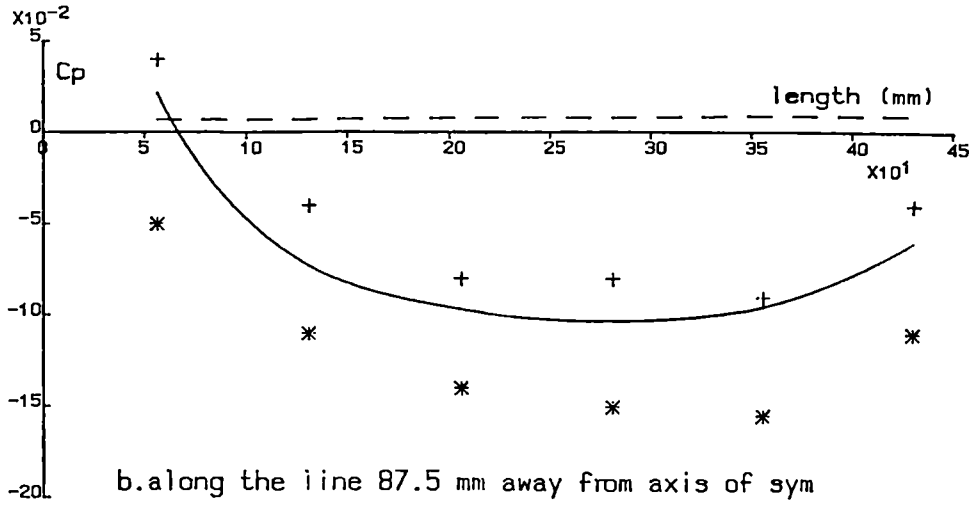

b.along the line 87.5 mm away from axis of sym

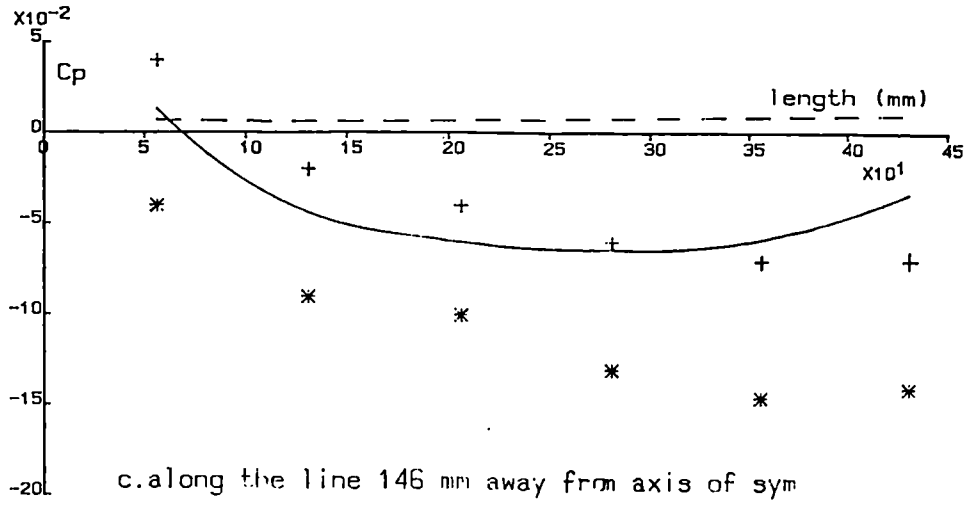

c.along the line 146 mm away from axis of sym

Figure 6.37 Cp distribution, wind in the longitudinal direction

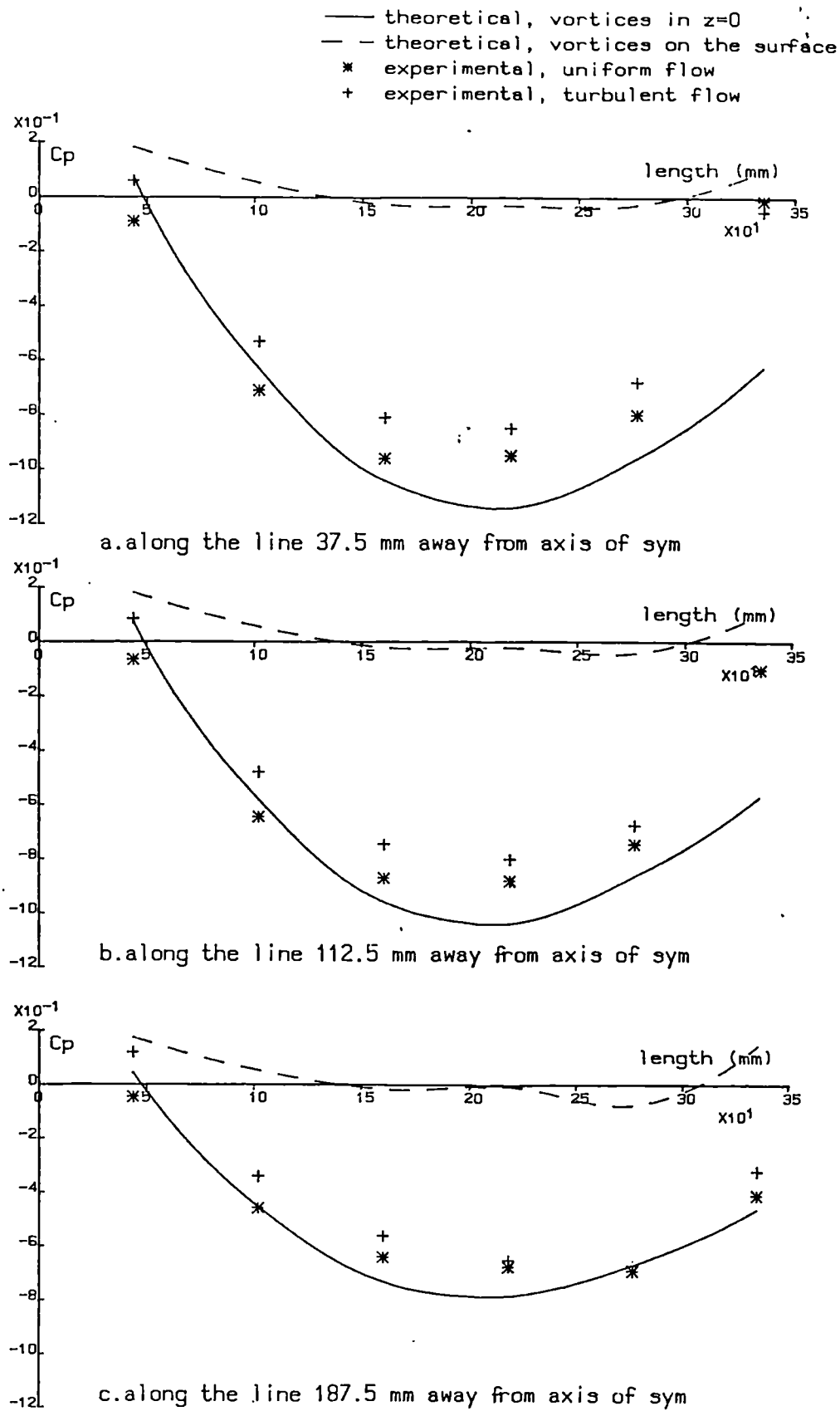

Figure 6.38 Cp distribution, wind in the traverse direction

CHAPTER 7

Review of methods of analysis for air-supported structures

Contents:

Introduction, Linear analyses (Static analyses, Dynamic analyses), Nonlinear solutions (Shells of revolution, Finite element methods), Analyses of Structures with strong geometric nonlinearities (Static analyses, Dynamic analyses)

7.1 Introduction

Air-supported structures are a special case of membrane structures with positive Gaussian curvature. Their ability to support various loads is due to the prestressing of the construction material by tensile membrane forces, which depend on the magnitude of the internal overpressure and the geometric form of the structure. Since the jacket of an air-supported structure behaves as an anisotropic membrane of zero flexural rigidity, only membrane states of stress can be produced in it by external loads. Thus air-supported structures might be investigated by means of membrane theory for surface structures.

Two main aspects in the analysis of air-supported structures are [165]:

1. determination of the necessary inflation pressure, and
2. establishment of the maximum tensile stresses and the maximum deflections occurring in the system at the given internal pressure, combined with various forms of live loading.

The inflation pressure is obtained under the requirement that no compressive stresses can appear at any point of the membrane under the combined effect of static (or 'quasi-static') external loading and internal pressure , and that the structure remains stable under the action of dynamic loading (mainly wind) on the pretensioned membrane.

The minimum principal stress under static loadings should be tensile. This condition is a guarantee against formation of (fairly large) folds, as confirmed by experiments [165]. Usually, smaller folds are formed near the membrane edges, but these do not affect the stability, being caused by local accommodation of the membrane to the shape of the constraining members.

The design of air-supported structures involves three interrelated aspects:

1. The problem of form-finding
2. Determination of cutting patterns for fabrication
3. The load analysis

Form-finding

Form-finding is concerned with defining the geometry of the surface of an air-supported structure under internal pressure only. The fundamental requirement is that under internal pressure all principal stresses in the membrane are tensile. The stress distribution under the internal pressure should be reasonably uniform. The state of stresses is controlled by the overall geometry of the

surface and is modified locally by, for example, cutting pattern inaccuracies or the incompatibility of strains in the surface with boundary support conditions.

Analytically three equilibrium equations, in the x, y and z directions of the surface under the inflation pressure may, for particular cases, give the relationship between stresses in the surface and the geometry of the surface [129, 110, 69]. The equilibrium equations consist of three simultaneous partial differential equations and there are therefore three unknowns. The unknowns can either be the stresses or the geometry. Thus two approaches are possible [202]:

i) define geometry, inflation pressure and boundary forces and then calculate stresses. The membrane is statically determinate as there are only three unknowns at each location: two direct stresses and one shear stress. The defined geometry must be that which applies under the inflation pressure. The no load geometry can then be found by consideration of the strains necessary to produce the inflation stresses. This approach, however, is not practicable from the point of view of employing coated fabric material to form the membrane, which is the most usual form of construction. The reason for this is that such fabrics can sustain only very low shear stresses and, if reasonably free-form geometry is specified a priori, significant shear stresses are likely to occur under inflation pressure.

ii) The second more fruitful approach is to define stresses, inflation pressure and boundary geometry, and then calculate the resulting surface geometry. If the stresses are defined to be uniform, then this process is physically equivalent to determining the shape of a "soap-film" on a given boundary with a given inflation pressure [28]. This approach can be combined with the determination of cutting patterns. [202, 87, 15, 115]

Cutting patterns

When a surface with a given state of stresses has been defined we need a way to construct it from planar stress-free pieces of real membrane material. The pieces should be designed such that they yield the best possible approximation to the desired membrane shape and state of stresses when fitted together and erected. Cutting patterns can be computed, to some approximation, in a purely geometric manner without considering the deformation. The strains in the material under the initial stress are taken into account by adjustment of the pattern during construction [28, 151]. Alternatively, in a more rigorous way, the initial shape may be determined by solution of the nonlinear stress-displacement relations [129].

Load analysis

The third problem area is that of the calculation of static deformations and stresses of an initially prestressed membrane under external loadings (for example snow or wind). Here the problem is usually more complicated than in form-

finding, as generally both the stresses and geometry are unknown. Since membrane materials allow large deformations and as a consequence of zero bending stiffness also allow large displacements, the problem is, in many cases, both materially and geometrically non-linear.

In practice approximations can be employed for simple cases of form-finding and cutting pattern determination. Load analyses generally require the inclusion of all nonlinearities. However, various simplified linear analyses have been applied

7.2 Linear analyses

7.2.1 Static analyses

The behaviour of air-supported structures, under the assumptions of small deflections and that the membrane material behaves in an elastic manner can be described by the classical linear theory of thin shells with zero bending stresses (the membrane state of stresses) [69].

The basic equations employed in thin elastic shell theory were originally derived by Love [138] in 1888. Since then many additional theories for thin shells have been proposed [110]. In the majority of these a curvilinear coordinate system is employed which coincides with the orthogonal lines of principal curvature of the surface under consideration. (for basic definitions employing differential geometry see 110, 69, 74). The choice of an orthogonal curvilinear coordinate system allows a convenient derivation of the

fundamental relationships of the theory of thin elastic shells.

When in a thin elastic shell theory, the bending resistance is discounted, there results a reduction of the number of stress components in the shell and thus the set of equations describes linear membrane behaviour.

In classical thin elastic shell theory, the membrane state of stresses is assumed as an approximation, deduced from the fact that under appropriate loading conditions, the resulting bending moments are so small that they may be neglected. Hence, with the invention of air-supported structures, analyses suitable for some of these structures, using the analog of a shell of revolution with straight and curved generators under uniform or axisymmetric loading, were available [110].

The works which are devoted to air-supported structures, and which discuss them in wider scope than the classical theory of thin shells, are those by Otto [165] or more recently by Firt [69] and Leonard [129].

In the static analysis of air-supported structures Firt [69] uses a rectangular projection system of coordinates and derives equations of equilibrium by projecting all the forces (external and internal), acting on an infinitesimal element of a very thin shell, onto two tangential directions and the normal to the curved element. This results in three

linear differential equations and under the assumption that the geometry of the element remains basically unchanged during the loading process, the membrane state of stresses is a statically determinate problem since for three unknown membrane forces, one normal and two tangential, there are three equations of equilibrium.

The equations may be solved analytically by direct integration when a particular shape of membrane structure and type of loading are assumed. The greatest number of analytical solutions exist for surfaces of revolution (elliptical, spherical, parabolic or conical) [69]. For more complicated shapes, and/or loadings, analytical solutions are derived by employing classical functions of mathematical physics such as Bessel function, and Kelvin or Legendre functions. When a shell is shallow the three differential equations can be reduced, by expressing stresses as pseudo-stress resultants acting on the projected differential element and introducing a stress function (for example Pucher's stress function), to a single second-order partial differential equation for the stress function [129].

When the stresses are known, the strains are found from Hooke's law for anisothropic materials [69], and under the assumption of small deformations the strain-displacement relations are given in the form of three linear differential equations [69, 110], which can be used to calculate displacements [69, 165].

In the linear static analysis of an arbitrary shell, or assembly of arbitrary shells, under static loadings, the only possible solution is in general numerical. Various methods have been employed, the most common of which are: the finite difference method [110], the finite element method [210], and the method of stepwise integration [110].

7.2.2 Dynamic analyses

Dynamic behaviour of air-supported structures, under free or forced vibration, may in some cases be analytically investigated with reference to a particular shape of structure [69]; cylindrical membranes being the most common. Equations describing the movement of a structure are formulated under the assumption that the mass of the surrounding air and damping are neglected. The governing equations, which can be obtained by resolving all forces into tangential and normal directions is a partial differential equation of fourth order. Assuming harmonic vibration (and for forced vibrations harmonic external loading), the dynamic equation is reduced to an ordinary differential equation (homogeneous for free vibration, and non-homogeneous for forced vibration), which may be solved by means of Fourier series analysis or modal analysis [42, 69, 110].

As emphasised previously the total design of air-supported structures cannot be based, in general, on linearised theories, but the theories may be used to deal with a particular class of problem. The equations describing the

mutual relationship between external forces, internal stresses and deflections are much simpler than in nonlinear problems, hence:

1. there is a greater chance to derive an analytical solution using linear theory and thus the stress distributions can be better illustrated and possible shapes of air-supported structures may be explicitly defined [69].

2. linear equations are easier to employ in two field problems (air-structure or water-structure interactions). Coupling between these two fields can be more precisely modelled, and thus some phenomena, such as flutter in potential flow [113], can be more closely investigated.

7.3 Nonlinear solutions

The behaviour of an inflatable membrane structure is such that, very frequently, the classical linear theory is inadequate for proper analysis.

Nonlinear membrane theories have been studied since 1960. Theories and solutions for axi-symmetric shells of revolution have been proposed by Green [78], Grigor'ev [79], Rivlin [173] and Simmonds [183]. The theories and solutions are valid for large elastic displacements of membrane-type shells.

Another branch of work on air-supported structures is concerned with the superposition of infinitesimal

displacements on previously deformed inflatable shells [128, 180]. The majority of these works on superposition problems have assumed a rubber like material whose constitutive relations were studied by Mooney [148]. In this theory account is taken of the behaviour of the rubber or similar superelastic material which, when strained in any manner to the point of rupture, experiences tightening or stiffening before rupture. In mathematical terms this means that the derivative of the stress with respect to strain shows a marked and continuous increase.

7.3.1 Shells of revolution

There are a few nonlinear solutions which do not require discretization of a continua a priori. For membrane structures they are mainly for shells of revolution [128]. One group is based primarily on the assumption of a prescribed initial shape and of a nonlinear, isotropic incompressible material of the Mooney-type for fabrication of the shell. Glockner [73] and Vishwanath [196], by employing the Newton-Raphson numerical technique, predicted the stresses and displacements of an inflatable structure with a prescribed initial revolute configuration subject to axisymmetric static and thermal loads. The prime advantage of the Newton-Raphson technique besides its convergence characteristics, is the capability to more easily determine possible equilibrium states when a highly nonlinear elastic material of the Mooney-type is considered. Other investigators [128] have used numerical integration techniques for the same type of problem (i.e. prescribed

initial shape and Mooney-material).

There is an exact solution based on perturbation theory for the special case of linear elastic (Hookean) and isotropic shells with an initial spherical shape and loaded axisymmetrically [129, 195]. The perturbation method consists of superposing an infinite set of asymptotically convergent linear solutions on the nonlinear equations for the membrane with the deformed surface used as a reference.

Another direction of research into the behaviour of inflatable shells of revolution concerns the determination of the initially unstrained shape required to obtain a desired final shape after pressurisation. The constitutive relations for the material have been taken mainly as linear Hookean or as generalised Hookean in nature, i.e. with stress expressible as a nonlinear power series expansion of the strains. Since the deformed middle surface is taken as the reference state, the stress distribution is statically determinate [122]. The initial shape is determined by solution of the nonlinear stress- displacement relations. If perturbation theory is used, the nonlinear equations degenerate into an infinite set of linear equations, which are solvable in closed form for an arbitrary shell of revolution. The terms in the perturbation series are determined recursively and have been shown to be asymptotically convergent. Leonard in [122] proved convergence by forming the closed sum of the series in one sample problem.

Once the desired shape has been attained and its stress distribution determined, the behaviour of an air-supported structure during external loading must be analysed. A solution technique based on superposition theory has been developed to determine the static response of shells of revolution subject to symmetric [123] and non-symmetric [124] external loads. The superposed displacements were assumed linear. This restriction was later removed [126] by considering the superposed loads incrementally. After each increment of load was applied, and the response calculated, the geometry and stress state was updated before the next increment of load was added.

Solution methods developed for pattern cutting design and load analysis are applicable to arbitrary shells of revolution. More general geometries, for which exact descriptive equations are not available for the typical meridian, have been treated using Chebyshev polynomial interpolation for the meridian [125].

The dynamic behaviour of inflatable shells of revolution, described by the free and forced response of these structures to external symmetric and asymmetric dynamic loads, has been considered by various researchers [128]. Solution techniques for shells with arbitrary meridiant contours are available. Free vibration mode shapes and natural frequencies have been given for numerous examples.

7.3.2 Finite element methods

The prime effort devoted to air-supported structures of arbitrary configuration has been toward the development of finite element techniques for the nonlinear static and dynamic analysis of membrane shells. Oden was one of the first to use flat triangular elements to predict the response of a prescribed initial geometry to internal pressure [160, 161, 162]. Large strains of a nonlinear material of the Mooney-type were considered. It was assumed that the node points were sufficiently close that displacement fields within each element could be approximated by linear functions of the local coordinates. On the basis of this assumption, the Lagrangian strain tensor was expressed in terms of the node displacements and a nonlinear relation between node forces and displacements was derived. Group transformation was introduced to re-assemble the elements.

In static analyses this led to a system of highly nonlinear equations which were solved by the Newton-Raphson method. In this method, the nonlinear stiffness relations are expanded in a Taylor's series and truncated to only two terms. The first term represents a linear stiffness relation and the second term represents a correction due to increments in the node displacements. The linearised equations are solved for the displacements produced by increments in the node forces and these are introduced into the nonlinear equations to obtain corrected values for the force increments. A new set of linearised equations is then

computed using the truncated Taylor's series. By successively solving the corrected linearised equations for displacements produced by the corrected forces of the previous cycle, and correcting the node forces each time using the nonlinear equations, an iterative scheme is established. Thus obtained, numerical results compared favourably with experimental results.

The finite element formulation of the transient dynamic behaviour of air-supported structures using flat triangular elements resulted in a large system of highly nonlinear second-order ordinary differential equations for the unknown nodal displacements [163, 24]. From two classes of direct numerical time-integration methods for systems of nonlinear equations: a conditionally stable explicit scheme and an implicit scheme, which is often unconditionally stable for linearised problems, Oden [163] chose the former. In this case, the principal advantage of an implicit scheme (normally unconditionally stable for large time steps) is overshadowed by the necessity of solving a set of simultaneous nonlinear equations at each time step. The explicit dynamic procedure employed by Oden was central difference time-integration with a lumped-mass representation.

The response of air-supported structures has also been determined using strongly curved quadrilateral elements [85, 86, 127, 131-133] with Hookean isotropic behaviour assumed. Problems involving both known initial and final geometries

have been considered, with the Newton-Raphson technique being used for those problems in which the final geometry was prescribed. Incremental methods have alternatively been employed for problems in which the initial geometry was prescribed. In general, an incremental method, in which deflection increments are calculated using a tangent stiffness set not at the beginning of each increment but near the mid-point of each increment, is most efficient.

The nonlinear dynamic solution of membranes using cubic quadrilateral finite elements with Hookean material was investigated by Benzley [24] and Leonard [129]. They employed an explicit method with central difference time operators. Leonard [129] and Lo [137] suggested ways of including nonlinear stress-strain relationships (Mooney-type) into static and dynamic analyses of air-supported structures by the finite element method using quadrilateral and other elements.

7.4 Analyses of structures with strong geometric nonlinearities

7.4.1 Static analyses

Static analyses of air-supported structures by finite element methods generally rely on an estimate of the initial stiffness of the structure [200]. This implies that a stable initial state can be defined. In the most common nonlinear structural problems, the initial reference state is quite easy to define. This is so because most structures have sufficient stiffness to support their own weight. When

the weight loading is small compared to the design loads, the dead load state is not very different from the 'weightless' state.

When a very thin flat membrane is idealised by ignoring the small bending stiffness, the flat initial state has a nonsingular stiffness matrix only if the membrane is pretensioned. Attempts to calculate, by normal finite element methods, the dead loaded shape of such a membrane without pretension are thus likely to cause problems [200].

A thin flat membrane, when in an unloaded weightless condition, is essentially a mechanism with negligible intrinsic stiffness, and this general type of problem has strong geometric nonlinearities even if the initial singularity is overcome.

Presenting the statical structural problem as a functional minimisation problem and performing the minimisation numerically is an alternative to matrix type iterative (for example the Newton-Raphson method) or incremental methods. The approach usually relies on a minimum energy principle and employs nonlinear programming methods to search the problem parameters which correspond to the minimum [200]. Many nonlinear structural solutions have been obtained by energy search methods: Schmidt [178], Buchholdt [33] and Murray [152]. The last two have used energy search methods on cable networks. Very little has been done however in the application of these methods to highly nonlinear problems [200].

Another procedure for moving towards a correct solution from a nonequilibrium starting guess involves the use of dynamic equations. The starting guess with zero velocity is taken as the initial condition. The static loads are then applied and held constant and the system is allowed to move dynamically until it is artificially damped to a static solution. This effectively avoids the singularity problem if the damping and mass terms are appropriately defined. The method is termed Dynamic Relaxation.

Dynamic Relaxation was originally proposed by Day [55] and Otter [164] and was extended to the form-finding and static analysis of cable and membrane structures by Barnes [8-10, 12-15]. The method is based solely upon Newton's second law of motion and the stress-strain relations of the structural components under consideration. It has been frequently used in conjunction with finite differences [9].

In this basic form, dynamic relaxation traces the movement of a structure from the time when it is initially loaded until, due to viscous damping, the system reaches a steady equilibrium state. Most rapid convergence is achieved when fictitious nodal mass components are all adjusted to be proportional to corresponding direct stiffness components, and viscous damping is near the critical value [9].

An alternative dynamic relaxation procedure suggested by Cundall [48] for rock mechanics problems, termed 'kinetic damping', has been found to be more stable with convergence

more rapid when large residuals are imposed [197]. In this procedure, the undamped motion of the structure is traced and when a local peak in the total kinetic energy of the system is detected, all velocity components are set to zero. The process is then restarted from the current geometry and continued through further (generally decreasing) peaks until the energy of all modes of vibration has been dissipated and static equilibrium is achieved.

In a comparative study of dynamic relaxation with other vector and matrix methods applied to tension structures it was concluded [10, 130], that dynamic relaxation was the most efficient vector method and compared in efficiency with the Newton-Raphson matrix method; the latter being preferable for structures with a small stiffness matrix band width, and the former for surface structures. Dynamic relaxation has a number of other advantages, especially when used for membrane structures [14]:

1. the analysis always converges provided mass components comply with the stability criterion,
2. the separation of equilibrium and compatibility conditions allows complex stress/strain relations or on/off nonlinearities to be accounted for,
3. high localised energy disturbances tend to be rapidly dissipated before their effects are propagated throughout other regions (especially useful in form-finding),
4. Stiffness and mass matrices of the complete assemblage need not be calculated; the calculations are

essentially carried out at the element level, and

5. the process can be easily extended to solve dynamic problems by the explicit method known as central difference integration.

7.4.2 Dynamic Analyses

Generally applicable methods for the dynamic analysis of arbitrary nonlinear systems are the numerical step-by-step direct integration methods which can be performed by two different techniques: implicit or explicit. The implicit techniques require fewer time steps as they are more stable (and for linear problems unconditionally stable) but at each time step a complete set of simultaneous nonlinear equations has to be solved. When nonlinearities are large this may involve iteration by the Newton-Raphson method; hence the stiffness matrix has to be calculated not only at the beginning of each time step but as frequently as is required by the Newton-Raphson scheme [14].

In explicit methods, which are conditionally stable (generally smaller time steps are essential for stability), due to the introduction of a simple relationship between displacement, velocity and acceleration, only one vector needs to be calculated at each step, and this may be evaluated by any standard simultaneous-equation-solution procedure. If, in addition, the mass matrix is diagonal, the method may be formulated as a vector method (the re-assembled stiffness matrix is not generated and calculations are carried out on the element level) The explicit approach

using a central difference scheme is very often regarded as the best for solving highly nonlinear dynamic problems [42, 46, 17]. The main shortcomings, in a general sense, of this approach are: that the time step used in the finite difference formulation must be smaller than a critical value which is calculated from the mass and stiffness properties of the element assemblage, and that the effectiveness of the procedure depends on the use of a diagonal mass matrix and the neglect of general velocity-dependent damping forces [17].

Oden et al [163] suggested, in relation to flexible membranes, that as one of the parameters taken into account in choosing the time step in an implicit method is dependent upon the required accuracy of modelling, the time step used in an implicit method can be as small as that required for numerical stability of an explicit scheme. Krieg and Key [111] compared the accuracy of explicit central difference integration with a family of implicit schemes for modelling the frequency response of membrane and bending deformations of shells. For equal computational work the central difference process with lumped masses was shown to be more efficient than the best available implicit scheme. Johnson and Grief [101] considered a wider class of problems and concluded that the central difference process is most efficient when the response varies rapidly.

Barnes in his investigations [7, 11] of vibration decay in a pneumatic dome compared experimental results for the

deflections at the apex of a suddenly loaded inflated dome with numerical analysis predictions. The dome was approximated numerically by triangular flat elements with masses lumped at the nodes and the results compared well with experimental values. The explicit method using a central difference scheme, was formulated in such a way that displacement components at each node were determined purely in terms of the previous displacements and residual nodal forces predicted from these displacements and the creep strains which had previously taken place. The membrane material was assumed to be visco-elastic and was represented numerically by a single Kelvin model [208]. The creep strain calculations, checking for buckling and reformulation of stiffness matrices were performed at less frequent intervals than the basic finite difference time step procedure.

Many other explicit methods are available such as the Euler method or higher order schemes [98], all of which may be adopted for nonlinear dynamic analysis. Few of these have, however, been applied to air-supported structures [13].

CHAPTER 8

Dynamic relaxation method for the static analysis of air-supported structures

Contents:

In this chapter, pneumatic domes constructed from orthotropic woven fabric and lightweight polythene, subject to static loads applied centrally and asymmetrically are analysed using dynamic relaxation. The dynamic relaxation method for tension membranes is reviewed with emphasis on a version employing kinetic damping. Structural idealisation depending on the fabric patterning, type of loading and membrane material are discussed. The static analyses of the domes are performed in such a way that they describe the behaviour of the models used in the tests discussed in chapter 10. The resulting stresses and deflections are employed as initial states in the dynamic analyses of chapters 9, 11 and 12.

8.1 Dynamic relaxation - a review

8.1.1 Formulation of the method

The static equilibrium state of a structure initially unbalanced can be found by following its movement step by step for small time increments, Δt, from the moment of loading until the point when, due to damping, all velocities tend to zero.

The equation of motion for a structural system, which is idealised by a discrete assembly of elements is [42]:

$$M\ddot{X} + C\dot{X} + KX = R_E \qquad 8.1$$

where

M, C, K are the mass, damping and stiffness matrices,

R_E is the external load vector, and

X, $\dot{X}$ and $\ddot{X}$ are the displacement, velocity and acceleration vectors.

A dot above any symbol represents differentation with respect to time. Each term on the left hand side of equation 8.1 represents component force vectors:

$M\ddot{X} = F_I$ - are the inertia forces,

$C\dot{X} = F_D$ - are the damping forces, and

$KX = F_E$ - are the internal elastic forces

Equation 8.1 can be rearranged as:

$$M\ddot{X} + C\dot{X} = R_E - F_E = R \qquad 8.2$$

Now the left hand side of equation 8.2 represents the forces which are motion dependent; i.e. the forces which are equal to zero when the static state of equilibrium is reached. This implies that, if equation 8.2 is applied to the static analysis any divergence from the real values of forces F_I and F_D does not influence the final static displacements and stresses.

There are broadly two different types of dynamic relaxation method employed for the static analysis of pneumatic structures [12]:

1. With viscous damping. By appropriately adjusted coefficients in the damping matrix, which when a body is in motion results in 'viscous forces', the system is brought to rest;

2. With kinetic damping. In this procedure the damping forces are set to zero and the motion of all structural nodes is traced until a kinetic energy peak is reached. Then all velocity components are reset to zero and the process is continued through further decreasing kinetic energy peaks until equilibrium is obtained.

In the majority of efficient dynamic relaxation schemes the real masses are substituted by fictitious masses which are determined from the stability criteria [12].

Equation 8.2 can be expressed in terms of velocities, namely

$$M\dot{V} + CV = R \qquad 8.3$$

Where $V = V(t) = \dot{X}$ is a velocity, and

$\dot{V} = \ddot{X}$

Knowing the value of velocity at time t, V(t), a velocity at time $t + \Delta t/2$ and $t - \Delta t/2$ can be incorporated in the Taylor's expansion of function V(t) [169]:

$$V(t + \Delta t/2) = V(t) + \frac{t}{2}\dot{V}(t) + \frac{\Delta t^2}{8}\ddot{V}(t) + \ldots . \qquad 8.4a$$

$$V(t - \Delta t/2) = V(t) - \frac{t}{2}\dot{V}(t) + \frac{\Delta t^2}{8}\ddot{V}(t) + \ldots . \qquad 8.4b$$

If $\Delta t/2$ is small all the terms of order $(\Delta t/2)^2$ and higher can be neglected, i.e.

$$V(t + \Delta t/2) = V(t) + \frac{\Delta t}{2}\dot{V}(t) \qquad 8.5a$$

$$V(t - \Delta t/2) = V(t) - \frac{\Delta t}{2}\dot{V}(t) \qquad 8.5b$$

By subtracting equation 8.5b from equation 8.5a the following can be obtained:

$$\dot{V}(t) = \frac{V(t + \Delta t/2) - V(t - \Delta t/2)}{\Delta t} \qquad 8.5c$$

Equation 8.5c known as the Euler-Cauchy or second order formula is employed in the central finite difference scheme.

For a small time interval, Δt, changes in velocities can be assumed to be linear, hence equation 8.2 in the central finite difference scheme takes the form:

$$R^t = \frac{1}{\Delta t} M(V^{t+\Delta t/2} - V^{t-\Delta t/2}) + \frac{1}{2} C(V^{t+\Delta t/2} + V^{t-\Delta t/2}) \qquad 8.6$$

The left hand side of equation 8.6, R^t, comprises external forces defined as a vector for each node and internal, elastic forces, F_I, which can be evaluated on an element level from the 'natural element stiffness' and nodal displacements of an element. When the finite element formulation is used the internal elastic forces can then be expressed in a vector form for each node of the element. Next, by assuming the mass and damping matrices in diagonal form the whole equation 8.6 can be reduced to a vector form. The equation expressing the equilibrium condition for any node i in the x direction is:

$$R_{ix} = \frac{M_i}{\Delta t} (V_{ix}{}^{t+\Delta t/2} - V_{ix}{}^{t-\Delta t/2}) + \frac{1}{2} C_i (V_{ix}{}^{t+\Delta t/2} + V_{ix}{}^{t-\Delta t/2}) \qquad 8.7$$

Thus defined, the analysis enables separated treatment of equilibrium and compatibility conditions which may be particularly useful for the solution of nonlinear problems.

(In nonlinear static analysis, almost all matrix methods require combining these two conditions together). In the dynamic relaxation method, one higher order equation is replaced, by two lower order equations.

8.1.2 Dynamic relaxation with viscous damping [9]

Graphs shown in figure 8.1 illustrate typical responses of a viscously damped single degree of freedom system with various damping levels, ξ, and

$$\xi = \frac{C}{2 m \omega_n} \qquad 8.8$$

where

m is the mass

C is the viscous-damping, and

ω_n is the undamped circular natural frequency

For $\xi = 1$, the system is critically damped and the amplitude decays more rapidly than in either the underdamped ($0 < \xi < 1$) or overdamped ($\xi > 1$) cases.

The obvious conclusion is that in order to obtain the quickest convergence in the dynamic relaxation method, the value of fictitious damping should be as close as possible to the critical damping or just sub-critical. The damping constant C_i (see equation 8.7) generally takes the form

$$C_i = M_i \, (C'/\Delta t) \qquad 8.9$$

where $C' = 4\pi \, f M_i$ and f is the fundamental frequency.

The structural frequency, f, may be obtained as the lowest frequency from a short undamped run [9]. The recurrence equation for velocities, using dynamic relaxation with viscous damping can be derived from equations 8.7 and 8.8 as

$$V_x^{t+\Delta t/2} = V_x^{t-\Delta t/2} \frac{1 - C'/2}{1 + C'/2} + R_{ix}^{t} \frac{\Delta t}{M_i} \frac{1}{1 + C'/2} \quad 8.10$$

8.1.3 Dynamic relaxation with kinetic damping [197, 14]

Figure 8.2 shows a ball suspended from a fixed point on an inextensible string and allowed to move only in the plane of the drawing, (a single degree of freedom system). The ball is set into motion by applying a force F and immediately releasing it. The point of maximum kinetic energy of the system, figure 8.2c, is the same as the point of static state equilibrium. This analogy, when extended to multi degree of freedom systems, is the core of the dynamic relaxation method with kinetic damping.

For a real structure, however, the process does not terminate, when a first peak of kinetic energy of the system is reached, but must be continued, eliminating the kinetic energy from other modes by tracing the energy through further peaks, until static equilibrium is reached (in practice, until the maximum residual unbalanced force at any node has a very small value).

The recurrence equation for velocity at $t = t + \Delta t/2$, is obtained from equation 8.7 by setting C_i to zero:

$$V_{ix}^{t+\Delta t/2} = V_{ix}^{t-\Delta t/2} + R_{ix} \frac{\Delta t}{M_i} \quad 8.11$$

To account for $V_x = 0$ at the start of the process and the linear variation in velocities between times $t-\Delta t/2$ and $t+\Delta t/2$, velocities at the mid-point of the first time step are given by [14]:

$$V_{ix}^{\Delta t/2} = R_{ix} \frac{\Delta t}{2M_i} \qquad 8.12$$

The new x coordinates of node i is then

$$X_i^{t+\Delta t} = X_i^{t} + \Delta t * V_{ix}^{t+\Delta t/2} \qquad 8.13$$

and the kinetic energy component, KE, is:

$$2 \quad KE_{xi}^{t+\Delta t/2} = V_{xi}^{t+\Delta t/2} \times M_i \times V_{xi}^{t+\Delta t/2} \qquad 8.14$$

The kinetic energy of the complete system is calculated by summing up the kinetic energies of all nodes in the x, y and z directions.

If the kinetic energy of the system computed using velocities at $t+\Delta t/2$ is then found to be less than the previous value at $t-\Delta t/2$, a peak has been passed. Ideally, velocities should be set to zero and the process restarted with coordinates corresponding to the point at which a local maximum kinetic energy occurred. Barnes [13, 14] and Wakefield [197] suggest three different approaches to establish nodal coordinates, X_{iKEP}, at this kinetic energy peak:

1. By assuming that the kinetic energy peak occurred at time $t-\Delta t/2$, and that nodal coordinates vary linearly between $t-\Delta t$ and t; for a small Δt,

   $$X_{iKEP} = X_i^{t-\Delta t/2} = \tfrac{1}{2} (X_i^{t} + X_i^{t-\Delta t}) \qquad 8.15$$

   Both velocities and coordinates are incremented within the same loop in the program (see figure 8.7), hence X_i^{t}, $V_{ix}^{t+\Delta t/2}$ and R_{ix}^{t} are the variables currently in store when a peak is located. The reinitialisation coordinates in terms of variables currently in store

can thus be obtained using equations 8.11, 8.13 and 8.15 [197] as:

$$X_i^{t-\Delta t/2} = X_i^{t+\Delta t} - \frac{3\Delta t}{2} V_{ix}^{t+\Delta t/2} - \frac{\Delta t^2}{2M_i} R_{ix}^{t} \qquad 8.16$$

2. In the central difference approximation to the dynamic analogy, nodal velocities are assumed to vary linearly between $t-\Delta t/2$ and $t+\Delta t/2$. Consequently the variation of displacement increment is quadratic within that interval. Working on this assumption Wakefield [197] gives an alternative expression for the reinitialisation coordinates as

$$X_{iKEP} = X_i^{t-\Delta t/2} = X_i^{t+\Delta t} - \frac{3}{8}\Delta t \left(4 \times V_{ix}^{t+\Delta t/2} - \frac{\Delta t}{M_i} R_{ix}^{t}\right) \qquad 8.17$$

3. The kinetic energy peak is obtained more accurately by fitting a quadratic polynomial through the current (C) and two previous kinetic energy values (A and B) (see figure 8.3). For linearly varying displacements between $t-\Delta t$ and t, and a more precisely traced energy peak, Barnes [13] derived the formula for the coordinates corresponding to the kinetic energy peak as:

$$X_{iKEP} = X_i^{t+\Delta t} - \Delta t\ (1 + q) \times V_{ix}^{t+\Delta t/2} + \frac{\Delta t^2}{2} q\, R_{ix}^{t} \qquad 8.17$$

Where

$$q = \frac{C - B}{(C-B) - (B-A)}$$

and A, B, C are values of kinetic energy at $t = t-3\Delta t/2$, $t = t-\Delta t/2$ and $t = t+\Delta t/2$ respectively.

On restarting the process, velocities at the mid-point of the first time step are given by equation 8.12. Thereafter velocities are updated according to equation 8.11 until the next energy peak.

The dynamic relaxation method with kinetic damping does not require a trial analysis to establish any parameters (contrary to the method with viscous damping), hence it is easier to implement with automatic control. Additionally it has been found [197, 13] that the method copes very well with any gross out of balance forces.

The dynamic relaxation method with kinetic damping will be used for static analysis of air-supported structures described in this chapter.

8.1.4 Stability criteria and fictitious nodal masses

Dynamic relaxation is an explicit time integration scheme which is conditionally stable i.e. the time step, Δt, should be smaller than a critical value, Δt_{cr} otherwise deflections, velocities and forces grow without any bound.

For the conditionally stable, central difference scheme, the time step length is limited by the expression [166]

$$\Delta t \leq \frac{2}{\omega_{max}} \qquad 8.18$$

where

ω_{max} is the highest circular frequency of the finite element assembly. Providing that ω_{max} represents the

maximum nonlinear frequency, equation 8.18 holds for nonlinear problems. The estimate of the critical time step does not necessitate the solution of the eigen value problem for the whole system, or any trial run. The bound on the highest eigen value can be obtained by consideration of an individual element. This is established by an important theorem proposed by Irons [96] which proves that the highest system eigen value must always be less than the highest eigen vlue of the individual elements.

The critical time step with a reference to dynmic relaxation was estimated by Casell [36, 37], and also directly derived by Barnes [9]. The latter considered the relative motion of adjacent nodes of a net like structure and obtained the expression for the critical time step for a node i as

$$\Delta t_{crit} = \sqrt{\frac{2M_{xi}}{S_{xi}}} \qquad 8.19$$

where

X refers to the local maximum stiffness direction.

For static analysis, no real values of masses need to be used, hence the problem of formulating the stability criteria can be reversed. The value of Δt may be chosen arbitrarily and, from equation 8.19, 'fictitious' mass components may be evaluated [13] as:

$$[M_i] = \frac{\Delta t^2}{2} [S_i] \qquad 8.20$$

where $[M_i]$ and $[S_i]$ are 3 x 3 diagonal matrices whose components are expressed in the coordinate system related to

the principal stiffness directions. Equation 8.20 when transformed to the global system {X*} by the transformation

takes the form $$\{X_i\} = [T_i] \{X_i^*\} \qquad 8.21$$

$$[M_i^*] = \frac{\Delta t^2}{2} [T_i]^T [S_i] [T_c] = \frac{\Delta t^2}{2} [S_i^*] \qquad 8.22$$

where

$[M_i^*]$ and $[S_i^*]$ are square full matrices.

Computationally it is more convenient to use a diagonal mass matrix.

For analysis of membrane structures, Barnes concludes [13], that a stable procedure is to set lumped mass components according to the Gershorin bound as

$$[\overset{*}{M}_{xi}] = \frac{\Delta t^2}{2} (\mid \overset{*}{S}_{xx} \mid + \mid \overset{*}{S}_{xy} \mid + \mid \overset{*}{S}_{xz} \mid)_i \qquad 8.23$$

Where

$\mid \overset{*}{S}_{xj} \mid_i$ are the absloute values of the global direct stiffness components at node i.

In the form-finding of tension structures, changes in geometry are so large that the greatest possible stiffness at any node should be used for each coordinate direction. Thus

$$\overset{*}{M}_{xi} = \overset{*}{M}_{yi} = \overset{*}{M}_{zi} = \frac{\Delta t^2}{2} \cdot S_{i\ max} \qquad 8.24$$

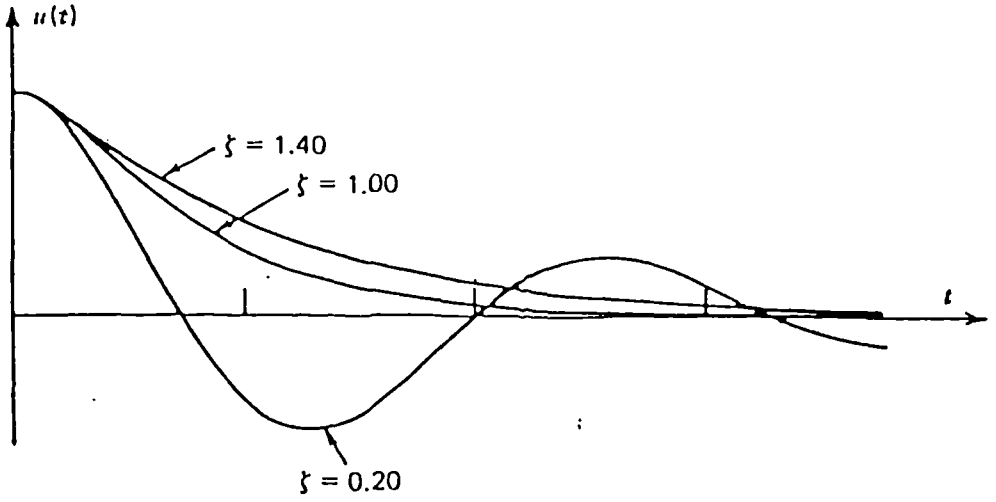

Figure 8.1

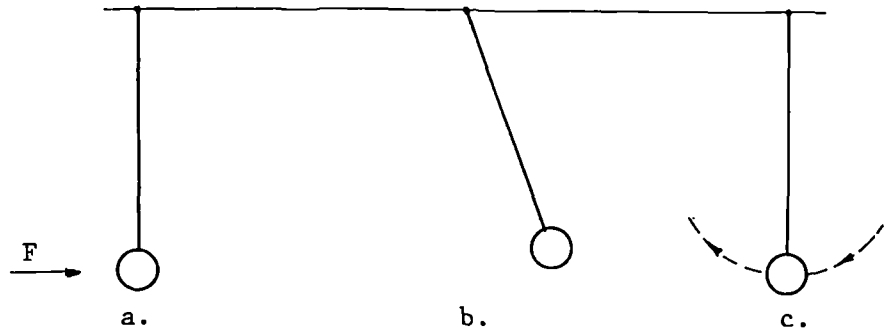

Figure 8.2

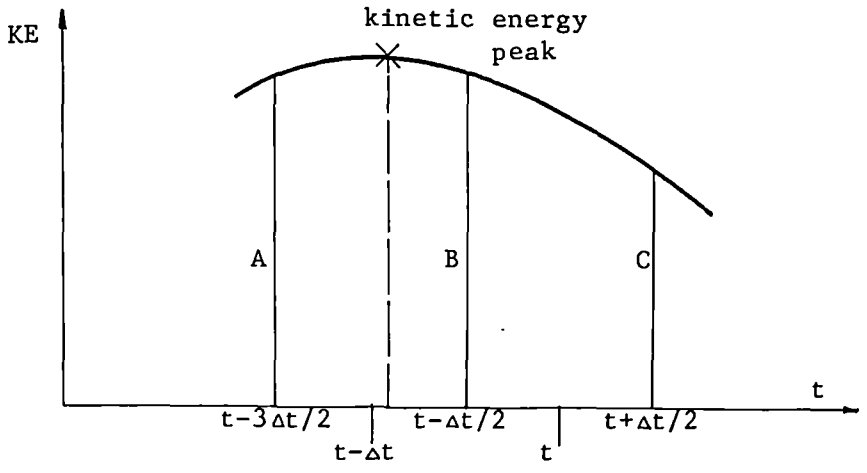

Figure 8.3

8.2 Structural idealization and natural stiffness matrices

Membranes of pneumatic structures are idealised most commonly [13], for purposes of numerical analysis by dynamic relaxation, into a set of nodes interconnected by straight links forming the edges of constant strain triangular elements (and/or discrete constant strain line elements). The size, layout and type of idealisation depend mainly upon: the size and shape of structure, pattern cutting and material properties.

Four types of idealization can be distinguished:

1. isotropic - membrane material posses isotropic properties
2. orthotropic - membrane material, like most coated fabric, has two dominant, mutually perpendicular directions of stress path: warp and weft (USA fill). The pattern cutting is such that, when the structure is assembled and pretensioned, the directions of principal stresses coincide with those of warp and weft.
3. line elements - the membrane material is similar but in analysis the directions of principal stresses are forced to be those of warp and weft, and the shear stiffness of the membrane is disregarded.
4. line elements and coating - similar to type 3, but with shear stiffness accounted for

The procedures for calculation of the natural stiffness matrix for each element of the assembly and hence also the internal forces for given nodal displacements, are different for each type of idealisation. The similarities between

these approaches, especially between types 1 and 2, and between 3 and 4, enable us to discuss them in pairs:

For any type of membrane triangular element, i, the side tensions at any stage of the dynamic relaxation scheme are given by [9]

$$\left\{\begin{matrix} T_1 \\ T_2 \\ T_3 \end{matrix}\right\}_i^t = \left\{\begin{matrix} T_1 \\ T_2 \\ T_3 \end{matrix}\right\}_i^{in} + [K]_i^t \times \left\{\begin{matrix} \delta e_1/l_1 \\ \delta e_2/l_2 \\ \delta e_3/l_3 \end{matrix}\right\}_i^t \qquad 8.25$$

where

$\{T\}_i^{in}$ are the intial side tensions,

$[K]_i^t$ is the natural 3 x 3 stiffness matrix in a local coordinate system (see figure 8.4). (When large changes of geometry occur, the natural stiffness matrix needs to be recalculated after each few steps), and

$\{\delta e_j/l_j\}_i^t$ are the elastic side strains from the initial state.

In practice the initial side tensions, $\{T\}_i^{in}$, are calculated from the initial stresses as follows [9]

$$\{T\}_i^{in} = \left[\frac{1}{l_1}, \frac{1}{l_2}, \frac{1}{l_3}\right] \times [G^T]_i^{in} \times \left\{\begin{matrix} \sigma_x \\ \sigma_y \\ \sigma_{xy} \end{matrix}\right\}_i^{in} \times A_i^{in} \times th \qquad 8.26$$

where

A_i^{in} and th are the area and thickness of the element, and

$[G^T]_i^{in}$ is the transpose matrix of $[G]_i^{in}$.

The $[G]_i^{in}$ ($[G]_i^{t}$) transforms the initial (current) vector of side strains $\{\delta e_j/l_j\}_i^{in}$ ($\{\delta e_j/l_j\}_i^{t}$) into the strains expressed in the local coordinate system:

$$\begin{Bmatrix} \varepsilon_x \\ \varepsilon_y \\ \gamma_{xy} \end{Bmatrix}_i^{in} = [G]_i^{in} \begin{Bmatrix} \delta e_1/l_1 \\ \delta e_2/l_2 \\ \delta e_3/l_3 \end{Bmatrix}_i^{in} \qquad 8.27$$

For a 'constant strain' triangular element, the natural stiffness matrix, $[K]_i^{t}$, is defined in local coordinates as [9]:

$$[K]_i^{t} = [1/l_1,\ 1/l_2,\ 1/l_3] \times [G^T]_i^{t} \times [D]_i^{t} * [G]_i^{t} \times A_i^{t} \times th \qquad 8.28$$

Where

$[D]_i^{t}$ is the elasticity matrix

Isotropic and orthotropic elements

For plane stresses in an isotropic material, matrix [D] is obtained from the generalised Hooke's law [188]

$$[D] = \begin{bmatrix} E/_{1-\nu^2}, & \nu \frac{E}{1-\nu^2} & 0 \\ \nu \frac{E}{1-\nu^2} & \frac{E}{1-\nu^2} & 0 \\ 0 & 0 & \frac{2E}{1+\nu} \end{bmatrix} \qquad 8.29$$

where

E is the modulus of eleasticty, and

ν is the Poisson's ratio.

For orthotropic membrane material [D] is [188]:

$$[D] = \begin{bmatrix} \frac{E_x}{1-\nu_x \nu_y}, & \nu_y \frac{E_x}{1-\nu_x \nu_y}, & 0 \\ \nu_x \frac{E_y}{1-\nu_x \nu_y}, & \frac{E_y}{1-\nu_x \nu_y}, & 0 \\ 0 & 0 & d_{33} \end{bmatrix} \qquad 8.30$$

Where

E_x, E_y are the moduli of elasticity in the x and y directions respectively, here in the warp and weft directions,

ν_x, ν_y are the Poisson's ratios in the x and y directions respectively, and

d_{33} is the shear rigidity, which is normally less than 1/15 of the rigidity in tension.

Here it is assumed to be

$$\frac{d_{11} + d_{22}}{30} = \frac{E_x + E_y}{30(1-\nu_x \nu_y)}$$

The membrane is idealized by a set of triangular elements, as shown in figure 8.5, in such a way that local coordinates coincide with warp and weft directions (for orthotropic membranes) and additionally, to simplify mathematical calculations, the x direction is parallel to one side of an element.

The matrix [G] is more conveniently obtained, as the inverse of matrix [A], where [A] is defined by

$$\begin{Bmatrix} \varepsilon_1 \\ \varepsilon_2 \\ \varepsilon_3 \end{Bmatrix} = [A] \times \begin{Bmatrix} \varepsilon_x \\ \varepsilon_y \\ \gamma_{xy} \end{Bmatrix} \qquad 8.31$$

and in general:

$$[A] = \begin{bmatrix} \cos^2\theta_1 \; ; \; \sin^2\theta_1 \; ; \; \cos\theta_1\sin\theta_1 \\ \cos^2\theta_2 \; ; \; \sin^2\theta_2 \; ; \; \cos\theta_2\sin\theta_2 \\ \cos^2\theta_3 \; ; \; \sin^2\theta_3 \; ; \; \cos\theta_3\sin\theta_3 \end{bmatrix} \qquad 8.32$$

Where θ_1, θ_2 and θ_3 are the angles between the positive x axis direction and the sides of the element (see figure 8.4). When $\theta_1 = 0$, as shown in figure 8.5

$$[A] = \begin{bmatrix} 1 & 0 & 0 \\ \cos^2\theta_2 \; ; & \sin^2\theta_2 \; ; & \cos\theta_2\sin\theta_2 \\ \cos^2\theta_3 \; ; & \sin^2\theta_3 \; ; & \cos\theta_3\sin\theta_3 \end{bmatrix} \qquad 8.33$$

Line, and line and coating elements

For cross-coupled line elements:

$$[D] = \begin{bmatrix} \frac{E_x}{(1-\nu_x\nu_y)} & \nu_y\frac{E_x}{(1-\nu_x\nu_y)} \\ \nu_x\frac{E_y}{(1-\nu_x\nu_y)} & \frac{E_y}{(1-\nu_x\nu_y)} \end{bmatrix} \qquad 8.34$$

and for line and coating elements

$$[D] = \begin{bmatrix} \frac{E_x}{1-\nu_x\nu_y} & \nu_y\frac{E_x}{1-\nu_x\nu_y} & 0 \\ \frac{\nu_x E_y}{1-\nu_x\nu_y} & \frac{E_y}{1-\nu_x\nu_y} & 0 \\ 0 & 0 & d_{33} \end{bmatrix} \qquad 8.35$$

where d_{33} is the 'shear rigidity' the value of which is obtained directly from tests (see chapter 10), as a modulus of elasticity for the coating.

In the line idealization it is assumed that the shear stiffness of the membrane is of small order when compared with the direct stiffnesses, hence it may be disregarded. Consequently at each point of the membrane only direct stresses (tensile) exist and their directions are those of warp and weft. The most obvious elements to be used are quadrilateral, as close as possible to rectangular with sides being parallel to the warp and weft directions. In cases where this type of idealization is included in the general numerical procedure used to analyse membrane structures, it may however be more convenient to employ triangular elements. Right angle elements as shown in figure 8.6 are especially suitable.

In the case of 'line' idealizations equations 8.25-8.28 take much simpler forms. They are given below:

$$\begin{Bmatrix} T_1 \\ \\ T_2 \end{Bmatrix}^t_i = \begin{Bmatrix} T_1 \\ \\ T_2 \end{Bmatrix}^{in}_i + [K]^t_i \begin{Bmatrix} \delta e_1/l_1 \\ \\ \delta e_2/l_2 \end{Bmatrix}^t_i \qquad 8.25a$$

$$\{T\}^{in}_i = \left\{ \frac{1}{l_1}, \frac{1}{l_2} \right\} \times \begin{Bmatrix} \sigma_x \\ \sigma_y \end{Bmatrix} \times A^{in}_i \times th \qquad 8.26a$$

$$\begin{Bmatrix} \varepsilon_x \\ \varepsilon_y \end{Bmatrix}^{in}_i = \begin{Bmatrix} \delta e_1/l_1 \\ \delta e_2/l_2 \end{Bmatrix}^{in}_i \qquad 8.27a$$

and

$$[K]^t_i = \{1/l_1, 1/l_2\} [D]^t_i \times A^t_i \times th \qquad 8.28a$$

The matrix [G] is equal to unity and the 'natural' stiffness is only 2 x 2.

The most common materials used for air-houses are coated fabrics in which direct tensile stresses are resisted mainly by warp and weft fibres of the fabric. On the other hand, when this material is stretched in the diagonal direction, the coating which acts as a diaphragm and a stabilizer of fabric will oppose any movement. Hence, the behaviour of coated fabrics can be represented using a line and coating idealization as a superposition of two actions: fabric working in direct tension and coating preventing gross distortion produced by shear stresses.

In the case of a line and coating idealization, when a membrane is modelled by an assembly of triangular elements as shown in figure 8.6, the internal forces and 'natural' stiffness matrix are given by equations 8.25-8.28, in which the [G] matrix is equal to unity.

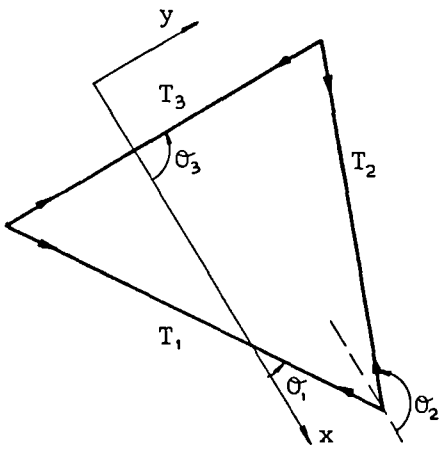

Figure 8.4

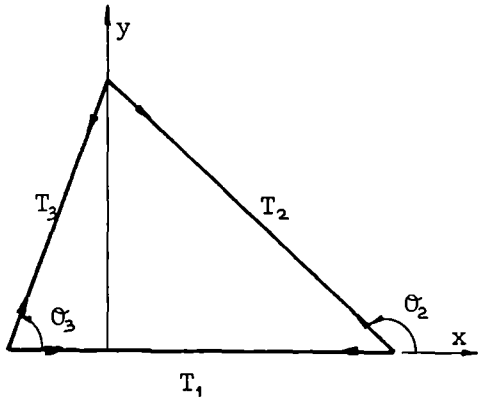

Figure 8.5

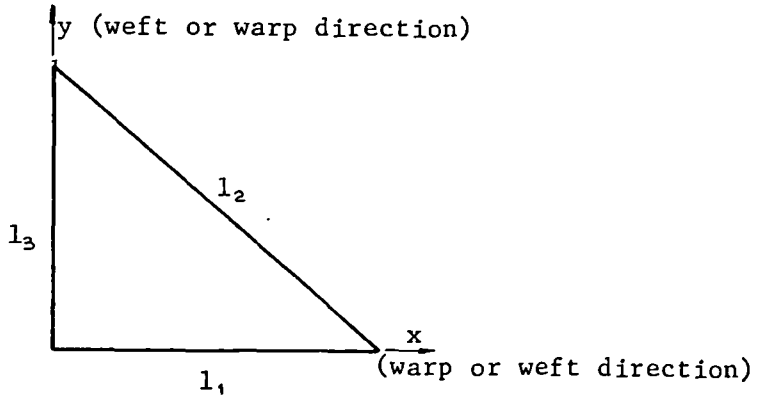

Figure 8.6

8.3 Scheme for analysis of air-supported structures

The main steps in the numerical analysis of air-supported structures by the dynamic relaxation method with kinetic damping are shown in figure 8.7. Calculations of initial tensions in every element (for the load analysis) are based on equation 8.25 (or 8.25a). Stiffness matrices are, as explained in the subclause 8.2, found in the local coordinate system at the element level only. Fictitious masses, as defined by equation 8.24 are obtained first for each node of every element and then their appropriate values are summed up to give the global nodal masses:

$$M_i = \sum_{i=1,n} M_{ki} \qquad 8.36$$

The residual forces at a node i, resulting from the tension, T_{jk}, in a link j belonging to an element k are given (in global coordinates) by:

$$R_{ix} = R_{ix} + \left(\frac{DX_j}{L_j}\right)_k \times T_{jk} \qquad 8.37$$

where

DX_j denotes the difference between the end nodal coordinates of the link j in the x direction, and

L_j is the current length of link j.

Contributions to the residual static forces due to external forces are:

1. concentrated applied loads and distributed gravitational loads lumped at nodes (P_{ix}, P_{iy}, P_{iz})
2. distributed pressure load, p_i, normal to the membrane elements: internal pressure with outward resultant, p_{in}, and external (for example due to wind or snow) with inward or outward resultant, p_{ex}.

The internal pressure component is expressed as a function of changes in the internal volume, caused by deformation of the whole structure, (at approximately constant internal air mass) by [7]:

$$p_{in}^{t} = (p_{in}^{t-\Delta t} + p_{ex}) \left(\frac{V_o^{t-\Delta t}}{V_o^{t}}\right)^{\alpha} - p_{ex} \qquad 8.38$$

where

t and Δt are the time and the time step used in the dynamic relaxation scheme,

p_{ex} is the external atmospheric pressure,

$V_o^{t-\Delta t}$, V_o^{t} are the internal volumes of the pneumatic structure at $t-\Delta t$ and t respectively, and

$\alpha \longrightarrow 1 \div 1.4$

Equation 8.38 is derived from the thermodynamic law describing isentropic expansion or compression of air [193].

The external static pressure due to wind is given by (see chapter 4, equation 4.1):

$$p_{ex} = \tfrac{1}{2} \rho_a C_p V \qquad 8.39$$

If $\bar{A}$ and $\bar{B}$ represent two vectors of common beginning lying along two adjacent links of an element K_e and if

$$\bar{A} = a_x\bar{i} + a_y\bar{j} + a_z\bar{k}$$
$$\bar{B} = b_x\bar{i} + b_y\bar{j} + b_z\bar{k} \qquad 8.40$$

where $\bar{i}$, $\bar{j}$, $\bar{k}$ are the unit vectors in the x, y and z direction respectively,

then the x, y and z components of pressure forces at each node of the element, k_e, are

$$\begin{Bmatrix} p_x \\ p_y \\ p_z \end{Bmatrix} = \frac{p}{6} = (\bar{A} \times \bar{B}) \qquad 8.41$$

where

$p = p_{int} + p_{ext}$, and

$\bar{A} \times \bar{B}$ is a vector product:

$$\bar{A} \times \bar{B} = \begin{bmatrix} i & j & k \\ a_x & a_y & a_z \\ b_x & b_y & b_z \end{bmatrix} \qquad 8.42$$

The recurrence equations for nodal velocities, coordinates, total kinetic energy, and the reset nodal coordinates are given by equations 8.11 to 8.17.

The three approaches to estimate values of coordinates at the kinetic energy peak were investigated for a pneumatic membrane structure, and, similarly to the findings of Wakefield [197] (see 8.13) for net structures it was found that there was no clear advantage in using any one particular method. The simplest approach, the method Nr 1, in which it is assumed that displacements vary linearly between $t-\Delta t$ and t, and that the kinetic energy peak occurs at $t=t-\Delta t/2$, will be used in this work.

In most cases, the principal static stresses in pneumatic structures are tensile [165]. In some investigations, like for example: examining instability or behaviour of low inflated air-houses, areas of zero stresses may occur. The numerical procedure, where checking for buckling is included in the dynamic relaxation scheme for tension structures is presented in works by Barnes [9, 13] and Wakefield [197]. This requires additional operations at every few cycles in addition to those given in figure 8.7. These operations

include: determination of principal stresses, setting to zero those which are negative, modifying the D matrices, and recalculating modified stresses. Adding the check for buckling increases the amount of computing and can cause slower convergence [197, 9]. Hence, in cases where this phenomenon is not likely to be present at the final static solution, it may be preferable not to include the checking. Such checks are however essential at the end of the program when the static equilibrium state has been determined. If any area of zero stresses are detected, the structure should then be recalculated using the scheme with checking for buckling every few cycles.

For those air-supported structures which experience large deformations, stiffness matrices should be recalculated at every NSM cycle (see figure 8.7). The number of cycles, NSM, depends mainly upon the degree of geometric nonlinearity and varies from 1 for highly deformable structures to infinity for a linear analysis.

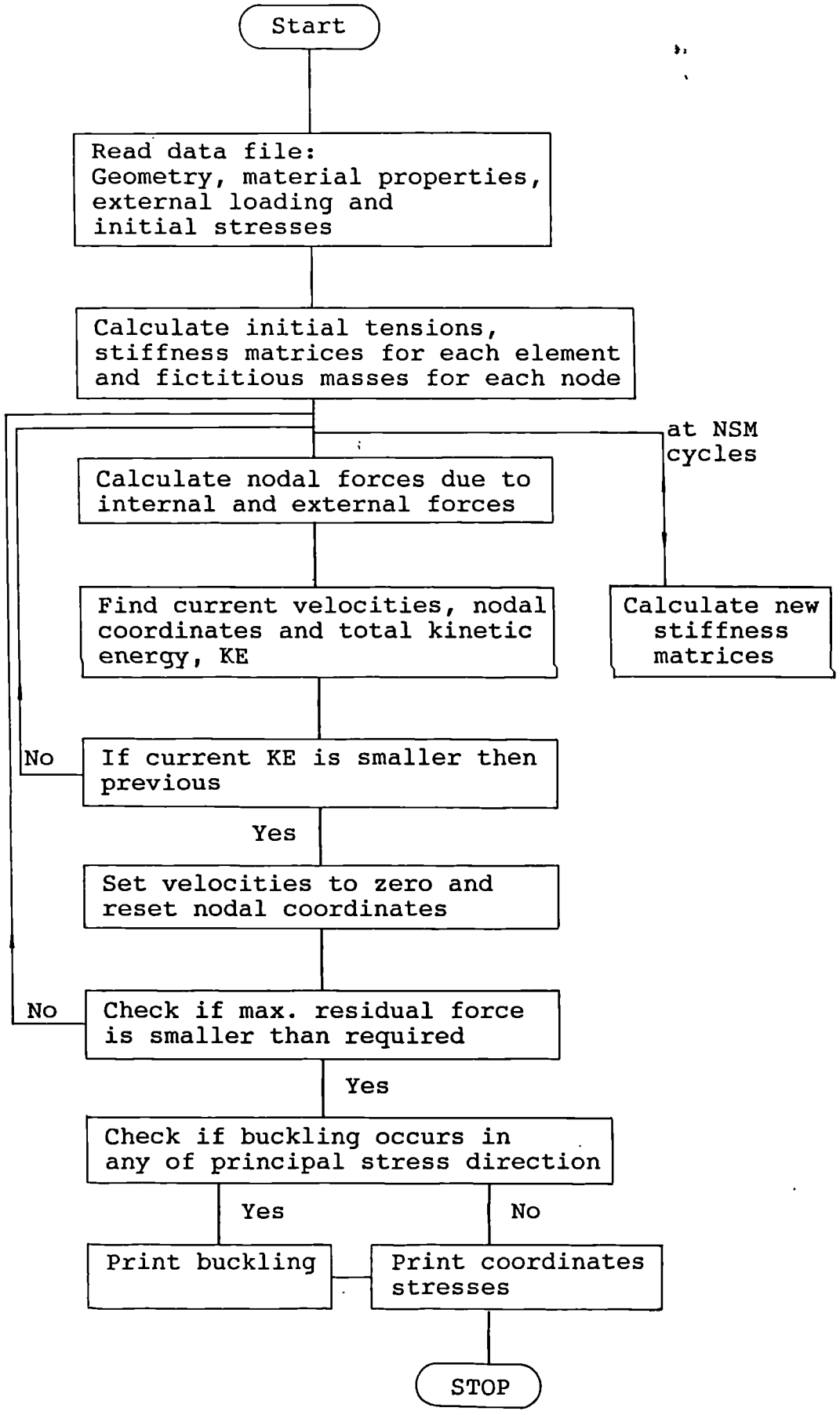
Start
Read data file:
Geometry, material properties,
external loading and
initial stresses
Calculate initial tensions,
stiffness matrices for each element
and fictitious masses for each node
at NSM
cycles
Calculate nodal forces due to
internal and external forces
Find current velocities, nodal
coordinates and total kinetic
energy, KE
Calculate new
stiffness
matrices
No
If current KE is smaller then
previous
Yes
Set velocities to zero and
reset nodal coordinates
No
Check if max. residual force
is smaller than required
Yes
Check if buckling occurs in
any of principal stress direction
Yes
No
Print buckling
Print coordinates
stresses
STOP

Figure 8.7

8.4 Numerical examples

The main purpose of static analyses discussed in this chapter is to prepare data files for the dynamic analyses. Two air-supported structures to be examined are the models described in detail and shown in the photographs of chapter 10. They are both domes with the same diameter at their bases, 4.74 m; with one produced using orthotropic material and the other using isotropic material.

8.4.1 Orthotropic membrane dome

The model dome, a general view of which is shown in the photograph of figure 10.12 in chapter 10, was assembled from 10 'armadillo' segments cut from P.V.C. coated fabric in such a way that the warp direction aligned with the longitudinal axis of symmetry of each slice. The zero stress membrane geometry is presented in figure 8.8 together with the membrane properties; figure 8.8a shows the section along the axis of symmetry and figure 8.8b the warp directions together with the EA values and Poisson ratios for the weft and warp directions.

The dome was to be analysed:

1. subject to internal pressure p_{int} = 100 pa
2. subject to internal pressure, p_{int}, and a central load of:
   a. 150 N, and
   b. 300 N

Due to the shape of the model, pattern cutting and loading, only a quarter of the structure needed to be analysed.

The shape of the dome in the prestressed condition (internal pressure only) was first determined with the structure idealized into orthotropic triangular membrane elements, as shown in figure 8.9, possessing the EA values and Poisson's ratios obtained from static tests on cruciform specimens (see chapter 10). The layout of elements was predefined by the cutting pattern. Each slice of the dome was divided into two rows of triangles, in such a way that one edge of them was approximately parallel to the warp direction and the other to the weft direction. The principal stresses obtained from the analysis were in general in the radial and circumferential directions. However, for this type of membrane material there are two preferable stress paths, namely the warp and the weft direction, hence the orthotropic idealization seemed to be unsuitable for this case.

Two alternative approaches were therefore employed:

1. line idealization
2. line and coating idealization with EA for coating obtained from uniaxial tests, (EA) coat = 6050 N/m.

Prestress State Analysis

The prestressed geometry was calculated assuming internal pressure , p_{int}, constant, and as deformations were expected to be small, NSM was taken to be infinity. The analysis was based on stiffness matrices found at the beginning of the process. Similarly, the vector product, $\overline{A} \times \overline{B}$, for each element was was obtained only from the zero stress membrane geometry.

For each type of idealization convergence was good and the final stresses were everywhere positive.

The resulting nodal coordinates obtained from the two idealizations differ only slightly, the largest discrepancies are at the crown area and they are smaller than 1%. The assumption of small deflections proved to be right, as the maximum deflection occurring in the apex node was 1.8 cm, which represents only 1.8% of the dome height at this point.

The stresses existing in the dome under the prestressed condition are given in the table of figure 8.10 for elements lying along the sections A-A and B-B (for position of sections and locations see figure 8.9). For the 'armadillo' cutting pattern the orthotropic membrane material stresses are not constant throughout the dome. The lowest stresses in the warp direction occur, regardless of the idealization, in the crown area and increase in value away from the centre, with faster increase in the direction parallel to the warp direction.

The stresses in the weft direction when using a 'line' type idealization tend to decrease when moving from the centre outwards parallel to the warp direction, and increase for the perpendicular direction. When shear stresses taken by the coating are introduced, this pattern is slightly disrupted.

In the 'line and coating' idealization the warp and weft stresses are smaller in the central area than in the 'line' idealization, but in the remaining parts of the dome this situation is reversed. Including coating in the analysis causes the greatest changes in the centre of the dome, both for stresses and deflections.

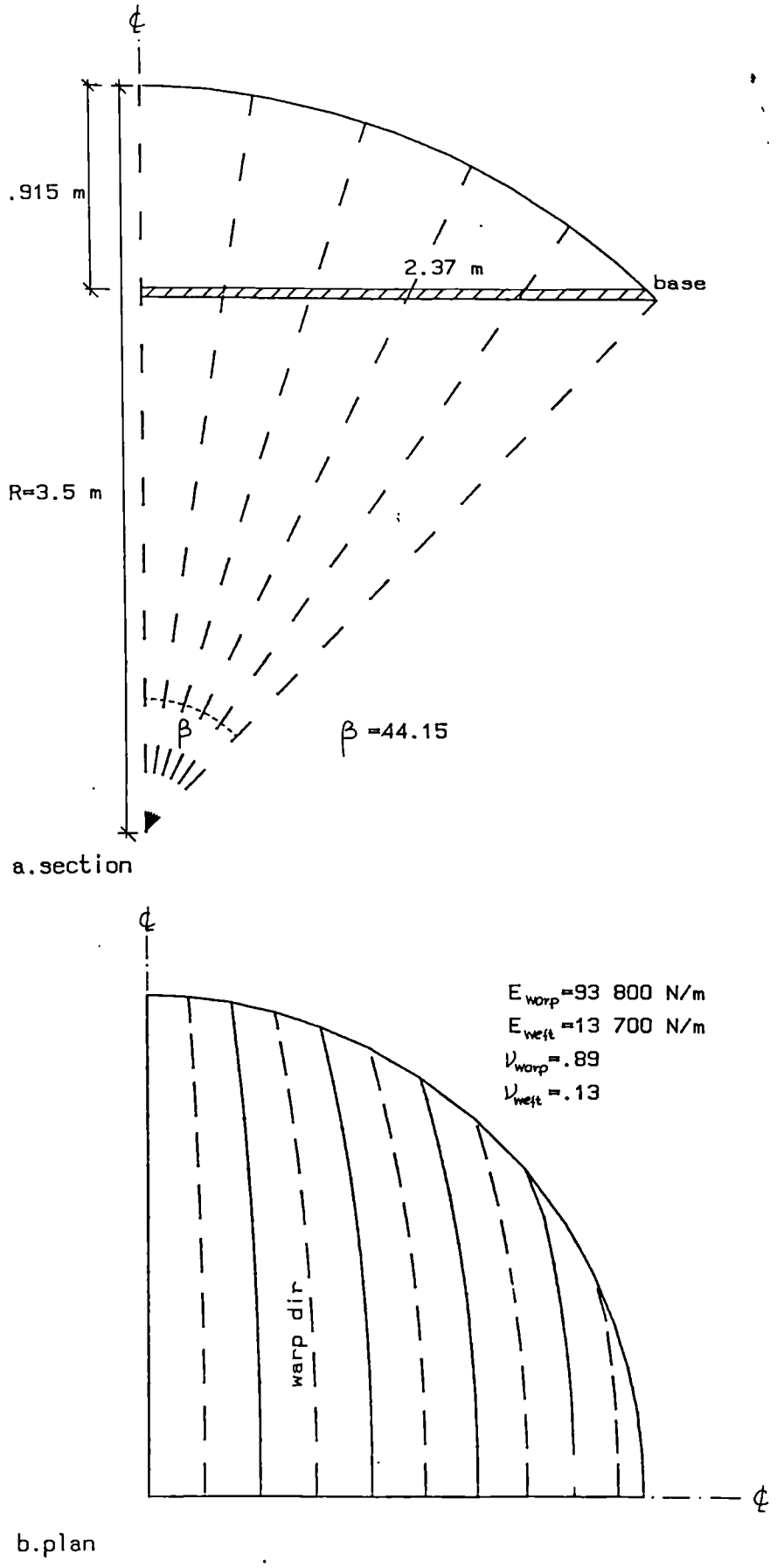

Figure 8.8 Zero stress dome geometry

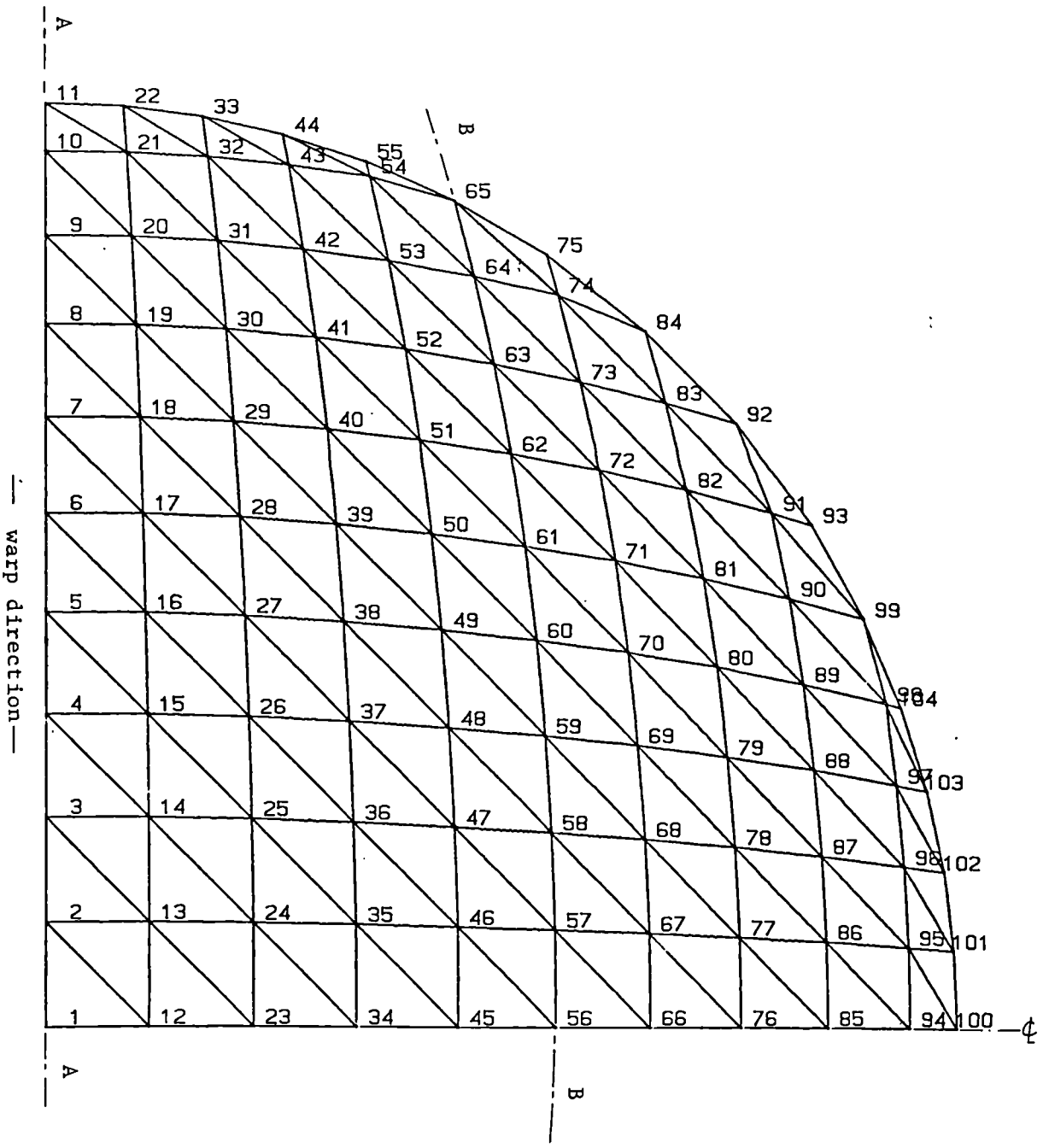

Figure 8.9 A quarter of the dome divided into triangles

Location	Line		Line and coating		
	Warp	Weft	Warp	Weft	Coating
1	261	76	222	48	11
3	265	74	247	71	10
5	276	67	276	68	7
7	295	55	309	56	6
9	325	42	355	43	9
56	264	85	259	85	6
58	269	82	262	81	10
60	280	73	274	71	9
62	297	58	290	56	61
64	316	45	312	43	0

Figure 8.10

Load State Analysis

In the load analysis, a quarter of the central load, P_c, (equal to 150 N or 300 N) was spread between the three central nodes 1, 2 and 12 (see figure 8.9) in such a way that, after applying the load, the heights above the base level of the crown points were the same (to comply with experiments; see chapter 10). This required recalculation of FF(i) (i = 1, 2, 12) at each cycle, where FF(i) x P_c is the external load acting on the dome at node i. In the final stage, when the nodal residuals were very small and the structure reached the static equilibrium state, the FF(i) had the following values:

FF(1) = .0125 (for 150 N) and .0089 (for 300 N)

FF(2) = .0928 (for 150 N) and .0923 (for 300 N)

FF(12)= .1447 (for 150 N) and .1489 (for 300 N)

The nonlinear analysis was followed with stiffness matrices reset at each 20 cycles. The numerical procedure was found to be highly sensitive to the frequency at which pressure changes were calculated. For stability of the entire system the pressure, p_{in}^{t}, given by equation 8.38, had to be assessed at every cycle. The pressure vector, equation 8.42, needed not to be calculated as often but only at each 20 intervals, together with stiffness matrices.

The results for the deformed shapes along the axis of symmetry when the dome was subject to the centrally applied loads are shown in figure 8.11. For comparison each figure includes also the prestressed dome shape. The deflections

of the dome obtained using the two idealizations differ only slightly (in the figure 8.11 the differences are not discernible). The greatest difference in terms of the absolute value is at the apex point; for 150 N load its value is 2 mm and for 300 N load it is smaller than 1 mm. Figure 8.11 shows the results for the 'line and coating' idealization.

The stress distributions do not show such a regular pattern as in the prestressed state. For the 150 N central load the stresses vary from 300 to 500 N/m in the warp direction and from 90 to 120 N/m in the weft direction. For the 300 N central load, stresses varied from 400 to 650 N/m in the warp direction and from 90 to 160 N/m in the weft direction.

The final principal stresses were in all cases positive.

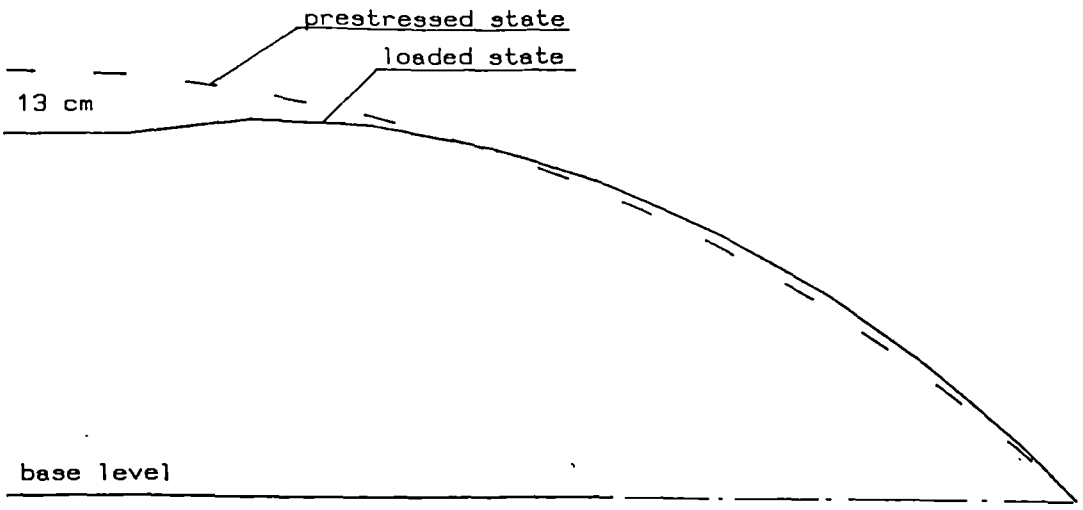

a.150 N centrally applied load

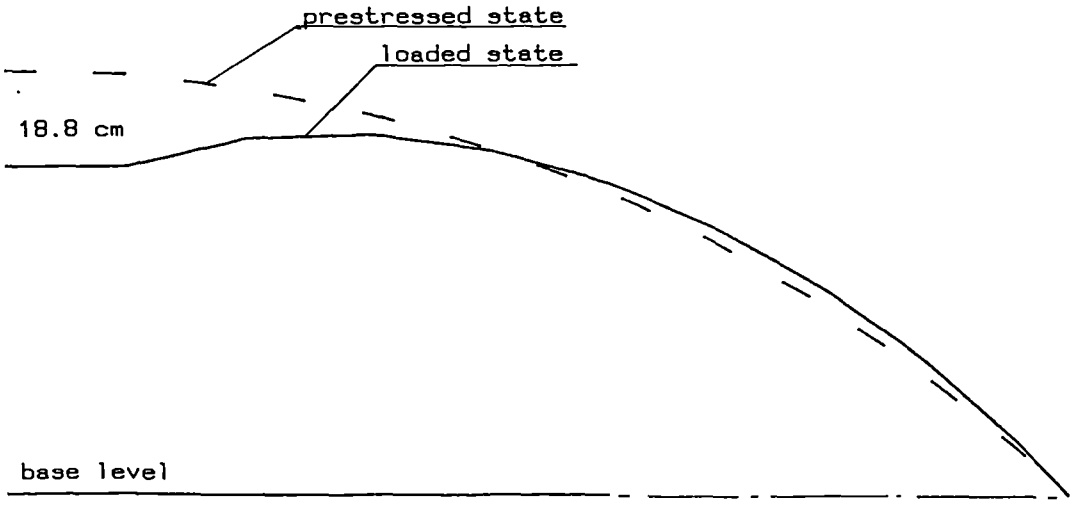

b.300 N centrally applied load

Figure 8.11 Static deflections of dome along axis of symmetry

8.4.2 Isotropic membrane dome

A dome, which is shown in Figure 10.22 of chapter 10, was formed by inflating an initially uniformly prestressed and flat isotropic membrane. External loads spread by means of platens to neighbouring nodes, was applied to the structure, in separate tests, centrally and symmetrically. For purposes of numerical analysis, the dome was idealized by an assembly of isotropic triangular elements as shown in figures 8.12 for the central load, and figure 8.13 for the asymmetric load.

Due to the axisymmetry, both of the loading and the structure, in the case of the centrally applied load, only a slice of the dome needed to be considered. Theoretically, it is desirable that the slice angle is small as this influences the size of elements which, when smaller, better resemble the dome. On the other hand, the size of the smallest element of the assembly will in the explicit dynamic analysis, influence the time step used to ensure overall stability of the procedure (the smaller the elements, the smaller the time step). In order to compromise, after a series of trial runs, a 10° angle was chosen for the segment analysis.

When a tension structure is analysed by employing the dynamic relaxation method, it has been found [9], that the best results are obtained using a uniform subdivision of elements. Therefore, an alternative idealization for the centrally loaded dome was considered, where all triangles

are approximately equal in area, as shown in figure 8.12b. The differences between stresses and especially deflections (for form finding and load analysis), obtained from analyses employing the dome modelling as shown in figure 8.12a and 8.12b, was found to be very small (less than 1%). The division of figure 8.12a results in shorter computer time and hence this type of membrane modelling was used in further calculations.

In the case of the asymmetrically loaded dome, half of the dome has to be considered, as there is only symmetry about one axis (see figure 8.13).

The isotropic pneumatic dome, when inflated and either centrally or asymmetrically loaded, experiences large geometric nonlinearities. Hence for all cases, stiffness matrices and, for efficiency, also pressure vectors, have to be reset at frequent intervals. A value for NSM = 20 was found to be suitable.

When the initially flat membrane (with E = 5260 N/m, ν = .52 and uniform prestress of 37 N/m) was subject to an internal pressure of 15.4 N/m^2 the resulting principal stresses obtained from both types of idealization (figure 8.12a and figure 8.13) were in the range of 90 to 100 N/m. The difference in deflections is negligible, although the division of figure 8.13 is coarser. The discrepancy at the apex point in the vertical direction is only 0.1 mm (Z slice = 228.4 mm, Z half = 228.3 mm).

In order to comply with experiments (see chapter 10) and to prepare the data file (for the later purpose of dynamic analysis) as accurately as possible, in the static load analyses the internal pressures were not calculated but were assumed to be constant; their values being obtained from the experiments.

In the case of the centrally loaded dome, during the load analysis with internal pressure of 28 N/m^2, the load of PA = 80 N was spread between the crown points to cause the z coordinates of the nodes to have the same values. When equilibrium was found, the load was distributed between points 1, 2 and 10 (see figure 8.12a) as follows:

$$P(1) = .00084 \times PA$$

$$P(2) = .0136 \times PA$$

$$P(10) = .0133 \times PA$$

The difference in loads between points 2 and 10 results from the idealization: point 2 is common to three elements, but point 10 to two only. The resulting principal stresses were positive and on average they were:

100 - 108 N/m in the circumferential direction and

110 - 120 N/m in the radial direction, except in the area very near to the crown, where they were as shown in the figure below:

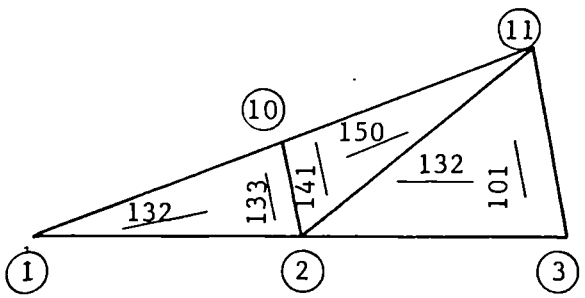

The deflection of the dome along a radius is shown in figure 8.14a with the prestressed state geometry superimposed on it.

In the case of asymmetric load, the load of PA = 80 N was represented in the analysis by vertical forces applied at nodes 6, 7 and 15 (see figure 8.13). The distribution of load was calculated in such a way that the plane formed by the three points was perpendicular to the plane of symmetry and inclined at 5° to the horizontal with node 6 being higher than 7 (the position of the plane was found during the tests described in chapter 10). In the final stage of the analysis, when the static equilibrium state was reached, the external nodal forces were found to be:

$$FF(6) = .0633 \times PA$$

$$FF(7) = .1984 \times PA$$

$$FF(15) = .2383 \times PA$$

Applying the 80 N asymmetric load, while internal pressure was kept at the constant value of 26 N/m resulted in all positive principal stresses with the average values between 100 - 115 N/m except for the area shown below:

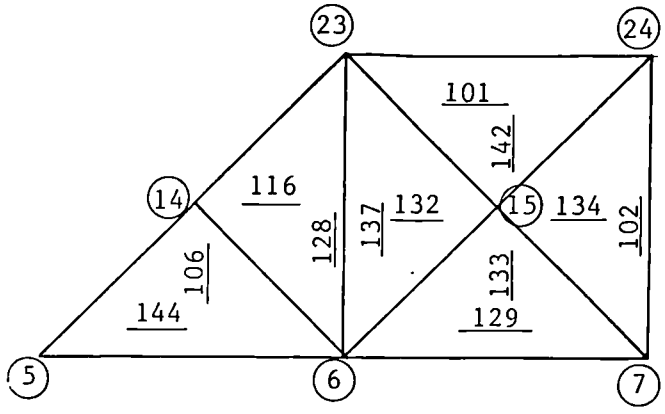

The deflected shape along the axis of symmetry together with the prestressed state geometry is shown in figure 8.14b.

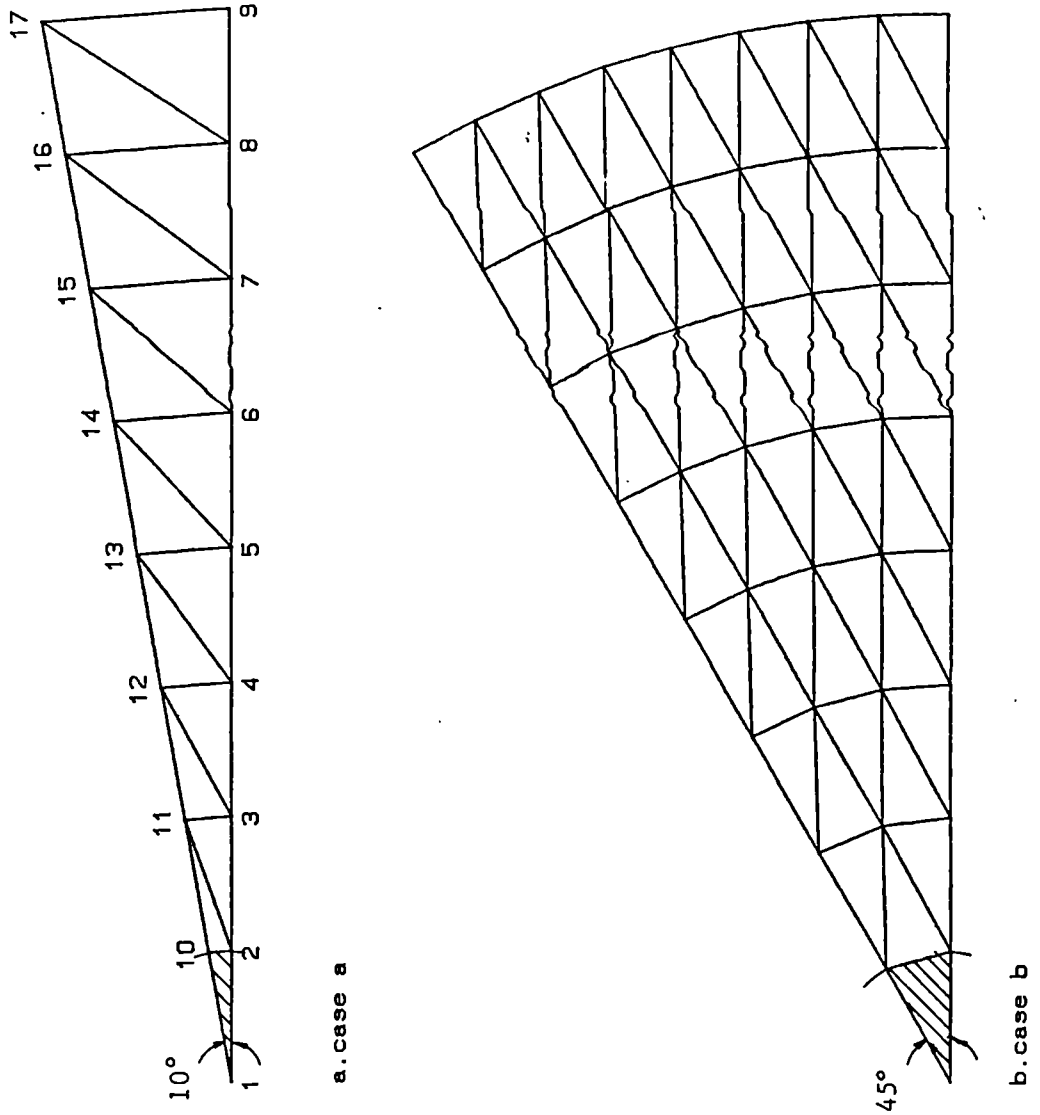

Figure 8.12 Idealization for central load

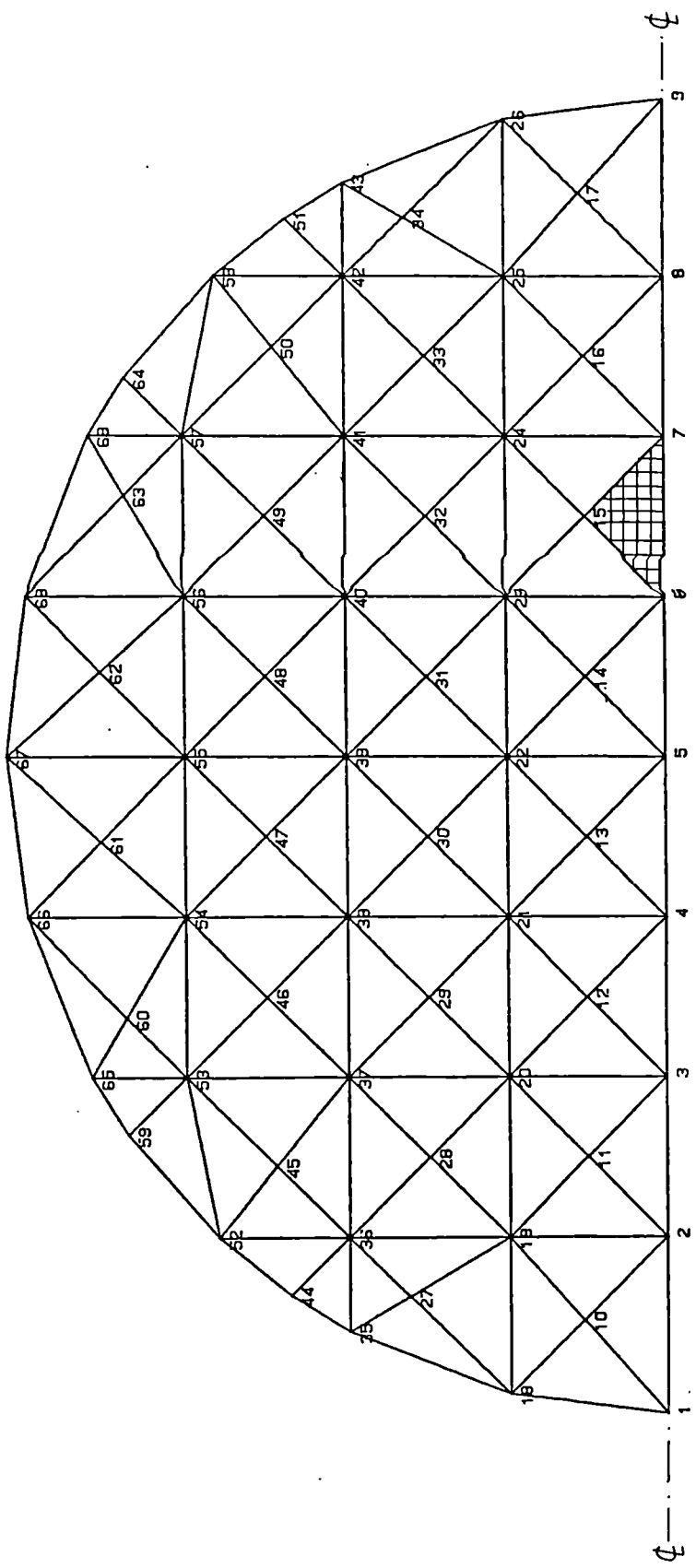

Figure 8.13 Idealization for asymmetric load

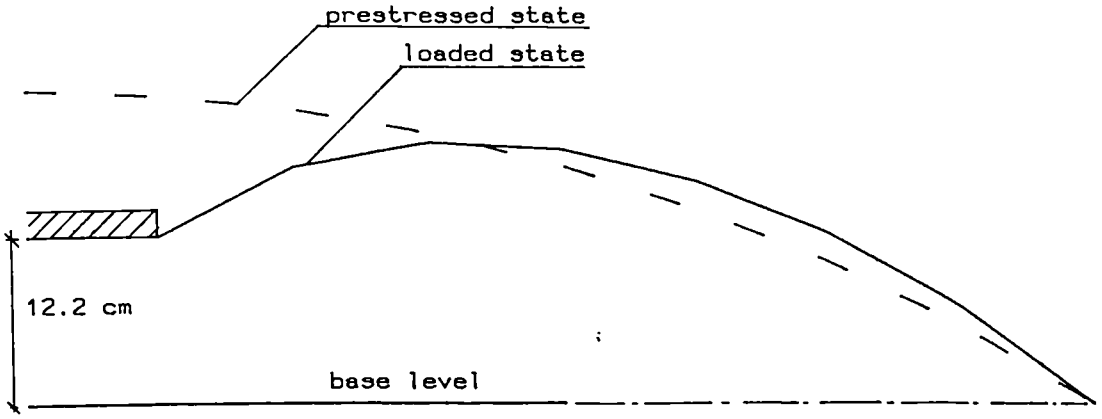

a.centrally applied load

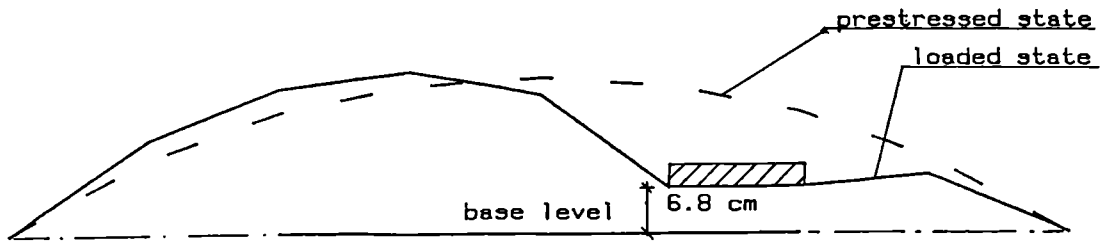

b.asymmetrically applied load

Figure 8.14 Static deflections of dome

CHAPTER 9

Explicit dynamic analysis of pneumatic structures

Contents:

In this chapter explicit dynamic analysis of pneumatic (membrane) structures is discussed with reference to two air-supported domes constructed with woven fabric and lightweight polythene, and subject to impulsively applied loads. The influence of the external surrounding air is disregarded in the analysis. An iteration scheme which includes visco-elastic membrane behaviour modelling and an incremental procedure accounting for on/off buckling is reviewed and implemented. For the lightweight dome with an impulsively lifted load a more efficient explicit dynamic scheme is proposed and discussed.

9.1 Explicit dynamic analysis - a review

9.1.1 Iteration schemes for explicit dynamic analysis

The dynamic relaxation method discussed in chapter 8 is based on explicit integration of the equations of motion. In order to use the method for static analyses, artificial devices such as fictitious masses and kinetic damping were employed. When the real dynamic response is of interest, the artificial values need to be substituted by actual quantities for: masses, time step and damping in a suitable form. A version of explicit dynamic analysis as formulated for pneumatic structures by Barnes [7, 8, 9, 11] and presented below satisfies this requirement. The numerical analysis compares well with experimental results for a heavily loaded pneumatic dome [11, 186].

For the purpose of explicit dynamic analysis, the membrane of a pneumatic structure can be idealised by an assembly of 'constant strain' triangular elements. The layout and type of triangles will depend mainly upon the size and shape of the structure, pattern cutting and material properties and can be similar to that used for the previous static analysis.

The membrane mass matrices in a lumped form are obtained from the real membrane mass, ρ_m, assuming that the mass of each element is uniformly distributed between its nodes:

$$\begin{bmatrix} m_i & 0 & 0 \\ 0 & m_i & 0 \\ 0 & 0 & m_i \end{bmatrix} = \sum_{k=1,\ n} \begin{Bmatrix} m_{ki} & 0 & 0 \\ 0 & m_{ki} & 0 \\ 0 & 0 & m_{ki} \end{Bmatrix} \qquad 9.1$$

where

$\begin{bmatrix} m_i & & \\ & m_i & \\ & & m_i \end{bmatrix}$ is a diagonal mass matrix for node i,

n is the number of elements surrounding node i,

and

$$m_{ki} = \frac{1}{3} A_K \quad \rho_m \qquad 9.2$$

where

A_K - is the area of element K and

ρ_m - is the mass of the membrane per square metre.

At each step of an explicit dynamic analysis, a flow chart for which is given in figure 9.1, displacement components and hence the elastic strains in all links may be determined

purely in terms of the previous displacements and the residual nodal forces. For visco-elastic structures these residual forces will be affected by the creep strains which have previously taken place. After the new displaced form has been determined, link forces and their resolved contributions to the next residual forces are calculated using the separate natural stiffnesses of elements.

The recurrence equation for velocity, V_{ix}, in central difference form at time step $t+\Delta t/2$ is given by:

$$V_{ix}^{t+\Delta t/2} = \frac{\Delta t}{m_i} R_{ix}^{t} + V_{ix}^{t-\Delta t/2} \qquad 9.3$$

and at time $\Delta t/2$, the first step

$$V_{ix}^{\Delta t/2} = 0.5 \frac{\Delta t}{m_i} R_{ix}^{t} \qquad 9.4$$

where

R_{ix}^{t} is the residual force at node i, which can be expressed in terms of the applied load P_{ix}^{t} and the current internal forces and position vectors of the structural elements connected to node i.

The new geometry at time $t+\Delta t$ is thus:

$$X_i^{t+\Delta t} = X_i^{\Delta t} + \Delta t \; V_{xi}^{t-\Delta t} \qquad 9.5$$

from which the new link extension and residual forces at $t+\Delta t$ may be determined. The process then continues with iteration between steps 3 and 4 (see figure 9.1), utilising equations 9.3, 9.5 and the appropriate expressions for determining residual forces.

The time step, Δt, is governed by the stability condition (see chapter 8), namely

$$\Delta t < \sqrt{\frac{2m_i}{S_{pi}}} \qquad 9.6$$

where

S_{pi} is the principal direct stiffness at node i.

In nonlinear analysis, the stiffness obtained from the starting geometry may not be the maximum value occurring during the process, hence the time interval, Δt used in the analysis, has to be sometimes as small as 50% of that calculated at the beginning of the numerical procedure.

The nodal residuals result from the unbalanced internal and external forces. The nodal internal forces, $R_{i\ int}$, at time t are:

$$R^{t}_{i\ int\ X} = R^{t}_{i\ int\ X} + \left(\frac{DX}{L}\right)^{t}_{k} * T^{t}_{k} \qquad 9.7$$

where $\frac{DX}{L}$ is shown in figure 9.2, and

T^{t}_{k} is the tension in a link k of element j.

The tension vector for element j is given by:

$$\begin{Bmatrix} T_1 \\ T_2 \\ T_3 \end{Bmatrix}^{t}_{j} = \begin{Bmatrix} T_1 \\ T_2 \\ T_3 \end{Bmatrix}^{t}_{inj} + [K]^{t}_{j} * \begin{Bmatrix} \delta e_1/l1 \\ \delta e_2/l2 \\ \delta e_3/l3 \end{Bmatrix}^{t}_{j} \qquad 9.8$$

where

$\{T\}^{t}_{in}$ is recalculated at every NSDB iterations from the

stress level at times equal to k * Δt * NSDB.

Formulation of the explicit dynamic analysis in a way represented by the flow chart of figure 9.1 enables dynamic analysis of pneumatic structures by dividing the process into two levels:

first: the 'quasi linear' response of the structure (steps 3 and 4), and

second: accounting for the membrane behaviour, including: material nonlinearity, visco-elastic properties of the membrane (which give rise to material damping), and purely tensile behaviour.

The latter processes are superimposed on the former by passing to the main iteration cycle new values of $\{T\}^t_{in}$ and element stiffness matrices.

The most common forces acting on a pneumatic structure are:

1. concentrated applied static and dynamic loads, including distributed gravitational loads lumped at the nodes $(P^t_{ix}, P^t_{iy}, P^t_{iz})$
2. distributed static and dynamic pressure loads, p^t, normal to the membrane elements.

The internal pressure components (the difference between the absolute internal and external pressure) consist of two parts:

a. static pressure, exactly the difference between

internal and external pressure; p_{ins}^{t} is given by the equation

$$p_{ins}^{t} = (p_{ins}^{t-\Delta t} + p_{ex}) \left(\frac{V_o^{t-\Delta t}}{V_o^{t}}\right)^{\alpha} - p_{ex} \qquad 9.9$$

where

$\alpha \longrightarrow 1 - 1.4$

p_{ex} is the external pressure, and

V_o^{t} and $V_o^{t-\Delta t}$ are the internal volumes of the pneumatic structure at times t and t-Δt respectively.

b. the dynamic pressure, resulting from the movement of air mass due to externally applied loads, which can be expressed as [8]

$$p_{ind}^{t} = 0.5 * \rho_{air} * C \times (\bar{V}_n^{t})^2 \qquad 9.10$$

where

$\bar{V}_n^{t}$ is the average normal velocity, and

C is a coefficient

The external pressure caused by wind pressure velocity divided into a mean component, $\bar{V}$, and a randomly fluctuating component, ν , at any point (x, y, z) on the structure, is given by

$$p_{ex} = .5\ \rho_{air} \times C_p\ (x,y,z) * [\bar{V}\ (x,y,z) + \nu\ (x,y,z,t)]^2 \qquad 9.11$$

where

C_p (x,y,z) is a non-dimensional coefficient which is mainly a function of position, shape of structure, and the characteristics of the approaching flow. For highly deformable structures, C_p is also a function of deformations.

The x,y and z nodal components of pressure forces for each element are:

$$\begin{Bmatrix} P_x \\ P_y \\ P_z \end{Bmatrix} = p^t \quad \begin{Bmatrix} u_x \\ u_y \\ u_z \end{Bmatrix} \qquad 9.12$$

where

$p^t = p_{ex} + p_{int}$

$\begin{Bmatrix} u_x \\ u_y \\ u_z \end{Bmatrix}$ is a unit pressure vector, as shown in figure 9.3

and $\begin{Bmatrix} u_x \\ u_y \\ u_z \end{Bmatrix}_i = \begin{Bmatrix} u_x \\ u_y \\ u_z \end{Bmatrix}_j = \begin{Bmatrix} u_x \\ u_y \\ u_z \end{Bmatrix}_k = \frac{1}{6} \cdot \bar{A} \times \bar{B}$ 9.13

9.1.2 Modelling visco-elastic properties of the membrane

The majority of membranes for pneumatic structures are produced from materials (plastics or similar) for which a suddenly applied and maintained state of uniform stress induces an instantaneous deformation followed by a flow process, which is limited in magnitude as time grows. A material which responds in this manner is said to exhibit both an instantaneous elasticity effect and creep characteristics. Its behaviour can be described by visco-elastic theory.

In static load analyses, when long term response is of interest, the visco-elastic theory can be substituted by an approximate elastic stress-strain relationship which is

valid only for a particular range of stresses, using strains resulting from both elastic and viscous deformations. It has been found experimentally that almost all membranes respond to an applied load in such a way and that about 90-95% of total deformations take place in the confined period of time, ranging from 0.5 h to 12-24 hours [5].

When dynamic response is traced, any such approximations may lead to erronous results. Visco-elastic phenomena are characterised by the fact that the rate at which creep strains develop depends not only on the current state of stresses and strains, but, in general, on the full history of their development. *Materials exhibiting these properties* show a pronounced dependence on the rate of loading; the strain being larger if the stress has grown more slowly to its final value [40, 71].

The behaviour of visco-elastic materials in uni-axial stress closely resembles that of models built from discrete elastic and viscous elements. The basic building elements are a spring and a dashpot, which represent respectively the elastic (stress proportional to strain) and viscous behaviour (stress proportional to strain rate). The simplest model for creep in solids, shown in figure 9.4, is known as a Kelvin (or Voigt) element, and is obtained by connecting in parallel two different discrete elements.

When a material is characterised by a Kelvin model (figure 9.4) the creep stress-strain relationship is [40]:

$$\sigma = E_i \ \varepsilon_c + \eta_i \ \dot{\varepsilon}_c \qquad 9.14$$

where

ε_c is the creep strain (separated from instantaneous elastic deformation),

$\dot{\varepsilon}_c = \frac{d\varepsilon_c}{dt}$, and E_i and η_i are shown in figure 9.4

The creep rate may be written from equation 9.14 as

$$\dot{\varepsilon}_c = \frac{d\varepsilon_c}{dt} = \frac{1}{\eta_i}\sigma - \frac{E_i}{\eta_i}\varepsilon_c = a\sigma - b\varepsilon_c \qquad 9.15$$

Equation 9.15 implies that the creep rate is a function of

1. current stress and
2. total accumulated creep strains.

If several Kelvin elements are placed in series to represent more complex material behaviour, then equation 9.15 becomes

$$\dot{\varepsilon}_c = \sum_{r=1}^{n} \dot{\varepsilon}_c^{\,r} = \left(\sum_{r=1}^{r=h} a_r\right)\sigma - \sum_{r=1}^{r=h} b_r \ \varepsilon_c^{\,r} \qquad 9.16$$

where, the first summation can be replaced by a lumped, known constant, and the second gives the sum of accumulated creep strains due to the individual 'elements' of the model.

The complexity of the model chosen will depend on the type of loading [7,8,9,11]: for short-term dynamic loading a single element model may suffice particularly if the main concern is a qualitative study of the vibration damping effect of the visco-elastic membrane. For long term quasi-static creep investigations of a pre-stressed structural membrane, a more complex model may be necessary. Barnes [7,8,9,11] investigated the response of an air-supported

dome due to suddenly applied dynamic loading, and by using a single model obtained theoretical predictions of deflection decay which match well with the experimental trace.

A single Kelvin model seems to be a rather crude representation of the membrane characteristics. On the other hand, employing this model results in: simplicity of the numerical analysis, a fairly easy procedure for establishing the membrane dynamic properties and, as will be shown in chapter 10, a single Kelvin model represents very well the property of coated fabrics in the warp (predominant) direction. Due to the above advantages, a single Kelvin model will be employed to predict the dynamic response of the test pneumatic domes due to suddenly applied loads.

Assuming that ε_c varies linearly during the time intervals $(t-n\Delta t/2) \longrightarrow (t+n\Delta t/2)$, in interlacing finite difference form equation 9.15 can be written [11] as:

$$\frac{\varepsilon_c{}^{t+n\Delta t/2} - \hat{\varepsilon}_c{}^{t-n\Delta t/2}}{n\Delta t} = a \cdot \sigma^t - b \frac{(\varepsilon_c{}^{t+n\Delta t/2} + \varepsilon_c{}^{t-n\Delta t/2}}{2} \qquad 9.17$$

The recurrence equation for creep strain ε_c appropriate to the mid-point of the time interval $n\Delta t$ is:

$$\varepsilon_c{}^{t+n\Delta t/2} = \frac{an\Delta t\ \sigma^t}{1+bn\Delta t/2} + \frac{1-bn\,\Delta t/2}{1+bn\Delta t/2}\ \varepsilon_c{}^{t-\Delta t/2} =$$

$$a'\ \sigma^t + b'\ \varepsilon_c{}^{t-n\Delta t/2} \qquad 9.18$$

where

n is an integer, n = NSDB (see the flow chart of figure 9.1), and

Δt is the time step used for the dynamic iteration scheme.

For a membrane element subject to a two-dimensional state of stress, the vector of creep strains is given by [208, 11]:

$$\begin{Bmatrix} \varepsilon_{xc} \\ \varepsilon_{yc} \\ \gamma_{xyc} \end{Bmatrix} = \{\varepsilon_c\}^{t+n\Delta t/2} = \begin{bmatrix} a_x' & 0 & 0 \\ 0 & a_y' & 0 \\ 0 & 0 & a'_{xy} \end{bmatrix} [\Psi] \{\sigma\}^t + \begin{bmatrix} b_x' & 0 & 0 \\ 0 & b_y' & 0 \\ 0 & 0 & b'_{xy} \end{bmatrix} \{\varepsilon_c\}^{t-n\Delta t/2} \qquad 9.19$$

When a material is isotropic, the creep is associated only with deviatoric stress components [71]; the volumetric behaviour being elastic and the matrix $[\Psi]$ is the one which pertains if the Poisson's ratios were made equal to 0.5.

For isotropic idealisation the matrices in equation 9.19 are

$$\Psi = \begin{bmatrix} 1 & -.5 & 0 \\ -.5 & 1 & 0 \\ 0 & 0 & 3 \end{bmatrix} \qquad 9.20a$$

$$a_x' = a_y' = a_{xy} = a \frac{n\Delta t}{1+bn\Delta t/2}$$

$$b_x' = b_y' = b'_{xy} = \frac{1-bn\Delta t/2}{1+bn\Delta t/2} \qquad 9.20b$$

where a and b are values obtained from triaxial tests (see chapter 10).

For a 'line' idealisation equation 9.19 takes the form

$$\begin{Bmatrix} \varepsilon_{xc} \\ \varepsilon_{yc} \end{Bmatrix} = \begin{bmatrix} a_x' & 0 \\ 0 & a_y' \end{bmatrix} \begin{bmatrix} 1. & -.5 \\ -.5 & 1. \end{bmatrix} x \{\sigma\}^t + \begin{bmatrix} b_x' & 0 \\ 0 & b_y' \end{bmatrix} \{\varepsilon_c\}^{t-n\Delta t/2} \qquad 9.19a$$

where

a_x, a_y, b_x, b_y are constants obtained from uniaxial tests conducted separately for the warp (x) and the weft (y) direction (see chapter 10).

When a 'line and coating' idealisation is employed the creep strain vector is found from equation 9.19 with

$$\Psi = \begin{bmatrix} 1 & -.5 & 0 \\ -.5 & 1 & 0 \\ 0 & 0 & 1 \end{bmatrix}$$

and

$$a_{xy}' = a_c' = a_c \frac{n\Delta t}{1+bcn\Delta t/2} \qquad 9.21$$

$$b_{xy}' = b_c' = \frac{1-b_c n\Delta t/2}{1+b_c n\Delta t/2}$$

Where a_c, b_c are obtained from biaxial tests on coating (see chapter 10), and

a_x, a_y, b_x and b_y are similar to values for a 'line idealisation'.

Matrix (Ψ) was defined originally in the paper by Zienkiewicz et al [208] in the form given by equation 9.20a for an isotropic material.

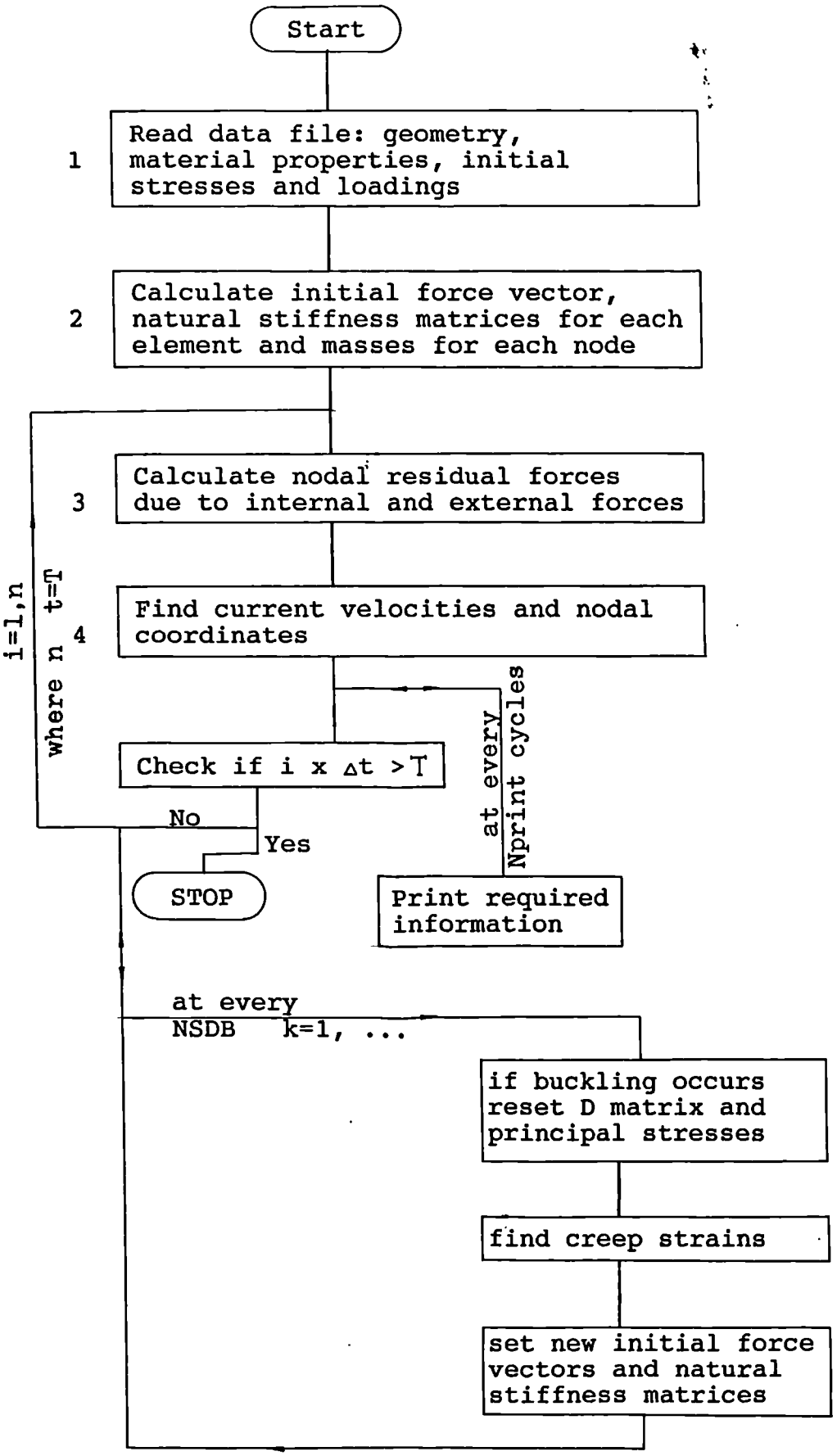
Start
1
Read data file: geometry, material properties, initial stresses and loadings
2
Calculate initial force vector, natural stiffness matrices for each element and masses for each node
3
Calculate nodal residual forces due to internal and external forces
4
Find current velocities and nodal coordinates
i=1,n
where n t=T
Check if i x Δt >T
No
Yes
at every Nprint cycles
STOP
Print required information
at every NSDB k=1, ...
if buckling occurs reset D matrix and principal stresses
find creep strains
set new initial force vectors and natural stiffness matrices

Figure 9.1

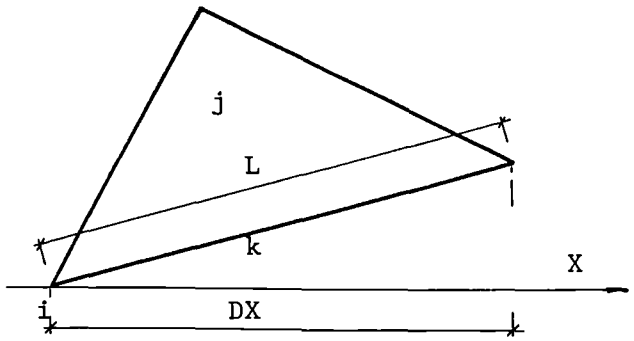

Figure 9.2

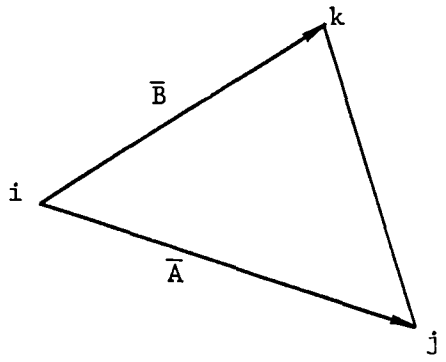

Figure 9.3

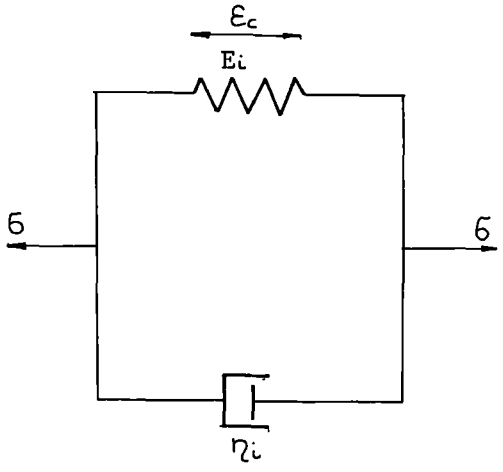

Figure 9.4 Kelvin model

9.1.3 Incremental procedure allowing for buckling

A membrane material is capable of sustaining only tensile stresses and strains without resistance in compression. While an explicit stress-strain relation cannot be generally written to describe this phenomenon, it has been shown that it suffices to carry out the analysis elastically (step 4 and 5 in the flow chart of figure 9.1) and wherever compressive stresses develop to reduce these to zero [209]. Such checking, in general, does not have to be performed at each time interval, but can be coupled with creep strain calculations as given by Barnes [7].

The main steps of this procedure, *for each element, are as* follows [7, 186]:

1. check stresses relative to chosen local axes

$$\{\sigma\}^t = \{\sigma\}^i + [D]\,[G]\,\{e/l\}^t - [D]\,\{\varepsilon_c\}^{t-n\Delta t/2}$$

where

$\overset{e}{-}_l$ is the vector of total strain from the stress level $\{\sigma\}^i$.

2. determine principal stresses $\{\sigma_p\}$ and inclination to local x, y axes.
3. if the principal stresses are greater than zero, calculate $\{\Delta\sigma\}^t = \{\sigma^t - \sigma^i\}$ and go to step 6;
   if not, set the negative stresses to zero and modify accordingly the $[D_p]$ matrix relative to the principal axes.

4. transform the $[D_p]$ matrix to local x, y axes

$$[D]' = [C^T]\ [D'_p]\ [C]$$

where $[C^T]$ denotes the transpose of matrix [C]

5. set modified stresses $\{\sigma'\}^t = [C^T]\ \{\sigma_p\}$;

$$\{\Delta\sigma'\}^t = \{\sigma'^t - \sigma^i\}$$

6. set new creep strains

$$\{\varepsilon_c\}^{t+n\Delta t/2} = [a]'\ [\Psi]\ \{\Delta\sigma'\}^t + [b]'\ \{\varepsilon_c\}^{t-n\Delta t/2}$$

7. set new initial force vector:

$$\{T\}^i = [G^T]\ \{\sigma'\}^t - [G^T]\ [D]'\ \{\varepsilon_c{}^{t+n\Delta t/2} - \varepsilon_c{}^{t-n\Delta t/2}$$

8. set new natural stiffness

It should be noted that calculation of the stresses in step 1 is always based on the matrix [D] as for unbuckled isotropic or anisotropic materials. (Using a modified [D'] matrix would imply that an element is buckled before the buckling check is carried out).

When a principal stress is found to be zero or negative (step 3), the material is assumed to be highly anisotropic or even behaving uni-axially with zero (or very small) elastic modulus in the direction indicated by the compression. This implies, that if $[D_p]$ is defined as:

$$\begin{Bmatrix} \sigma_x \\ \sigma_y \\ 0 \end{Bmatrix} = \begin{bmatrix} d_{11} & d_{12} & 0 \\ d_{21} & d_{22} & 0 \\ 0 & 0 & d_{33} \end{bmatrix} \begin{Bmatrix} \varepsilon_x \\ \varepsilon_y \\ 0 \end{Bmatrix} \qquad 9.22$$

the necessary modifications are

1. if $\sigma_x \leq 0$ then $d_{12} = d_{21} = d_{11} = d_{33} = 0$ and $d_{22} = E_y$
2. if $\sigma_y \leq 0$ then $d_{12} = d_{21} = d_{22} = d_{33} = 0$ and $d_{11} = E_x$
3. if $\sigma_x \leq 0$ and $\delta_y \leq 0$ then $d_{11} = d_{12} = d_{21} = d_{22} = d_{33} = 0$

The matrix [C] is defined by equation

$$\{\varepsilon_p\} = [C] \{\varepsilon_{xy}\} \qquad 9.23$$

where

$$C = \begin{bmatrix} C^2 & S^2 & CS \\ S^2 & C^2 & -CS \\ -2CS & 2CS & C^2-S^2 \end{bmatrix}$$

and C and S denote cosine and sine respectively of the angle between the local x axis and the direction of maximum principal stress.

When a 'link' or 'link and coating' idealisation is employed, checking for buckling is simplified, as the directions of the local axes must coincide with the principal axes. Steps 2 and 4 are fully omitted and in step 5 only an increase from the initial stress is found.

The incremental procedure allowing for buckling, discussed here in the context of explicit dynamic analysis, may also be employed, excluding creep strain calculations, in static analyses. The approach has been tried, with success in most cases, but unfortunately its convergence cannot always be guaranteed. Some alterations to prevent this setback have been suggested: for static analysis of rocks by Zienkiewicz [209] and for static and dynamic analysis of tension structures by Barnes and Tan [9, 186].

Barnes and Tan noticed that the main area likely to cause a problem is the resetting of stresses in step 5, where the modified [D] matrix is not taken into account. Hence an

alternative equation to the first in step 5, and an additional equation for 'link' and 'link and coating' idealizations has been proposed as:

$$\{\sigma'\} = \{\sigma_i\} - [D'][G] \{\overset{e}{\underset{1}{-}}\}^t - [D]'\{\varepsilon_c\}^{t-n\Delta t/2} \qquad 9.24$$

This procedure has been employed successfully for the dynamic and static analysis (with $\{\varepsilon_c\} = \{0\}$) of an impulsively loaded axisymmetric dome [186].

9.1.4 Influence of surrounding air

If an air-supported structure vibrates in air, the motion of the membrane will set the surrounding air in motion. Therefore, the structure might be viewed not as containing the membrane alone but as a thin membrane between two layers of air. Hence consequently, the dynamic mass, equations 9.1 and 9.2, should be extended to account for the entire structure including the added mass of the surrounding air. For lightweight constructions such as tension membranes the additional mass of air has a profound effect on dynamic response [34].

The surrounding air, while in motion, exerts pressure on the membrane. The pressures due to the vibrating air mass are proportional to the normal acceleration of the roof [34]. If these pressure are in phase with the vibration and proportional to its amplitude, energy is neither added nor dissipated by the presence of the surrounding air. If, on the other hand, they either lead or lag behind the structural response, then the air will act either as an

exciter, which may lead to instability, or as a damper respectively.

Jensen in his papers [99, 100] which are based on various experiments with tension structures (air-supported structures were not tested) concluded that the effect of surrounding air on the wind response of tension structures can be accounted for by including the following terms (see chapter 4):

1. pressure as $C_m \rho_A \frac{A_o}{D} \frac{dV}{dt}$
2. mass as $C_m \rho_A a^3$ and 9.25
3. damping as $\delta = \frac{1}{2} C_d \frac{m''}{A_o} \frac{A}{m}$

An alternative approach, which is suggested by Barnes [14], is to model the surrounding air by simplified fluid mechanics equations subject to boundary conditions. Thus obtained the equations can be solved numerically, together with the structural dynamics equations describing the membrane behaviour, by employing an explicit dynamic approach. This method has the potential to represent the phenomenon more accurately but it is likely to require much longer computation than the others. This approach will be discussed in more detail in chapter 11.

9.2 Numerical examples and discussion

Numerical calculations presented in this chapter are examples of explicit dynamic analysis applied to air-supported domes. The structures are described briefly in chapter 8 and in detail in chapter 10.

The discussion will relate to:

1. an orthotropic membrane dome impulsively loaded at the centre
2. isotropic membrane dome suddenly unloaded centrally and asymmetrically.

9.2.1 Impulsively loaded orthotropic dome

The prestressed orthotropic dome assembled from 'armadillo' segments, as described in chapter 8 was analysed for response to central impulse loading. Two cases were considered:

1. 150 N central load, and
2. 300 N central load.

As a starting point for the dynamic analyses, the geometry and stress distribution in the structure, due to internal pressure only (p_{in} = 100 Pa), was obtained by employing the dynamic relaxation method (see chapter 8). The idealisation of the membrane for the purpose of numerical analysis was discussed in chapter 8 and is shown in figure 8.9. Here, it will be recalled that two kinds of elements were used: 'line' and 'line and coating'. When the dome was loaded or only prestressed the differences , especially in deflections, between results obtained from these two idealisations were very small.

In the dynamic analysis it was assumed that the external load was applied after the membrane had reached its long-term steady equilibrium state i.e., that the gross deformations of the dome to balance its internal pressure had already taken place. This implies that we have to model the visco-elastic behaviour of the membrane due only to the suddenly applied load, and hence a single Kelvin model may suffice.

In air-supported structures the action of external forces causes movement of both internal and external air, with changes in the internal volume which, according to the laws governing addiabatic contraction (or expansion) of gases, results in an increase (or decrease) in the value of the internal pressure. The vibrations of the air create additional dynamic forces. However, in the present case, when a heavy central load is suddenly released, its influence on the membrane behaviour is much greater than that resulting from the secondary dynamic forces (movement of air).

The nodal lumped masses, m_i, contained two parts; the mass of the membrane (.345 kg/m^2) (which on average resulted in nodal masses of order .023 kg) and, for the central nodes, their share of the central applied load mass. Calculation of the central mass distribution between the crown nodes was based on the following:

When Pa = 150 N was applied, the masses at nodes 1, 2 and 12 (see figure 8.9 of chapter 8) were increased by

.0125 x Pa/9.81, .0928 x Pa/9.81 and .1447 x Pa/9.81 respectively;

for Pa = 300 N the additional masses were .0089 x Pa/9.81, .0923 x Pa/9.81 and .1486 x Pa/9.81.

The additional masses lumped at the top nodes of the dome were approximately 100 and 200 times greater, for 150 N and 300 N load respectively, than those of the membrane.

If the nodal masses had been increased by the mass of vibrating air (calculations could have been based on formula given by Jensen [100]), the resulting total mass (mass of membrane plus mass of vibrating air) would be very much less than that due to the central mass. Therefore, in this case, the added masses are reckoned to be of secondary order and omitting them in a numerical analysis should not influence the results.

Similarly the damping resulting from the creep of the membrane material would be of much higher order than that due to air damping, as defined by Jensen (see chapter 4 and 9.14).

The critical time step was determined from those free surface nodes with lowest mass to stiffness ratio; i.e. nodes adjacent to the smallest elements. The nodes giving the lowest value are nodes 54 and 98 (see figure 8.9).

Idealization of the membrane was carried out to approximate most accurately the shape of the dome, and the warp and weft directions of the weave. For almost all other nodes the critical time would have been twice as large as for nodes 54 and 98. The time interval used for the numerical integration was 50% of the critical value, namely .00005 second.

The dynamic analysis was performed for the following cases:

1. A 150 N central load with 'line' and 'line and coating' idealisation
2. A 300 N central load with 'line' idealisation.

In all cases pressure changes were calculated at each cycle as part of the 'quasi-linear' dynamic response, but pressure vectors were updated at NSDB = 20 (see flow chart shown in figure 9.1) together with other parameters accounting for both material and geometric nonlinearities. The buckling was checked and accounted for, as given in figure 9.13.

The membrane dynamic properties were obtained from experiments (see chapter 10) and their values were as follows:

for the warp direction

E_x = 160 000 N/m

a_x = .000033 m/N sec

b_x = 14.4 1/sec

ν_x = .752

for the weft direction

E_y = 57 000 N/m

a_y = .0004 m/N sec

b_y = 26.9 1/sec

ν_y = .268

for the coating

E_c = 9 050 N/m

a_c = .0033 m/N sec

b_c = 50.8 1/sec

Where

E_x, E_y and E_c are immediate elastic moduli,

ν_x, ν_y are the Poissons ratios, and

a_x, b_x, a_y, b_y, a_c, b_c are the Kelvin model constants.

The results from analysis for a two-cycle trace of the central node (node nr1) deflection are shown in figure 9.5a for the 150 N load and in figure 9.5b for the 300 N load. Longer responses are shown and compared with experimental results in chapter 10.

The difference between dynamic displacements of the central node, in the case of 150 N (figure 9.5a), obtained from the two different idealisations is very small.

Including coating in the analysis using a 'line and coating' idealization required not only additional time, but also more computer storage as larger matrices are used (instead of 2 x 2, 3 x 3 matrices are employed). Therefore, when the

300 N dynamic load was considered, especially as the static results showed a smaller discrepancy than for the 150 N load, only a 'link' idealization was employed.

Shapes of the dome along its axis of symmetry in the direction parallel to the warp direction are shown in figures 9.6a and 9.6b for the 150 and 300 N central loads respectively. Each figure contains the dome cross section shape at: the prestressed state, static loaded state, and at maximum and minimum deflection of the central node (see figure 9.5). The maximum dynamic deflection of the central point is approximately 1.5 times greater than the static value for both 150 N and 300 N loads.

Similarly, as noticed in the static load analysis, the dynamic stresses in the orthotropic membrane material of the dome are not uniform. As an illustration of their variation, figure 9.7 shows values in the first row of elements nearest to the central line in the direction parallel to the warp direction. In general, they provide a fair representation of all values of stresses existing in the dome. For comparison, the stress values are given for:

1. prestressed state (100 Pa internal pressure)
2. for the central Pa = 150 N applied load with:
   a) the stresses corresponding to the maximum dynamic deflection of the central nodes
   b) the stresses corresponding to the minimum dynamic deflection of the central nodes
   c) static loaded state (vibrations dissipated)

3. for the central 300 N applied load with:

   a) the stresses corresponding to the maximum dynamic central node deflection.

   b) the stresses corresponding to the minimum dynamic central node deflection.

   c) static loaded state.

The minimum dynamic stress values for both loads are very close to their prestressed state value, as could have been expected. The maximum dynamic stress values, when the 150 N dynamic load is applied are approximately 1.6 to 1.7 times larger in the warp direction than those resulting from the static load analysis; and for the weft direction the ratio varies from 2.6 to 3.5. The 300 N dynamic load suddenly released on the pneumatic dome causes the maximum stresses (in the warp direction) to be approximately 2.1 times greater than those existing in the structure when the static-steady state is reached. The influence of the dynamic load on stresses in the weft direction is even larger; the dynamic load increases the stresses by 3 to 4.5 times when compared with the static loaded state.

Although dynamic loads cause a greater increase in stresses than in deflections, the latter may be of greater importance in design. In general, membrane material is capable of sustaining greater stresses (with a reasonable safety margin) that designed for by static analysis, but large deflections which may not be dangerous from the point of view of the overall stability of an air-supported structure, can

cause discomfort for users of the airhouse and preferably should be kept reasonably small.

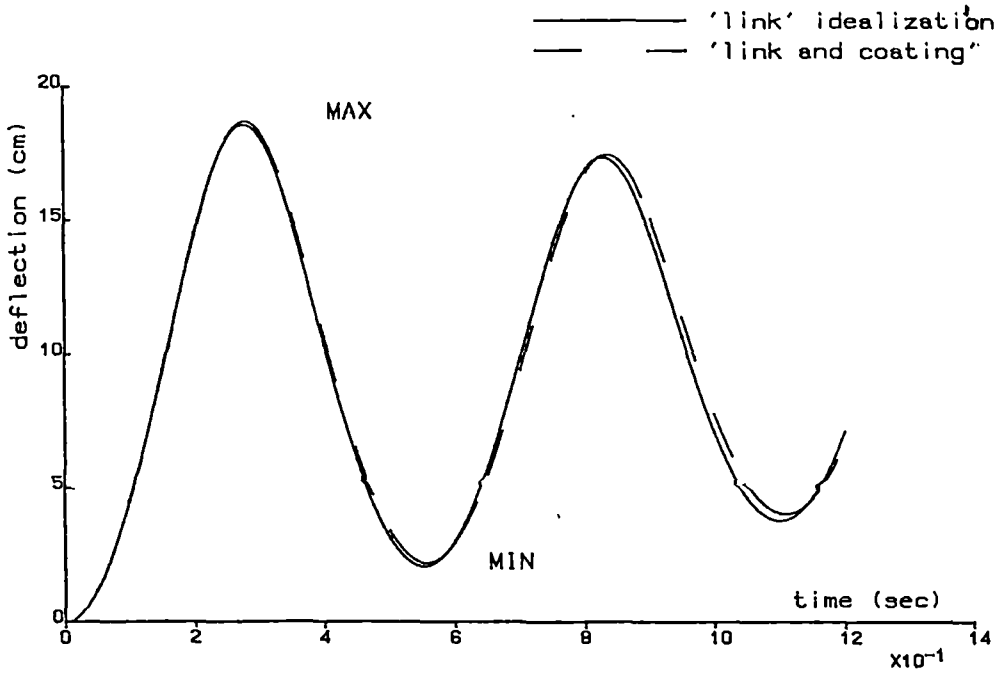

a.150 N central load

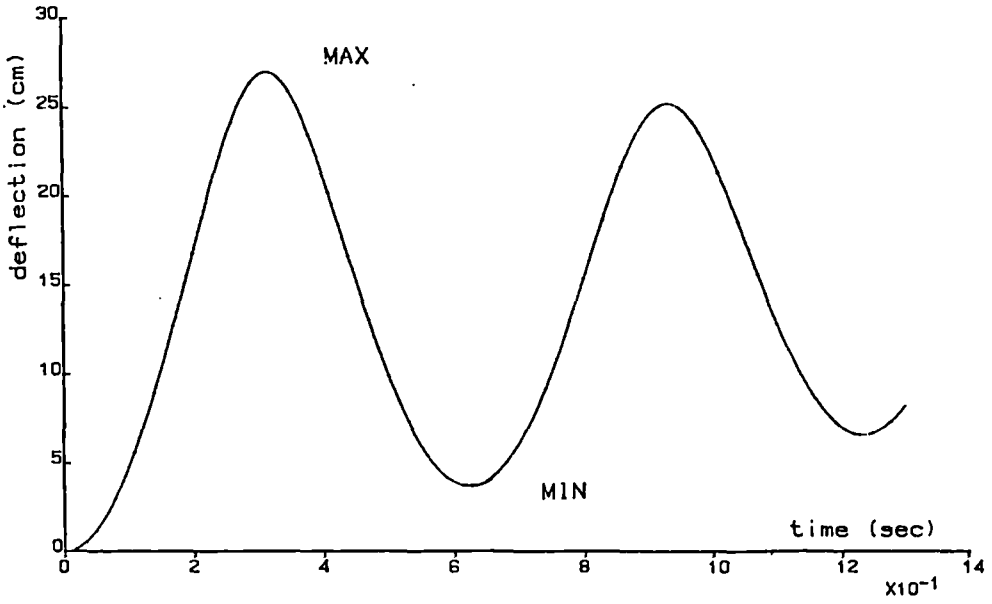

b.300 N central load

Figure 9.5 Pneumatic dome, dynamic deflection of central node

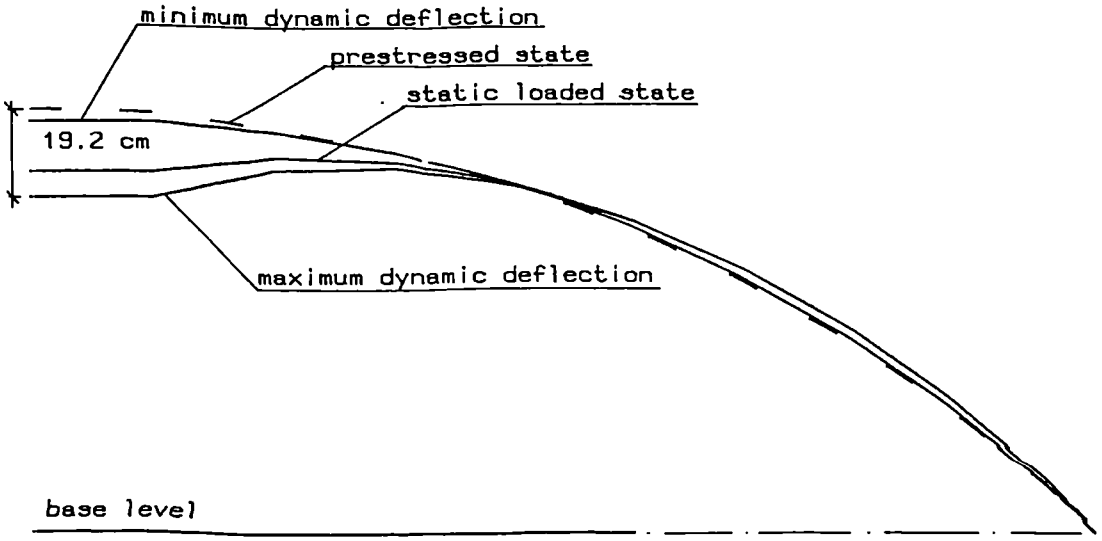

a.150 N centrally applied load

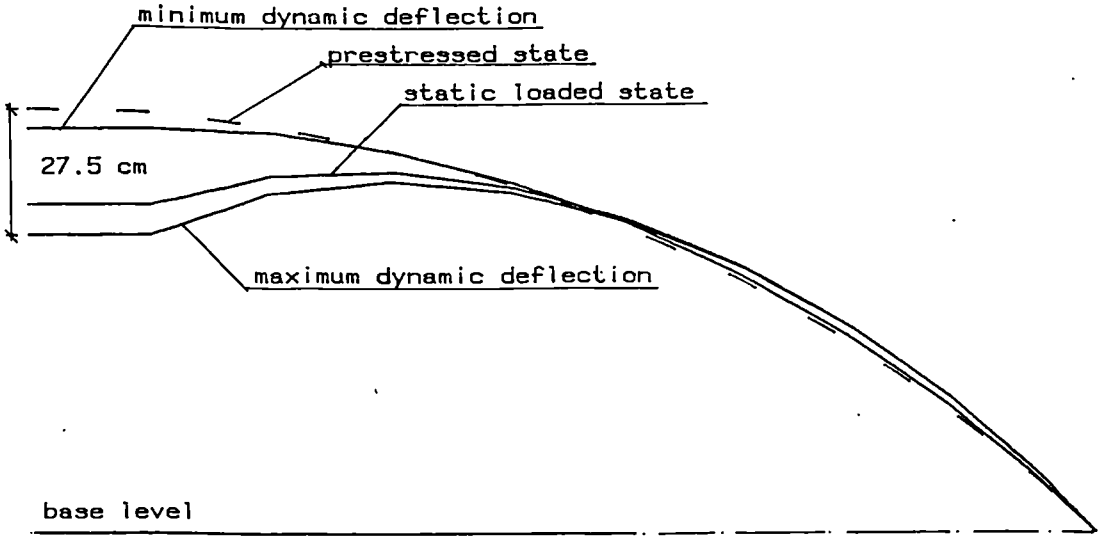

b.300 N centrally applied load

Figure 9.6 Deflected shape of dome along axis of symmetry

1. prestressed state

1	2	3	4	5	6	7	8	9	10	11
261	262	265	270	276	284	295	308	325	345	
76	76	74	71	67	62	55	50	42	40	

warp dir. ——————>

2. 150 N
a. dynamic maximum stresses

402	455	467	492	489	505	524	576	598	599
270	247	149	207	250	276	283	291	253	197

b. dynamic minimum stresses

196	238	252	243	247	289	278	276	317	336
47	65	74	70	68	73	60	51	50	45

c. static stresses

257	266	270	276	285	296	308	324	341	364
103	89	68	87	99	103	100	96	80	64

3. 300 N
a. dynamic maximum stresses

690	774	766	797	787	822	872	897	951	1026
504	489	241	319	396	453	482	479	429	356

b. dynamic minimum stresses

212	218	246	236	238	252	267	274	288	309
53	62	75	75	73	71	67	63	50	44

c. static stresses

327	356	359	366	376	392	410	430	455	485
170	144	74	100	126	139	140	135	115	89

Figure 9.7 Stresses distribution in the dome

9.2.2 Impulsively unloaded isotropic pneumatic dome

The initially flat and uniformly prestressed (37 N/m) isotropic membrane of circular shape was inflated to 15.4 N/m^2 internal pressure, and then loaded as described in chapter 8.3.2. A load of 80 N was applied to the dome and distributed by means of a platen. Two cases were considered:

1. central load, with final internal pressure of 28 N/m^2.
2. asymmetric load, with final internal dome pressure of 26 N/m^2.

The loaded dome geometry and resulting stresses, obtained by applying the dynamic relaxation method, were the starting point for the explicit dynamic analysis. Two different layouts of isotropic triangular elements were employed to approximate most accurately the shape of the dome and the way in which the load was applied:

i) a 'cheese slice' of 10 degrees was used for the central load (figure 8.12a of chapter 8), and
ii) the half dome idealization was used for the asymmetric load (figure 8.13 of chapter 8).

Both the static analysis of chapter 8.4.2. and the dynamics discussed here were carried out to simulate the experiments described in chapter 10.

In the dynamic analysis, it was assumed that the load was suddenly lifted when the dome had reached its long term steady equilibrium state. Although only a single Kelvin model was used to model the visco-elastic behaviour of the

membrane material it was considered that, as only short term response was to be considered, this simple idealization would not produce significant errors.

In the numerical analysis, the following dynamic properties for the membrane material, obtained from experiments (see chapter 10), were used:

Immediate elastic modulus E = 36500 N/m,

Poisson's ratio ν = 52, and

Kelvin model constants: a = .00024 m/N sec

b = 10.5 1/sec

When a pneumatic dome is set into motion by, for example, a suddenly lifted load, the vibration of the membrane causes movement of air which, in the absence of any significant mass resting on the structure, greatly influences the response. However, the investigation presented in this chapter focuses on the membrane response to a suddenly lifted load, disregarding the dynamics of the surrounding air; with only internal air stiffening considered. Attempts to model the internal and external air movement will be discussed in chapters 11 and 12.

The axisymmetric case (impulsively central loading) is the simpler case, since the idealization requires a smaller number of elements to obtain the same modelling accuracy as for half the dome. Also, during the analysis the directions of principal stresses are known. Therefore, this case will be discussed first.

Calculations of the lumped nodal masses were based solely on the mass of the membrane material (equal to .057 kg/m^2). As a direct consequence of keeping the number of elements as small as possible, the smallest mass was for node nr1 (.00014 kg), and the largest value at the rim was .0021 kg. The smallest central mass governed the critical time step.

As a first approach, the suddenly unloaded dome was analysed as described in subclause 9.1, with modification for axisymmetry. The numerical stability of the entire system is highly dependent on the frequency at which checking for buckling is performed. Accounting for this nonlinearity and the incapability of the membrane to sustain compression stresses, required the time step to be decreased to 50% of the critical time and NSDB to be reduced from 20 to 1.

When the previous impulsively loaded dome (subclause 9.2.1) was analysed, buckling occurred only at intermediate stages, between local maximum and minimum values of the central node deflection. In the present case, however, areas of zero stresses existed almost at all stages of the dynamic numerical analysis, except the starting and the last few iterations before static equilibrium was reached. It has been suggested that to improve the efficiency of the computation procedure, some stages of the process, namely those concerning the buckling check, should be reformulated. The new procedure is presented in the flow chart of figure 9.8.

The main differences between the new "stress" scheme for very light impulsively unloaded domes and that discussed in subclause 9.1 and used for the impulsively loaded dome ('force' scheme) are as follows:

1. In the "stress" buckling is checked in the main loop at each cycle and in the secondary loop, hence the [D] matrix needs not to be modified.
2. In the new stress scheme calculations are performed on stress level instead of force. This requires storing two matrices for each element: [D] x [G] and $[G^T]$ (transposed [G] matrix), and passing, from the secondary loop to the main, two updated matrices [D] x [G] and $[G^T]$, and new initial stress vectors [SI] and unit pressure vectors.

The extension of links, e, in step 8 is calculated from the starting geometry but e* in step 3 denotes the difference of link lengths from the level set in the secondary loop, similarly to the old process.

The new numerical procedure results in great savings in computer time compared with the old scheme, but only if the number NSDB is greater than one (preferably at least 5) and if the case under consideration requires checking for buckling at each cycle.

For the analysis of an impulsively heavily loaded dome, the procedure suggested by Barnes [7, 8, 9, 11] is more efficient in terms of computer time and space: instead of

two matrices [D] x [G] and [G^T], only one stiffness matrix is stored and the buckling check at every time step is almost redundant.

The new numerical procedure (stress scheme) was employed to calculate the dynamic response of the centrally unloaded dome. The time interval was 50% of the critical time step (t = .00007 sec), as in the "force scheme", but NSDB was set to 20. During the numerical procedure attention was focused on the vertical displacement of a point .584m away from the centre of the dome. This point coincides with node 3 for a single division (figure 9.10a) and with the node 5 for a double division (figure 9.10b). The traces obtained from both methods: "force" scheme and "stress" scheme differ only slightly (in the case of figure 9.9 the difference is almost negligible, therefore, the 'force' scheme results are not shown separately).

The main advantage of the 'stress' scheme, in this case, is a great saving in computer time. The 'stress' scheme requires only 1/3 of the time necessary for the 'force' scheme. The shorter computer time resulted from less frequent updating of [D] x [G] matrices, creep strains, and the unit pressure and initial stress vectors. The number NSDB, in this scheme, is influenced by changes in geometry taking place and values of applied forces, but not directly by on/off buckling checks.

Further improvement of the numerical procedure can be achieved by observing that, for shallow structures like the dome in question, the highest mass to stiffness ratio (the crucial factor influencing the time step) is for the x and y directions, but the motion due to any central impulse takes place principally in the z direction, perpendicular to the base plane. Increasing nodal masses m_x and m_y therefore results in a time step larger by approximately $\sqrt{MF}$. The number MF depends on the height to span ratio, the deflection relative to overall size, and the character of the response. For the dome under consideration where, in the prestressed state, the height to span ratio is 1:20 (though the dynamic maximum height to span ratio is smaller than 1:20), a value of MF equal to 2 allowed a time step of .0001 sec (an increase of approximately 1.4). For this case the response was almost identical to that obtained using a line step of 0.00007 with $m_x = m_y = m_z$ (see figure 9.9). An increase in value of MF to three, however, led to discrepancies in deflections of 15% and in frequency of 20%.

Figure 9.9 shows the vertical deflection decay at node 3 (for a single division) or node 5 (for a double division) due to a suddenly lifted central load. The deflection, def, is expressed as:

$$def = Z_{3(5)}(t) - Z_{3(5)}(to) \qquad 9.26$$

where

$Z_{3(5)}(t)$ is the vertical distance between the dome base and node 3 or 5 at time t, and

$Z_{3(5)}(to)$ is the vertical distance between the dome base and node 3 or 5 at the beginning of the process.

Three traces are given:

1. for the dome idealised as shown in figure 9.10a with the same masses in all directions ($m_x = m_y = m_z = m$)
2. for the dome idealised as shown in figure 9.10b with the same masses in all directions, and
3. for the dome represented by triangular elements as shown in figure 9.10a with the x and y masses increased by a factor of 2.

The results are almost the same for the first two cycles, then the differences are slightly larger and higher frequencies are present in the response. In general, the discrepancies are small. The following conclusions can be drawn:

a) a single division is adequate for modelling the dome for purposes of an explicit dynamic analysis, and
b) appropriate multiplication of the masses in the x and y direction reduces the computational time without significantly changing the response.

The numerical dynamic analysis of the dome with a suddenly released asymmetric load was based on the 'stress' scheme, with NSDB = 20, and a half dome idealization, as shown in figure 8.13 of chapter 8. The time step (.0002 sec), approximately 55% of the critical time step was higher than for the axisymmetric analysis. In the present case larger elements were used and the maximum deflections were smaller.

Although the dynamic displacements of nodes were still larger in the z direction than in the x and y directions, this time the x and y components were greater in proportion to z than in the previous case. Factorising the x and y masses led to a noticeably different response. During the analysis the vertical displacement of node 4 was traced. This point lay on the axis of symmetry but on the opposite side of the dome to the point at which the load was released. The results of deflection as a function of time, from 0 to 0.5 of a second, are shown in figure 9.11. This time deflection, def, was calculated as:

$$def = Z_4\ (to) - Z_4\ (t) \qquad 9.27$$

Sudden release of asymmetric load induces frequencies associated with higher nodes. In contrast, when a dome is impulsively centrally unloaded, only symmetrical modes of deflection are present.

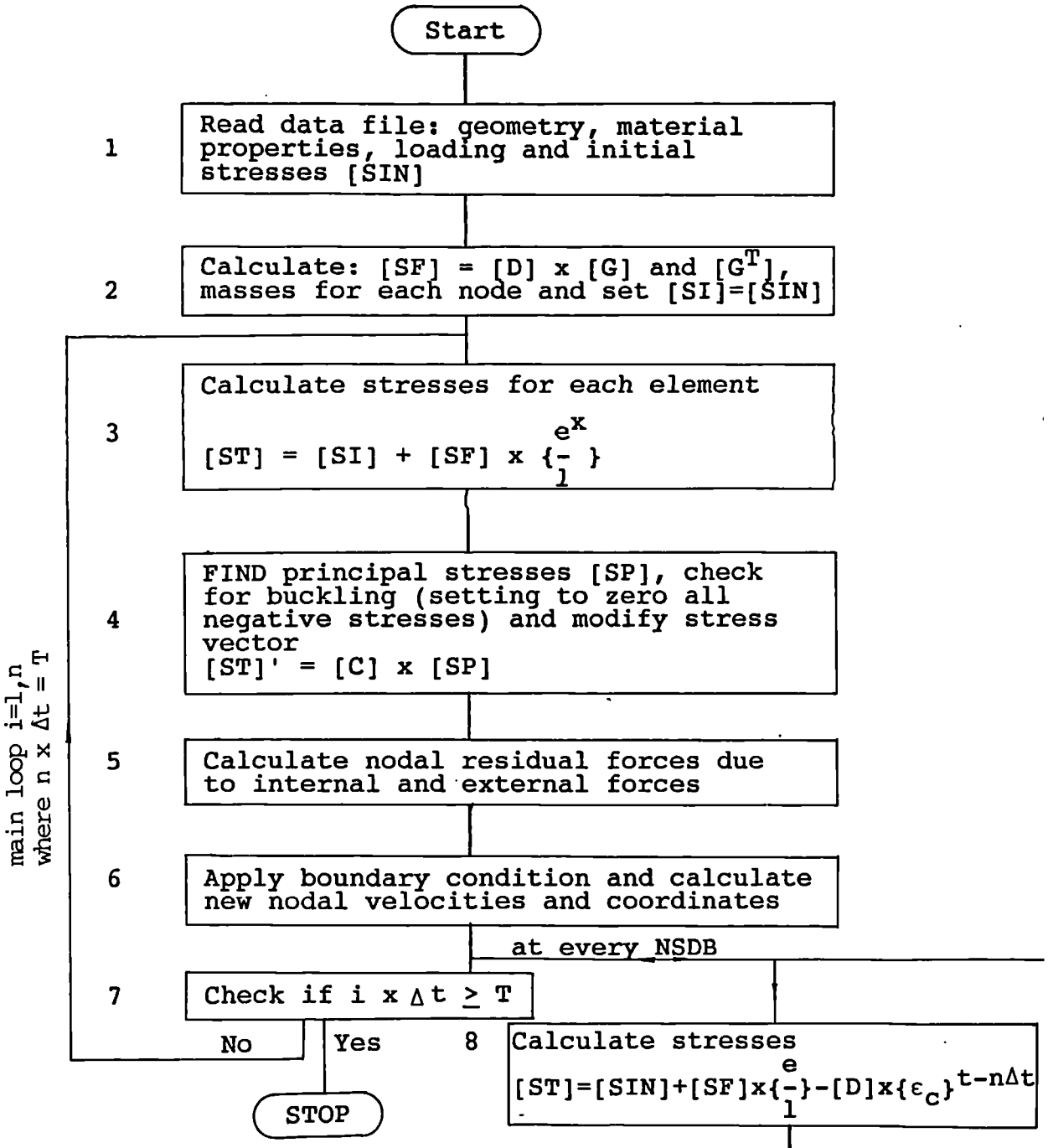
Start
1
Read data file: geometry, material properties, loading and initial stresses [SIN]
2
Calculate: [SF] = [D] x [G] and [G^T], masses for each node and set [SI]=[SIN]
3
Calculate stresses for each element
[ST] = [SI] + [SF] x {e^x / 1}
4
FIND principal stresses [SP], check for buckling (setting to zero all negative stresses) and modify stress vector
[ST]' = [C] x [SP]
5
Calculate nodal residual forces due to internal and external forces
6
Apply boundary condition and calculate new nodal velocities and coordinates
main loop i=1,n where n x Δt = T
at every NSDB
7
Check if i x Δt ≥ T
No
Yes
STOP
8
Calculate stresses
[ST]=[SIN]+[SF]x{e/1}-[D]x{ε_c}^{t-nΔt}
9
similar as 4
Find principal stresses [SP]
.....
10
Find increase in stresses from initial value [ST]'-[SIN]=[ΔS]
11
Set new creep strain {ε_c}^{t+nΔt/2}
12
Reset matrices SF=[D]x[G], [G^T], find unit pressure vector and new initial stress
[SI]=[ST]'+[D]x{ε_c^{t+n t/2} - ε_c^{t-nΔt}}

Figure 9.8

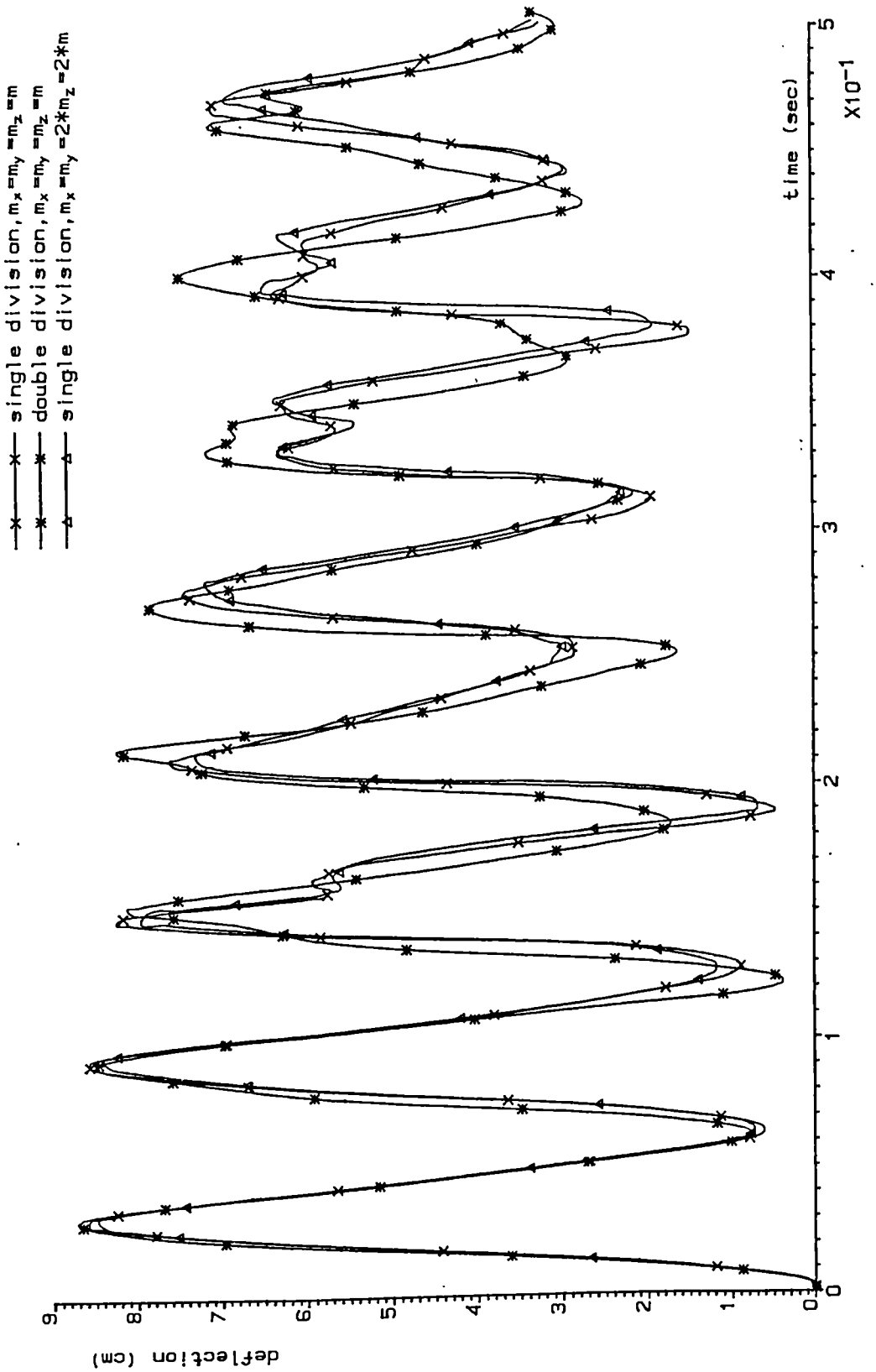

Figure 9.9 Node 3 (5) dynamic deflection decay

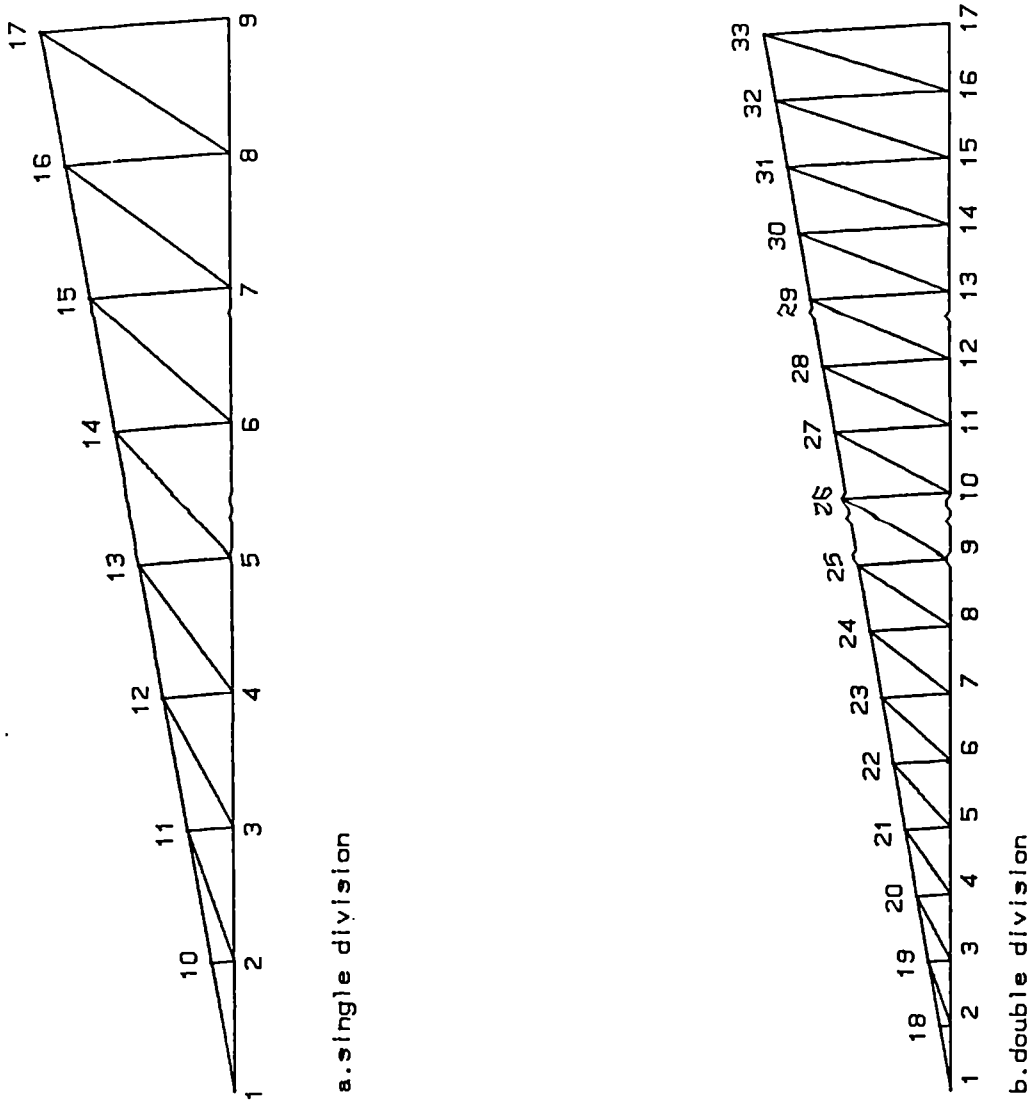

Figure 9.10 Idealization for central load

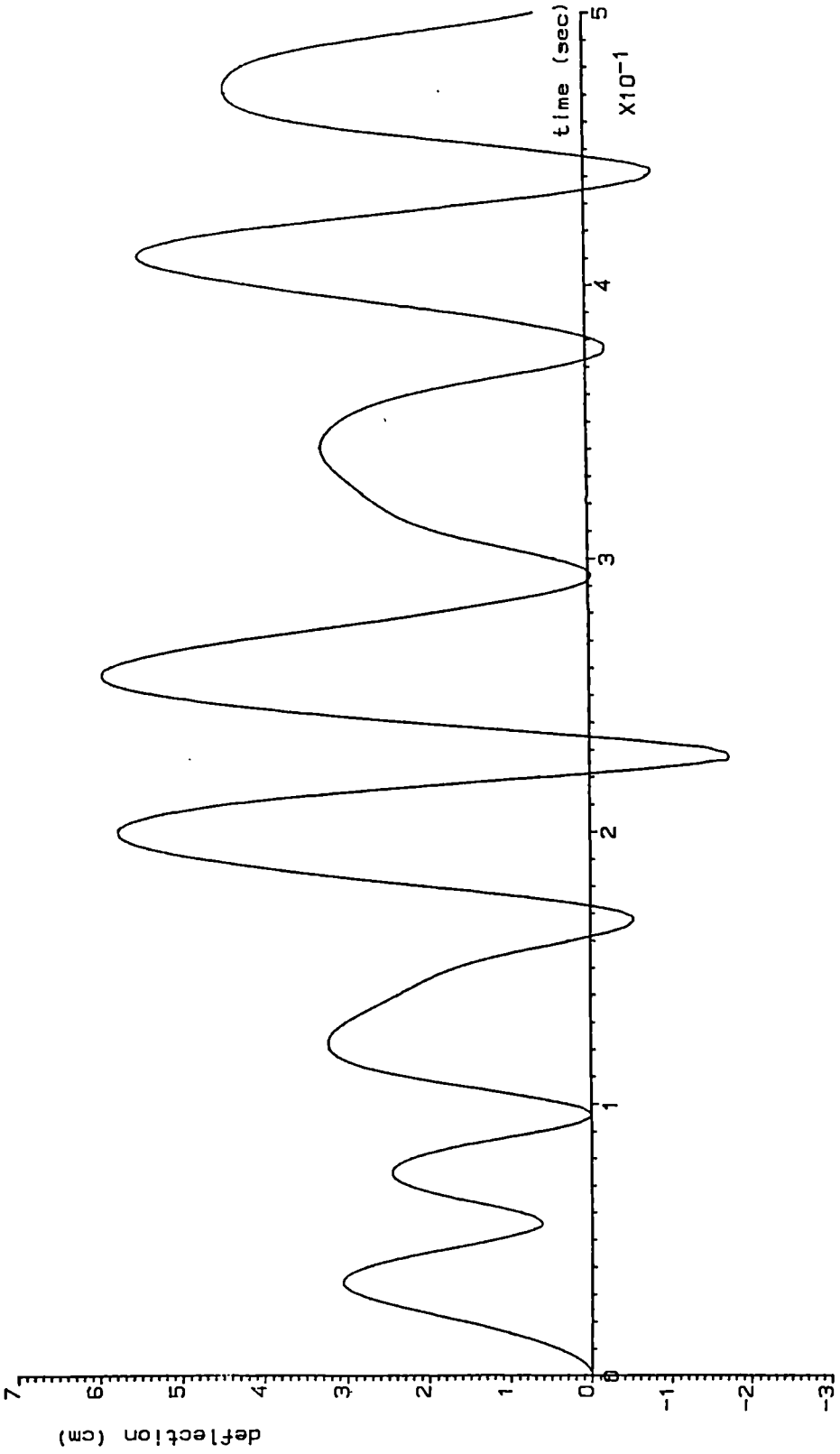

Figure 9.11 Node 4 vertical dynamic deflection decay (asymmetric load)

CHAPTER 10

Contents:

Tests on impulsively loaded and unloaded pneumatic domes

In this chapter static and dynamic tests on two large scale pneumatic dome models, constructed from coated fabric and lightweight polythene sheeting, are described. The static membrane properties for the warp and weft direction of the orthotropic membrane and for the isotropic membrane are obtained from biaxial tests on cruciform specimens. The coating Young modulus of the coated fabric is derived from uniaxial strip tests. A modified biaxial dynamic test for membrane dynamic properties is devised and employed to establish immediate Young moduli and visco-elastic constants.

The coated fabric model, assembled from 'armadillo' elements, and inflated, is subjected to static and dynamic centrally applied loads. Theoretical predictions agree well with experimental results.

The initially flat and uniformly prestressed lightweight membrane dome is inflated and statically loaded followed by a sudden unloading process. Two cases are considered: centrally and asymmetrically applied loads. Theoretical static prediction compares very well with experimental. There are, however, great discrepancies between theoretical and experimental dynamic deflection traces, caused mainly by disregarding the surrounding air effects in the theoretical analysis (except that of internal air stiffening).

10.1 Structural properties tests for the dome membranes

10.1.1 Introduction

An ideal material for the envelope of air-supported structures should be lightweight, low cost, durable and should have a high tensile strength and stiffness in the directions of maximum stress under the most extreme operating conditions. The membrane should be flexible and of very low air permeability. The material should be resistant to the propagation of minor accident damage and it should be capable of being seamed or jointed in a simple, cheap, air tight and mechanically efficient manner. Since the material is intended mainly for outdoor use it should be resistant to all aspects of environmental degradation, such as sunlight, oxidation, moisture and fungal and chemical attack over long periods of exposure. In order to ensure the safety of occupants the material should be non-flammable or at least incapable of sustaining combustion.

Although some monophase materials like sheet metal or foil materials have been used, in general they do not satisfy many of the properties described above. The best compromise is a composite material comprising a woven fabric, for stiffness and shear flexibility, coated normally with polyester PVC, to satisfy permeability and environmental considerations.

Fabrics are composed of fine filaments: synthetic or glass, twisted into yarns and woven into cloths. Coatings can be divided into two classes: lower cost materials (PVC,

polyurethanes and rubbers) and high cost fluoroelastomers (PTFE, Silicon, PVDF) [134]. The most commonly encountered coated fabric systems in use today are [134] for temporary air-houses: PVC coated polyester, and for permanent use: PTFE (for example Teflon) - coated glass. After weaving and coating the warp yarns are usually straight and the weft yarns are undulating. Under load in the weft direction these yarns will straighten and the warp yarns will undulate. The process is known as crimp interchange. The membrane responds inelastically when it is loaded triaxially to a tension of 5% or more of the strip tensile strength in each direction [134].

When an air-supported structure is designed various properties of the membrane should be established . These mainly comprise: stress/strain relation, stretch compensation for cutting patterns, resistance to tear propagation, bursting strength, weathering properties, strength of fabric and seams, translucency, thermal performance and resistance to fire. Many of these can be measured according to BS 3424 Part 0 to 35, or as suggested by Ansell, Barnes and Williams [5].

During tests, membrane specimens should be subject to conditions similar to those likely to occur during the life span of the structure. In this work our attention is focused on one aspect of the design of air-supported structures; namely finding the structural response to externally applied load. Numerical analyses have been

carried out (chapters 8, 9 and 11, 12) to model tests conducted on pneumatic domes, which will be described in subclauses 10.2 and 10.3. For these purposes only some of the membrane properties are needed. These are the static and dynamic stress-strain relationships and, therefore, only they will be discussed in more detail.

Properties of membrane materials will vary more or less randomly. The amount and accuracy of information required about a given property will depend on the effect that the property has on the behaviour of the structure. For example, in calculating the deflection of an air-supported structure due to wind or snow load, it would seem reasonable to use the mean stiffness of the fabric, but in assessing the safety of the structure one needs an estimate of the minimum strength of the fabric rather than its mean value. Similarly, when deflections and mean stresses are sought in a model subject to a point load, the mean properties are used.

10.1.2 Static stress-strain relations

BS 3424: Part 4: 1982 describes test procedures for the uniaxial determination of breaking strength and elongation at break, and Part 21: 1987 gives a method of uniaxial test for determining the elongation and tension set of coated fabric (the extension remaining after a test specimen has been attached and allowed to retract in a specified manner). The extension or elongation may be measured between gauge marks and expressed as a percentage of the original length.

The approaches of both methods can be used to obtain a record of the uniaxial stress/strain relations throughout the loading range for warp, weft and, if necessary, coatings (bias direction) of specimens.

When a typical uncoated woven fabric is stretched, the effective elastic modulus will include apparent strain contributions from several mechanisms, other than the true elastic (or visco-elastic) extension of the fibres themselves [4]. Even at low stresses these are:

1. Yarn shear or rotation. If the principal stresses are not aligned with the warp and weft of the fabric.

2. Crimp interchange. For example, if a highly crimped weft yarn is directly loaded it will not begin to extend elastically until it has lost the crimp, which will be in some measure transferred to the originally straight warp yarns.

These mechanisms depend mainly on the principal stress ratio. At higher stresses additional mechanisms are present, like yarn flattening, yarn compaction or fibre straightening and/or rotation [81].

For small-strain extensional behaviour in the warp or weft direction, the coating has little intrinsic strength or stiffness, but even a non-rigid matrix will significantly raise the in-plane shear resistance of a coated fabric. The general two-dimensional form of Hooke's law for a coated fabric contains nine stiffness coefficients [81]

$$D = \begin{bmatrix} d_{11} & d_{12} & d_{13} \\ d_{21} & d_{22} & d_{23} \\ d_{31} & d_{32} & d_{33} \end{bmatrix} \qquad 10.1$$

Since the straining of such materials is not necessarily conservative, i.e., the values of the coefficients may be dependent on the state of strain in the material and its loading history, all nine coefficients are independent and multi-valued. Furthermore, in a coated fabric some of the coefficients are likely to be time-dependent. In non-linear anistropic membranes, therefore, the setting up of precise constitutive relations can be an exceptionally unwieldy process.

Static stress-strain relations can be obtained by an alternative approach as suggested by Barnes, Ansell and Williams [5] and which will be followed here. A specimen is subjected to a similar range of biaxial stresses to that existing in the loaded state of a structure, and it is assumed that throughout these stresses the highly complicated stress-strain relation can be approximated for orthotropic material by:

$$\sigma_x = d_{11}\ \varepsilon_x + d_{12}\ \varepsilon_y$$
$$\sigma_y = d_{21}\ \varepsilon_x + d_{22}\ \varepsilon_y \qquad 10.2$$
$$\text{with } d_{12} = d_{22}$$

and one shear modulus, which for most coated fabrics, will be very low, and

$$d_{11} = \frac{E_x}{1-\nu_x\nu_y}\ , \quad d_{12} = \frac{\nu_y E_x}{1-\nu_x\nu_y}\ , \quad d_{22} = \frac{E_y}{1-\nu_x\nu_y}$$

Although three coefficients can be obtained from a single test it is preferable to use at least two tests

1. σ_x constant with σ_y varied,
2. σ_y constant with σ_x varied

and, when higher accuracy is required, σ_x and σ_y varied with $\sigma_x/\sigma_y = 1$, and obtain a best fit to the stress/strain curve.

Orthotropic membrane tests

A model pneumatic dome, which will be described in 10.2 was constructed from P.V.C. coated terylene voile approximately .25mm thick and of mass .345 kg/m^2. The membrane is lighter and of much lower strength than a typical coated fabric used for air-houses (average mass is about .9kg/m^2).

The following static properties were required (see chapter 8)

1. elastic modulus and Poisson's ratio for the warp direction
2. elastic modulus and Poisson's ratio for the weft direction, and
3. elastic modulus for the coating

The first two sets of parameters were obtained from biaxial tests and the last one from a uniaxial test.

a. Biaxial tests

The test specimens were cruciform in shape 50 x 50 cm with a 10 cm square central test area. The warp and weft directions were parallel to the two cruciform arms (see photographs in figure 10.1). In order to ensure a

reasonably uniform stress state in the central area, three slits were cut in these cruciform arms. The slits were stopped at both ends by drilling small holes before cutting the material. The stops before the fabric enters the clamps were to avoid failure near the end clamps, and those near the central test area were to prevent tear propagation. The corners, where the arms of the material meet were joined by a small radius curve to avoid possible areas of stress concentration. Four gauge points were arranged in the central square with 50mm gauge lengths.

Each of the specimen arms was cut 12 cm longer to allow for fixing by means of clamps. The clamp assembly consisted of two metal plates drilled with holes, a metal rod, and nuts and bolts. The specimen arm was wrapped around the rod, doubling onto itself and the plates were added, sandwiching the membrane between them. The nuts and bolts were tightened, effectively gripping the material in its jaws. To each of four clamps, a flexible thin steel wire was attached and led over pulleys fixed to a steel frame. The specimen was kept in equilibrium by balanced suspended loads, namely, (referring to figure 10.2):

$p_{h}^{l} = p_{hr} = p_{h}$

$p_{vt} = p_{vt}$ + weight of clamps 2 and 1

and adjustable supports for clamps 3 and 4.

The loading frame, pulleys and clamps were already available from previous tests.

The specimen was loaded, in a manner similar to the way the load was applied to the model; namely, strains were recorded immediately after applying loads. The distances between gauge points were measured by means of an electronic vernier; three readings for each distance were taken and their mean was used for processing results.

Two cruciform specimens were used, each for a separate test:

Test 1

The stress in the warp direction , σ_x, was kept constant and the weft direction stress, σ_y, was varied. The specimen was positioned in the steel frame with the warp direction being vertical. The values of loadings were chosen as follows:

$p_{vt} = p_{vb}$ + weight of clamps 1 and 2 - to induce a warp tension in the specimen of approximately the same value as the average in the dome, under the prestressed and loaded state. Here, as two loading cases were considered, 150 N and 300 N centrally applied load, the average value was found from the mean stresses for the three cases. The approximate value was 350 N/m.

p_h - loading which induces stress in the weft direction was applied in steps from p_{hs} to p_{hf} in steps of Δp_h

p_{hs} - to induce tension in the specimen of approximately the same value as the minimum stress under prestressed conditions; here p_{hs} was taken to induce a stress of 50 N/m

p_{hf} - to induce tension in the specimen of 175 N/m approximately, which is the same value as the average maximum stress which occurs when the dome is loaded by the 300 N central load.

For convenience Δp_h was chosen as 25 N/m to allow for six steps.

After the stresses in the weft direction reached the final value, p_{hf}, the specimen was unloaded, but this time in steps of 50 N/m.

Test 2

Stress in the weft direction, σ_y, was kept constant and the stress in the warp direction , σ_x, was varied. The specimen was placed in the frame with the weft direction being vertical. The loads were found in a similar manner to test 1, but this time:

p_{vb} + weight of clamps 1 and 2 corresponds to tension in the weft direction and it was calculated to be 125 N/m.

p_h applies to the warp direction, and p_{hs}, p_{ht} and Δp_h were 250, 500 and 50 N/m respectively.

The unloading test was performed in steps of 100 N/m.

For both tests the datum levels were the p_{hs} and p_{vt} stress conditions and all strains were calculated from these geometries. Young's moduli and Poisson's ratios were found assuming stress-strain relation as given by equation 10.2,

which can also be written in the following form:

$$\varepsilon_x = \frac{\sigma_x}{E_x} - \nu_y \frac{\sigma_y}{E_y} \qquad a$$

10.3

$$\varepsilon_y = \frac{\sigma_y}{E_y} - \nu_x \frac{\sigma_x}{E_x} \qquad b$$

where

the moduli of elasticity E_i and Poisson's ratio ν_i are interrelated as follows:

$$\frac{\nu_x}{E_x} = \frac{\nu_y}{E_y} \qquad c$$

Each test result allowed two parameters to be established. From test 1, where σ_x was kept constant, plotting the results for strains and stresses in the weft direction and approximating it by a straight line (as the best possible fit) E_y was found. Then plotting ε_x against ε_y led to determining ν_y. From test 2, in a similar way, E_x and ν_x were obtained. It should be noticed that each parameter was found as the mean of four results; loading and unloading tests with two gauge lengths used for each case.

The properties obtained from these two tests and equation 10.3 resulted in an overdeterminated problem. While processing the test results it was noticed that the plots to establish ν_y showed the greatest discrepancies. During the tests, varying stresses in the weft direction resulted in very small changes in the warp direction which were difficult to measure accurately. Therefore, Poisson's ratio, ν_y, was calculated from 10.3c. The experimental

value of ν_y was slightly higher than the theoretical one.

Finally, the immediate Young's moduli and Poissoin's ratios for the warp and weft directions were found to be:

E_x = 93800 N/m

E_y = 13700 N/m

ν_x = .89

ν_y = .13

Throughout both tests all values of p_h and p_v were determined from the state of stress in the pneumatic dome. On the other hand, stresses in the structure can be only obtained from an analysis when the membrane properties are known. One way to solve this problem is to conduct simple uniaxial tests, assume Poissoin's ratios, and then carry out an analysis. The resulting state of stresses can then be used to conduct biaxial tests, followed by analysis based on the new properties. In this case, the biaxial results had been already available, though for a slightly different range of stresses, and they were thus employed in preliminary numerical analysis.

An additional test was conducted to establish the creep occurring in the dome under prestressed conditions. The specimen was placed in the frame and loaded to induce tension of approximately the same value as the average stresses in the dome under prestressed conditions, namely 280 N/m and 65 N/m in the warp and weft direction respectively. The distances between gauge points were monitored immediately after applying load and again after 2 hours. The two values were within 5%.

b. Uniaxial test for coating

Coating does not contribute considerably to the direct stiffness but gives shear resistance to a coated fabric. In order to perform an investigation on the influence of coating on the behaviour of a composite, knowledge of certain coating properties is essential. Here, in order to carry out the analysis as described in chapter 8, only Young's modulus is needed.

Two specimens of rectangular shape 14 x 2.6 cm, with 12 cm extensions on both ends to allow for fixing, were cut from the membrane in a 45 bias direction, to be tested as a pair. The strips were attached to two clamps as shown in the picture of figure 10.3. The top clamp was suspended from the steel frame by means of a steel rod and the bottom hung freely. During the test the extension/distance between clamps was measured.

The weight of the bottom clamp introduced in the specimen an initial stress of 30 N/m, which was used as a datum level. Loads were then applied to induce tensions in specimens varying from 30 N/m to 210 N/m in steps of 30 N/m, and strains were recorded by means of an electronic vernier. The test was repeated with loads being decreased in steps of 30 N/m. The Young's modulus for the coating was obtained as the average from 4 sets of results (two for loading and the other two for unloading) to be E_c = 6050 N/m.

The plots of strain against stress for the coating show more regularity than those for the warp and weft direction tests. They form more closely a straight line. Therefore, although the shear stresses obtained from the dome analysis are of smaller values (the maximum stress is 100 N/m) than the range of stresses used during the test, an additional test did not have to be conducted.

Isotropic membrane tests

The second pneumatic dome model used in the experimental work was constructed from polythene sheeting, approximately .06 mm thick and of mass .057 kg/m^2. The membrane is a homogeneous material with the same properties in any direction. When this material is stretched, mechanisms related to the response are much simpler than those in a coated fabric. Stress-strain plots are expected to be more like those for a coating than those for the warp or weft direction of a fabric. On the other hand, the material experiences much greater creep in the range of stresses occurring in the isotropic dome model than the coated fabric model.

Preliminary tests were conducted on strip specimens; the size and arrangement of which were the same as during the coating uniaxial tests. The pair of strips was subjected to the same cycle of loading and unloading with stresses varying from 30 N/m to 280 N/m in steps of 30 N/m. Strains were recorded immediately after applying loads. Thus obtained, as the mean of sets of results, the Young modulus was 5000 N/m.

During these preliminary tests it was noticed that, due to the creep, readings of the same distance taken with a few minutes interval (while the specimen is subject to the same stress) differ considerably. As these tests were conducted before experiments on the pneumatic dome, it was concluded that in order to obtain more accurate results and closer correlation between the numerical and experimental results, all recordings should be taken after the main creep had taken place for both the material tests and the dome tests.

Biaxial tests on the material are necessary:

1. to provide Poisson's ratio
2. the Young modulus will be more accurate, as it will be obtained in similar stress conditions to those which exist in the dome.

The appropriate range of stresses for the biaxial tests was obtained from preliminary numerical analysis with the Young modulus determined from the uniaxial tests and Poisson's ratio assumed to be 0.5.

Two cruciform specimens were used for the biaxial tests. The arrangement of the rig, shape and size of specimen was the same as used for the tests on the coated fabric membrane (see figures 10.2 and 10.4 for the general arrangement).

In the first stage, tests were conducted to establish the time during which the main creep takes place. The specimen was loaded in such a way that the tensions induced in both

directions were equal and approximately of the same value as the average in the dome under the prestressed and loaded states, namely 110 N/m. The gauge lengths in the central rectangular area were recorded by means of an electronic vernier placed between each pair of gauge points. The measurements were taken after each 15 minutes for 1 hours. Then the test was performed again with the specimen loaded to induce tensions of 90 N/m and 150 N/m in the horizontal and vertical directions respectively. The loads were chosen such that:

p_h = induced tension in the specimen of approximately the same value as the average minimum in the dome, and

p_v = induced tension in the specimen of approximately the same value as the average maximum in the dome.

The conclusions from both tests were similar; when a load is applied to the specimen the main response (immediate elastic and primarily creep) takes place within one hour.

Tests to obtain Young's modulus and Poisson's ratio were conducted on two specimens. During each test, the vertical stress was kept constant at 110 N/m and the horizontal stress varied from 70 to 190 N/m in steps of 20 N/m. At every step the readings were taken one hour after the load increment had been applied. A similar procedure was followed during unloading.

The specimens were tested in two perpendicular directions, to investigate whether the rolling process during production

of the membrane influences the material properties. The results did not show any discernible dependency upon the direction of the membrane.

The results were processed in a similar manner to that already explained for the case of the coated fabric membrane tests. This time, however, equation 10.3 was amended to account for isotropic material:

$$\varepsilon_x = \frac{\sigma_x}{E} - \nu \frac{\sigma_y}{E} \qquad a \qquad 10.4$$

$$\varepsilon_y = -\nu \frac{\sigma_x}{E} + \frac{\sigma_y}{E} \qquad b$$

As a direct consequence of the above, both E and ν were found as the average from eight values to be:

$E = 5260$ N/m

$\nu = .52$

The difference between Young's moduli obtained from the uniaxial instantaneous test and the biaxial long term test was 5%.

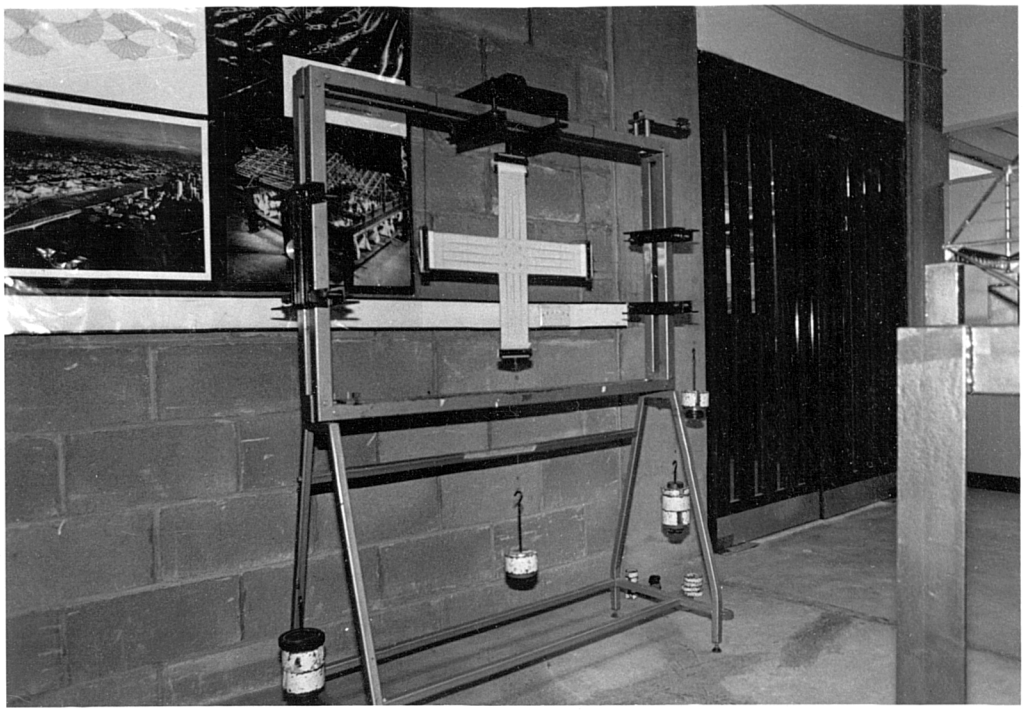

a.

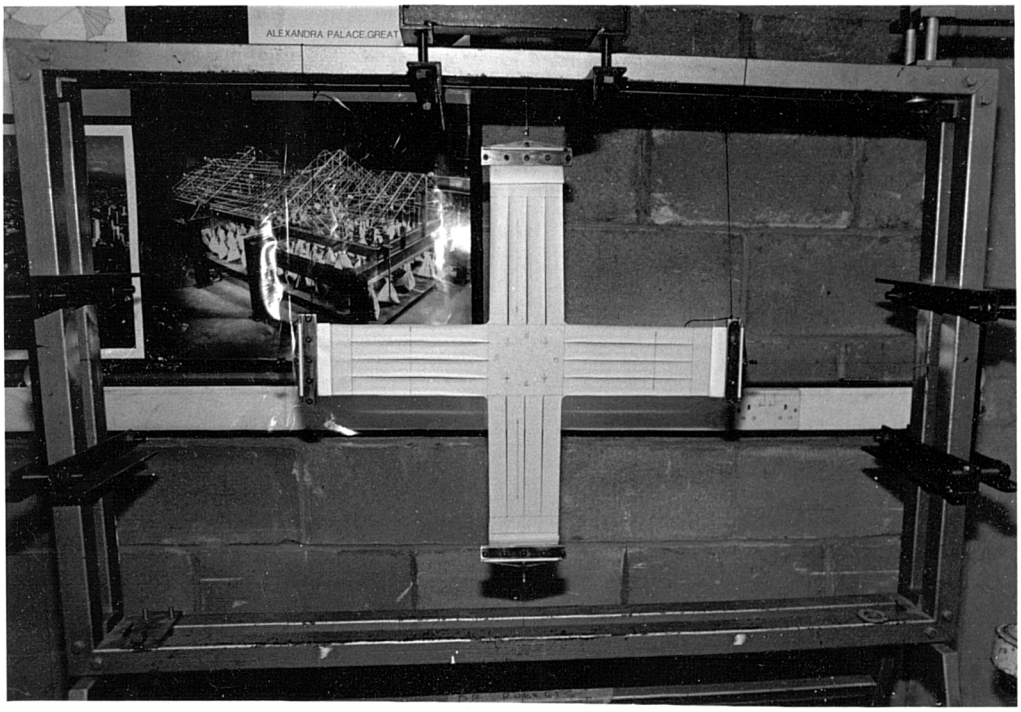

b.

Figure 10.1 Static biaxial test of coated fabric

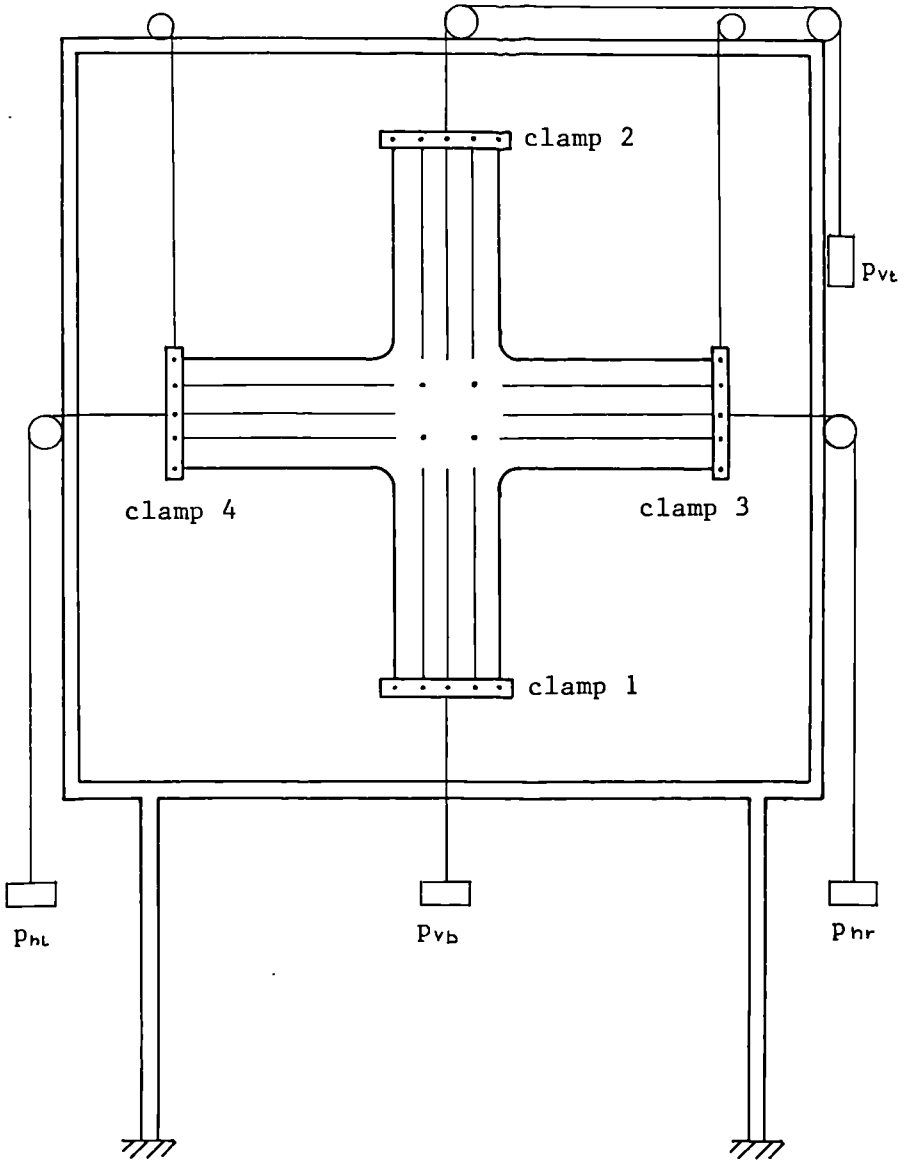

Figure 10.2

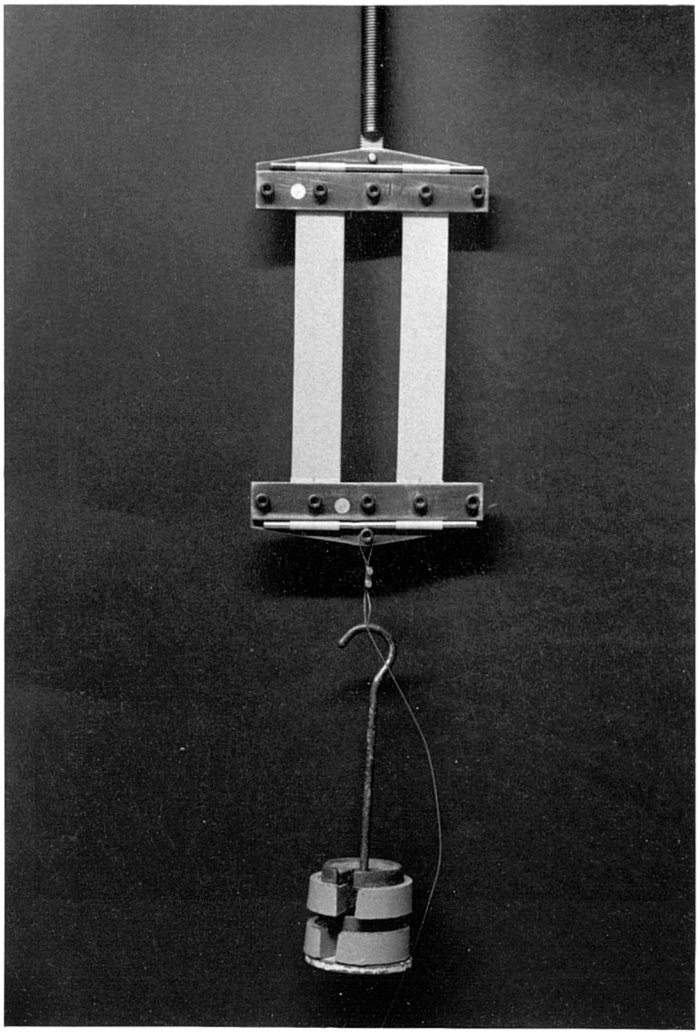

Figure 10.3

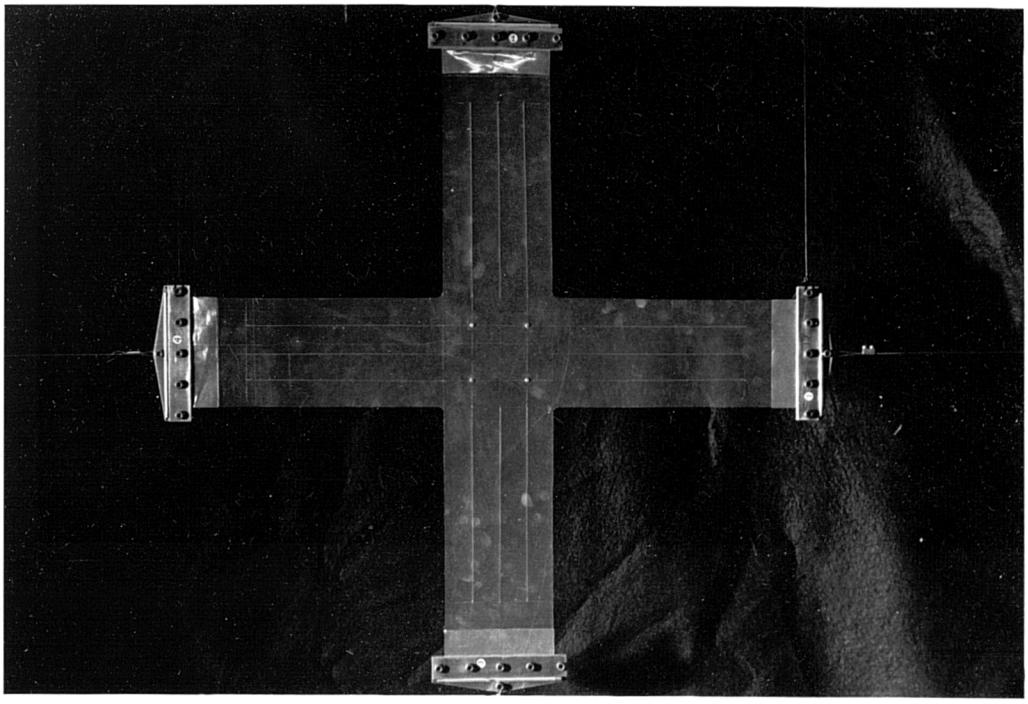

Figure 10.4

10.1.3 Dynamic properties test

In chapter 9 it has been assumed that the dynamic behaviour of coated fabrics and of materials like polythene sheeting can be represented by Kelvin models placed in series and coupled with an elastic response. In some cases, for example short term dynamic response of a suddenly loaded or unloaded pneumatic dome, a single Kelvin model may suffice. To represent numerically the process the following parameters are needed: the immediate elastic modulus, E, and Poisson's ratio, ν,(to predict the elastic response); and the Kelvin model constants a *and* b, *to calculate the primary* creep, which is time dependent and results in visco-elastic material damping. For orthotropic membranes these properties should be known for the warp and weft direction, and for the coating when shear rigidity is included. For isotropic materials one set is adequate, as the three parameters hold the same values for any direction.

Barnes in his work [9] gives a simplified procedure to establish the required properties by means of uniaxial dynamic tests performed on strip specimens followed by a simple numerical analysis involving curve fitting. Since, in general, material 'constants' for a membrane, especially a coated fabric, depend on the kind of stress (whether uniaxial or biaxial) and its level, attempts have been made to model stress conditions in a specimen more closely to those existing in the structure. A report on the method, where biaxial stresses are induced in a specimen is presented in the work by R F De La Salle [56]. The proposed

test was performed on a vertical pressurised cylinder made of the membrane specimen. Internal pressure induced tension in the specimen in both the circumferential and longitudinal directions, and a suspended and suddenly applied load induced additional stress in the longitudinal direction, for which the dynamic modulus and visco-elastic constants were sought. The procedure was rather troublesome and due to the presence of seams in the wall (two were used to maintain symmetry), the stress distribution was not exactly uniform.

In this work an alternative method to the pneumatic cylinder is devised, which can be viewed as an extension of the static cruciform test to allow a dynamic properties test. The test specimen is rectangular in plan 10 x 50 cm with 12 cm extensions, as shown by dotted lines in figure 10.5, to allow for fixing. The shorter side of the rectangle is parallel to the direction for which E, a and b are sought. To ensure a uniform state of stresses in the central area 10 x 10 cm, slits are cut in both arms. They are stopped on both ends to prevent any failure near clamps and tear propagation in the central area.

The specimen was initially held in position by suspending on adjustable side clamp supports, with loading , p_h, only in the horizontal direction. The specimen was allowed to creep for approximately one or two hours (depending upon the material). The top and bottom clamps were then positioned and a dead vertical load, p_{vd}, applied. After one or two hours an additional vertical load, p_{vl}, was suddenly

released by cutting a supporting wire in such a way that no lateral disturbance was caused. Response, namely the deflection of point A was recorded by means of a frictionless linear LVDT (low voltage displacement transducer) with range 5 mm, coupled to an ultra violet recorder.

The recorder can produce an output at a scale suitable for further data processing, according to the sensitivity of the inserted galvanometer. Each arrangement: transducer + ultra violet recorder with a galvanometer, should be carefully calibrated by processing known deflections in the same range as the experimental values. Deflections can be measured by means of a digital micrometer head.

The loads: p_{vd}, p_{vl}, p_h depend upon a particular situation; their values are chosen to approximate as closely as possible the state of stress existing in the structure.

The top and bottom clamps, which are placed very close to the central area of the specimen, introduce some restraint, which results in a non uniform stress distribution. This effect is partially alleviated by fixing the top and bottom clumps only after the main extension of the specimen due to horizontal loading has taken place. Therefore, the restraining effect on the central area, in the horizontal direction, is only associated with the additional strains caused by the vertically applied load.

Orthotropic membrane

The P.V.C. coated terylene fabric membrane was tested:

1. for dynamic properties in the warp direction,
2. for dynamic properties in the weft direction, and
3. for the coating dynamic properties.

The warp and weft dynamic material 'constants' were obtained from biaxial tests using the arrangement shown in figure 10.5 and in the picture of figure 10.6.

Loads were chosen as follows:

p_h - to induce horizontal tension in the specimen of approximately the same value as the sum of the average tension in the dome in the weft (for test 1) or warp (for test 2) directions under the prestressed condition and half and the the difference in tensions between the loaded state of prestressed condition,

p_{vd} + weight of bottom clump - to induce a tension in the specimen in the vertical direction of approximately the same value as the average in the dome in the warp (test 1) and weft (test 2) directions under prestress only,

p_{vl} (when applied statically) to induce a tension in the specimen in the vertical direction of approximately the same value as the average difference in stresses between the loaded and prestressed conditions in the warp (test 1) or weft (test 2) directions.

The loaded state stresses were taken as the mean of the two average stresses in the dome when 150 N and 300 N central loads were applied.

The specimen was allowed to creep for two hours.

In the test for the warp direction dynamic properties the following loads were used:

p_h to induce tension of 115 N/m

p_{vd} + weight of bottom clump - to induce tension of 250 N/m

p_{vl} - to induce additional tension of 30 N/m;

and for the weft direction they were:

p_h - to induce tension of 35 N/m

p_{vd} + weight of bottom clump - to induce tension of 70 N/m, and

p_{vl} - to induce tension of 60 N/m.

For each calibration test, trial and error curve fitting was carried out to establish the dynamic modulus and visco-elastic constants. For the purpose of numerical analysis a quarter of the specimen central area (advantage was taken of symmetry) was divided into 25 triangular elements. The geometry and stress distribution, due to the static load (p_h and p_{vd} + weight of bottom clump) was obtained by employing the dynamic relaxation method. In the dynamic analysis, the

intermediate nodal masses were assumed as 15% of the bottom load mass and $\Delta t = .5\ \Delta t_{crit}$. In each case creep strains were incremented at every time interval. For the first trial, as suggested by Barnes [9], the immediate elastic modulus was taken as $\frac{\sigma}{\varepsilon_c}$, where ε_c is the final creep strain and σ is the static stress in the vertical direction; and by assuming the value of a (for example taken from previous test), b can be calculated as $b = \frac{a\sigma}{\varepsilon_c}$.

The results for the warp and weft directions are shown in figure 10.7a and 10.7b respectively. In the warp direction, due to comparatively small creep, material constants can be found which closely simulate the test results. In the weft direction, however, the three constants have been chosen to comply with the first peak deflection, the rate of decay, and the 'quasi-static' terminal deflection. In the intermediate stages the results are as good as can be expected, bearing in mind the crudeness of the single Kelvin model for creep. Unfortunately this method does not allow dynamic Poisson's ratios to be obtained. Therefore, the static Poisson's ratios, slightly adjusted to comply with equation 10.3c, were used in the dynamic analysis of the dome.

Dynamic properties for the coating were obtained from a uniaxial test, by applying a sudden load to two identical strips 50 x 2.6 cm cut from the coated fabric in a 45 bias

direction. The set up is shown in the picture of figure 10.8. The shape of the specimen is similar to the uniaxial test described by Barnes [9], but the way of applying vertical static and dynamic loads is as shown in figure 10.5 for the biaxial test.

The vertical loads applied to the specimen were:

p_{vd} + weight of bottom clump - to induce a tension of 90 N/m

and

p_{vl} to introduce an additional tension of 120 N/m.

The numerical analysis was carried out using six bar elements for the idealization. The results are shown in figure 10.10. As the creep is significant the three constants give only an approximate trace of the experimental dynamic response. In order to obtain closer theoretical simulation of the test, two or three Kelvin elements placed in series could have been used.

The load applied to the specimen caused a stress which was too high. The test was performed before any analytical analysis accounting for the coating had been carried out, and was anticipated to give only preliminary results. However, the effect of the coating on the dynamic response of the dome was found to be comparatively small, hence further work to derive more accurately the visco-elastic constants and the elastic modulus for the coating seemed to be unnecessary.

Isotropic membrane

The isotropic pneumatic dome was initially prestressed, inflated, statically loaded and then dynamically unloaded. Two loading cases were considered: centrally and asymmetrically applied loads. Dynamic numerical analyses were carried out for the suddenly unloaded dome to match the experimental procedure. In the biaxial method employed for testing the dynamic properties of the coated fabric, a vertical load is impulsively applied to a specimen and a response is followed. The static tests performed on the isotropic polythene sheeting material did not show great discrepancy between loading and unloading cycles. Therefore, it seemed quite reasonable to assume that a similar behaviour would be observed in dynamic tests.

The dynamic modulus and visco-elastic constants for the isotropic membrane were calibrated as shown in the picture of figure 10.9, by a procedure similar to that described and shown in figure 10.5 for the warp or weft direction of the coated fabric. The only differences were the applied load and the time allowed for long-term creep which was shortened to one hour. The loads were as follows:

p_h - to induce horizontal tension of 130 N/m

p_{vd} + weight of bottom clump - to induce vertical tension pf 90 N/m

and

p_{vl} - to induce vertical tension of 70 N/m.

The results are shown in figure 10.11. The primary creep for this type of membrane is rather high and therefore modelling visco-elastic behaviour by the single Kelvin model is not as accurate as, for example, in the warp directions of plastic coated fabrics. On the other hand, the dynamic response of a suddenly unloaded dome does depend very strongly upon another factor: the movement of the surrounding air. Accounting for this involves a lot of additional calculation, as will be shown in chapter 11. Therefore, it is very important to restrict modelling of membrane behaviour to a procedure which is as simple as possible. From the above explanation it is reasonable to assume that the inaccuracy resulting from this simplified membrane behaviour model will result in an error of secondary order in numerical prediction of the dynamic response of the dome.

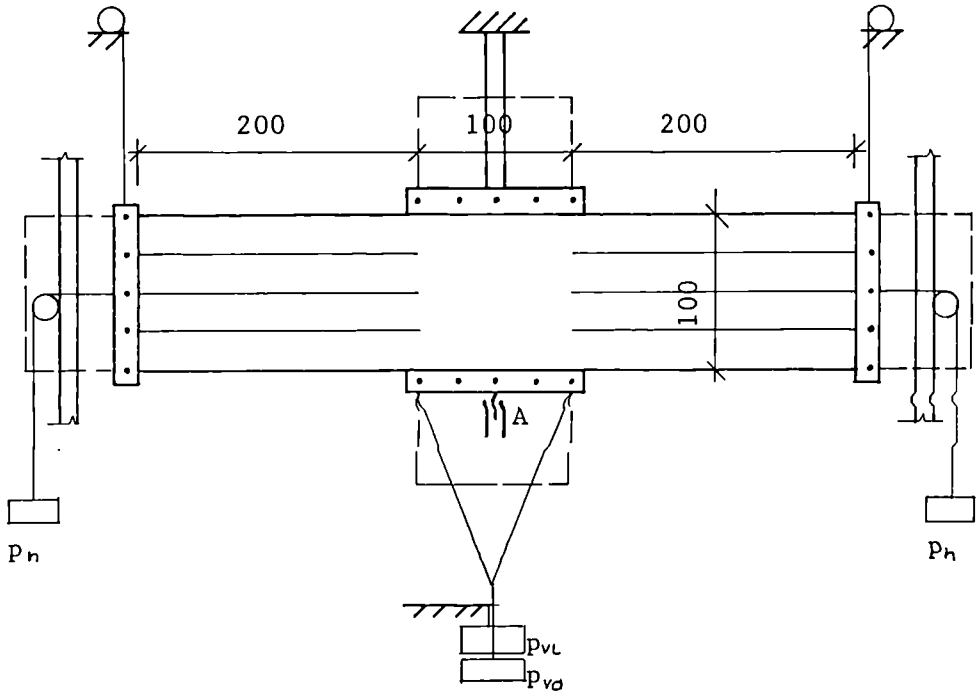

Figure 10.5

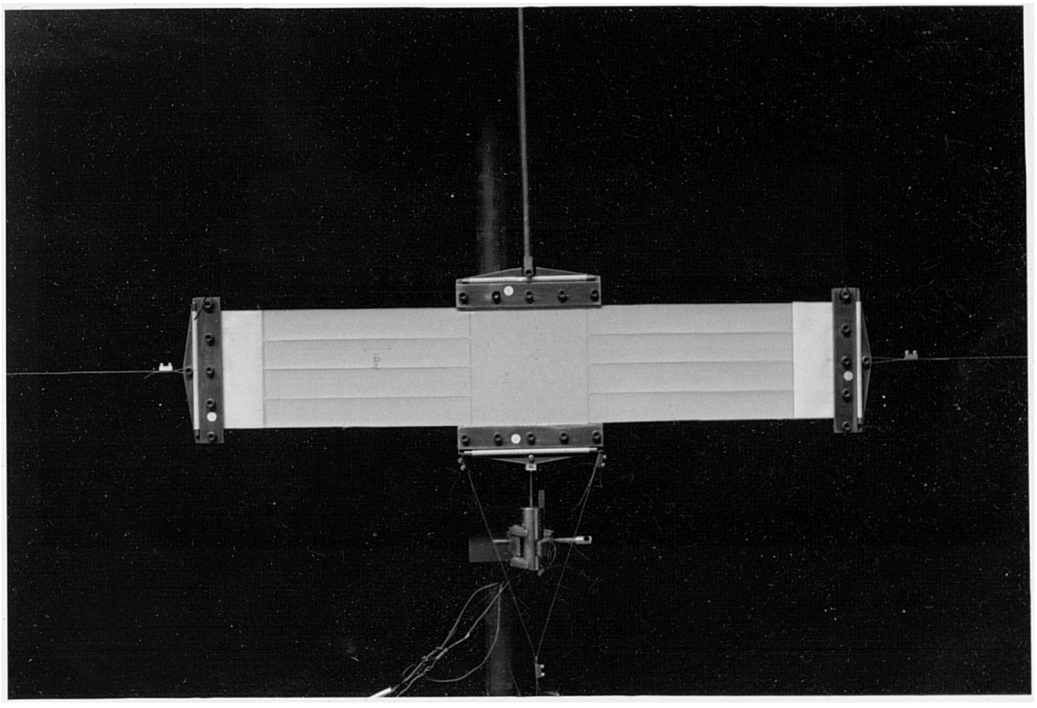

Figure 10.6

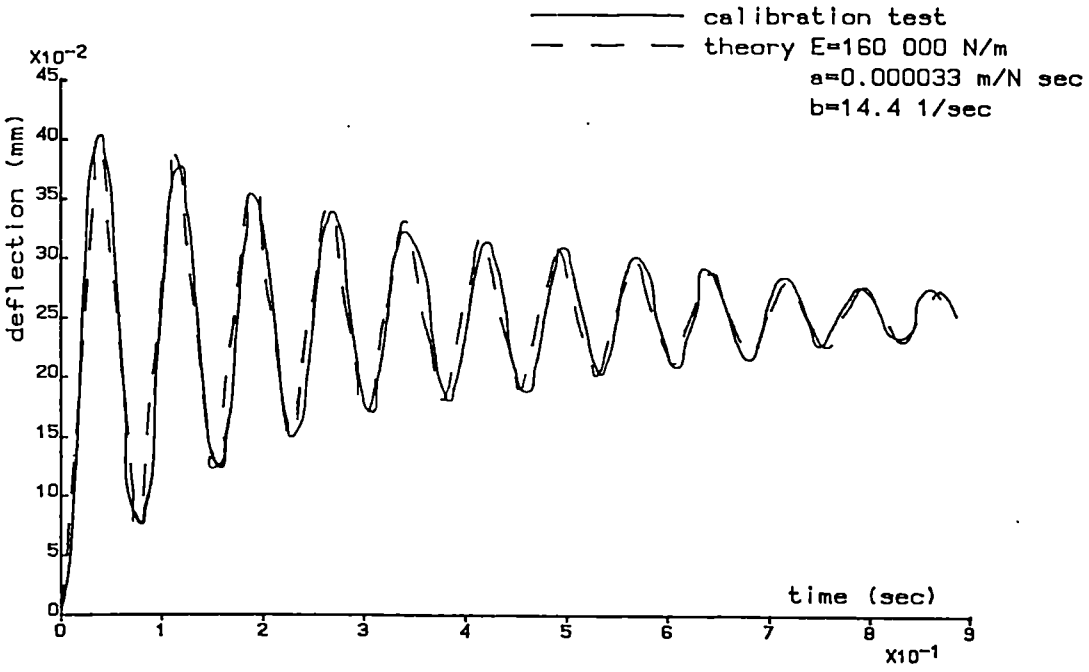

a.for the warp direction

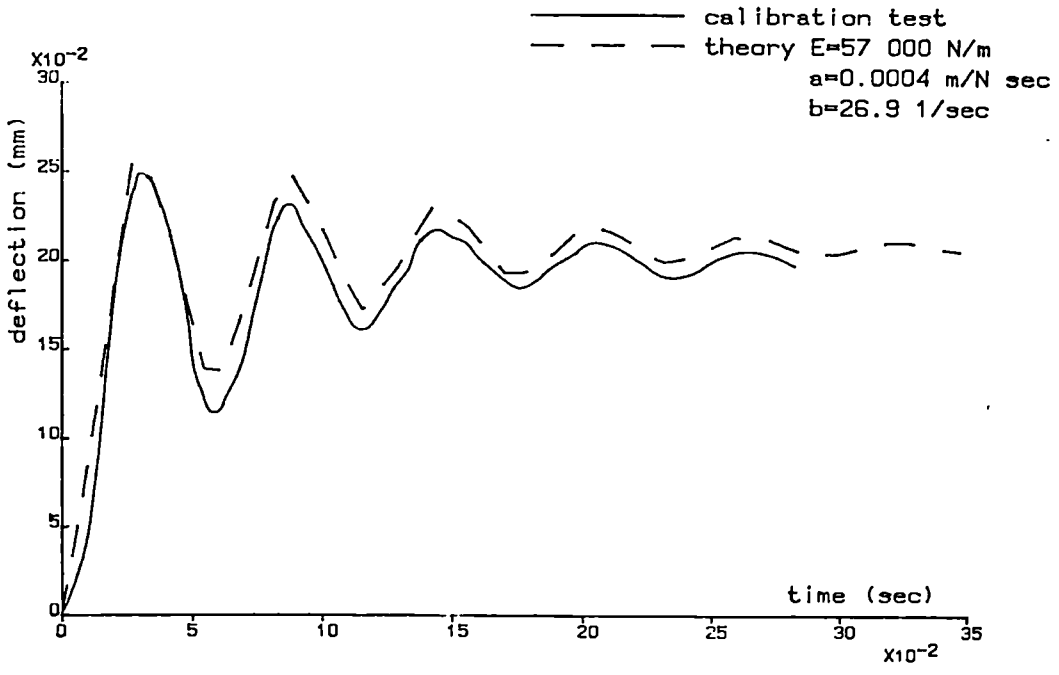

b.for the weft direction

Figure 10.7 Calibration analysis for the coated fabric

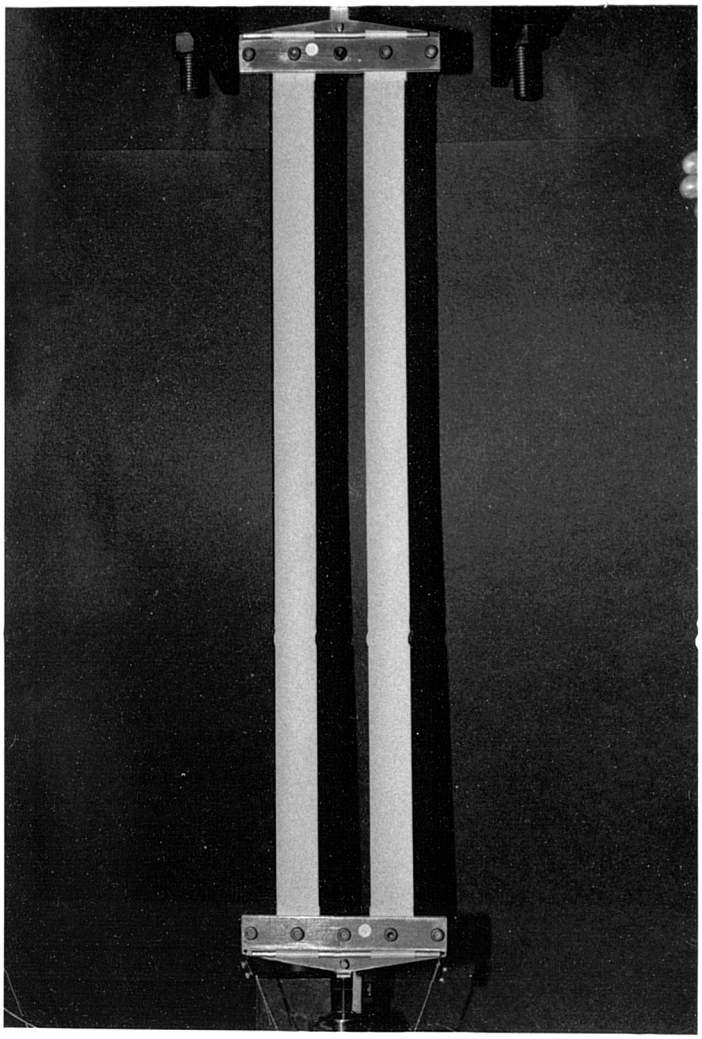

Figure 10.8

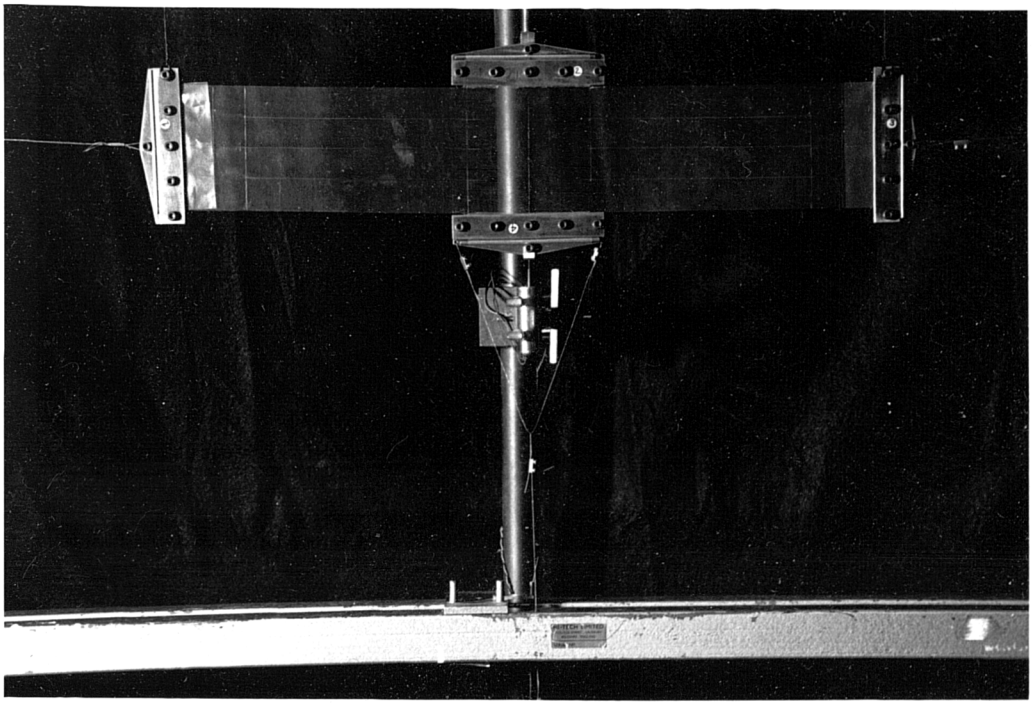

Figure 10.9

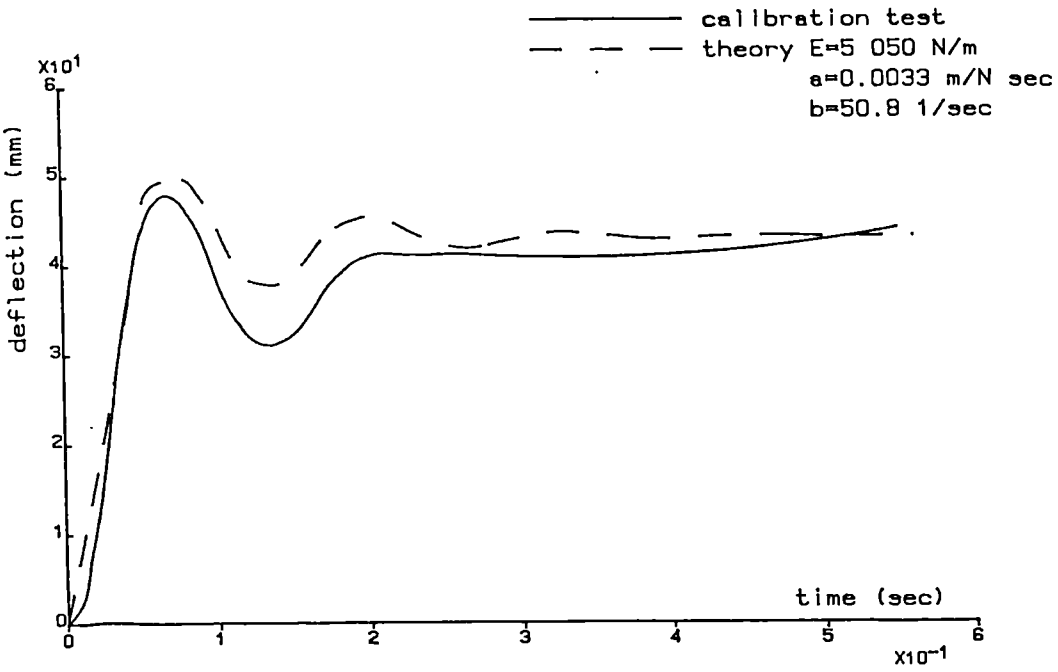

Figure 10.10 Calibration analysis for coating of coated fabric

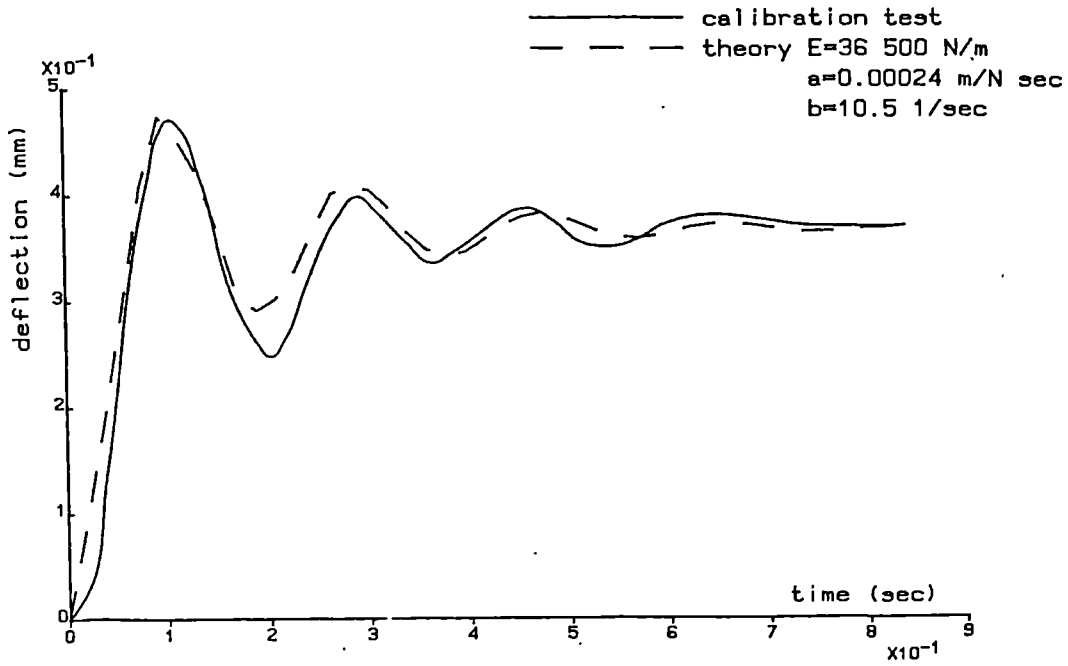

Figure 10.11 Calibration analysis for lightweight polythene

10.2 Tests on the orthotropic membrane dome

10.2.1 The model

The model dome, a general view of which is shown in the photograph of figure 10.12 was attached to a base unit of 4.89 m external diameter. The base unit, used in previous experiments at City University and described by Barnes [9] was constructed in hardwood with a top skin of plywood. The circumference of the base was bevelled off at 45 to enable the membrane to be attached by means of double sided type, so that the joint would be subject to shear rather than peeling. The whole assembly was mounted on a wire braced framework of steel legs, which evenly supported the base unit.

Three holes were made in the base: one 15 cm in diameter to allow for inflating the dome by means of a large displacement centrifugal fan, a small 3 mm diameter hole to enable constant pressure to be maintained inside the dome by connecting a small high pressure pump coupled to a regulator, and an additional small hole for connecting an inclined manometer filled with blended paraffin. To minimise leakage the remainder of the base was covered by very thin polythene sheeting attached to plywood by means of P.V.C. adhesive tape. An additional layer of polythene sheet was laid over the 15 cm hole and surrounding area to form a diaphragm so that the air stream coming from the large fan would not hit directly the membrane, but would be dispersed to avoid causing locally high stresses.

The dome was assembled from five pairs of 'armadillo' elements (the name armadillo comes from a small burrowing animal of S. America, with a body covered with a shell of bony plates). The membrane material was P.V.C. coated terylene fabric approximately 0.25 mm thick. The segments were cut so that the warp was aligned with the longitudinal axis of symmetry of each segment. The cutting template for the segments was shaped to give as closely as possible a spherical diameter of 7.0 m for zero membrane stress. The segments were 8 mm lap jointed with plasticised 'Superglue', over a former of the correct curvature on a specially designed and constructed cradle (see figure 10.13). One quarter of the dome was marked by sticking small dark self-adhesive circular stickers along the centrelines of each segment (see figure 10.14).

The jointed membrane segments were sealed to the supporting base by double sided tape, which enabled some initial adjustment. Thus formed, the model dome had a base diameter of 4.74 m and a crown height of approximately .93 m when prestressed by internal pressure.

10.2.2 Impulsively centrally loaded dome - static and dynamic tests

Static tests

In the static test the orthotropic pneumatic dome was loaded centrally and static deflections of the marked points were recorded by a still camera. The load to be applied was placed on a plywood circular platen of .58 m external

diameter, with a vertical scale attached to it, and suspended on a steel wire from a pulley situated directly above the centre of the dome. The other end of the wire was equipped with a handle to give better control over the load releasing process, and a clamp so that the suspended load can be safely secured, when required, in a position just above the apex of the dome.

The camera images are not merely diminished or enlarged pictures of real objects, but they are deformed, mainly due to compressed perspective effects and lens observations. The compressed perspective effects are a direct result of the basic optics law for lenses; the relationship between conjugate distances and the focal length is expressed by the following formula:

$$\frac{1}{u} + \frac{1}{v} = \frac{1}{f} \qquad 10.5$$

where

f is the focal length,

u is the object conjugate (object distance) and

v is the image conjugate (image distance)

The f, u and v are illustrated in figure 10.16 showing an example of ray paths through a simple positive lens. By the geometry of figure 10.16 equation 10.5 can be transformed to the practical form:

$$m = \frac{I}{O} = \frac{v}{u} \qquad 10.6$$

where m is a magnification factor.

When a film frame or a picture is analysed to obtain the real vertical dimension of the object, equation 10.6 is used in the form:

$$0 = I \times \frac{1}{m} = I \times \frac{u}{v} \qquad 10.6a$$

In such circumstances, the following conclusions can be drawn:

1. the inverse of the magnification factor depends linearly upon the object distance, and
2. (as a direct consequence of 1) if the exact position of the camera relative to the photographed object is not known, two vertical scales are adequate to work out the inverse of the magnification factor for any point on the object.

Therefore, for reasons given above, two surveying staffs were placed vertically near to the dome but not obscuring the view (see figure 10.17). Their positions were carefully measured and recorded.

The ray paths shown in figure 10.16 (and corresponding to equation 10.5) assume the ideal conditions that the lens is perfect and that the central ray of an oblique beam of light passes through the centre of the lens itself. In practice, the lenses can only approximate this ideal [118]. A full list of principal lens abberations is given in [114, 88]. The main concern for us was so-called curvilinear distortion (or just distortion) which results in the image varying in its magnification across the field. The distortions are greater when a picture is taken from a short distance using a wide angle lens, and can be easily observed on the image, where straight lines of the object become curved. To

alleviate this abberation all pictures were taken by a camera situated more than 20 metres away from the dome. A telephoto lens: Vivitar 400 mm f15.6 (6° angle) was used to obtain images of maximum possible size on 35 mm film.

The test procedure

The dome was initially inflated by means of the large displacement centrifugal fan. Then the fan was switched off and the small high pressure pump was set up so that the internal pressure was kept constant at 100 Pa (the amount of air lost due to any leakage was recompensated). The geometry of the dome was recorded by means of the still camera.

The loading platen of 150 N total weight was then gently lowered onto the dome. When the dome had reached a steady-state condition, a photograph was taken of the deflected shape of the dome and the internal pressure was recorded. The platen was raised and the membrane was allowed to relax for two hours. Then the dome was inflated to the desired pressure 100 Pa and the test was repeated with a 300 N central load.

Dynamic test

In dynamic tests the dome was impulsively loaded and deflections of the central point were recorded by means of a high speed camera. This time, the camera was placed close to the dome and positioned in such a way that the camera lens level was a few centimetres above the apex of the dome.

The camera speed was set at 100 frames per second.

The handle on the wire supporting the central load was replaced by a turnbuckle to allow for small adjustments in the wire length. The dome was prestressed by internal pressure of 100 Pa by the large fan and the small pump in a similar way to the static test. The centrally positioned platen of 150 N was lowered to 1 mm above the dome (very close to the dome but not touching it). A thin prestressed wire was stretched in front of the platen scale (as close as possible allowing for a few millimetres horizontal movement of the central loading system during the test) to give a fixed horizontal line. The wire level was chosen in such a way that during the test the wire remained within the platen scale.

The camera was sighted on the vertical scale attached to the loading platen (see figure 10.15). Finally, the central 0.575 cm diameter ring load of 150 N was suddenly applied to the dome by cutting the supporting cable and deflections were recorded for a few seconds. Then the platen was raised and the same experiment was repeated after 2 hours for the 300 N central load.

10.2.3 Comparison of theoretical and experimental results

Static results

The photograph of figure 10.14 shows a quarter of the inflated dome with reference points marked on the structure; similar pictures were taken for the 150 N and 300 N central

load cases. On enlarged pictures (28 x 28 cm), the required distances were measured by means of a digitizer. Two points of the base line, all visible marked dome points, a point on the loading platen and two points on each of the surveying staffs were digitized.

The ratio of the vertical image distances on the surveying staff to their real lengths gave the inverse of the magnification factors M_1 and M_2. The points on the surveying staffs were chosen to give the maximum possible vertical length; so that the influence of digitizing error is minimised. The values of M_1 and M_2 were then used to obtain the coefficients of the linear function defining the inverse of the magnification factor (the value by which the image length should be multiplied to obtain the actual distance) in terms of y coordinates (see figure 10.17).

The dome base was assumed to lie in the plane $z = 0$; therefore, all vertical distances between marked points on the surface of the dome and the base were expressed by z coordinates. Figure 10.17 shows the points for which z coordinates were obtained from the experiments; the node numbers are the same as those used in the theoretical analysis and shown in figure 8.9. The experimental and theoretical z coordinates for both 'line' and 'line and coating' idealizations, for prestressed, 150 N load and 300 N load states are given in the table of figure 10.18. The y coordinates obtained from the geometry of the cutting pattern were used to find the inverse magnification factor

for each point and hence the experimental z values.

The difference between the theoretical values for both types of numerical modelling are very small, as noted in chapter 8. Even the maximum discrepancy is within 1%. In general, the theoretical results using a 'line and coating' idealization are closer to the experimental results; the discrepancies between them being within 0.5 cm which represents about 1%. The z coordinates obtained using only 'line' elements have the greatest differences and, when compared with the test values in the central area of the dome, the theoretical values are generally lower by a maximum of 2%.

The theoretical deflections for the central point under the 150 N load, being 0.127 m and 0.130 m for 'line' and 'line and coating' idealizations respectively, compare very well with the experimental 0.129 m deflection. When the 300 N central load is considered, the theoretical deflections of node 1 are 0.188 for both idealizations and the test gave 0.184 m.

The pressure read from the inclined manometer, after applying the central load and reaching a steady-state, were in both cases lower than the theoretical. For the 150 N central load, the experimental value was 148.5 Pa whilst the theoretical values were 153.9 and 152.3 Pa for 'link' and 'link and coating' idealization respectively. For the 300 N central load, the pressures were 204.6 Pa

experimentally, and 217.7 Pa and 214.6 Pa with 'link' and 'link and coating' idealizations respectively.

Some precautions (see 10.2.2) were taken to ensure that the experimental procedure would provide results which were as accurate as possible. In spite of this fact, there were still some weak points which influenced the test precision. It can be easily observed (see figure 10.14) that the stickers to mark nodes on the dome did not define exact points - the error was of order 2 to 3 millimetres. The theoretical results also depend on experimental material properties, which are not error free. The main source of errors in the static material tests were:

1. inaccuracy in the measurement of distances between gauge points in the first two steps in the loading cycle and the last two in the unloading cycle. When under the low stresses in a specimen the measurements were taken, the central part of the specimen tended to move out of plane and the studs tilted slightly outwards.
2. the time influence on results. Instantaneous Youngs moduli for the membrane were required; therefore strain measurements were recorded just after applying loads (in the dome test a similar procedure was followed). In order to eliminate reading or other related errors, each distance was measured three times in the cycle. Although the differences were not great, the time dependent creep strain slightly influenced the results. A similar effect was observed during the dome tests.

After initially pressurising the dome by means of the large fan, some time was required to set up the right rate of pumping which would account for leakage; hence, before applying the load some time elapsed. In that time creep strains could have taken place which are not accounted for in the material tests. On the other hand, the difference in geometries: that obtained from the pattern cutting and that after applying internal pressure, were comparatively small and the stresses due to pressurising only were not very high. Hence, the time factor could be expected to be of secondary order.

In general, the theoretical predictions using even 'line' elements were very close to the experimental results. For practical purposes, for these types of coated fabric, the analysis discussed in chapter 8 based on a 'line' idealization may therefore be considered adequate.

Dynamic tests

Records of the test, the movie films, were analysed using a motion analyser to view the film frame by frame, and a sonic digitizer to find the positions of any points on the frame. The system was coupled to a BBC microcomputer using 'Modular Film Analysis system' software.

The platen scale and the base diameter were used to define magnification factors for the vertical and horizontal directions respectively. On each frame two points were recorded: one to account for movement or displacement of the film and the second to find a deflection. The deflection at

any instance of time, t_i, was found as the difference between coordinates at t = 0 and t = t_i. For the first 50 frames, each one was analysed as the differences (movement of point 2) were large. After 50 frames digitizing the points on every second frame proved to be sufficient.

The deflection of the central point of the dome, for the centrally applied 150 N and 300 N loads, are plotted as a function of time on figures 10.19 and 10.20 respectively. The theoretical results are superimposed on the graphs; for the 150 N loading two theoretical plots are shown for: 'link' and 'link and coating' idealizations, but for the 300 N loading only the 'link' idealization is shown.

Both theoretical results, for 150 and 300 N loadings compare well with the experimental trace for point 1. The main sources of error seem to lie in distortions caused by the considerable deformation of the dome and the use of only a single Kelvin model for the visco-elastic constants, especially in the weft direction. Introducing the coating did not noticeably improve the results, but increased computer time and, therefore, for this type of membrane material may be considered unnecessary. Disregarding the surrounding air vibrating with the membrane did not cause an error of high order. The stiffness of the membrane material seems to be rather under-determined; the theoretical deflections are larger and the basic theoretical frequency is smaller than observed experimentally.

There are discrepancies of about 1.5 cm between the static results for the deflection of point 1 and the corresponding 'quasi-static'dynamic terminal deflection in both the theoretical and the experimental results. The static deflection and 'quasi-static' dynamic terminal deflection of point 1 cannot, however, be directly compared. The dynamic tests were not performed at the same time as the static tests, but with a month interval. During this time the double-sided tape used to fix the dome to the base partially lost its sticking properties and had to be replaced by a new layer. New adjustment, especially in highly stressed areas (near the edges in the smallest segments) was necessary to avoid wrinkles and displaced the membrane compared with its original position. The new geometry was, however, accounted for in the numerical dynamic analysis.

Figure 10.12

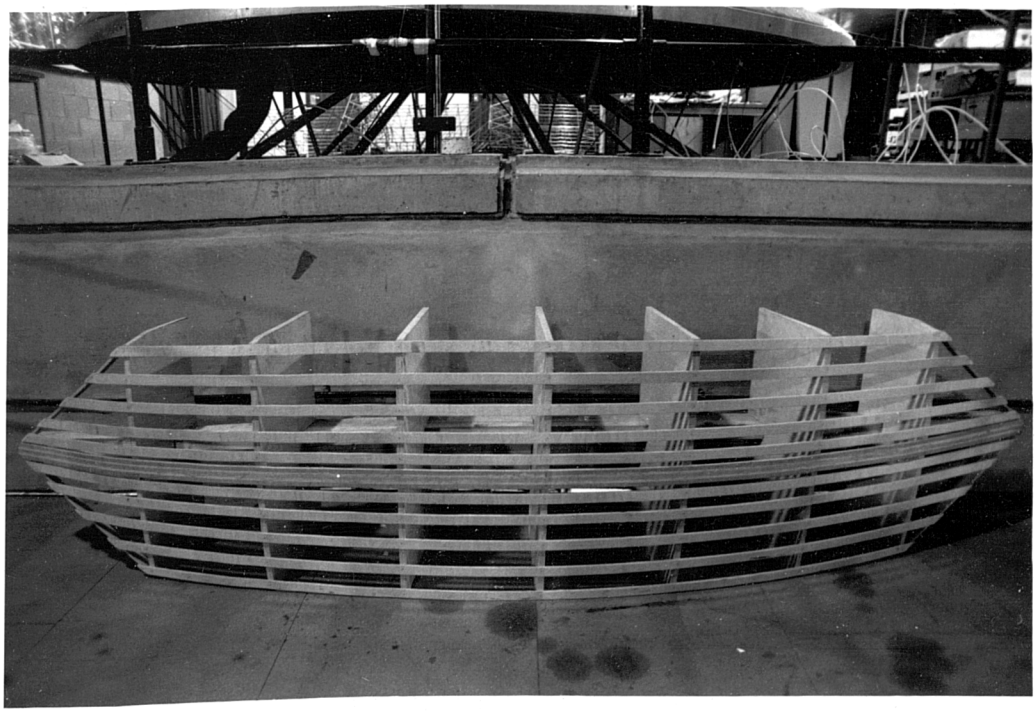

Figure 10.13

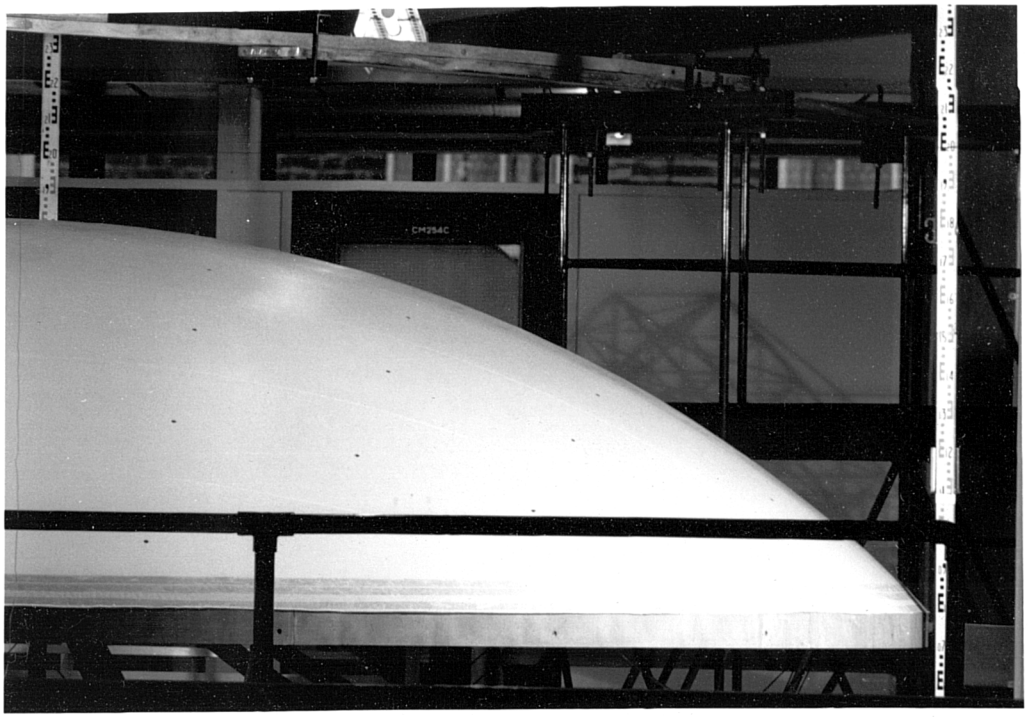

Figure 10.14

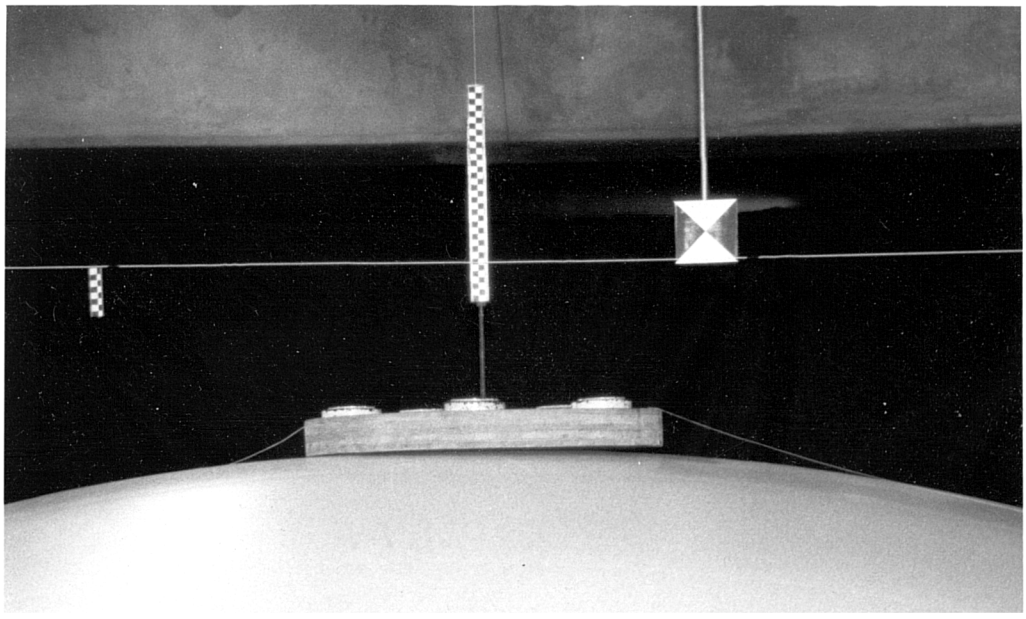

Figure 10.15

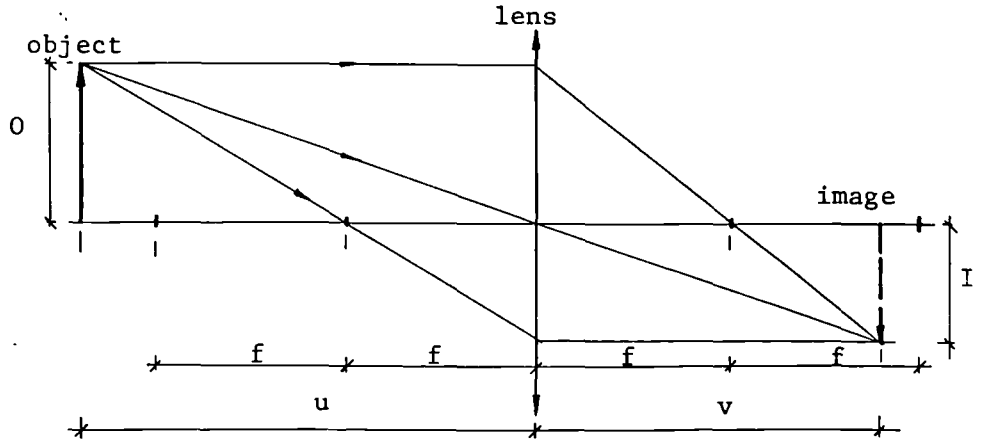

Figure 10.16

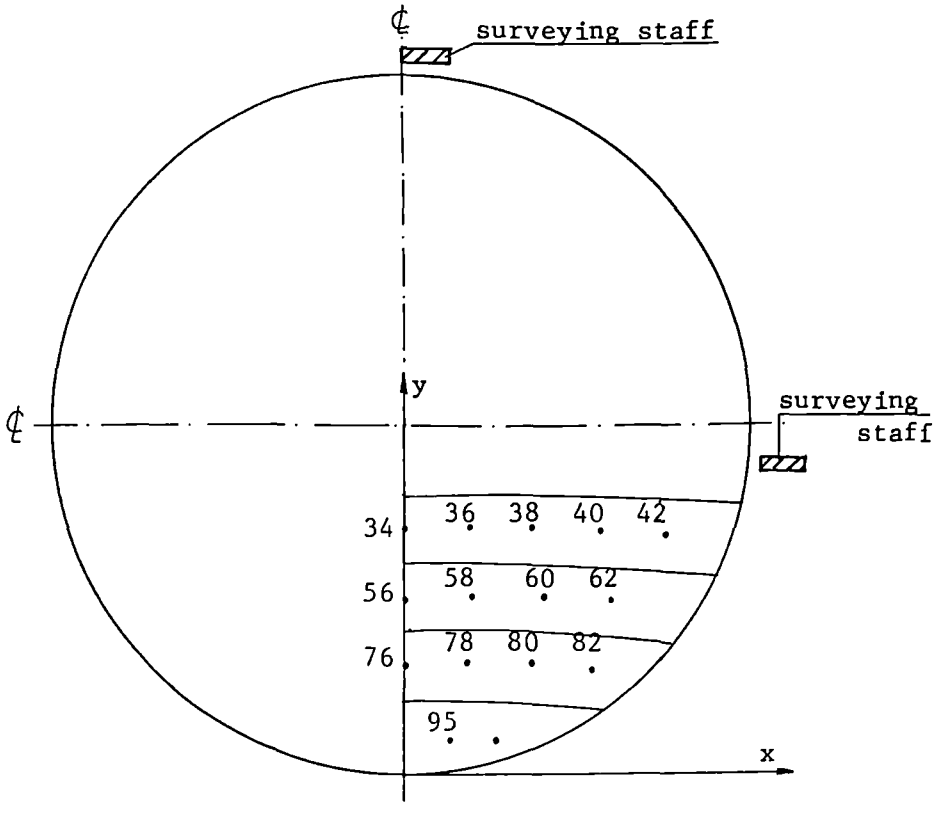

Figure 10.17

Node Number	Prestressed state			150 N central load			300 N central load		
	theoretical 'line'	theoretical 'line and coating	experimental	theoretical 'line'	theoretical 'line and coating'	experimental	theoretical 'line'	theoretical 'line and coating'	experimental
1	.926	.933	.934	.799	.803	.805	.738	.745	.750
34	.837	.838	.842	.832	.835	.838	.823	.828	.829
36	.798	.798	.801	.798	.799	.798	.797	.799	.801
38	.681	.680	.683	.687	.685	.685	.692	.691	.690
40	.487	.487	.484	.494	.493	.489	.502	.500	.498
42	.222	.222	.219	.226	.226	.224	.231	.230	.229
56	.672	.672	.677	.679	.679	.680	.684	.684	.687
58	.638	.638	.640	.644	.643	.642	.650	.649	.651
60	.536	.536	.536	.541	.540	.538	.547	.546	.542
62	.366	.366	.364	.369	.369	.365	.374	.373	.377
76			-	.436	.435	.433	.442	.441	.441
78	.402	.402	.400	.408	.407	.403	.414	.413	.410
80	.320	.320	.317	.324	.324	.321	.329	.328	.325
82	.181	.181	.180	.181	.182	.182	.185	.185	.185
95	.109	.107	.970	.112	.110	.108	.114	.113	.109

Figure 10.18

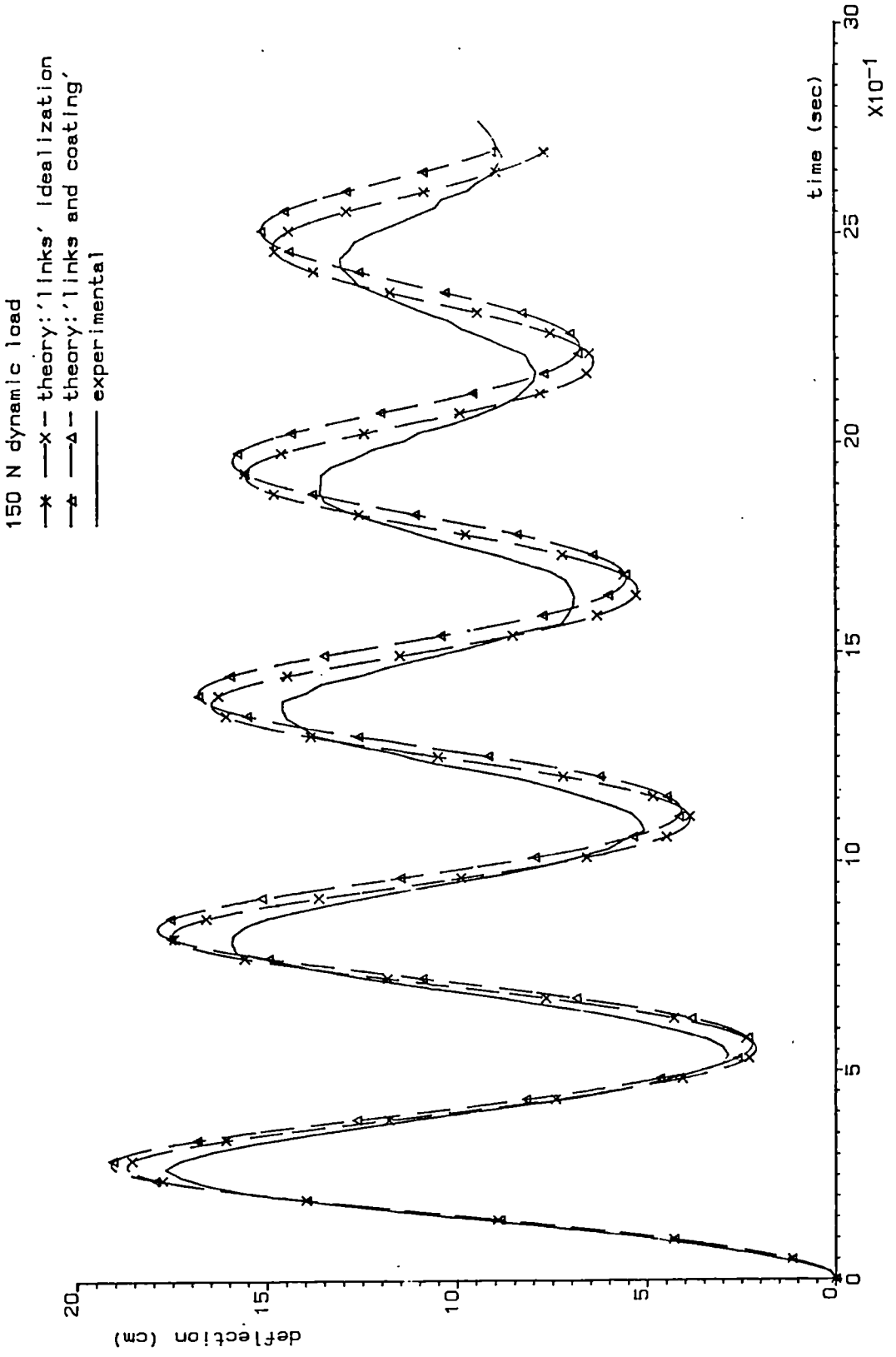

Figure 10.19 Pneumatic dome deflection decay test

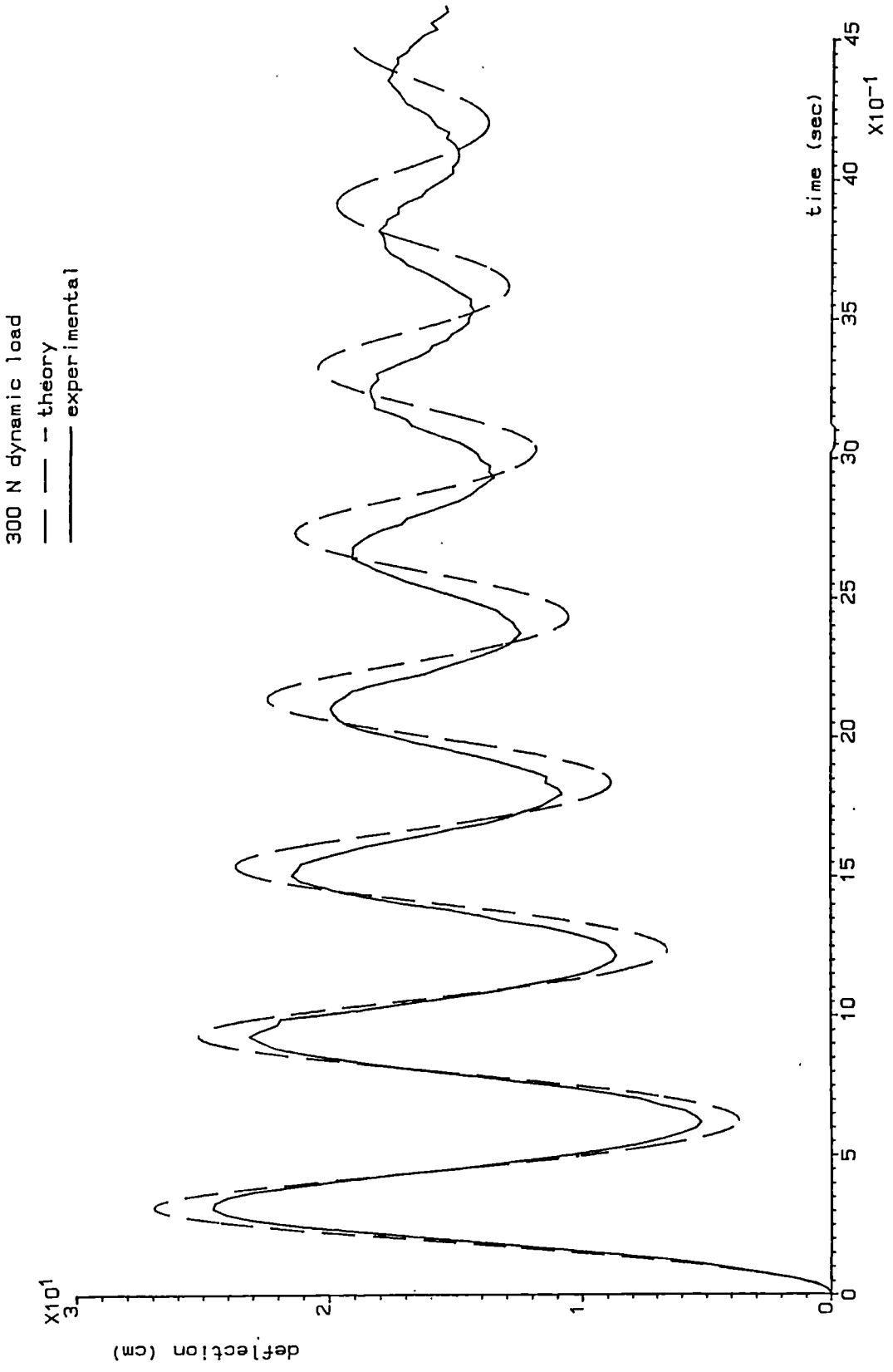

Figure 10.20 Pneumatic dome deflection decay test

10.3 Tests on isotropic membrane dome

In tests of the isotropic membrane dome the same base unit and pumping-measuring devices were used as describe in subclause 10.2. On the initially flat dome the positions of points for which experimental deflections were to be obtained were marked (see figure 10.21a). Six points were required for the static tests: three points to coincide with nodes 3, 5 and 6 of the cheese slice idealization, and three points to coincide with nodes 20, 21 and 23 of the half dome idealization (used for asymmetric load see figure 8.13 of chapter 8). For the dynamic tests only two points were required. These coincided with node 3 in 'cheese slice' and node 4 in the half dome idealizations. The dynamic test points were chosen to give the maximum deflection and not to interfere with the loading platen.

The membrane of .06 mm thick polythene sheeting, was placed on the base unit and gently attached to it. A 10 mm wide strip was marked around the base edges (see figure 10.21a), and the flat membrane was then pulled outwards in the radial direction so that the marked line coincided with the table edge. In order to obtain uniform stresses the procedure was performed in steps: first the material was stretched along line 1-1 from both ends, then 2-2, 3-3, 4-4 and then the process was carried on in a similar way until the whole sheet was in the correct position with a small uniform initial stress.

From a trial test it was concluded that the dome was too shallow for using a marking system similar to that employed for orthotropic dome tests since the stickers attached directly to membrane were here not clearly visible. An alternative approach was therefore devised: 14 x 14 x 14 mm expanded polystyrene cubes, with stickers on the side facing the still camera, were glued to the membrane. For the purpose of the dynamic test, a sticker with a clearly defined point faced the high speed camera. For the static test, where pictures were to be taken from over 20 m, a full black circle on the stickers had to be used (see figure 10.21a).

10.3.1 Static and dynamic tests on loaded and unloaded dome

The dome was inflated and the static geometry was recorded by still camera for both prestress and static load states. Afterwards the dome was impulsively unloaded and the dynamic deflections were traced by means of the high speed camera.

Three surveying staffs facing the still camera were positioned vertically, very close to the base unit but not obscuring the view (see figure 12.21a and 10.23), to give the magnification ratio functions for the static tests, and to account for compressed perspective and camera lens aberration. A simple aluminium frame was assembled and positioned very close to the dome centre-line (see figure 10.21 and 10.22) with a horizontal member being approximately 50 cm above the highest point of the dome when

inflated. This allowed for raising and releasing the platen without any interference. Directly above the dynamic point, a square 20 x 20 cm board was attached to a vertical rod suspended from the frame (see figure 10.21b and 10.22). Surveying signs stuck to the board defined: a fixed point (to be used during film analysis to account for displacement of the film frame) and the magnification factors for the horizontal and vertical directions. Dynamic deflections were expected to be smaller than in the orthotropic dome test, therefore, for better accuracy the high speed camera was focused to cover as small area as necessary. For these reasons the square board was positioned very close to the dynamic point, just allowing for dynamic movement.

The uniformly prestressed flat membrane was inflated to 15.44 Pa by the large displacement centrifugal fan. The fan was switched off and the rate of pumping for the small high pressure pump was set up so as to maintain constant internal pressure. The dome, a view of which is shown in the picture of figure 10.22, was left for one hour to allow for creep to take place, and then a photograph was taken. The 80 N loading platen, suspended on the wire from a pulley situated directly above the centre of the dome, was slowly lowered and eventually fully released. An hour elapsed before recording the deflected dome geometry.

Applying the load causes an increase in internal pressure, which results in higher leakage, hence the rate of pumping had to be increased. On the other hand this membrane

material was prone to creep, hence changes in geometry occurred under the same loading conditions, which in turn influenced the internal pressure. In practice it was found rather difficult to be able to set up the right rate of pumping to account for the above facts. Yet a precise knowledge of the resulting geometry of the dome, required as a starting point for the dynamic test, was of great importance. Therefore the problem was tackled in the reverse order; namely, the pumping rate was adjusted to maintain a constant internal pressure of 28 N/m^2, and an approximate value for the pressure increase was measured directly after applying the load.

After a photograph recording of the centrally loaded static state geometry had been taken, the 80N loading platen was impulsively raised and the dynamic deflections of point 3 were traced by means of the high speed camera sited on the square board and the cube defining node 3. The position of the pulley was then altered to enable the 80 N load to be applied asymmetrically, as shown in figure 10.21a. The test was performed in a similar manner to that described above, but with two differences:

1. After applying the load, the internal pressure was maintained at 26 Pa, and
2. As this time the loading platen was not horizontal, the precise angle of indication was measured, just after taking a picture of the loaded state, to be 5 degrees.

10.3.2 Comparison of results and conclusions

A photograph taken after inflating the dome is shown in figure 10.23. Similar pictures were taken after applying central and asymmetric loads. The pictures were enlarged and analysed as explained in 10.2.3 by means of a digitizer. The inverses of the magnification factors were this time defined more accurately by employing three surveying staffs. The results of z coordinates from the base for the three states: inflation, central and asymmetric load, are given together with theoretical values in the tables of figure 10.24. The coordinates are supplemented with static deflections.

Taking into account the fact that using dots of 10 mm diameter (dots of smaller size are not well visible when pictures are taken from over 20 m) limits the accuracy of digitizing coordinates to within 2-3 millimetres, the theoretical results are very close to the experimental values.

During static tests no wrinkles were observed on the dome membrane. This agrees with the theoretical prediction in which no elements sustained negative principal stress.

Results of dynamic tests for the deflection decay of node 3 following central unloading and node 4 following asymmetrically unloading, are shown together with the theoretical traces in figures 10.25 and 10.26 respectively. The most striking discrepancies are in frequencies. For the

centrally unloaded dome the theoretical frequency is 16, which is more than 6 times greater than the experimentally observed value of cycles per second. The most obvious reason for such a great difference is omitting, in the theoretical analysis, the influence of the surrounding air (apart from internal air stiffening) on the dome movement. Disregarding the added mass of vibrating air clearly causes the frequency of lightweight structures to be grossly over-estimated.

The maximum theoretical deflections for both the centrally and asymmetrically unloaded dome are higher than the experimental values, although the difference is not as great as in frequencies. The discrepancies in deflections are very likely to be caused by omitting 'air-damping' - damping associated with the pressure which the surrounding air exerts on a membrane to resist its movement.

When an asymmetric load is suddenly raised, the membrane in this area moves upwards to balance a new pattern of loading, creating a local area of low pressure underneath. The air in a different part of the pneumatic dome, having higher pressure, then surges towards this lower pressure region. This movement can be associated with the first peak in the graph of figure 10.26. Subsequently the air rebounces and returns to the previous position, thus creating again lower pressure in the local area under the membrane, where the platen rested. Then the movement of air mass carries on, caused more by impinging on the membrane and rebounding than

by differences in pressure. The peaks on the graphs become successively lower as the air momentum decreases. The analysis of chapter 9 does not cover this air movement, therefore the theoretical graph of figure 10.26 does not resemble, even in shape, the experimental trace.

The theoretical dynamic analyses of chapter 9, which disregard the surrounding air are not adequate for lightweight structures. Therefore, attempts will be made in chapters 11 and 12 to model air-supported structures more accurately by accounting for air structure interaction effects.

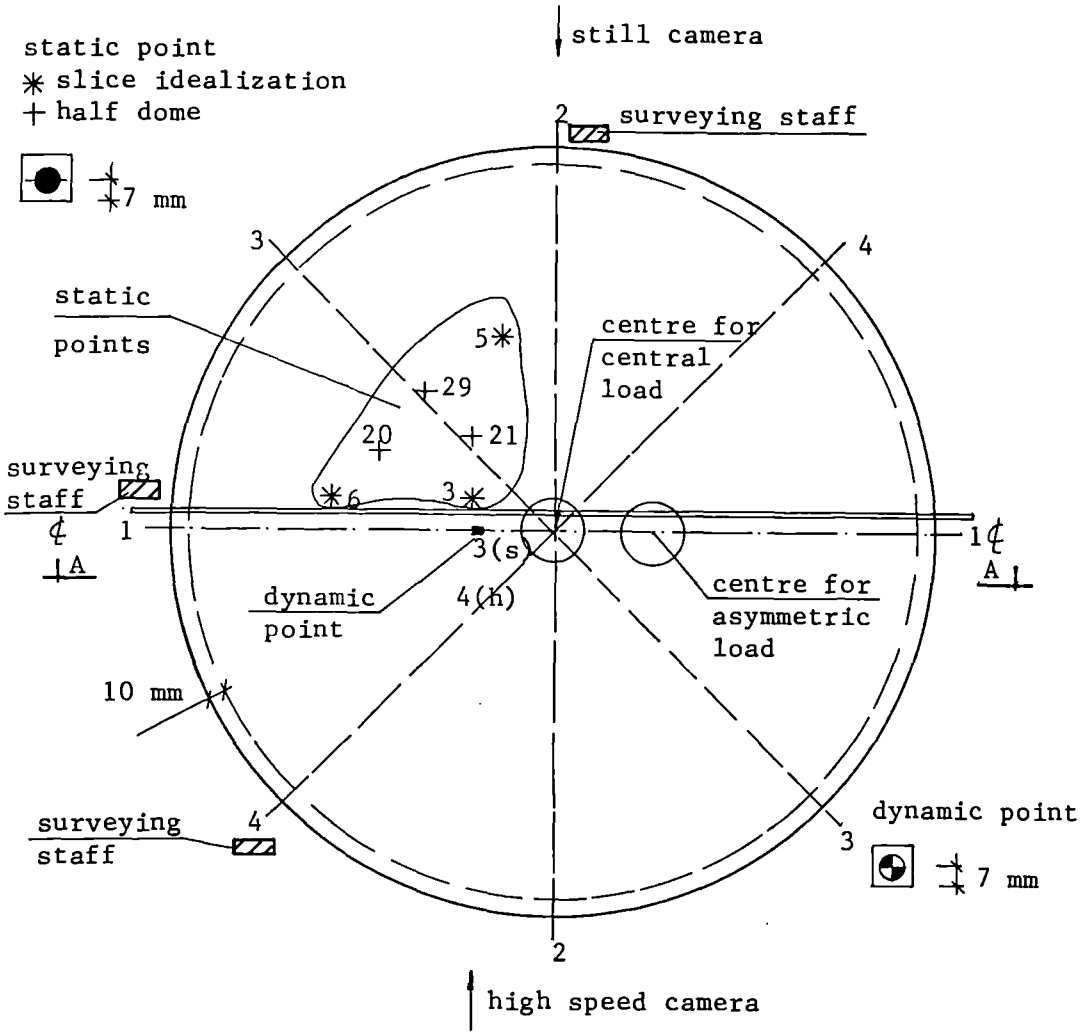

a.plan

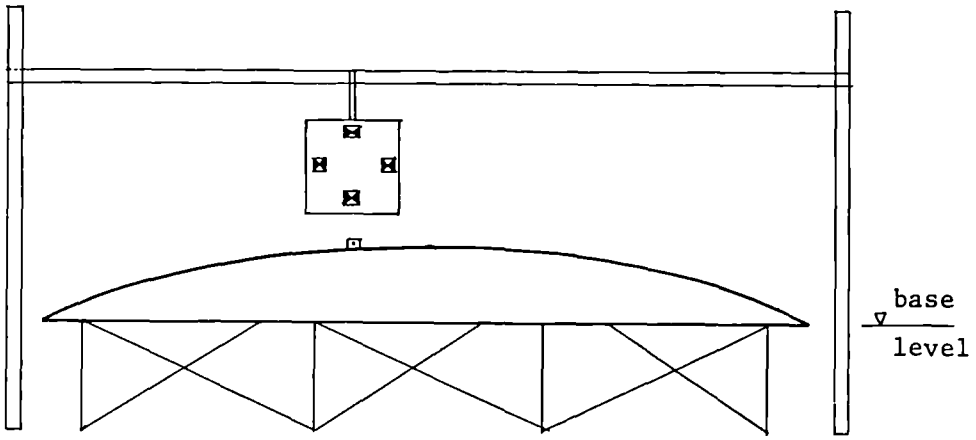

b.section A-A

Figure 10.21 Arrangement for isotropic membrane tests

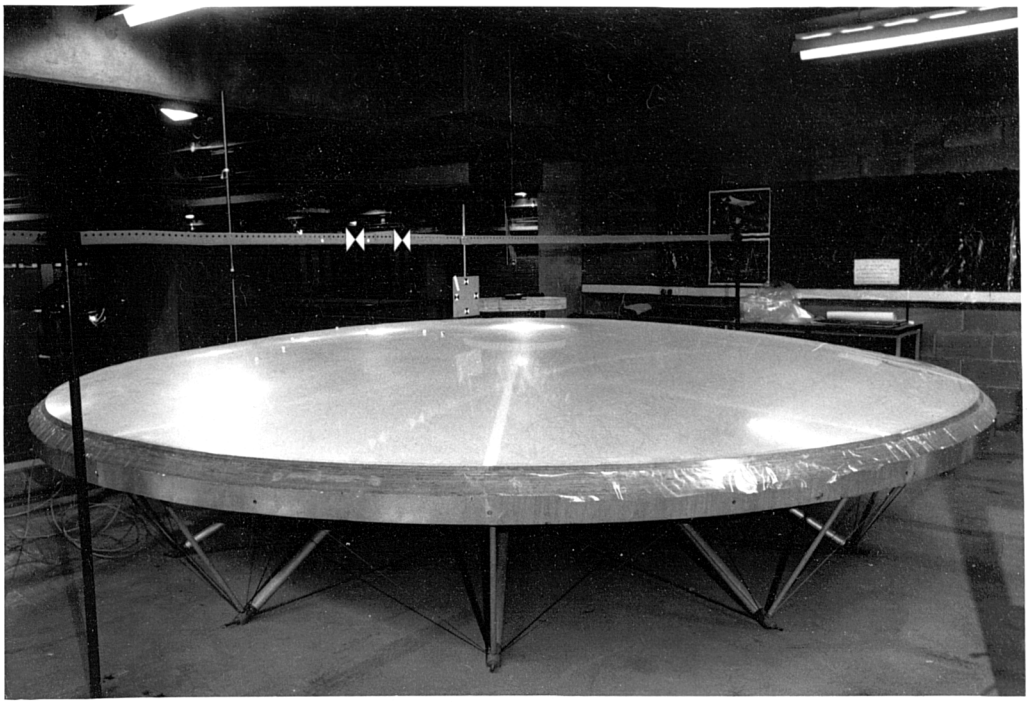

Figure 10.22

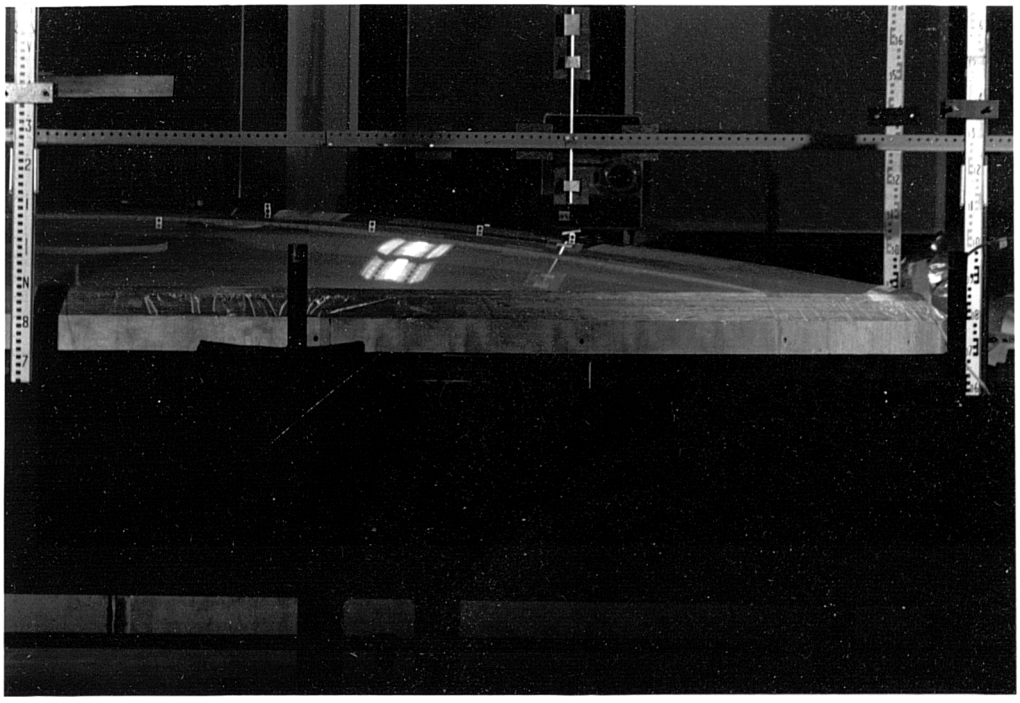

Figure 10.23

Node Number	Inflated Dome		Loaded Dome		Deflection	
	Theoretical Results	Experimental Results	Theoretical Results	Experimental Results	Theoretical	Experimental
3	.214	.217	.172	.172	-.042	-.045
5	.173	.173	.185	.183	+.012	+.010
6	.142	.140	.162	.159	+.017	+.019

a. centrally applied load

Node Number	Inflated Dome		Loaded Dome		Deflection	
	Theoretical Results	Experimental Results	Theoretical Results	Experimental Results	Theoretical	Experimental
20	.163	.163	.179	.198	.034	.035
21	.203	.203	.227	.226	.024	.023
29	.168	.169	.198	.202	.030	.033

b. asymmetrically applied load

Figure 10.24 Static test results

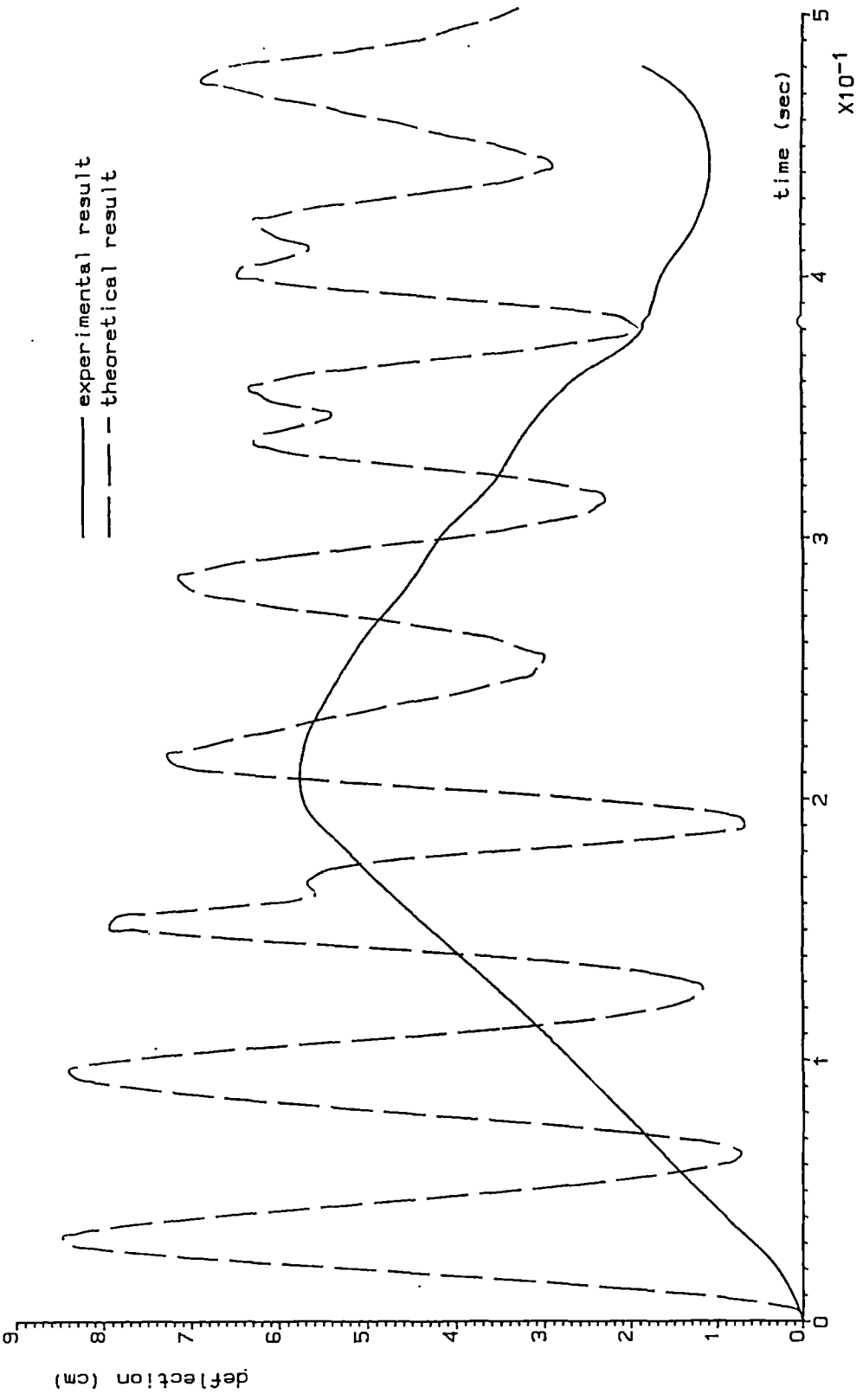

Figure 10.25a Centrally unloaded dome, node 3 dynamic deflection decay

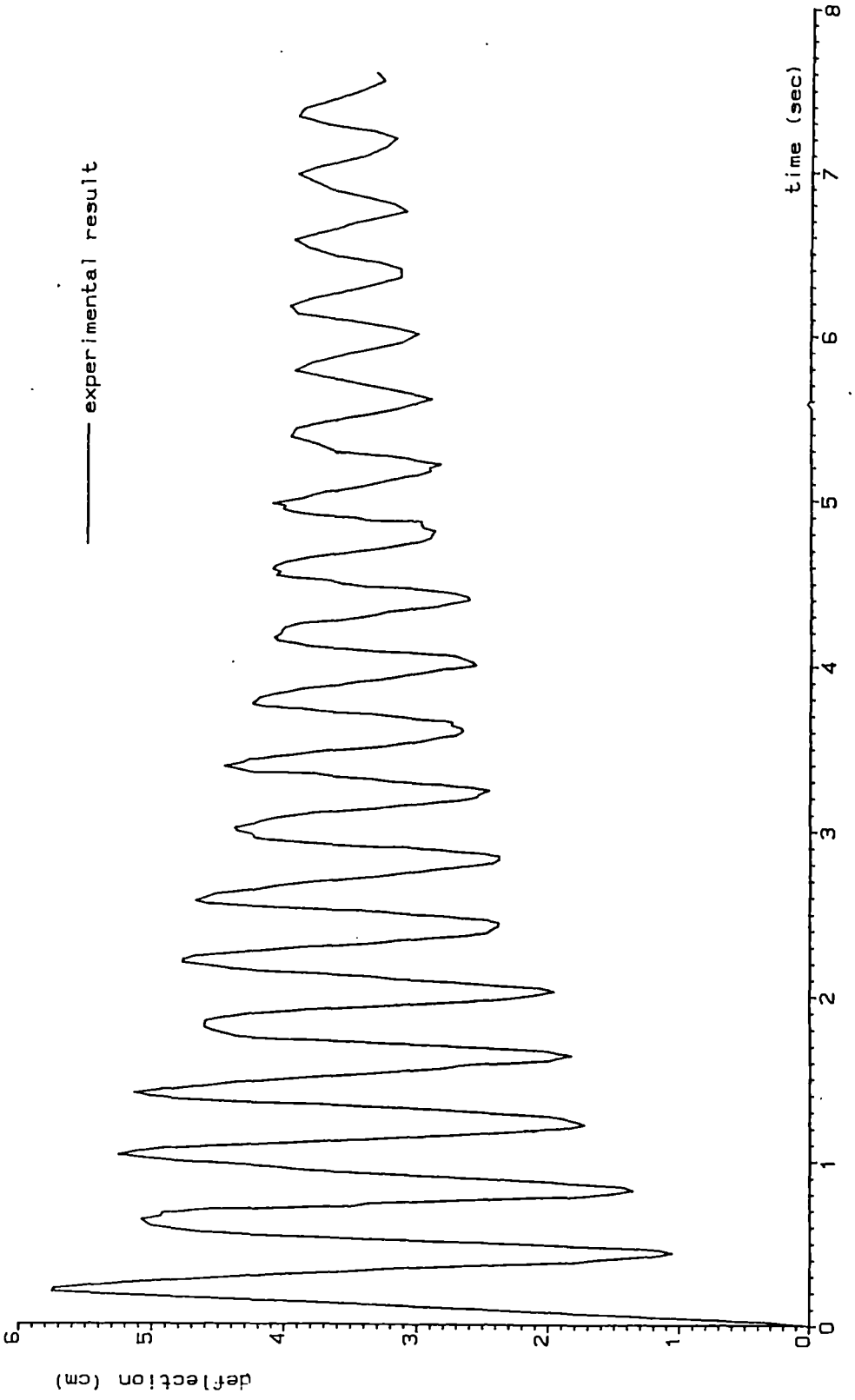

Figure 10.25b Centrally unloaded dome, node 3 dynamic deflection decay

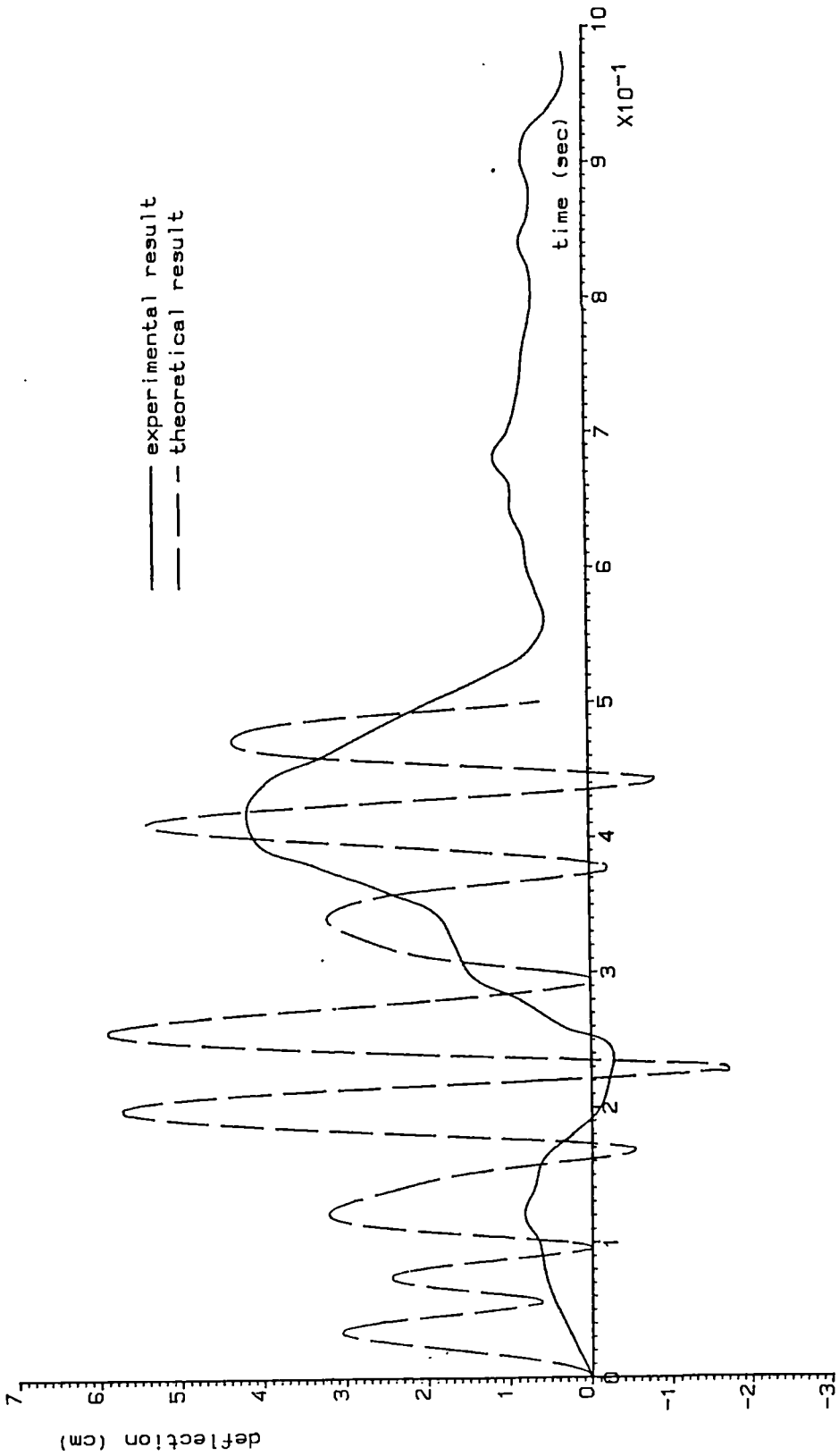

Figure 10.26a Asymmetrically unloaded dome, node 4 dynamic deflection decay

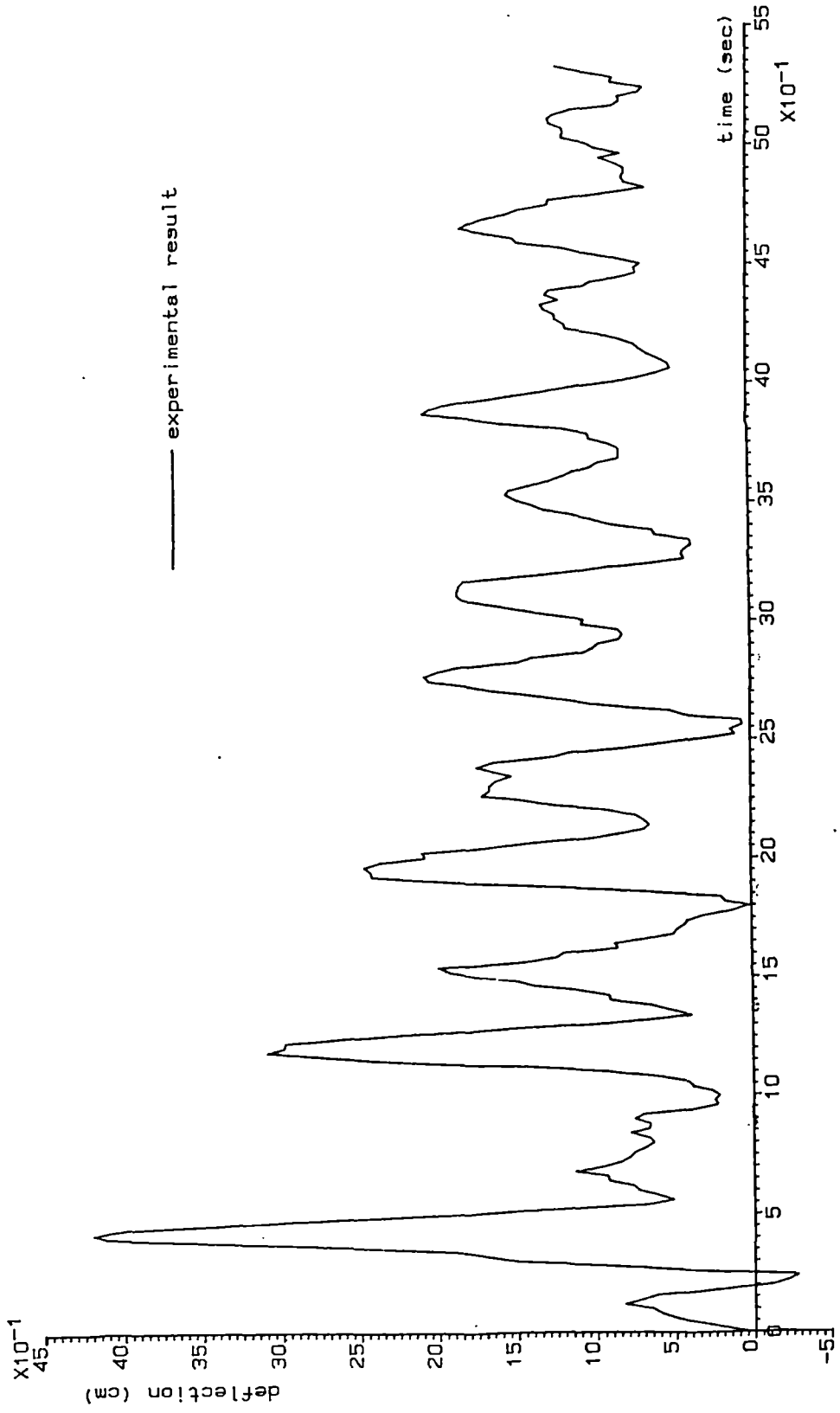

Figure 10.26b Asymmetrically unloaded dome, node 4 dynamic deflection decay

CHAPTER 11

Internal air modelling

Contents:

In this chapter a coupled fluid-structure explicit dynamic analysis is described. This includes membrane and air modelling for pneumatic structures. The behaviour of irrotational, inviscid, compressible fluid is described from a Langrangian point of view. A numerical iteration scheme for coupled analysis and stability conditions is given. The procedure is employed to investigate the dynamic response of a suddenly (centrally) unloaded lightweight polythene dome structure. Different idealizations of the surrounding air are considered but with emphasis on internal air modelling. Although only the simplest axisymmetric case is considered, the amount of computing is enormous.

11.1 Introduction

In chapter 9.2.2 the explicit dynamic analysis of a pneumatic membrane subjected to suddenly lifted loads was discussed, and in the following chapter (10.3) the theoretical results for vertical deflection traces of certain nodes were compared with corresponding experimental results. The differences between them were very large.

In the previous numerical analysis, the membrane was treated as the only structural part of the dome, and the internal air was accounted for only as far as air stiffening was concerned. The latter was introduced into the analysis by applying the isentropic relation, $\frac{p}{\rho^{\gamma}}$ = constant, to the

whole volume of air enclosed by the membrane. The observation during tests on the impulsively unloaded pneumatic dome indicated that the surrounding air should be treated as an intrinsic part of the structure in the dynamic analysis.

The above problem can be approached in three different ways:

first: The behaviour of surrounding air can be numerically modelled with the help of fluid mechanics (and if necessary thermodynamics), and coupled with the structural dynamic analysis;

second: The influence of surrounding air on the structural dynamic response can be carefully examined and accounted for by means of additional terms in the mass, damping and external force matrices of the dynamic equations. The values of air influence components can be derived from theoretical models and/or very simple fluid mechanics relations; and

third: An approach similar to the second, but with additional terms obtained from simple theories combined with experimental coefficients.

The last approach, in general, will result in the smallest amount of computing but requires a great number of tests; separate experiments may be needed for different types and shapes of structures. Jensen [99, 100] conducted a series of such tests on tension structures (pneumatic structures were not considered) and by observing and monitoring their dynamic responses, presented formulae for added mass,

damping and, when wind loading is considered, the additional term in wind loading formulae expressing the internal reaction associated with the acceleration of the surrounding air. Jensen's conclusions were discussed in more detail in the review of chapter 4.

The first approach is capable, in theory, of providing us with the most accurate solution. The drawback of this method can be the enormous computing time which is involved in solving the fluid mechanics time dependent equations, especially in 3D, and when coupled with the structural dynamic equations. A compromise, which may lead to a more practical solution is to simplify the behaviour of the surrounding and enclosed air. Williams in [203], under the assumption of irrotational incompressible air flow, suggested a way of deriving the added mass matrix for air surrounding a membrane structure by means of a boundary element method. Emphasis was placed on 2D solutions. An alternative approach to this, but allowing for compressibility and being easily extended to 3D, is that proposed by Barnes [14]. The method seems to be more appropriate for modelling the behaviour of a suddenly unloaded pneumatic isotropic dome, where the changes in internal pressure can be clearly observed during the tests.

Introducing more simplification to fluid dynamic equations cuts down the computing time, but may result in erronous solutions. On the other hand more precise modelling requires longer computing time, which at the present stage leads to more expensive solutions. Therefore, the second

approach may be a more appropriate alternative. The theoretical model is used to represent a particular feature such as the added mass effect. William's method can also be viewed as belonging to the second type of approach. This group will be discussed in more detail in chapter 12.

11.2 Air surges within an enclosed pneumatic stressed membrane - a review

Equations of motion can be formulated from two different points of view:

1. Eulerian or statistical, an approach more popular in fluid dynamics *(see chapter 2); attention is directed* to a particular point in space
2. Langrangian or historical, an approach used in dynamics of structures in which the progress of a particle is followed.

When fluid dynamic equations are combined with structural dynamic equations it may be advantageous to keep the same way of describing the motion. In the approach suggested by Barnes [14] and presented herein this uniformity is maintained, namely motion of air and membrane is represented using the Langrangian point of view.

In this method the derivation of the basic equation of motion will be given with direct reference to internal air enclosed by a pneumatic stressed membrane which is externally loaded. The method can be easily extended to external air as will be shown in 11.4. For a two-

dimensional problem the simplest example of an air-supported structure seems to be a very long cylindrical structure (see section in figure 11.1).

The total mass of air within the structure is assumed to be constant (the leakage is negligible).

Air can be represented by a hypothetical ideal fluid; a fluid assumed to be inviscid, or devoid of viscosity (i.e. frictionless). A further restriction, which is made, is the assumption of no heat transfer to or from the fluid, which for frictionless fluid movement results in an isentropic process. The internal air is divided into triangular elements in 2D (see figure 11.1) and into tetrahedral elements for a 3D case. Each element, in addition to volumetric deformation, may be subject to rigid body movements. The element faces are assumed to remain plane during apex nodal movements, and the internal mass of an element is assumed constant.

Considering an element of the air undergoing translation and rotation. The pressure at any time, t, is defined by the isentropic process relation

$$p^t = C(\rho^t)^k \qquad 11.1$$

where

C is a constant

ρ is the air density, and

k is the ratio of two specific heats of a gas, that at constant pressure, c_p, to that at constant volume c_τ;

for air k is found to be 1.4.

The current volume, V_o^t, may be determined from the nodal coordinates at time t, and since the mass

$$M = \rho^t V_o^t \qquad 11.2$$

is constant, equation 11.1 takes the form

$$p^t = C'/(V_o^t)^k \qquad 11.3$$

The pressure and density at any instant are assumed to be constant throughout the element.

There are two types of fluid mechanics equations (see chapter 2)

1. continuity (conservation of mass), and
2. equations of motion.

For the element under consideration the former relation is self-satisfied (the mass is constant). The equations of motion of chapter 2 were derived by application of a scalar form of Newton's second law. However, Newton's law is a vector relation and it can be written for an element of air in terms of the impulse provided by external forces (pressure, gravity etc.) and the resulting changes of the linear momentum of the element as:

$$(\sum \bar{F})\ dt = d(m\bar{V}_c) \qquad 11.4$$

where

V_c is the velocity of the centroid of the element,

mV_c is the linear momentum, and

$(\sum F)dt$ is the impulse during time dt from the sum of all external forces acting on the element.

The continuous time history from $t = t_o$ to $t = t_f$ is divided into n time intervals of a very small time step t ($t_f - t_o = \Delta t \times n$).

Approaching the problem in a similar manner to that of explicit dynamic analysis with finite difference application makes it compatible with the structural dynamic solution procedure for membrane structures (see chapter 9). The velocities will be calculated in the middle of each interval, but forces (pressures) acting on the element and its nodal coordinates at the end of time intervals. Forces and coordinates obtained at the end of any time interval are assumed to have the same value on the beginning of the next interval.

The increase of linear momentum of the element in the x direction during the small time interval

$$(t - \Delta t/2) \rightarrow (t + \Delta t/2) \text{ is:}$$

$$M^e \; u_c{}^{t+\Delta t/2} - M^e \; u_c{}^{t-\Delta t/2} \qquad 11.5$$

where

u_c refers to centroidal velocity in the x direction.

For simplicity, only the equation for the x direction will be presented. As the element is subject to rigid body motion and hence velocities vary linearly throughout the element, formula 11.5 can be expressed in terms of nodal velocities u_i:

$$\frac{M^e}{N} \sum_{i=1,N} (u_i{}^{t+\Delta t/2} - u_i{}^{t-\Delta t/2}) \qquad 11.6$$

where

N=3 for triangular (two dimensional) elements, or

N=4 for tetrahedral (three dimensional) elements.

The increase in momentum is equal, by equation 11.4, to the impulse of the forces acting on the element in the x direction during Δt, $(\sum F)\,\Delta t$. Assuming no body forces, $(\sum F)\,\Delta t$ is equal to

$$\Delta t \iint_S l'_x{}^t \; p'^t \; ds \qquad 11.7$$

where the integral extends over the whole surface area S of the element,

$l'_x{}^t$ is the x direction cosine of the inward normal to the surface, and

p'^t is the inward pressure (i.e. the pressure exerted by the surrounding elements)

For the elements under consideration the integral of 11.7 can be substituted by summation to give

$$\Delta t \; p'^t \sum_{f=1,N} l_x{}^t{}_f \; A_f{}^t \qquad 11.8$$

where

$l_x{}^t{}_f$, $A_f{}^t$ are respectively the area and the x direction cosine of the outward normal of face f of the element.

Equating 11.6 to 11.8 results in the following equation:

$$\frac{M^e}{N\Delta t} \sum_{i=1,N} (u_i{}^{t+\Delta t/2} - u_i{}^{t-\Delta t/2}) = p'^t \sum_{f=1,N} {}^t lx_f \; A_f^t \qquad 11.9$$

If the mass of the element is equally distributed to its apex nodes i.e.

$$M_i^e = \frac{M^e}{N} \qquad 11.10$$

then the relation of type 11.9 can be rewritten as a balance of nodal momentums:

$$\frac{M^e}{N\Delta t} (u_i^{t+\Delta t/2} - u_i^{t-\Delta t/2}) = \frac{p'^t}{N-1} \sum_{f=1,N-1} l_{xf}^t A_f^t \qquad 10.11$$

where the summation is over N-1 faces of elements meeting at node i.

Figure 11.2 shows a patch of elements with different pressures. The relation 11.11 can be satisfied in an overall sense for node n by summing up the relevant coefficients of equation 11.11 written at node n, for all elements surrounding this node:

$$\frac{M_n}{\Delta t} (un^{t+\Delta t/2} - u_n^{t-\Delta t/2}) = \sum_{j=1,E} \left(\frac{p_j^t}{(N-1)} \sum_{f=1,N-1} l_f^t A_f^t\right) \qquad 11.12$$

where

$M_n = \frac{1}{N} \sum_{j=1,E} M_j^e$ is the mass of node n (contributed by all surrounding elements j = 1,E), and

pj^t is the current pressure in the elements.

For an isolated triangular element (two dimensional case), with internal pressure p, the nodal forces are shown in figure 11.3. By examining one of the nodes, for example nr 3 (see figure 11.4) it can be concluded that the sum of two vectors $\frac{\overline{pA_2}}{2}$ and $\frac{\overline{pA_1}}{2}$ give a vector $\frac{\overline{pA_3}}{2}$ of direction

perpendicular to side A_3. For nodes 1 and 2 a similar procedure can be conducted. The resulting forces shown in figure 11.4 are equivalent to those shown in figure 11.3. Although the proof was only given for a two dimensional case, 3D elements will yield similar resultant nodal forces.

Equation 11.12 may thus be alternatively expressed as:

$$\frac{M_n}{\Delta t}\left(u_n{}^{t+\Delta t/2} - u_n{}^{t-\Delta t/2}\right) = - \sum_{j=1,E} {}^{t}p_j \, {}^{t}l_j \, \frac{{}^{t}A_j}{N-1} \qquad 11.13$$

where

l_j, A_j now refer only to the external face (not containing n) of elements j = 1,E surrounding node n.

Equation 11.13 may be regarded more directly as the external force component on the mass of air surrounding node n, as shown in figure 11.5. The external forces $p_i \cdot A_i/2$ will be the same, no matter what the surface (see figure 11.5) presumed to contain M_n is, provided the surface is regarded as passing through the mid-side points. Hence, although simplex elements and linear shape function are used, the resulting forces $p_i \, A_i/2$ are the same as with more complex elements and functions.

Equation 11.13 was derived for the internal air modelling of a pneumatic structure, but its application can be extended to external air modelling. For the purpose of doing so the external air should be divided into elements as far as any changes in pressure are likely to occur.

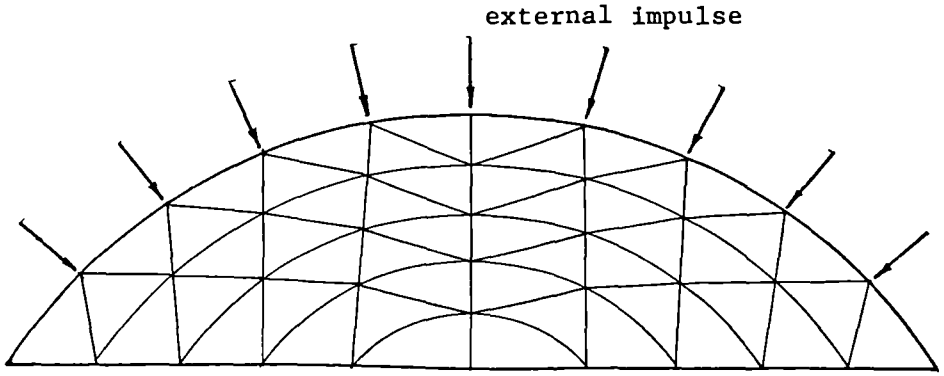

Figure 11.1

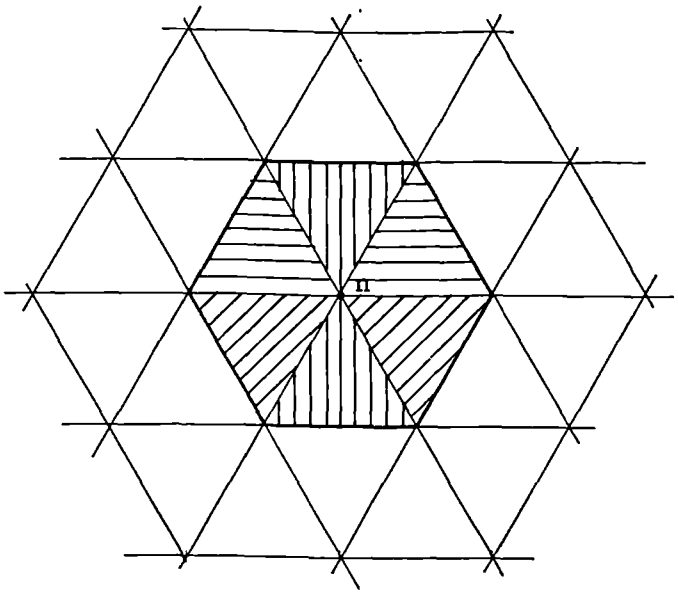

Figure 11.2

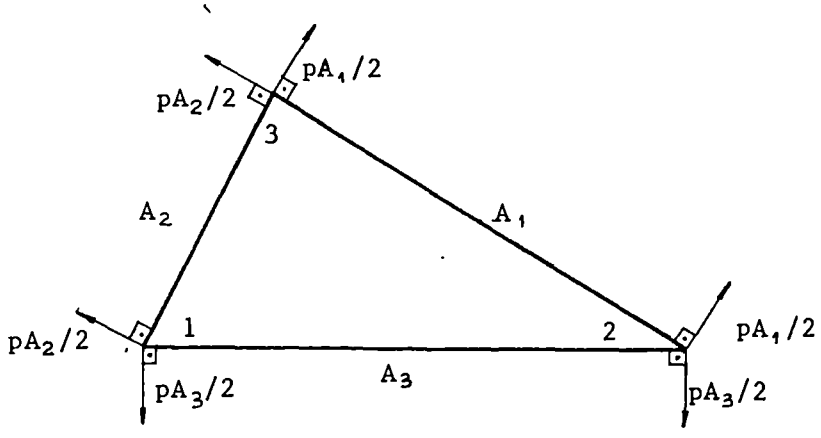

Figure 11.3

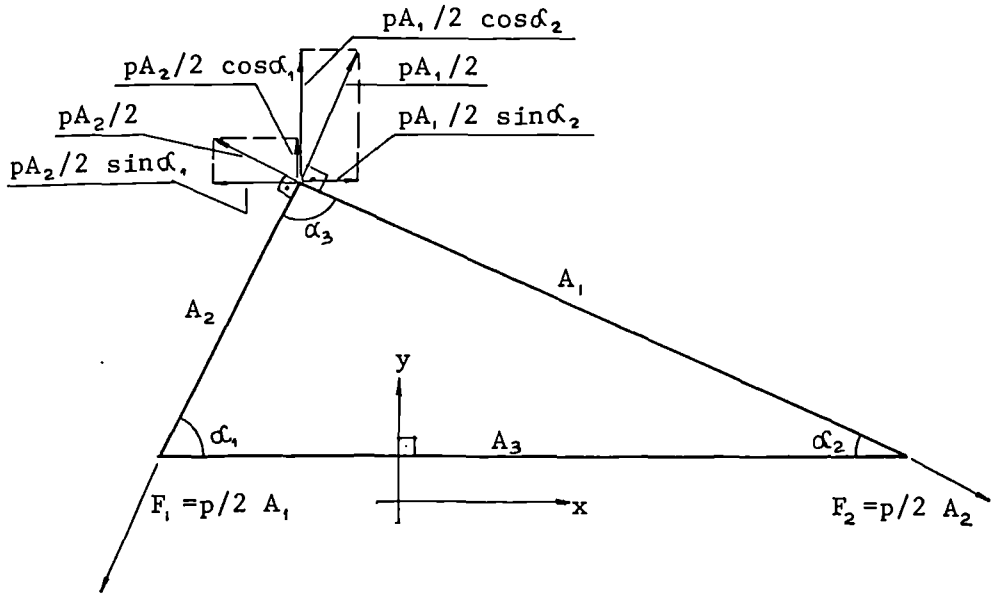

$F_{3x} = pA_1/2 \sin\alpha_2 - pA_2/2 \sin\alpha_1 = p/2(A_1 \sin\alpha_2 - A_2 \sin\alpha_1) = 0$

$F_{3y} = p/2(A_1 \cos\alpha_2 + A_2 \cos\alpha_1) = pA_3/2$

Figure 11.4

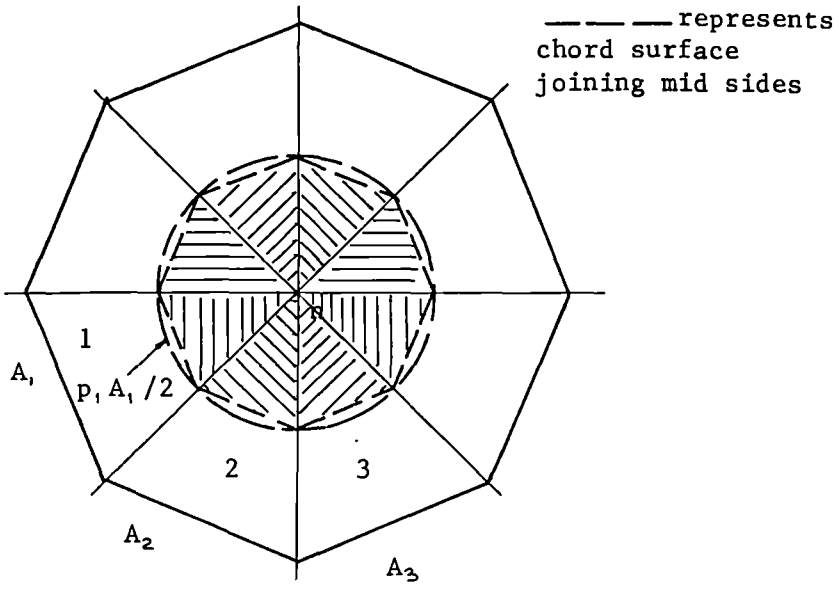

Figure 11.5

11.3 Iteration scheme for explicit dynamic analysis of pneumatic structures with internal air modelling

11.3.1 Numerical iteration scheme for air modelling

The recurrence equation for the velocity, u_{nx}, of node n common to E air elements, in central finite difference form, at time step $t + \Delta t/2$ is similar to that for explicit dynamic analysis of the membrane structure alone (see chapter 9, equation 9.3).

$$u_n^{t+\Delta t/2} = \frac{\Delta t}{M_n} R^t_{nx} + u_n^{t-\Delta t/2} \qquad 11.14$$

(and at time $\Delta t/2$ to start the iteration, and satisfy $u_n = 0$ at $t = 0$): $u_n^{t/2} = .5 \frac{\Delta t}{M_n} R^o_{xn}$ 11.15

Hence, the new coordinate of node n is:

$$X_n^{t+\Delta t} = X_n^t + \Delta t \cdot u_n^{t+\Delta t} \qquad 11.16$$

Similar equations can be written for the y and z directions and solved for time $t+\Delta t$ at all nodes to give the current geometry of the system. Hence, the new volumes $V_o^{t+\Delta t}$ for all elements can be determined, and the pressures are obtained from equation 11.3. For an element j the pressure at time $t+\Delta t$ is calculated as

$$p_j^{t+\Delta t} = p_j^t \left(\frac{V_o^t}{V_o^{t+\Delta t}}\right)^k \qquad 11.17$$

Then the forces are

$$R_{xn}^{t+\Delta t} = -\sum_{j=1,E} p_j^{t+\Delta t} \; l_j^{t+\Delta t} \; \frac{A_j^{t+\Delta t}}{N-1} \qquad 11.18$$

The integration proceeds through (11.14 to 11.18) for each time step.

For numerical stability $\Delta t < \Delta t$ crit, and the critical time for the whole system is found as the smallest of Δt crit for any node:

$$\Delta t_{\text{crit } i} = \sqrt{\frac{2M_i}{S_i}} \qquad 11.19$$

where

S_i, stiffness of node i is defined for a solid elastic material in terms of moduli of elasticity.

Considering a cubic element a x b x c, as shown in figure 11.6 made of isotropic material, the elastic stiffness of node n of the element in the x direction, according to the Gershgorim bound [13], can be found to be:

$$S_{xn} = (S_{xx} + S_{xy} + S_{xz}) \quad \frac{b}{2} \; \frac{a}{2} / c = \frac{E}{(1-2\nu)} \quad \frac{a\,b}{4c} \qquad 11.20$$

Since fluids (air can be classified as a type of fluid) do not possess rigidity of form, in place of the modulus of elasticity, E, another quantity, bulk modulus, K, is defined.

If an additional 'hydrostatic' pressure dp (i.e. equal in all directions), acting on a body of initial volume V_o causes a reduction or increase in volume equal numerically to dV_o, then the bulk modulus, K, is defined as:

$$K = - \frac{dp}{dV_o/V_o} \qquad 11.21$$

where the negative sign is used when dp causes reduction in volume.

An expression for the bulk modulus of a gas may be derived

assuming an isentropic process by writing the general form of equation 11.21 in terms of γ or ρ (specific density or gravity). As the relative increases of or are exactly equal to the relative decrease of volume [193]:

$$K = \frac{dp}{d\gamma/\gamma} = \frac{dp}{d/\rho/\rho} \qquad 11.22$$

When this equation is solved simultaneously with the differential form of equation 11.1, the result is found to be [193]:

$$K = k\ p \qquad 11.23$$

Equation 10.22 indicates that the bulk modulus for gases is not constant but increases with increasing pressure.

The relation between a bulk modulus and modulus of elasticity can be determined by substituting into equation 11.21 the following equation [188]:

$$\frac{dV_o}{V_o} = \varepsilon_x + \varepsilon_y + \varepsilon_z \qquad 11.24$$

(this states that the volumetric strain is equal to the sum of the linear strain components). The relationship between the two moduli is found to be:

$$E = 2K\ (1-2\nu) \qquad 11.25$$

But substituting equation 11.22 into the last form of equation 11.20, the elastic stiffness of node n of the cubicoidal air element, in direction x, can be defined in terms of the bulk modulus as:

$$S_{xn} = 3K\ \frac{a\ b}{4c} \qquad 11.26$$

or for the isentropic process in terms of pressure (equation

11.23 is substituted into equation 11.26):

$$S_{xn} = 3kp \frac{a\ b}{4c} \qquad 11.27$$

The critical time step for the iteration scheme for air modelling can be calculated from equations 11.19 and 11.27 (or equation 11.27 amended to account for a different shape of air element).

The procedure for internal air modelling outlined in 11.2 allows for compressibility, hence the pressure is not constant. The condition for numerical stability based on pressure and geometry at t = 0 may not be adequate and, therefore, choosing a time step as small as 50% of the critical value may be necessary.

11.3.2 Numerical iteration scheme for coupled analysis

The numerical iteration scheme for air modelling was formulated in such a way that it can be easily coupled with the explicit dynamic analysis scheme described in chapter 9.

The additional alterations to the flow chart presented in 9.2.2 comprise:

1. data file to be increased for information concerning internal (and external) air divisions, e.g: nodal coordinates and number of nodes for each air element.
2. before the main loop begins the following steps must be included:
   a) setting pressure in all elements to known values: atmospheric pressure for external elements and

defined pressure for internal elements.

b) defining an array giving the number of air elements surrounding any node

c) finding lumped nodal masses (or additional masses for membrane nodes) due to the air elements.

d) defining an array to contain the continuously updated vectors normal to all faces of every element in an outwards direction.

3. in the main loop

a) calculation of pressures based on equation 11.17 for all air elements

b) finding nodal forces due to element air pressure from equation 11.18

c) calculations of current nodal velocities and coordinates are extended to all nodes (those modelling both the membrane and the air)

4. in the secondary loop

a) calculations of outward normal vectors to all faces of every element.

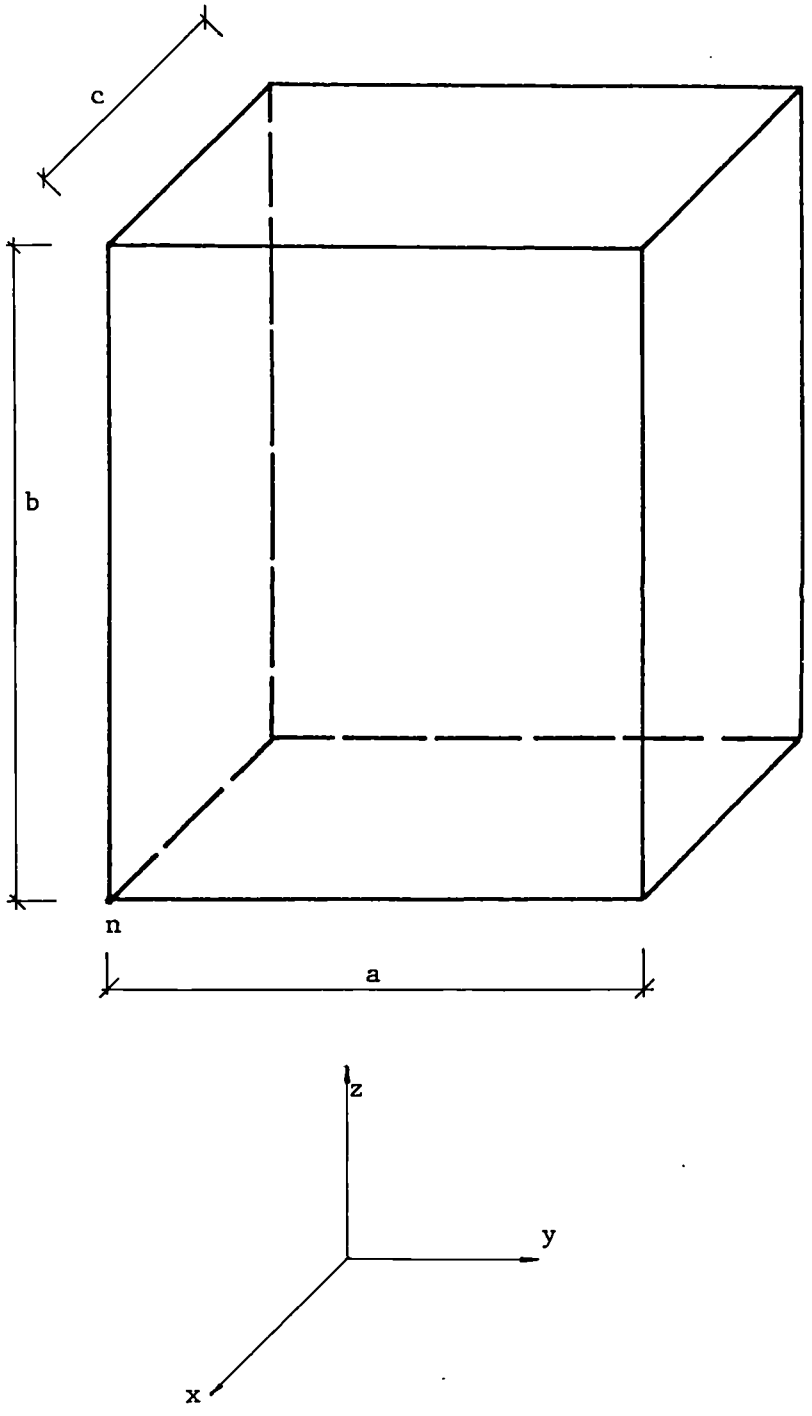

Figure 11.6

11.4 Numerical simulation of an impulsively unloaded pneumatic dome

The numerical scheme presented in chapter 11.3 was introduced by Barnes [14] to deal with a two dimensional case, an inflated very long cylindrical membrane structure subject to external load. The modelling of internal and external air, the number of nodes and air elements, the amount of computing involved and the results obtained, suggested that this method could be suitable for three dimensional explicit dynamic analysis of isotropic membranes subject to suddenly lifted loads. The theoretical trace of deflection at the central point was not, however, compared with an experimental trace [14].

In such circumstances it seemed to be prudent to investigate the numerical method including both structural (membrane) and fluid (air) modelling for a relatively simple case for which experimental results could be easily obtained. The dynamic tests on a lightweight polythene pneumatic dome, described in chapter 10.3, considered the following cases:

Test 1:

Impulsively centrally raised load. This is the easiest 3D case (full axisymmetry) and can be used to establish the number of air elements required, the accuracy obtainable and as a check for convergence.

Test 2:

Suddenly lifted asymmetric load better illustrating an internal air movement. This can be employed as an example

for explicit dynamic analysis of the dome subjected to arbitrary dynamic loading.

In both tests, the loads were lifted to prevent any influence of local high mass on dynamic response, as happens when load is placed on a dome.

The centrally unloaded dome, as an easier case, will be considered first. The membrane idealization, geometry and stresses, as a starting point for the analysis, were discussed in chapter 9.2.2 in the context of explicit dynamic analysis of the dome without including surrounding air. Certain facts will be recalled, briefly:

1. only a 10° 'cheese slice' was used to model the membrane, as shown in figure 9.10a of chapter 9.
2. the initially flat membrane was uniformly prestressed and then inflated. Following central loading, the numerical statical analysis yielded the stresses and geometry (which compared well with the experimental results)
3. response of the dome to suddenly raising the central load was modelled numerically disregarding the surrounding air. The theoretical response for the vertical movement of node 3 differed greatly when compared with the experimental trace.

As a first approach (case 1) to modelling the air, the external and internal air was divided into tetrahedral elements as shown in figure 11.7. The curve A-A, a sector

of a circle, representing the inflated state of the dome, was used as a guide. The radius of the curve C-C was chosen in such a way that distances OA and AC at y = 0 and x = 0 were equal. The points lying along the line z = 0 and y = 0, and along curve C-C at y = 0 were found as the intersections of lines passing through the centre of the circle (obtained from A-A) and the nodal points of the inflated membrane (lying along A-A). Remaining lines being sides of elements, were chosen to give the most uniform division. Thus obtained, the division resulted in 390 tetrahedral elements: 162 to model the internal air and 228 for the external air. It is worth noting that each triangle in figure 11.7b, except the first vertical row, represents three tetrahedrals. In the first row each of two triangles results in three 3-dimensional elements.

The critical time in this coupled structure - fluid analysis is chosen as the smallest for any node taking into account membrane and air stiffnesses. It was found that the pure air elements gave the lowest critical time. As indicated in 11.3.1 the stiffness of a gas element is not constant but depends upon its size and current pressure, therefore, calculations based on a starting geometry and pressure cannot give the precise value of time step for numerical analysis. In such circumstances it seems adequate to base calculation of the stability condition on a single element having the lowest Δt_{cr}. In the type of division shown in figure 11.7, the internal elements in the first row have the smallest Δt_{cr}. The time interval used for the numerical

integration was 70% of the critical value, i.e. .00002 sec. For the centrally unloaded dome, the most efficient computational procedure was to perform the operation of the secondary loop (updating stiffness matrices, resetting creep strains, initial stresses and unit vectors normal to the element sides) at every 20 time interval.

The results for the vertical deflection trace at node 3 are shown in figure 11.11. Computing time was longer than expected. When running on a Gould PN 6000 the real time used by the computer to obtain a trace from t = 0 to t = 0.5 sec was approximately 4 hours and 30 minutes. The computer, however, is a multi user machine of low power.

Where the theoretical results obtained from the analysis including air elements were compared with those derived from the analysis of chapter 9 (where surrounding air was disregarded), and also with the experimental results of chapter 10, the following conclusions were drawn:

1. there is improvement in the theoretical prediction of frequency (see figure 11.12)
2. deflections became very small (see figure 11.12)

The most obvious remedy for the discrepancy between experimental results and theoretical with air modelling seemed to be to increase the number of air elements. The second effect concerning the small value of deflections could have been explained by 'piston' behaviour of air elements. When a Lagrangian approach is used in fluid

mechanics and air is modelled by elements which are too large, each of the elements acts like a small piston, in which high pressure limits the nodal movements.

During the analysis the pressures in elements were monitored and it was noticed that in external elements pressure did not differ greatly from atmospheric. A second computer run was carried out, but this time only with internal air modelling. The resulting trace was very similar to that obtained with full modelling; the difference not being discernible in the scale of figure 11.11. In this run only 162 air elements were used and the computer time was reduced by a factor of two. This was encouraging and for further primary investigation only internal air modelling was employed.

In order to investigate the influence of air element size on response and to check for convergence three tests with different element sizes were run. As the case is axisymmetric, divisions in only two directions are important. Referring to figure 11.7, the important directions are along the axis and in the radial direction. The three types of membrane and internal air modelling: div 1, div 2 and div 3 are presented in figures 11.8, 11.9 and 11.10 respectively.

The first kind of idealization was chosen to give the least practical number of elements whilst allowing for a proper representation of the way the central load is applied (also to keep as a node, the point at which the experimental trace

was observed). This resulted in having two different sizes of elements: tetrahedral in the first two rows from the middle and two membrane triangles being approximately two times smaller than the remaining larger elements (see figure 11.8b). This type of division may be justified by an analogy with solid body stress analysis where areas of higher stresses require finer divisions. Here the central area, where the largest movement takes place, can have a higher pressure for a short period of time before dispersing the pressure to other parts of the dome.

In the second type of division (figure 11.9) elements were half the size of those in div 1; and in the third type (figure 11.10) elements are one third of the basic first division.

For each of the three idealizations, separate numerical static analyses had to be performed to give starting geometry and stresses. The numerically predicted deflections corresponding to the measured experimental values at node 3 for each of the idealizations are plotted in figure 11.11. The frequencies and the max deflections obtained from both the test and the theoretical analyses are tabulated and given in figure 11.12. In order to check for convergence the theoretical maximum deflections and frequencies from the three types of idealization are plotted in figure 11.14 against the size of elements, assuming unity for the first type of division.

From the comparison of theoretical and experimental results the following conclusions can be drawn:

1. The shape of the deflection trace from case 1 (first approach to model internal air) resembles more closely the experimental trace than the remaining three divisions. When a non-uniform division is used there is a noticeable presence of higher frequencies. A uniform division seems to be better suited for air modelling when employed in this type of analysis.
2. Maximum dynamic deflections from three types of division do not converge and frequencies tend to unrealistic values.

   The trace of deflection obtained using div 1 differs greatly both in shape and in the range of values when compared with the experimental trace. This would imply that the size of elements is too large and therefore this type of division is clearly not suitable for air modelling. From the remaining two sets of results it is impossible to assess convergence.
3. There is an observable improvement in the theoretical prediction of frequency when internal air is included in the analysis.
4. The maximum deflection predicted when 631 air elements were used (see figure 11.12 and 11.13) is still more than 3.5 times smaller than the experimental value.

   The dynamic analysis without air elements gives maximum deflections closer to the experimental: approximately 40% higher.

5. While increasing the number of air elements improves both frequency and maximum deflection, the real computer time grows enormously (see figure 11.13) due to an increase in the number of elements together with a reduction in their size and hence the time step for stability. As frequencies are lower, a trace of deflection has to be followed for a longer time.

No attempts have been made to refine the mesh to further investigate convergence, as the real computing time on a Gould 6000 *or 9000 would have been counted by days*.

This approach to the modelling of internal air-surges was intended to be employed in the case of arbitrary loading. In this case, however, the number of elements would have to be at least 18 times larger (for half dome modelling) than used for 10° 'cheese slice'. This illustrates quite clearly that at the present stage this method is not suitable for any practical purpose.

An alternative approach, probably more suitable for this kind of problem, may be to employ a Eulerian formulation for the problem; where nodes are used as stationary points to observe the movement of air through elements, as opposed to a Lagrangian approach in which deformable air elements are employed.

Unfortunately, if the large motions of the boundary membrane are to be accounted for, some of the elements must deform during a coupled analysis.

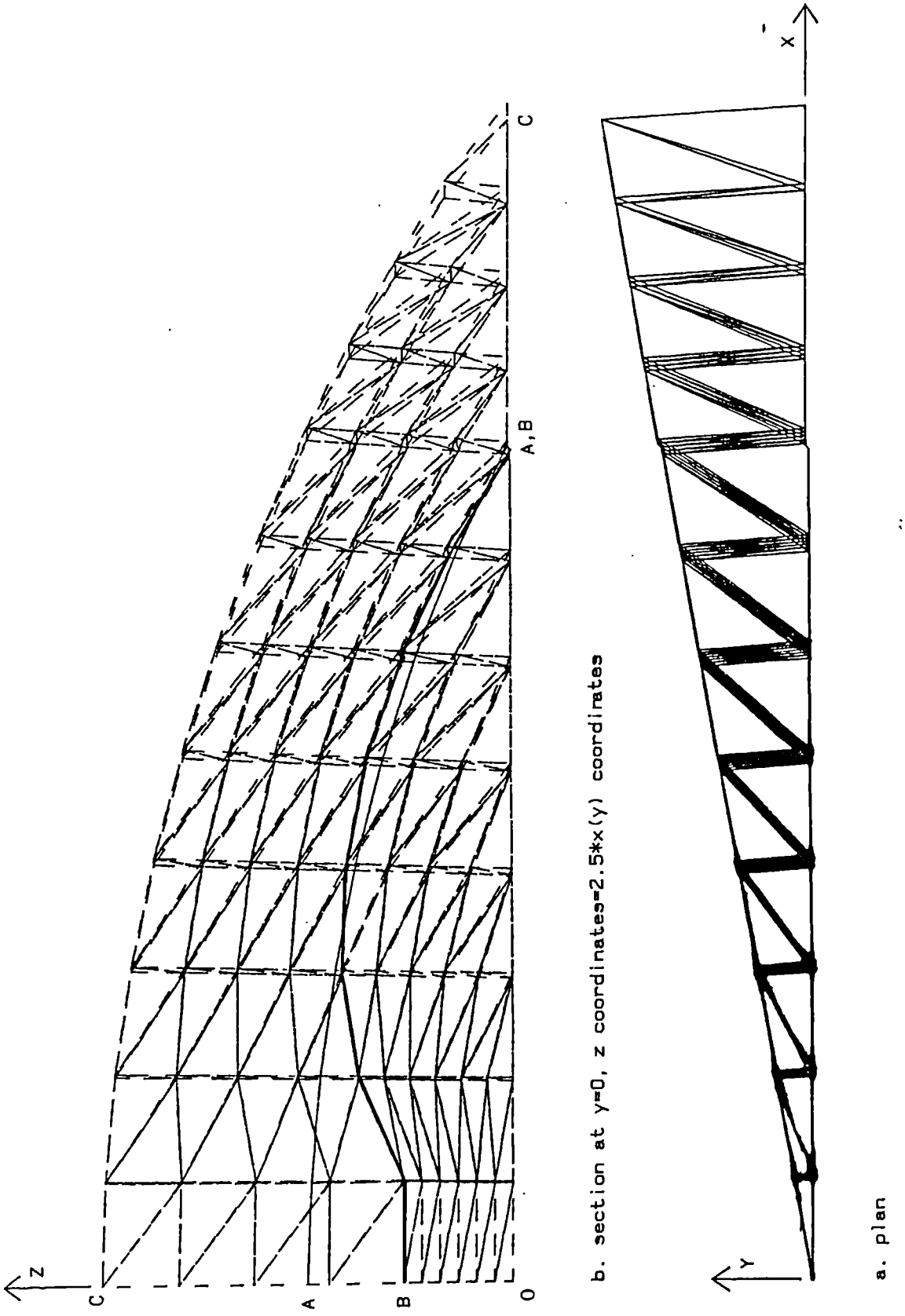

Figure 11.7 Air and membrane modelling, case 1

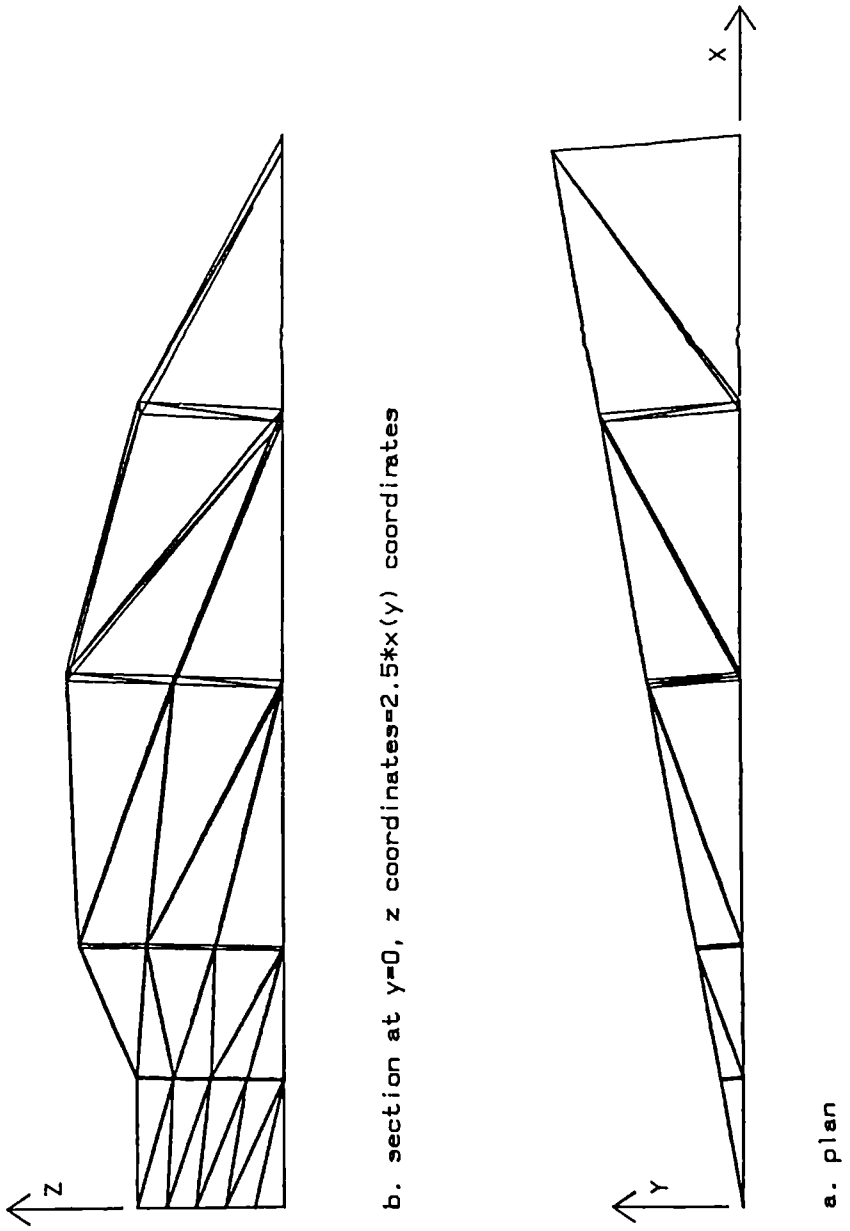

Figure 11.8 Internal air and membrane modelling, div 1

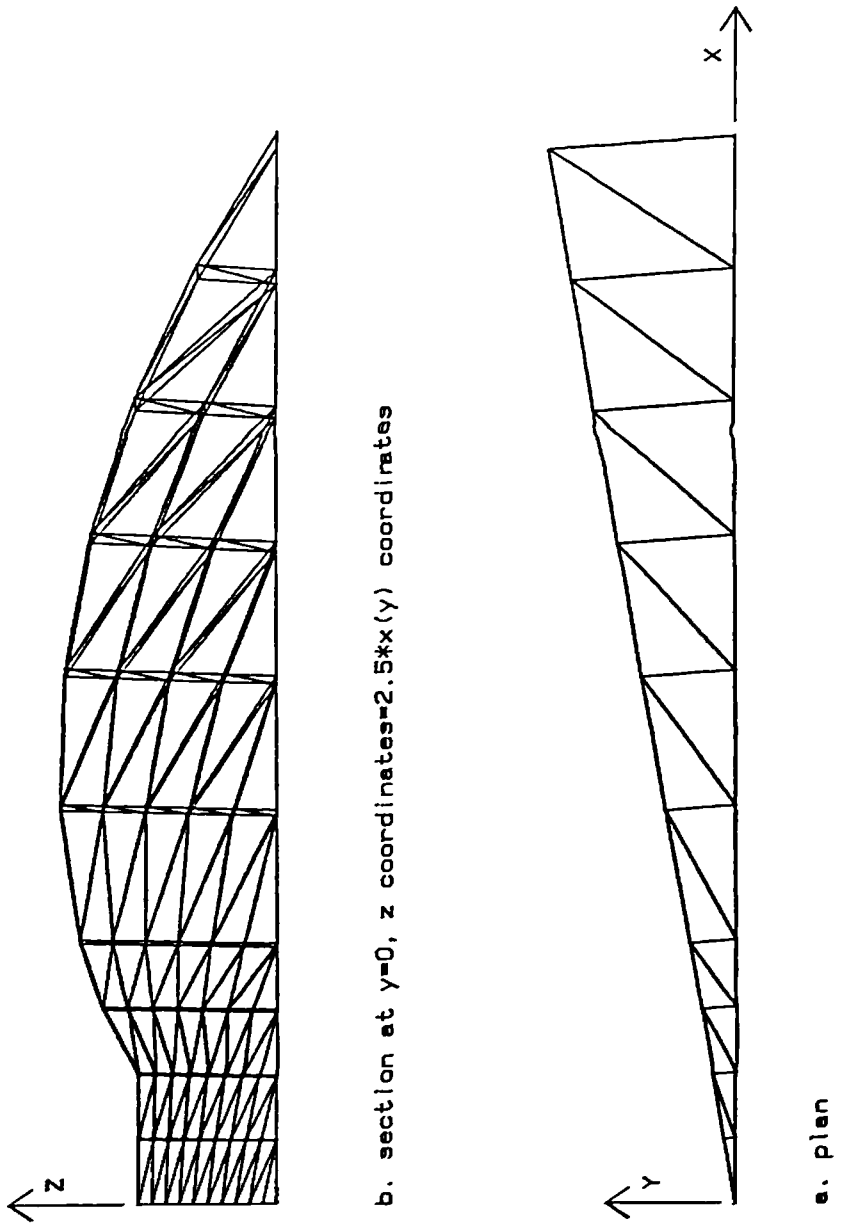

Figure 11.9 Internal air and membrane modelling, div 2

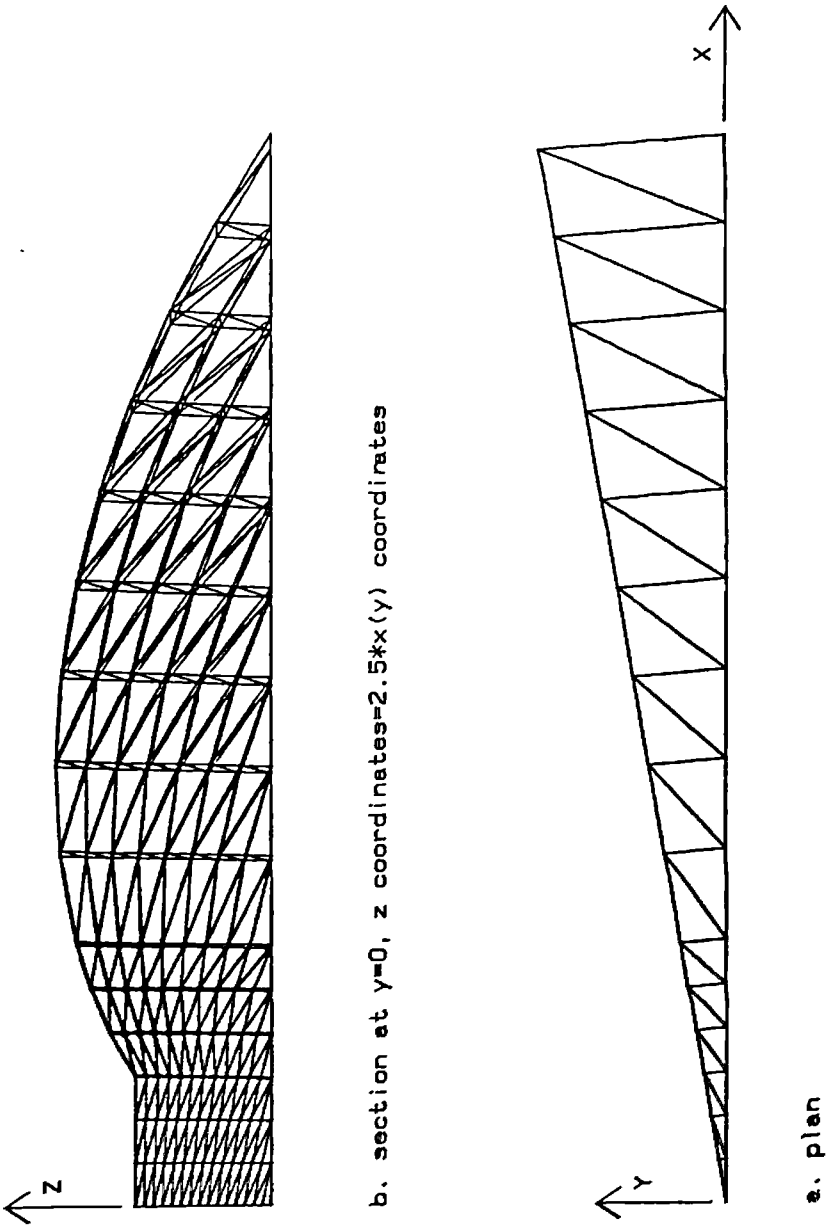

Figure 11.10 Internal air and membrane modelling, div 3

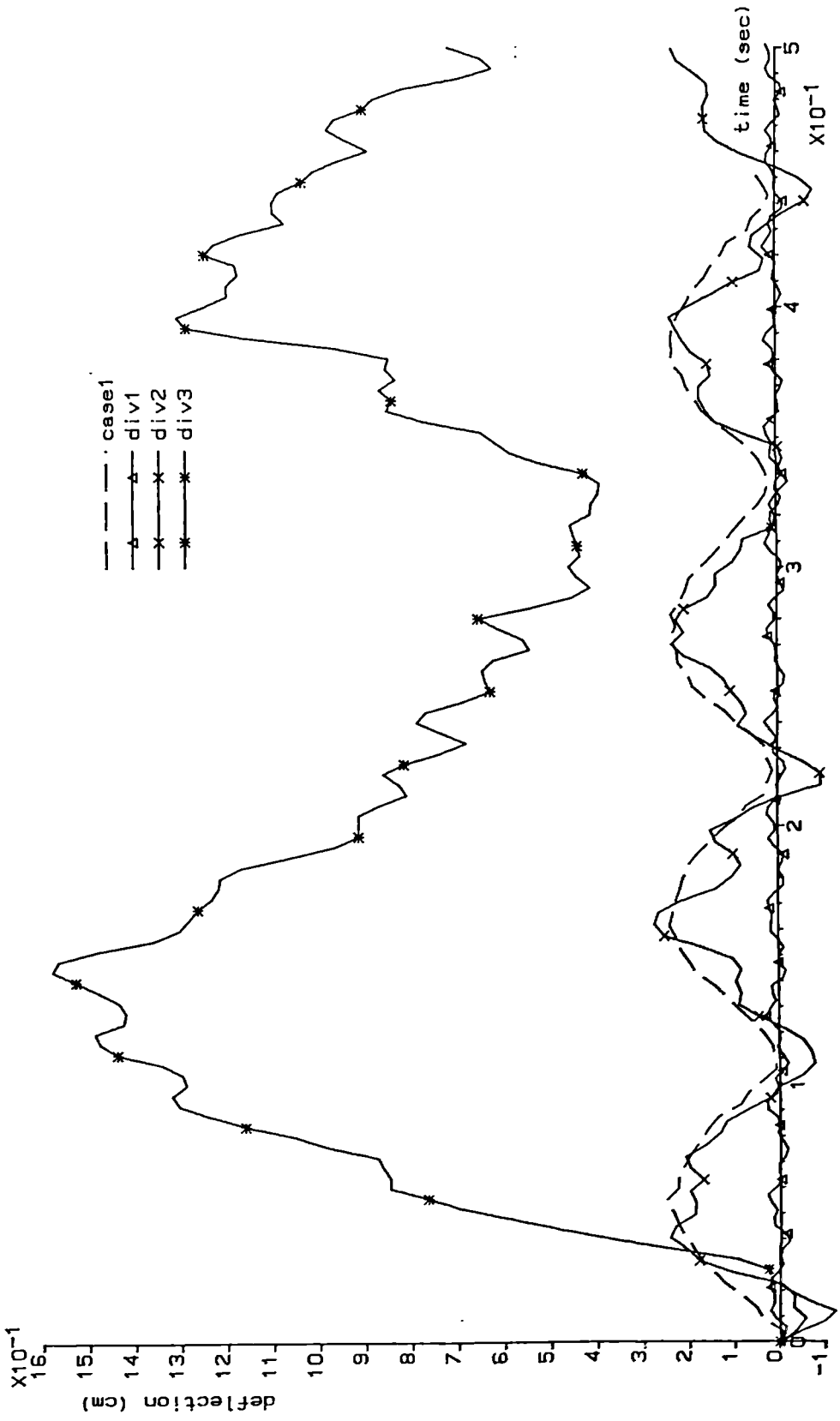

Figure 11.11a Unloaded dome, deflection decay

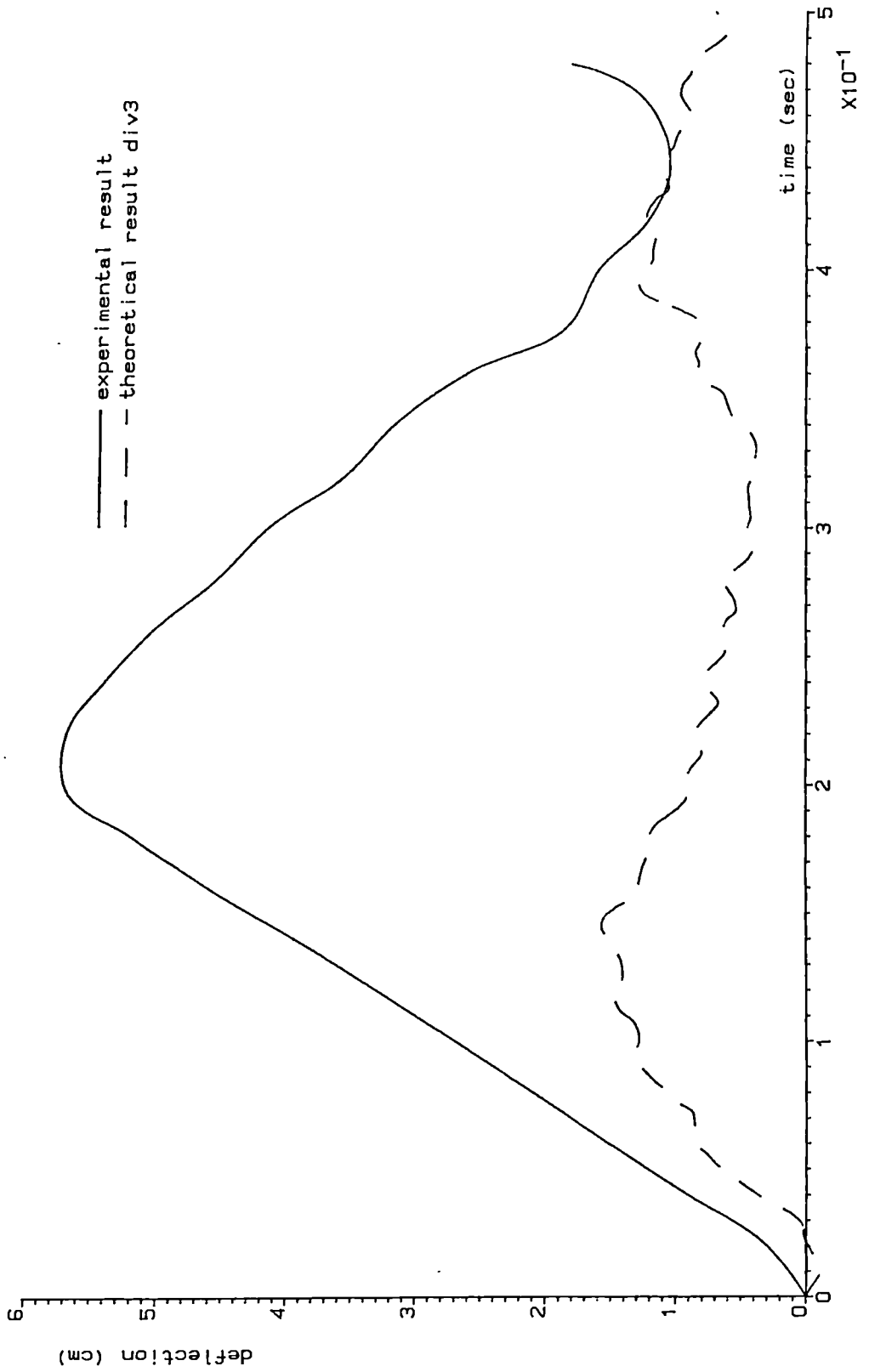

Figure 11.11b Unloaded dome, deflection decay

		max. dynamic deflection (cm)	frequency cycles/sec
experimental results		5.8	2.5
theoretical, only membrane modelling		8.4	16.0
theoretical,	case 1	.25	9.1
membrane	div 1	.034	28.8
and internal	div 2	.28	8.75
air modelling	div 3	1.6	3.8

Figure 11.12

Type of division	Number of air elements	time step used	Gould PN 6000 real computing time to obtain def from 0 to .5 sec
div 1	61	.00006	25 min
div 2	271	.00003	4 hr 15 min
div 3	631	.00001	27 hr 40 min

Figure 11.13

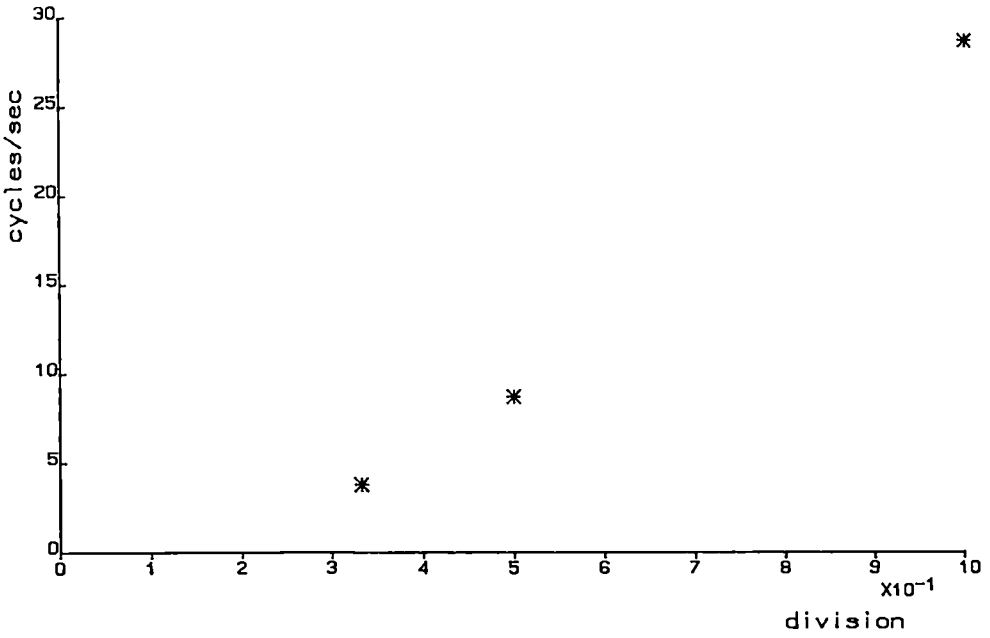

a. frequency

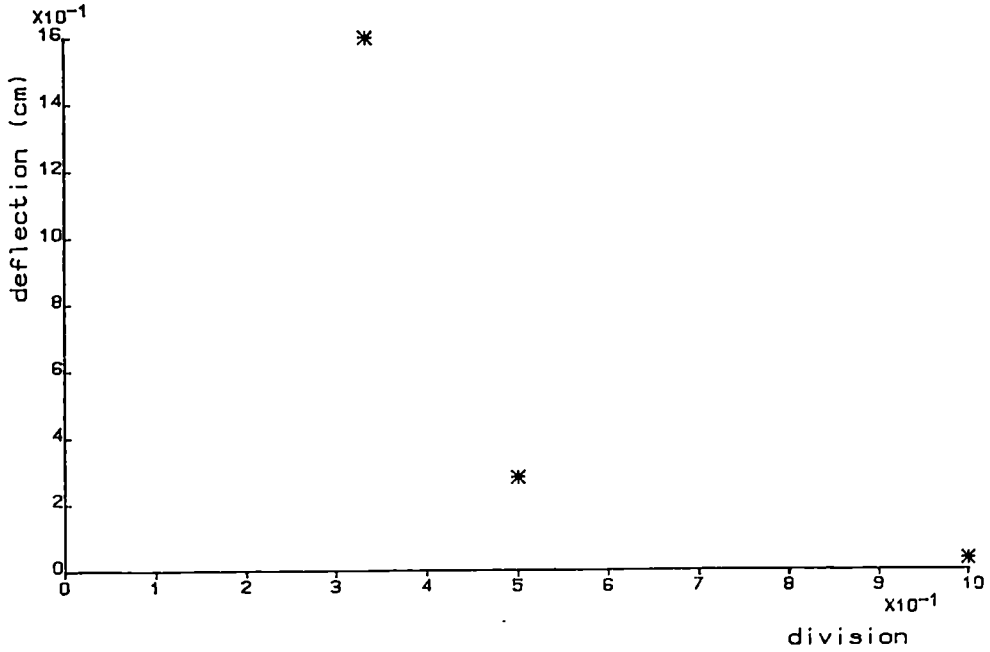

b. maximum dynamic deflection

Figure 11.14 Checking for convergence

CHAPTER 12

Added mass effect on dynamic response of pneumatic structures

Contents:

In this chapter the explicit dynamic analysis of chapter 9 is extended to account for the added mass effects of the surrounding air in shallow pneumatic structures. The concept of added mass, with emphasis on the mathematical representation under a potential incompressible flow approximation, is reviewed. The numerical modelling of the attached air by means of discrete sources is discussed in the contexts of a flat diaphragm embedded in a rigid surface, and a shallow pneumatic structure. An iteration scheme for the approximate fluid-structure explicit dynamic analysis is given, and examined with direct reference to the centrally unloaded lightweight pneumatic dome. The results for the dome show a great improvement in terms of frequencies with only a small increase in computing time compared with the numerical scheme of chapter 9.

12.1 Introduction: concept of added mass

In chapter 11 attempts were made to model the influence of surrounding air on the dynamic response of air-supported structures. In the analysis, internal air was idealized by tetrahedral elements. The method discussed in the previous chapter required a very fine mesh, hence in the explicit dynamic solution a very small time step was necessary to ensure a stable process. These two factors i.e. the great number of elements and the very small time step made the

method currently impractical in terms of the computing time involved.

An alternative approach belonging to the second classification group given in 11.1 will be discussed herein. Comparing the experimental response for the vertical deflection of node 3 in the impulsively centrally unloaded dome with the theoretical trace obtained from the analysis (disregarding surrounding air except internal air stiffening) it can be observed that:

1. the theoretical maximum dynamic deflection is about 45% greater than the experimental value.
2. there are small discrepancies in the shape of the response and the long term quasi-static deflections.
3. the theoretically predicted frequency is 5.5 times higher than the experimental value.

The last remark illustrates that the greatest discrepancy results from omitting the influence of surrounding air. As the number of cycles per unit of time can be viewed as depending mainly upon mass and stiffness, these two factors need closer examination.

The stiffness of the membrane was defined experimentally as described in chapter 10. Due to some approximation that Young's modulus remains constant for a certain range of stresses and that Poisson's ratio for dynamic response is the same as for static, small discrepancies may result. They are, however, not expected to be greater than 20-30%

(see figure 10.19 and 10.20 showing the central point deflection trace for the centrally loaded orthotropic dome).

The second factor influencing frequency, namely mass, has been discussed in various publications [34, 99, 100, 204]. It has been concluded that for lightweight structures it is essential that the mass of a structure here a membrane should be increased by the mass of the attached air. According to Jensen [99, 100] the additional terms in the mass matrix for tension structures can be approximately calculated as:

$$m'' = C_m \rho_a a^3 \qquad 12.1$$

where

ρ_a is air density,

a is a typical dimension of the structure, for a dome a can be assumed to be equal to its radius; and

$C_m = 2.7 - 7.5$

For the isotropic lightweight membrane dome, as described in chapter 10.3, which had a radius of 2.36 m, the additional mass from 12.1 will be in the range 43.5 kg to 120.9 kg, which is 44 to 121 times the mass of membrane (mass of membrane is .997 kg). Clearly, in this case, the added mass effect is large. This effect will be increased with size of roof and decreased when a heavier membrane is used. From a very simple investigation (assuming a flat two-dimensional membrane) Irwin et al [97] found that for the Montreal Olympic Stadium, which employed a 180 m x 120 m elliptical membrane roof, the added mass due to vibrating air was approximately 37 times larger than the membrane mass itself.

The above illustrates the importance of including the mass of surrounding air in the dynamic analysis of pneumatic structures. The surrounding air, and especially the enclosed air, should be treated as an intrinsic part of the structure. As methods where internal and external air are modelled by elements may require a great amount of computer time, a simpler approach should be devised where each aspect may be modelled separately and then coupled together in order to obtain the dynamic response. There are at least two main factors which should be taken into account when surrounding air is considered:

1. The stiffening effect of the enclosed air (in volume displacement modes) which, when leakage is negligible, may reduce the maximum dynamic deflection by a factor of 4 (this would depend mainly on internal pressure and an an enclosed volume); and
2. added mass; the importance of which is discussed above.

The first factor which influences both dynamic and static responses was examined, in the manner suggested by Barnes, in chapters 7 and 8. The latter will be discussed in more detail in the present chapter.

The concept of added mass is a familiar one. For example, when a light paddle is dipped into still water and given a rapid acceleration, the resistance to acceleration of the paddle is greatly increased by the water around it. In a similar manner, the force required to accelerate any body immersed in a fluid is greater than it would be in a vacuum.

The additional force is of course required to accelerate portions of the surrounding fluid, but it has been found useful to consider it to be due to an imagined or effective increase in the mass of the body itself, called added mass (or additional, induced, hydrodynamic or aerodynamic mass). The term virtual or apparent mass, as sometimes referred to, is usually taken to include the mass of the body itself as well as the added mass.

The added mass depends on the shape of the body, the nature of its motion, and the density of the fluid. From various experiments, and later by mathematical modelling [26], it has been found that this added mass for a sphere is approximately equal to one half of the mass of the fluid displaced by the body.

Most calculations of added mass have been made using ideal or potential flow theory, neglecting the effects of friction and of compressibility. The usefulness and applicability of such an approximate approach was illustrated in the context of static wind loading on a rigid shell in chapter 5. For the sphere the added mass calculated under the assumption of potential flow is then exactly one half of the mass of the displaced fluid. In many cases, however, the flow near the body in a real fluid will not be laminar with an attached thin boundary layer as assumed in potential flow, but highly turbulent, and given sufficient time, vortices will be formed and cast off into a turbulent wake. Fortunately ideal fluid theory can still be expected to give a

reasonably accurate description of what happens during the initial stages of accelerated motion, and also for small amplitude oscillating motion, before the vortices have had time to form [35].

The usual method for computing added mass in an ideal fluid is to calculate the kinetic energy in an infinite volume at rest at infinity, due to the uniform motion through it of the body in question [147]. The kinetic energy of the fluid, KE_F, is given by [147]:

$$KE_F = \int_V \rho\, q^2\, d\tau \qquad 12.2$$

taken throughout the volume V occupied by the fluid, where

ρ is the fluid density, and

q is the fluid velocity.

When the motion is irrotational,

$$q = -\nabla\phi \qquad 12.3$$

(ϕ is the velocity potential), and therefore by Green's theorem, if ϕ is single valued and since $\nabla^2 \phi = 0$, [147] then:

$$KE_F = \tfrac{1}{2}\rho \int_V (\nabla\phi)\,(\nabla\phi)\, d\tau = -\tfrac{1}{2}\rho \int_S \phi \frac{\partial\phi}{\partial n}\, ds \qquad 12.4$$

where R.H. integral is taken over the bounding surface of the liquid and dn denotes an element or normal directed into the liquid.

This result has a simple physical interpretation. Since the actual motion could be started from rest by the application of an impulsive pressure $\rho\phi$, and since $-\partial\phi/\partial n$ is the velocity of the liquid normal to the boundary,

$\rho\phi\,\delta s * (-\tfrac{1}{2}\,\partial\phi/\partial n)$ is the work done by the impulsive

pressure on the element δs in accordance with the following dynamic theorem:

The work done by an impulse is equal to the product of the impulse and half the sum of the components in the direction of the impulse of the initial and final velocities of the point at which it is applied. The surface integral therefore represents the work done by the impulsive pressure in starting the motion from rest.

The added mass may be viewed [97, 35] as a mass of air, attached to a body, with the kinetic energy given by equation 12.4. Therefore, the fluid kinetic energy may be expressed also as:

$$KE_F = \tfrac{1}{2} w_m^2 \times m_{add} = \tfrac{1}{2} KE_B \times C_{am} \qquad 12.5$$

where

w_m is a typical or representative velocity of the body,

m_{add} is the added mass,

KE_B is the kinetic energy of the body,

C_{am} is the added mass coefficient, and

$$C_{am} = \frac{m_{add}}{m_b} = \frac{KE_F}{KE_B} \qquad 12.6$$

here m_b is the mass of the body.

The ratio of kinetic energies: fluid to body, is a measure of the ratio of the added mass of the attached air to the membrane total mass.

12.2 Numerical scheme to account for added mass

12.2.1 General assumptions

The problem of added mass effects on the dynamic response of air-supported structures will be discussed under the assumption of potential flow of an irrotational inviscid and incompressible fluid. The implications of these simplifications and the governing equations were given in chapter 5. Here, only the most important facts will be recalled in order to emphasise the investigation of this chapter.

The main advantage of potential flow theory is that velocity may be determined independently of the pressure, and the problem of fluid mechanics is reduced to solving the Laplace equation:

$$\nabla^2 \phi = 0 \qquad 12.7$$

subject to the boundary conditions on a body [90]

$$\bar{V} \cdot \bar{n}|_S = F \qquad 12.8$$

where

$\bar{V}$ is the velocity field

$\bar{n}$ is the unit outward vector on the body S, and

F is a known function expressing normal velocity of a body in terms of a position on the body; and conditions off the body must also be satisfied.

The velocity field $\bar{V}$ is expressed as the sum of two velocities: velocity of the onset flow, $\bar{V}_\infty$, and the disturbance velocity $\bar{u}$ i.e.

$$\bar{V} = \bar{V}_\infty + \bar{u} \qquad 12.9$$

The velocity $\bar{u}$ is assumed to be irrotational and may be expressed as:

$$\bar{u} = -\text{grad } \emptyset \qquad 12.10$$

If the approaching velocity $\bar{V}_\infty = 0$, then the boundary condition on a body, equation 12.8, reduces to:

$$\frac{\partial \emptyset}{\partial n}\Big|_S = F \qquad 12.11$$

Under the general assumptions outlined above(for details see chapter 5, [116] or [147]) Green's third identity shows that any solution of equation 12.7 may be expressed as the perturbation potential induced by a combination of source singularities of strength δ and doublet singularities of strength μ distributed on the boundary of a body. Further, it can be proven (chapter 5, [116] or [147]) that the source and doublet strength per unit area are equal respectively to differences across the boundaries in: the components of the local fluid velocity normal to the surfaces and the local velocity potential.

12.2.2 Added mass of a diaphragm embedded in a rigid bounding surface

Consider a diaphragm rectangular in plan, a x b, embedded in a rigid surface so that during motion there is no mixing of air between the top and bottom layers. Assume also that the diaphragm undergoes only small normal displacement out of its plane and that the normal velocity distribution is known.

For an infinitesimally thin body, like the membrane under consideration, only one type of singularity is required to model its movement [116]. The decision on whether doublets or sources are to be employed should be based on the boundary conditions on and off the body. Continuity in normal velocity across the membrane suggests using doublets but the requirements of not mixing air between the top and bottom layers, indicates that sources will be better suited. For the purpose of calculating the kinetic energy, which depends on the square of velocities, the direction of normal velocity is irrelevant. Hence, efforts should be concentrated on modelling its value both on and off the body. In such circumstances, in order to find the added mass, the movement of the diaphragm will be better represented by source distributions along the membrane in the plane $z = 0$ as shown in figure 12.1.

The diagram of figure 12.1c can be viewed as representing a double diaphragm; the upper sheet models the top surface of the real membrane (of figure 12.1b) where the attached air moves with the same velocity as the membrane; and the lower sheet approximates the bottom side of the real membrane. In the model with source distributions the underside air moves in the opposite direction to the upper side which is in the reverse direction as in a real model. But, as explained earlier, for the purpose of solving this particular problem in the potential incompressible flow regime, this is not of any significant importance.

Sources may be distributed in a variety of different ways. For the purposes of numerical analysis the most obvious approach, similar to that used in chapter 5 with respect to vortices, would be to divide a diaphragm into rectangular elements with a separate singularity on each of the panels. Following Campbell's approach [35], a single source is placed in the centre of each panel.

In three-dimensional space, the potential $\emptyset$ at a point (x, y, z) due to a source Q at the origin is [116]:

$$\emptyset = \frac{Q}{4\pi r} \quad \text{where} \quad r^2 = x^2 + y^2 + z^2 \qquad 12.12$$

and the velocity w in the Z direction is [116]:

$$w = -\frac{\partial \emptyset}{\partial z} = \frac{\emptyset}{4\pi} \frac{z}{(x^2 + y^2 + z^2)^{3/2}} \qquad 12.13$$

For a source in the plane z = 0, the flow out of this plane vanishes everywhere except at the location of Q source. Taken over a small circle of radius ε, centred at the origin, the upward average velocity, w_{av} is [35]:

$$w_{av} = \frac{1}{\pi \varepsilon^2} \cdot \frac{Q}{4\pi} \lim_{z \to 0^+} \int_0^{\varepsilon} \frac{z}{(\omega^2 + z^2)^{3/2}} 2\pi\omega \, d\omega =$$

$$= \frac{1}{\pi\varepsilon^2} \frac{Q}{2} \lim_{z \to 0^+} \frac{-z}{(\omega^2 + z^2)^{1/2}} \Bigg|_0^{\varepsilon} = \frac{1}{\pi\varepsilon^2} \frac{Q}{2} \qquad 12.14$$

For $z \to 0^+$, the value of w_{av} has the opposite sign since half of the flux from the source flows out of the z plane, and half flows downward. Similarly, for a source Q centred in a rectangular element k (s x h, (see figure 12.1a)) in the plane z:

$$w_{avk} = \frac{1}{sh} \cdot \frac{Q_k}{2} \qquad 12.15$$

In order to calculate the kinetic energy of the fluid (equation 12.4), an additional quantity, the average potential over one elemental area due to a source located at the centre of another, is needed.

The average potential over the area of an element i due to a source at x_j, y_j can be calculated as [35]:

$$(\phi_{av})_{ij} = \frac{1}{(sh)_i} \frac{Q_j}{4\pi} \int_0^{x_F} \left(\int_0^{y_F} \frac{dy}{\sqrt{x^2 + y^2}} \right) dx =$$

$$= \frac{1}{(sh)_i} \frac{Q_j}{4\pi} \int_0^{x_F} \ln \left(\frac{y_F + \sqrt{x^2 + y_F^2}}{x} \right) dx = \frac{1}{(sh)_i} Q_j C_{ij} \qquad 12.16$$

The integral of 12.16 can be calculated numerically.

The total average potential of element, i, is:

$$(\phi_{av})_i = \frac{1}{(sh)_i} \sum_{j=1}^{n} Q_j C_{ij} \qquad 12.17$$

where n is the number of element, and Q_j is obtained from

$$Q_j = 2 \times w_{avj} \times (sh)_j \qquad 12.18$$

To calculate the added mass coefficient (equation 12.6) the ratio of the kinetic energy of the fluid to that of the body is required. The fundamental equation of fluid kinetic energy, equation 12.4, may be transformed into [35]:

$$KE_F = \rho_a \int_s \int_{z^+} \phi_s \, w_s \, dx \, dy \qquad 12.19$$

Since ϕ and $\frac{\partial \phi}{\partial n}$ are both symmetrical with respect to z for

the source distribution, instead of integration over both sides (as in equation 12.4) the summation is limited to one side and the result is multiplied by two. When the number of elements, n, is adequately large the integration can be substituted by summation and equation 12.19 take the form:

$$KE_F = \rho_a \sum_{i=1}^{n} ((\emptyset_{av})_i \ (w_{av})_i \ (sh)_i) \qquad 12.20$$

Similarly the kinetic energy of the diaphragm can be expressed as:

$$KE_b = \tfrac{1}{2} \rho_d \sum_{i=1}^{n} (w_{av})_i^2 \ x \ (sh)_i) \ x \ th \qquad 12.21$$

$$\text{or} \quad = \tfrac{1}{2} w_m^2 \ x \ M_m$$

where

ρ_d is the density of the diaphragm material,

th is the diaphragm thickness,

w_m is a typical or representative velocity of the membrane and

M_m is the total mass of the membrane.

Campbell in [35] investigated the discrete source distribution method for various velocities; in each case convergence being obtained. In order to gain more confidence the three-dimensional results with a/b = 100 (length to width of diaphragms) were extrapolated to the limit, n ->∞, and compared with two-dimensional theoretical values. The numerical results were all accurate to three significant figures. When the discrete source method results were compared for different length to width ratios against the Chebyshev polynomial method, the results were all about one percent lower.

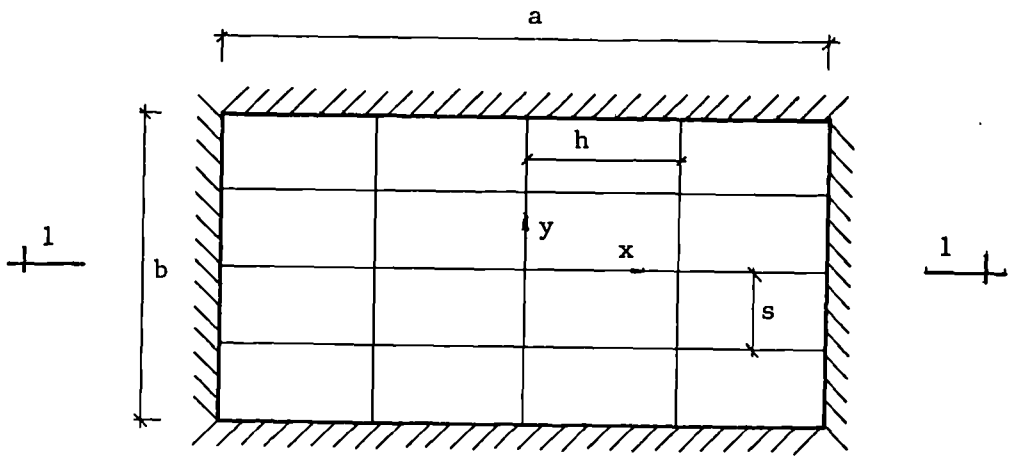

a.

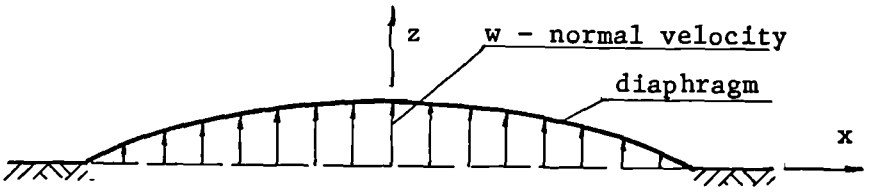

b.

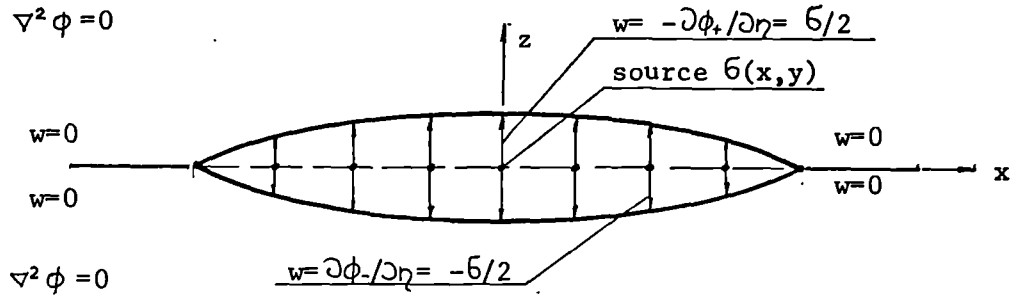

c.

Figure 12.1

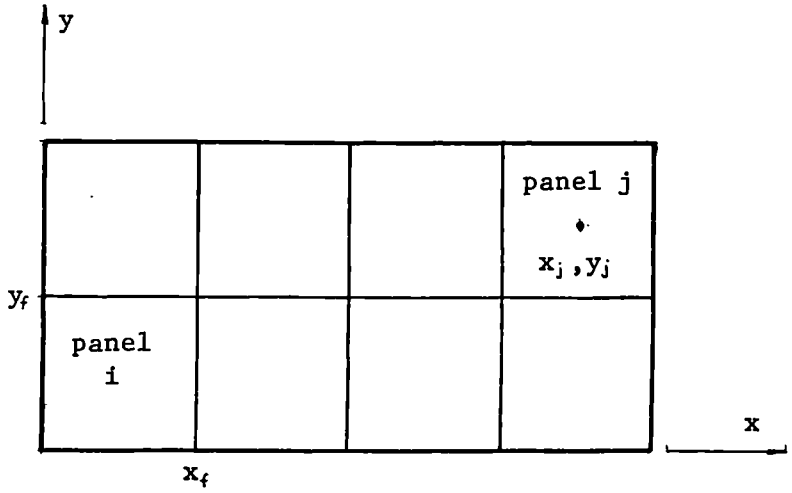

Figure 12.2

12.2.3 Modelling the shallow pneumatic dome

The discrete sources approach discussed in 12.2.2, in the context of a diaphragm embedded in a rigid surface, seems to be particularly well suited to deal with added mass effects for the dynamic response of a shallow pneumatic dome.

The isotropic lightweight centrally unloaded dome, described in chapter 10 and employed as an example for internal air modelling in chapter 11, is a shallow structure; the ratio of maximum dynamic height to span is less than 1:20. The normal displacements, experimental or theoretical are also small when compared with the dome diameter. Therefore, it seems to be reasonable to assume that the dome is flat for the purpose of calculating average potential (in equation 12.12 when $x >> z$ and $y >> z$, r^2 can be assumed to be approximately equal to $x^2 + y^2$).

The solution of Laplace's equation will be obtained by direct application of Green's third identity for a distribution of sources subject to the following boundary conditions:

1. on the body, defined by normal velocities on the dome, and
2. off the body; condition of no mixing of the air between the two sides of the membrane (see figure 12.3b).

The second condition is self-satisfied by choosing the right type of singularities (see figure 12.3c).

Taking advantage of full axisymmetry, the dome is divided into trapezoidal and triangular elements as shown in figure

12.3a and sources are positioned in the centre of each element. The kinetic energies of the fluid and membrane are given by equations 12.20 and 12.21 in terms of average potential velocities, areas, and fluid and membrane densities. The approach discussed here is intended to be coupled with the explicit dynamic analysis of chapter 9. During the analysis the nodal coordinates and velocities are known at the end of each time step, t, and at $t=t-\Delta t/2$ respectively. Due to the fact that the division of the dome is uniform and that the velocities and hence the strength of sources is a function of radius, some of the calculations, such as determining velocities at element centres, are performed only for elements in a single slice of the dome (see shadow area of figure 12.3a). For each of these panels, the area A_i and the centre in the x, y plane are found. The velocities w_{avi} at element centres are then obtained from the normal nodal velocities assuming a linear variation. It should be noted that velocities in the explicit dynamic analysis are calculated without the assumption that the dome is shallow.

By applying equation 12.15 the strength of the source at panel j is:

$$Q_j = w_{avj} \cdot 2. \cdot A_j \qquad 12.22$$

The average potential over an area of element i, due to a source at panel j is calculated as follows (see figure 12.3a):

$$\phi_{avij} = \frac{Q_j}{4\pi A_i} \int_{x_{Si}}^{x_{Fi}} \int_{-x\tan\alpha}^{x\tan\alpha} \frac{dy}{((x-x_j)^2 + (y-y_j)^2)^{\frac{1}{2}}} dx =$$

$$= \frac{Q_j}{4\pi A_i} \int_{x_{Si}}^{x_{Fi}} \ln \frac{|x\text{tg}\alpha - y_j| + \sqrt{(x-x_j)^2 + (x\text{tg}\alpha - y_j)^2}}{|x\text{tg}\alpha + y_j| + \sqrt{(x-x_j)^2 + (x\text{tg}\alpha + y_j)^2}} \, dx$$

$$= \frac{Q_j}{A_i} C_{ij} \qquad 12.23$$

When an element j belongs to the shadow area of figure 12.3a, equation 12.23 is simplified to:

$$\phi_{avij} = \frac{Q_j}{2\pi A_i} \int_{x_{Si}}^{x_{Fi}} \ln \frac{|x\tan\alpha| + \sqrt{(x-x_j)^2 + (x\tan\alpha)^2}}{|x-x_j|} \, dx = \frac{Qj}{Ai} Cij \qquad 12.23a$$

The coordinates of the centre of a panel lying outside the shadow area can be obtained from the shadow area values as: (see figure 12.3a)

$$x_j = \cos(n\alpha) \quad x_j'$$
$$Y_i = \sin(n\alpha) \quad x_j' \qquad 12.24$$

The total average potential of element is obtained by summing the contributions from all panels:

$$(\phi_{av})_i = \frac{1}{Ai} \sum_{j=1}^{n} Q_j C_{ij} \qquad 12.25$$

Due to axisymmetry the average potential is calculated only for panels of the shadow area. Coefficients C_{ij} for which j denotes an element of COB (see figure 12.3a) section of the circle are approximately the same as those from section, DOA. Therefore, only one set is determined and then multiplied by two. And finally, the kinetic energy of fluid is found from equations 12.20 and 12.25

$$KE_F = 2 \quad \rho_{air} \sum_{i=1}^{n_s} \left(\sum_{j=1}^{n} w_{avj} A_j C_{ij} \right) \quad w_{avi} \qquad 12.26$$

where

n_s is the number of elements in the shadow area of figure 12.3a,

and the kinetic energy of the dome is calculated from 12.21 as:

$$KE_D = \tfrac{1}{2}\ \rho d \sum_{n=1}^{n_s} (w_{avi})^2 \quad Ai \qquad 12.27$$

where ρd is the mass of the dome membrane per unit area.

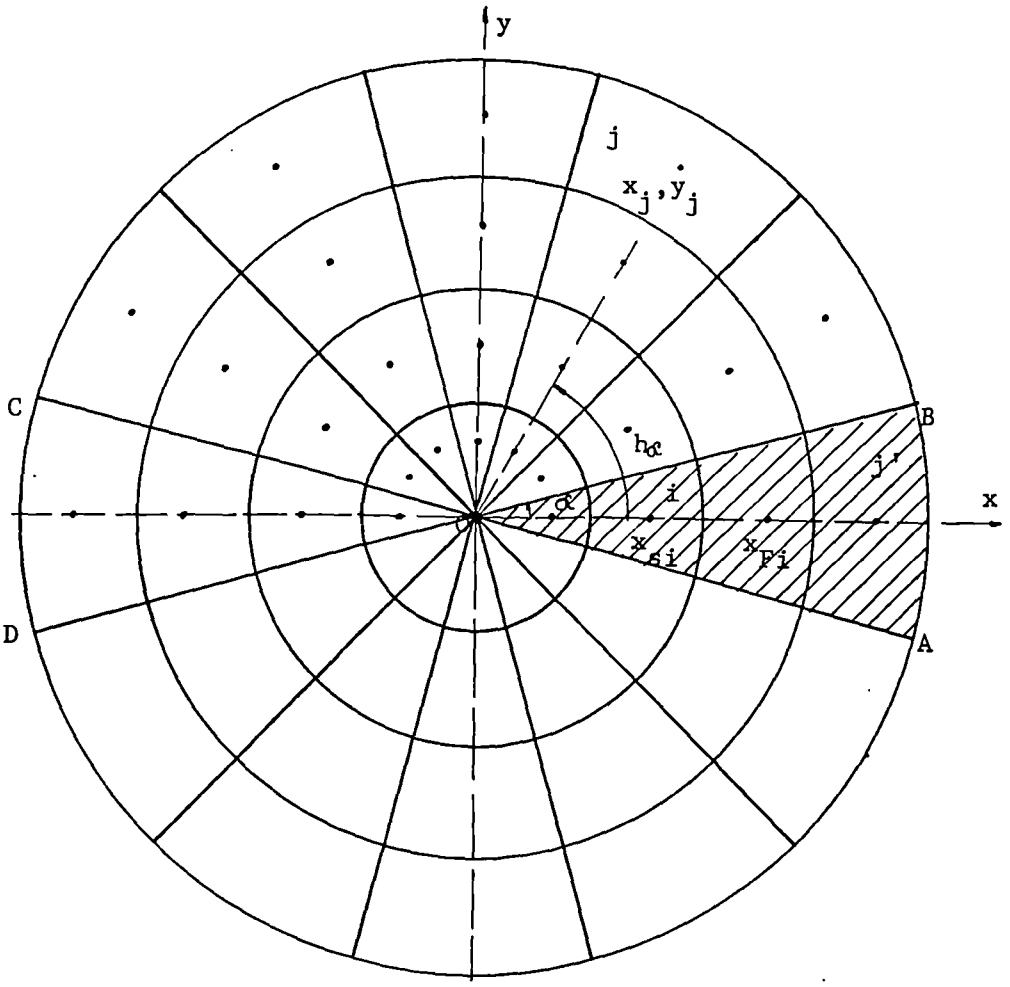

a.plan

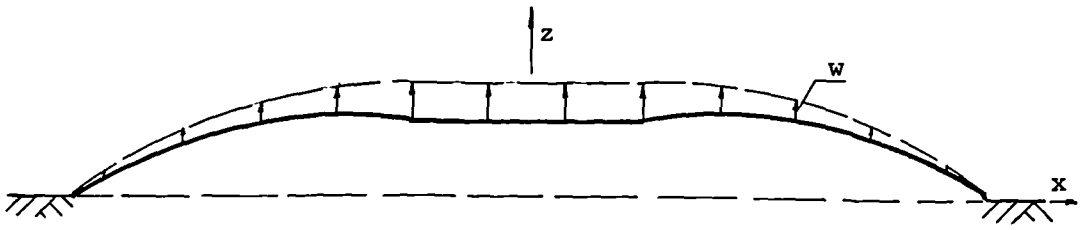

b.section

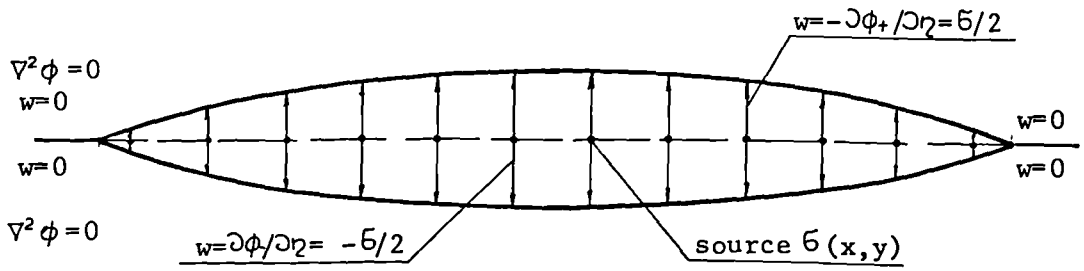

c.distribution of sources

Figure 12.3

12.2.4 Iteration scheme for explicit dynamic analysis of the pneumatic dome with added air mass.

In general, including the calculation of added air mass in the explicit dynamic analysis scheme should require an additional procedure at each time step in which, from nodal velocities, coordinates and relative density, the mass coefficients C_{am} are calculated. Then, under the assumption that the attached air is spread uniformly on the top and bottom surface of the dome, the coefficient C_{am} can be translated into nodal masses and added to the membrane nodal masses, m_n, to give the total nodal mass, m_t

$$m_t = m_n (1 + C_{am}) \quad . \qquad 12.28$$

This approach would result in an enormous amount of operations since the average potential over an elementary area of any panel is calculated due to all sources by numerical integration (see figure 12.23).

Both kinetic energies (equations 12.26 and 12.27) are expressed directly or indirectly by two types of quantities: the first depending purely on geometry in the x, y plane: specifically the areas and centres of elements; and the second depending on nodal coordinates and velocities.

The first group of parameters is calculated under the assumption that the dome is shallow. During the dynamic analysis of chapter 9 it was noticed that the x, y displacements (in the radial direction) are much smaller than in the z direction, and they are almost negligible in comparison with the overall dimensions of the dome.

Therefore, the quantities of the first group can be calculated only once and based on starting geometry.

In almost all structural dynamic analyses, including the analysis of chapter 9, the problem is formulated from the Lagrangian, historical point of view; attention being fixed on the structural elements and their motion. In the case under consideration, where at each time step a new value of additional mass is obtained, the whole scheme should be set in such a way that the behaviour of any fluid particle is clearly described. In order to account for the above, the recurrence equation for velocity

$$V_{ix}^{t+\Delta t/2} = \frac{\Delta t}{m_i} R_{ix}^{t} + V_{ix}^{t-\Delta t/2} \qquad 12.29$$

will be derived from Newton's second law written in a vector form in terms of the impulse provided by external and internal forces, R, and the resulting change of the linear momentum of the system:

$$\bar{R}\, dt = d\,(m\bar{v}) \qquad 12.30$$

Equation 12.30 in central finite difference form, for any node i in direction x at time t, is:

$$\Delta t R_{ix}^{t} = m^{t+\Delta t/2}\, V_{ix}^{t+\Delta t/2} - m^{t-\Delta t/2}\, V_{ix}^{t-\Delta t/2} \qquad 12.31$$

Rearranging equation 12.31 gives the recurrence equation for velocities:

$$V_{ix}^{t+\Delta t/2} = \frac{\Delta t\, R_{ix}^{t} + m^{t-\Delta t/2}\, V_{ix}^{t-\Delta t/2}}{m^{t+\Delta t/2}} \qquad 12.32$$

If a mass at $t=t+\Delta t/2$, m_1, is greater than m_2, the mass at $t=t-\Delta t/2$, equation 12.32 implies that the part of the mass equal to m_1-m_2 had zero velocity at $t=t-\Delta t/2$, therefore, its momentum at that time was zero.

In the central finite difference form of an explicit dynamic analysis, velocities are calculated at the middle of each time step, but coordinates and forces at the end/beginning of time steps.

Assume that at time $t-\Delta t/2$ the velocity of any node, i, is known. The added mass coefficient (as the ratio of equations 12.26 and 12.27) and hence the virtual mass (equation 12.28) is determined from these values to be say m_1. Then the updated velocity, $v^{t+\Delta t/2}$, is found from equation 12.32 (masses at $t-\Delta t/2$ and $t+\Delta t/2$ are the same) taking m_i to be $m_i^{t-\Delta t/2}$. Then new added masses, $m^{t+\Delta t/2}$ are calculated together with updated velocities $v^{t+3\Delta t/2}$. This procedure would result in accumulated errors due to the fact that the linear momentum at any time, $t+\Delta t/2$, would have two different values depending upon whether equation 12.32 is set up for A or B time step, as the masses differ (see figure 12.4).

In order to alleviate the problem the following procedure to be included at each step, is suggested:

1. At the end of the time step t to $t+\Delta t$, the forces R_i^t, masses $m_i^{t-\Delta t/2}$, velocities $V_i^{t+\Delta t/2}$ and coordinates $X_i^{t+\Delta t}$ are known
2. In a new cycle $t+\Delta t$ to $t+2\Delta t$ calculate new forces $R^{t+\Delta t}$ and new masses $m^{t+\Delta t/2}$
3. reset coordinates to X_i^t

$$X_i^t = X_i^{t+\Delta t} - \Delta t \cdot V_i^{t+\Delta t/2}$$

and velocities to $V_i^{t-\Delta t/2}$ by employing equation 12.29

$$V_i^{t-\Delta t/2} = V_i^{t+\Delta t/2} - R_i^t \cdot \Delta t/m_i^{t-\Delta t/2}$$

4. find new values for $V_i^{t+\Delta t/2}$ from equation 12.32 and then updated coordinates $X_i^{t+\Delta t}$

5. assuming that mass at $t = t + \frac{3}{2}\Delta t$ is $m^{t+\Delta t/2}$ calculate $V_i^{t+3\Delta t/2}$ from $R^{t+\Delta t}$ and finally $X^{t+2\Delta t}$.

It should be noted that the above scheme may still result in small errors due to the fact that the added mass $m^{t+\Delta t/2}$ is calculated from the original velocities $V_i^{t+\Delta t/2}$ from step 1, but the actual velocities used for further analysis are found from equations given in steps 3 and 4. The procedure, where necessary, may be further improved by determining a new value of added mass after step 4 and repeating the calculations of steps 3 and 4.

The additional procedures which are to be inserted into the explicit dynamic analysis of chapter 9 to account for added mass of the attached air, can be summarized as follows:

1. calculate the areas, centres and potential coefficients C_{ij} (equation 12.23) for all elements in the shadow area of figure 12.3a.
2. in the main loop :

   a) calculate fluid and membrane kinetic energies (equations 12.26 and 12.27), hence the added mass coefficients (equation 12.6, and finally the total nodal masses equation 12.28);

   b) substitute the main recurrence equation for velocities and coordinates (equations 9.3 and 9.5) by the scheme accounting for varying masses, as given above.

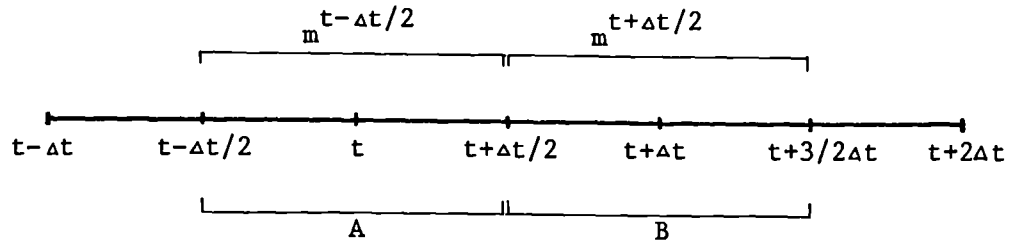

Figure 12.4

12.3 Numerical dynamic analysis of impulsively unloaded dome

The isotropic dome impulsively centrally unloaded, as described in chapter 10 and referred to in chapters 9 and 11, is once more used as an example for a new version of the explicit dynamic analysis scheme. The basic difference between the dynamic analysis of chapter 9 and the present is that the latter accounts for added mass due to surrounding air.

The dome under consideration is fully axisymmetric (shape of the structural and loading pattern), hence the obvious way of dividing the structure into building elements is along the radial and circumferential directions. For the purpose of structural modelling only a single 10° cheese-slice, with suitable boundary conditions is used to represent the membrane. Fluid dynamics aspects require account to be taken of the whole structure as far as the influence of sources on the average potential of a single cheese slice is concerned. The kinetic energy ratio can however be obtained for a single slice only. The divisions for these two purposes can differ, although the main pattern remains the same, as it is dictated by axisymmetry (see figures 9.10 of chapter 9 and 12.3a). When the same angle is employed for the division in the circumferential direction one trapezoidal element in the fluid dynamic idealization corresponds to two triangular elements in the structural division. For convenience, accuracy and computer efficiency the number of divisions in the radial direction should be kept the same.

The explicit structural dynamic analysis is not very sensitive to size of elements; the results for a 10° slice with 8 and 16 double elements (except for a single first one) do not show great differences (see figures 9.9 and 9.10 of chapter 9). The discrete source method, in which singularities are placed in the centre of every element, and where numerical integration is used to obtain potential coefficients (equation 12.23), may be dependent on three types of divisions:

1. division for purpose of numerical integration,
2. division in the circumferential direction. The number of slices will have to be chosen with respect to the largest element on the peripheral of the dome. However, although the strength of sources in the circumferential direction is constant, because of the use of single point singularities the size of panels should be reasonably small.
3. division in the radial direction; this seems to be of greater importance as the source strength, following the normal velocities, varies in this direction.

Numerical integration was performed using the simple Trapezium rule. The number of divisions was investigated outside the program. It has been calculated that potential coefficients C_{ij} for $i \neq j$ can be calculated by dividing the distance x_{Fi} to x_{si} (see figure 12.3a) into 12 segments (for 24 segments C_{ij} differ by less than 1%). When i=j the most suitable division was found to be 20 segments.

The 10° slice of the dome used for structural analysis, was divided uniformly into:

mem1 - 15 triangular elements (see figure 9.10a of chapter 9)

and

mem2 - 31 triangular elements (see figure 9.10b of chapter 9)

For each type of structural membrane idealization and (hence division in the radial direction), in order to obtain triangular and trapezoidal panels for the discrete source method, two cases for division in the circumferential direction were considered:

ang1 - to give 10° slice, and

ang2 - to give 5° slice,

The program (in Fortran 77 on a Gould PN 6000) was thus run for four different idealizations:

Type 1 - mem1 + ang1

Type 2 - mem1 + ang2

Type 3 - mem2 + ang1

Type 4 - mem2 + and2

Results for the vertical deflection during time (t=0 to 3 sec) of a node at a horizontal distance of .585 m from the centre of the dome are shown in figure 12.5. Added mass coefficients (the ratio of the added mass of attached air to that of the membrane mass) were calculated as an average value for the first few cycles and the frequencies obtained from the first few oscillations are tabulated and presented in figure 12.7.

The following conclusions can be drawn:

1. doubling the division in the circumferential direction causes only small differences between mem1 and mem2. For the first four cycles the changes in average added mass are within 1% and discrepancies in deflections are not visible. The smaller elements of the 5° slice tend to produce a more stable solution.
2. The type of division in the radial direction has a more profound effect on results, especially after the first few cycles. The finer mesh produces a deflection trace which closely resembles the experimental response, and the solution is more stable. The differences in added masses and frequencies between divisions type 2 and 4 based on the first cycle are 2.5%. As expected, these differences are higher than for the circumferential division.
3. The stability of solution is influenced by the way in which added mass calculations are implemented into the explicit dynamic analysis (see 12.2.4), and the size of elements used in an idealization, especially in the radial direction.

The theoretical trace when superimposed on the experimental trace (see figure 12.6) shows a great improvement in frequency when compared with the theoretical analysis of chapter 9. The theoretical frequency obtained from the analysis of this chapter was 2.5, that based on an analysis disregarding added mass effects (chapter 9) was 16.1, and the experimental value was 3.7. The increase in computer

time caused by adding the procedure to account for the added mass of the surrounding air is only 20%. The discrepancies in the prediction of frequency are reduced from 550% to 50%. On the other hand, those figures explain why further refinement of the mesh in the theoretical modelling of the dome by the method of this chapter has not been carried out, as this would improve the frequency by order of less than 1%.

When the added masses calculated from equation 12.1 given by Jensen [99, 100] are employed the resulting range of frequencies for the dome is 2.4 to 1.45, which is 4% to 40% lower than the experimental values but closer than the theoretical values obtained in this chapter. The main disadvantage of equation 12.1 is that it is expressed in terms of a^3 where 'a' is a dimension of the structure. For some complex airhouses it may be rather difficult to decide upon which dimension should be used for 'a'. The discrete source method combined with explicit dynamic analysis is more versatile; the added mass and the frequency can be determined for any pneumatic shallow structure. There is no other restriction on shape.

Bearing in mind the crudeness of the model to simulate the air flow (potential flow, incompressibility and assuming that the dome is shallow), the results are rather good. Compressibility of the internal air, expressed as air stiffening is added to the analysis separately as an overall effect based on total volume changes. Apart from the

discrepancies already discussed quite noticeable differences also exist between theoretically predicted and experimental long term deflections and rates of decay.

The former seems to be mainly caused by the dynamic properties of membrane material assumed in the theoretical analysis. During the experiment, the dome was loaded and then after time had elapsed during which viscous strains took place the structure was dynamically unloaded. The membrane dynamic properties were established during tests in which load was suddenly released; the procedure not allowing for accumulation of viscous strains. The crudeness of a single Kelvin model could have been another reason. This simple model cannot precisely represent the dynamic behaviour of material like this polythene sheeting.

The discrepancy in the rate of decay may be explained by the limitation of potential flow analysis which does not predict and account for the separation of flow which takes place after the first few cycles of vibration. Therefore, the mass of the attached air is then overestimated by the analysis thus causing too high level of damping.

It should be emphasised that the combined fluid structure model presented in this chapter is only an approximation as:

1. The membrane and surrounding air are analysed separately. The influence of air inserted into the structural analysis at each time step is assumed to be uniform throughout the dome and is expressed as an

increase or decrease in the internal pressure (the difference between internal and external pressure) and the added mass due to the attached air.

2. The "sloshing" (or momentum) effect of the internal air, and aerodynamic damping are not accounted for. The former factor may have a profound effect on the response of a very large scale air-supported structure. This aspect was especially discernible during tests on the asymmetrically unloaded dome, for which a theoretical prediction including added mass has not been conducted since it was felt that disregarding air momentum in the theoretical analysis would not lead to meaningful results (see chapter 10).

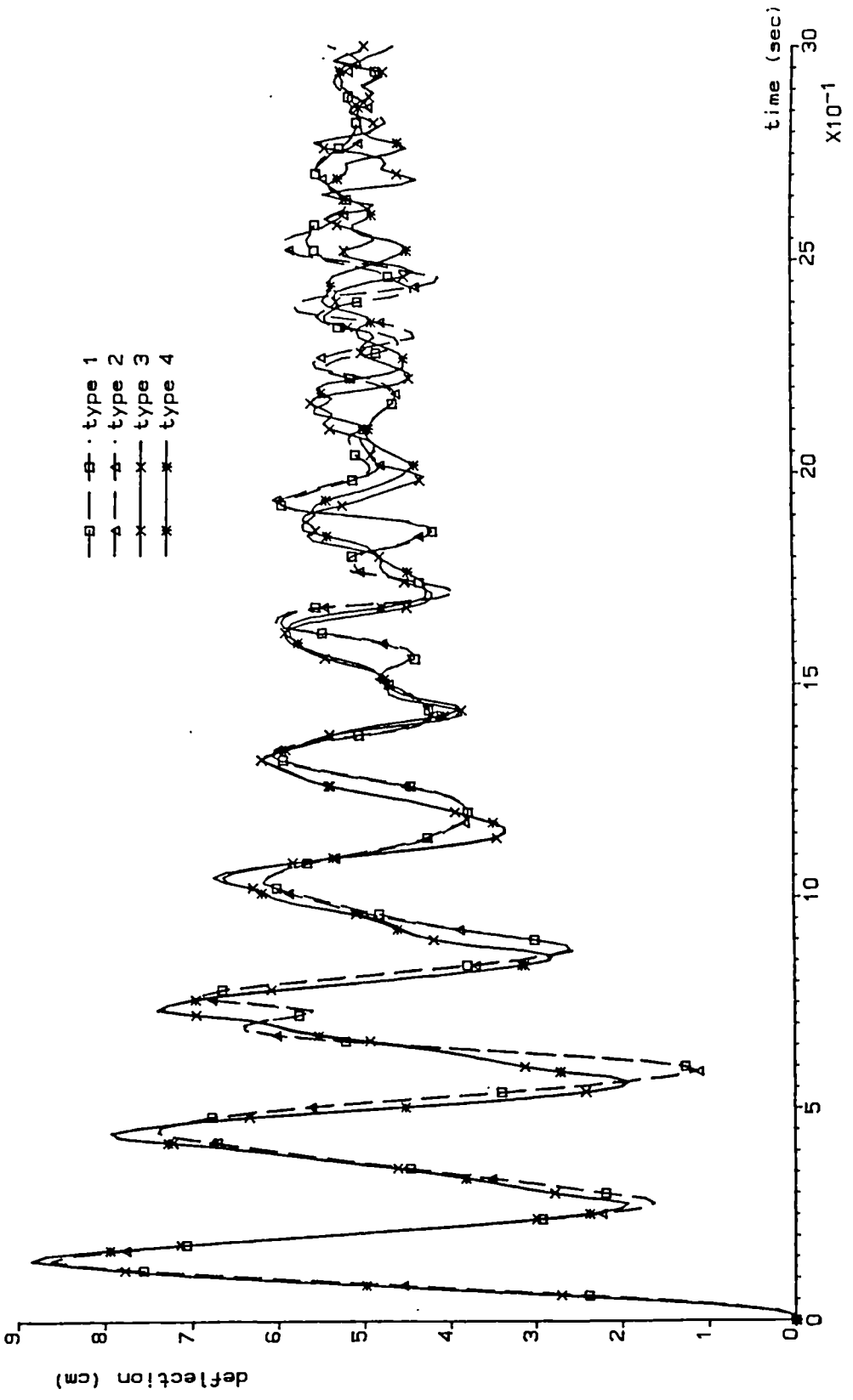

Figure 12.5 Theoretical deflection decay of centrally unloaded dome

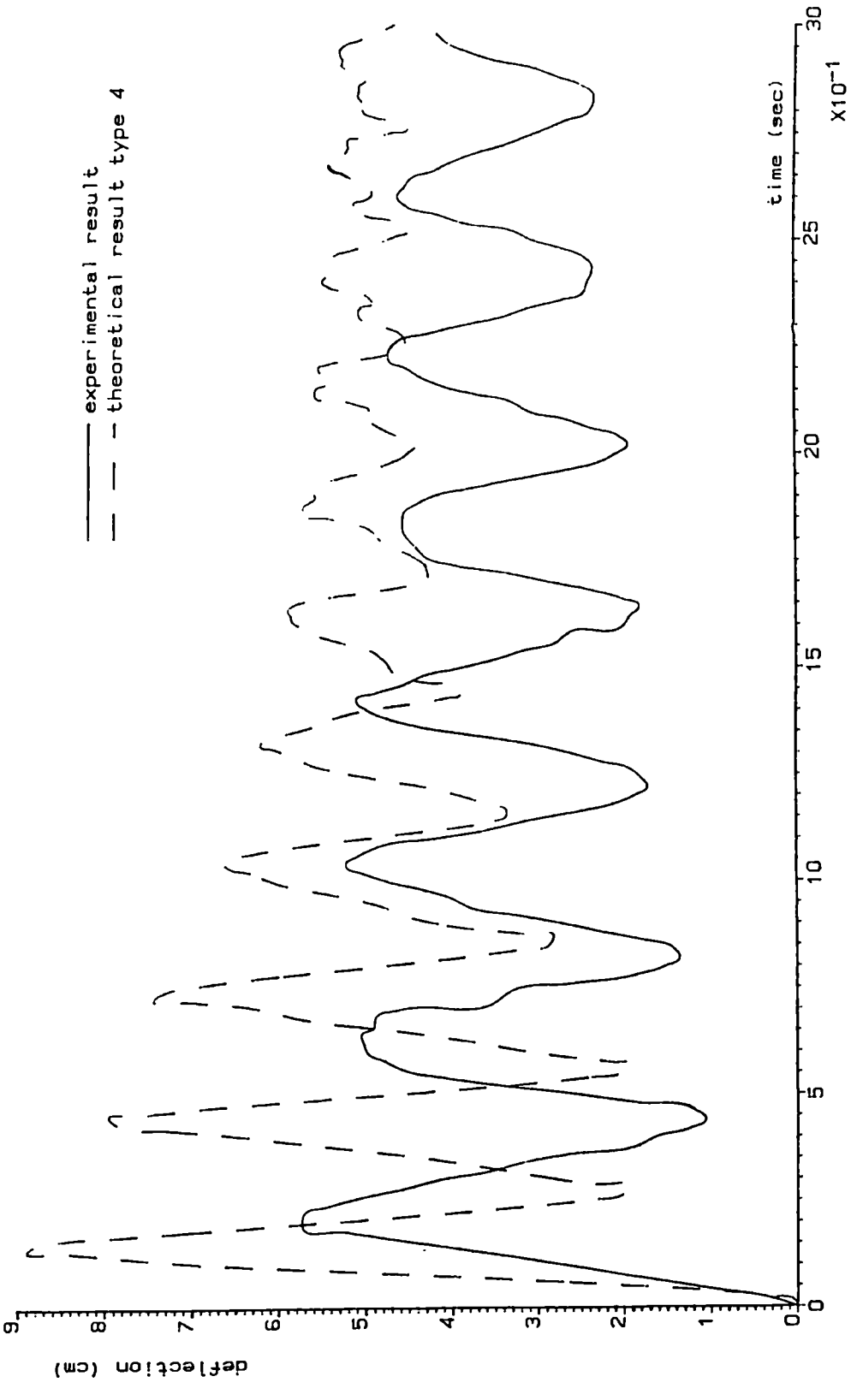

Figure 12.6 Deflection decay of centrally unloaded dome

Type of division / nr of cycle	Type 1		Type 2		Type 3		Type 4	
	added mass coefficient	frequency	added mass coefficient	frequency	added mass coefficient	frequency	added mass coefficient	frequency
1	19.01	3.6	18.93	3.6	18.63	3.7	18.48	3.7
2	19.16	3.2	19.03	3.2	19.12	3.5	18.98	3.5
3	17.91	3.5	17.76	3.5	17.31	3.4	17.30	3.4
4	18.87	3.1	18.89	3.1	17.92	3.4	18.05	3.3
5					15.60	3.6	16.43	3.5
6					15.78	3.5	17.06	3.8
7					14.85	3.6	18.24	3.3

Figure 12.7

CHAPTER 13

Summary, conclusions and lines of further research

This thesis has been concerned with examining problems related to the dynamic response of shallow, long span air-supported structures subject to wind loading. Wind loading on pneumatic structures is a two-domain problem (fluid - structure) with strong interactions between inertial elastic and aerodynamic forces.

In general, engineering problems can be solved by different approaches: by building an appropriately scaled model and testing it, by theoretical analysis, or by a combination of tests and analyses. For the problem under consideration, as discussed throughout this thesis, no rigorous theoretical analysis seems feasible at the present time; nor can wind-tunnel tests on a scaled model properly represent all relevant phenomena. Therefore, in this thesis attempts have been made to define the structural response of shallow air-supported structures to wind loading by applying approximate numerical methods. The problem was tackled by splitting it into two parts:

1. defining wind loading on a smoothly curved rigid structure by an approximate method (chapters 5 and 6) and
2. predicting the dynamic response of air-supported domes due to suddenly applied loads of known value (chapters 8 to 12).

Finally, it had been intended to couple the two parts by including a theoretical prediction of wind loading in the explicit dynamic analysis scheme for pneumatic structures.

In chapter 5, under the simplifying assumptions of three dimensional steady potential flow of air as an incompressible medium, the theoretical pressure coefficient distributions on an open sided shallow shell roof were obtained. Three versions of the vortex-lattice method differing in singularity distributions were investigated and compared against the experimental wind tunnel test results of chapter 6. The modified Hedman method with horse-shoe vortices in the plane $z = 0$, and boundary conditions of tangential flow applied on the body of the shell, yielded the best results.

The wind tunnel tests described in chapter 6 were conducted on a thin, rigid eliptic paraboloid shell subject to two flow conditions:

a) in a uniform flow, and

b) in the thick turbulent boundary layer simulating a terrain covered uniformly by small obstacles representing a residential suburb, small town or woodlands.

The theoretical results predicted fairly well the mean pressure distribution on the shell in uniform flow, except on the rearmost part of the model, where separation occurred. In the case of the turbulent boundary layer flow, discrepancies in mean pressure coefficient distributions were of the same order as for uniform flow. However, as the turbulent boundary layer is a much more complicated phenomenon than the theoretical description of potential

flow the above conclusions (for turbulent flow) cannot be generalised without further work.

The vortex-lattice method is very simple, can be applied to almost any shape of structure, and does not require a great number of panels. It is also not very sensitive to the pattern of panels chosen to represent the surface, except that panels behind each other should be in streamwise columns. Therefore, the method can be easily applied to any fluid-structure iteraction scheme either static of quasi-dynamic. In chapter 6 it has been shown, by comparing theoretically obtained pressure coefficient distributions with experimental results, that the greatest discrepancy occurs in the rearmost area. In air-supported houses this part of the structure is very near to a support. Therefore, it is reasonable to expect that, if the method based on potential flow solution is applied to define the static or dynamic response of air-supported structures, the resulting overall shape and membrane stresses are less likely to be affected by potential flow limitations (lack of separation) than inaccurate external pressure distributions.

One of the main weaknesses of the vortex-lattice method, its incapability of predicting the point (line in 3D) of separation and consequent sudden drop in pressure, is in some ways alleviated for the type of air-houses under consideration by their shape. In large shallow pneumatic structures the separation of flow is much further downstream than in high rise domes. Therefore, in spite of its

limitations, the vortex-lattice method may allow meaningful values of pressure coefficients to be obtained for large areas of shallow smoothly curved structures.

The modified Hedman vortex-lattice method was based on a distribution of singularities in the plane z = 0 together with the application of tangential boundary conditions on the surface of the body. Some improvements could have been obtained by more closely modelling the surface of the structure, for example by means of flat or curved panels with double/vortex distributions of varying strength. However, some of these methods may lead to ill-conditioning; as was the case in chapter 5, where the shell was modelled by means of flat panels with quadrilateral vortex-rings of constant strength.

Methods employing more sophisticated element modelling with distributions of singularities of varying strength result in additional mathematical operations. When these are applied to shallow, long span structures it is not likely that a significant improvement in the results can be achieved. A closer modelling could have been justified for high rise domes. On the other hand, for this type of structure, separation of flow may occur much earlier than in shallow structures, which would make the application of potential flow methods unsuitable.

Improvements in the results, especially for turbulent atmospheric boundary layer flow, are likely to be obtained by more accurate modelling of the approaching flow.

Attempts in this direction have been made by Newman and Goland and the results are presented in reference [155] in which the two dimensional turbulent boundary layer was simulated by an inviscid flow of uniform vorticity.

In the lower part of the atmospheric boundary layer, where most structures are situated, the air flow is turbulent and approximating it by potential flow may lead in many cases to great discrepancies. The situations most likely to cause these problems are those where bluff bodies or high rise domes are situated in centres of large cities or other terrains with high obstacles; they are outside the scope of this thesis. Shallow, long span air-supported structures, which are often sited in rather suburban environments may be less prone to extreme turbulence. However, the influence of turbulence or flow separation on their structural response to wind loading should not be disregarded.

In the Appendix to chapter 5 a real flow solution based on the 'SIMPLE' algorithm was examined for a numerical example. As a first approach an open sided thin shell of infinitely long parabolic section, was submerged in a steady uniform flow (the code can also be applied to model simple turbulent boundary layers). The results were compared with the 2D vortex-lattice solution. Cp distributions obtained from both methods tended to approximately the same values. The computer and the human time required to prepare the data and to run the numerical program based on the potential flow theory was, however, only a small fraction of that which

was necessary for obtaining the "real flow" solution. However, it should be borne in mind, that a real flow solution can model the atmospheric boundary layer and is capable of predicting points (line in 3D) of separation.

When a three dimensional problem, the open sided shallow eliptic shell was approximated by the two dimensional case of an infinitely long parabolic shell of the same centreline section shape, the results obtained from the real 2D flow analysis differed from the 3D experimental results much more than the simple 3D potential flow results. In view of the above it is evident that for a 3D structure, which cannot be approximately represented by a 2D model, a simple 3D potential flow solution is likely to yield more accurate pressure distributions than a sophisticated 2D real flow analysis.

Because of the large amount of computing time required for 3D real flow solutions it seems impractical to apply them to tracing the dynamic or quasi-dynamic behaviour of flexible air-supported structures, since pressure distributions would have to be updated at frequent intervals.

The second part of the thesis: chapters 7 to 12 was concerned with the structural response of air-supported structures, with special emphasis on the dynamic response following sudden release of a dynamic loading system. Theoretical numerical predictions of structural response were discussed with direct reference to two fairly large

scale pneumatic domes described in chapter 10. The first test model was constructed using an orthotropic woven fabric and was subject to a suddenly applied central loading. The second dome, built from a very lightweight polythene, was impulsively unloaded, both centrally and asymmetrically.

The dynamic relaxation method with kinetic damping was applied in chapter 8 to the static analysis of pneumatic structures. Structural idealizations depending on the fabric patterning, type of loading and kind of membrane materials were examined in the context of the two air-supported domes. The numerical examples of chapter 8 described the behaviour of the models used in the tests of chapter 10. The resulting static stresses and deflections were then employed as a starting point for the dynamic analyses of chapters 9, 11 and 12. The theoretical static deflections were compared in chapter 10 with experimental results.

Explicit dynamic analysis using a central finite difference scheme was employed in chapter 9 to analyse the response of pneumatic structures; and in particular the test domes. The iteration scheme used included visco-elastic membrane behaviour modelling, and accounted for on/off buckling and the influence of surrounding air as far as internal air stiffening was concerned. For the suddenly unloaded dome, a revised, more efficient numerical scheme was proposed, in which checking for buckling was carried out at each time step, but creep strains, updated stiffness matrices and unit

pressure vectors were calculated at less frequent intervals.

The static and dynamic tests performed on the pneumatic domes were described in chapter 10. Dome membrane properties were established from static and dynamic tests on specimens. For dynamic tests a new procedure was devised to model more closely the state of stresses, by inducing two dimensional stresses in the testing area of a specimen. Still and movie cameras were used in the static and dynamic tests on the pneumatic domes to record deflections, and the results were analysed by means of photogrammetric techniques.

The static results compared very well with the theoretical predictions of chapter 8 for both models. The theoretical dynamic trace for the apex nodal deflection of the impulsively centrally loaded dome differed only slightly from experimental results. However, large discrepancies between the theoretical and dynamic responses for the suddenly unloaded dome revealed the limitations of the theoretical analysis of chapter 9. The surrounding air in this analysis (apart from stiffening effects) was not properly modelled. In contrast, for the dome with a suddenly applied load, the heavy central mass dominated the response and the influence of internal and external attached air mass became of secondary order.

The suddenly unloaded lightweight membrane dome representing more closely the problems associated with the structural

response of real shallow air-houses to wind loading was further considered in chapters 11 and 12, where attention was focused on modelling the surrounding air behaviour coupled with membrane deformations.

In chapter 11, the behaviour of irrotational, inviscid, compressible fluid was described from a Lagrangian point of view. In the numerical analysis it was assumed that the dynamic response of the enclosed air bounded by the lightweight polythene membrane resembles that of 'blancmange'. It was presumed that the air mass is confined in highly deformable tetrahedral elements, the basic building blocks employed in the air modelling, and that the air can move as far as the elements can deform and displace.

Although only the simplest axisymmetric case was considered, the amount of computing was enormous. Hence, the procedure of chapter 11 cannot, at present, be advocated for use in practice. The excessive amount of computing resulted from the necessity of using very small elements and therefore a very short time step was required for stability of the entire procedure.

An alternative method of modelling air behaviour could be to employ a more common approach to describe the air flow, namely to use a Eulerian type of equations. The simplest solution of such equations under the assumptions of potential flow, is to reduce a 3D problem to a boundary solution by means of Green's identity. This type of approach was employed in chapter 5 to predict wind loadings

on the rigid shell roof. In the boundary solution, singularities of vortices and sources are used to model the air flow. For the problem under consideration, however, neither of the simple distributions of singularities can model the problem properly. Employing only sources results in a zero pressure jump across the boundary and a distribution of vortices does not satisfy boundary conditions off the body since there is a mixing between the enclosed and external air.

It appears that a more realistic approach would be to solve the Navier-Stoke equations by some kind of a numerical method, which would involve 3D air modelling and solving nonlinear differential equations. In such an analysis the displacement of mesh points between time steps should be allowed for. A pneumatic dome, to balance external loadings, undergoes large displacements and therefore in theoretical predictions of wind load response of shallow air-houses, the compressibility of the internal air should be included. Some works on generating a movable grid, as a domain changes, have been done with reference to aerodynamic problems. The available techniques are reviewed in reference [214].

Although numerical methods which can be directly or indirectly applied to determine the dynamic response of pneumatics are potentially available, the computer time required to run a dynamic two domain problem with fluid-structure boundaries highly deformable would be very large.

Therefore, no effort was made to develop these techniques into a computer coding. The available code for solving the Navier-Stokes equations, which was applied in the appendix to chapter 5, could not be directly applied to the problem in question, since the program is suitable only for time average turbulent boundary problems, in which a body remains at rest.

Due to the difficulties encountered in chapter 11 with the simplified coupled fluid-structure explicit dynamic analysis, no attempts have been made to combine the numerical analysis of chapter 5 - theoretical prediction of pressure coefficients, with the procedure of chapter 11. Under the potential flow assumptions, a simple distribution of singularities (vortices/doublets or sources), cannot model fully the air behaviour during dynamic response of air-supported structures. However, in chapter 12, a simple discrete sources distribution was employed to assess only the value of added mass due to vibration of air in a shallow air supported dome (external and internal air). The approach was then included in the numerical explicit dynamic procedure of chapter 9 and tested against the predicted response of the centrally unloaded lightweight shallow dome. The results showed great improvement in terms of frequencies, with only a small increase in computing time compared with the numerical scheme of chapter 9.

The discrete sources distribution method to calculate added mass effects can be easily extended to any shape of pneumatic structure, and when combined with an explicit

dynamic analysis can provide a useful scheme for calculating frequencies and the approximate dynamic response of air-supported structures. When vortices or doublets are employed as singularities a similar scheme could be derived to predict the approximate dynamic response of open sided lightweight tension structures (of course, the air stiffening effect should be excluded from the analysis of this type of structure).

In the approximate analysis of chapter 12, the effect of 'sloshing' of the internal air was disregarded. In the case of the centrally unloaded lightweight dome this resulted only in comparatively small errors. In general, however, when dynamic response of long span, shallow air-supported structures to wind loading is considered, this is very likely to lead to much greater discrepancies since the lowest mode of vibration would involve lateral movements of the structure. It would appear that there is no developed numerical method, based on potential compressible flow, to account for internal air momentum in a manner which could be applied to such structures when undergoing large deformations.

For further research on air-supported structures it would seem to be more feasible to concentrate, at present, on static analyses in which external wind loading is calculated from a real flow solution by one of the numerical methods which are available for rigid structures (for example the method based on the SIMPLE algorithm which was used in the

appendix to chapter 5). Some successful attempts have been made in three dimensional theoretical predictions of wind loading on isolated rigid structures, and even on a group of buildings [212, 213]. But with a flexible highly deformable structure, the problem is more complicated, as the numerical prediction of wind loading has to be performed many times. Firstly, wind loading has to be determined on the undeformed structure, then the new shape required to balance this external loading has to be calculated followed by predictions of the new wind loadings. The process has to be repeated until the stage is reached in which a new shape of the structure does not cause any (practically very small) changes in the prediction of wind loadings. In view of the above difficulties, it would seem prudent to commence the investigation from a simple two dimensional case.

The success of the scheme will largely depend on the type of available computer. A traditional serial architecture computer is not purpose designed to solve these types of problems, in which a large number of separate and independent calculations have to be performed. Such problems seem to be tailor-made for a parallel-architecture machine, the design of which allows many similar calculations to be executed simultaneously. Some success has been achieved in designing this type of computer, called the cellular automation model, with direct application to the modelling of air flow [198].

REFERENCES AND BIBLIOGRAPHY

1. Abu-Sitta S.H., Elashkar I.D.,
   The Dynamic Response of Tension Roofs to Turbulent Wind, Int. Conf. on Tension Roof Structures, London 1974.

2. Albano E., Rodden W.P.,
   A Doublet-Lattice Method for Calculating Lift Distribution On Oscillating Surfaces in Subsonic Flows, AIAA Journal, Vol. 7, No 2, 1969.

3. Almosnino D., Rom T.,
   Calculation of Symmetric Vortex Separation Affecting Subsonic Bodies at High Incidence, AIAA Journal, 1983.

4. Ansell M.P., Harris B.,
   Fabrics - Characteristics and Testing, Symposium on Air-Supported Structures: The State of the Art, London, 1980.

5. Ansell M., Barnes M., Williams Ch.,
   Structural Properties Tests for Coated Fabrics, Conf. on the Design of Air-Supported Structures, Bristol, 1984.

6. Anthony K.C.,
   The Background to the Statistical Approach, Seminar on the Modern Design of Wind-Sensitive Structures, CIRIA, London, 1971.

7. Barnes M.R.,
   An Investigation of Vibration Decay in a Model Pneumatic Dome, Int. Symp. on Wide Span Surface Structures, Stuttgart, 1976.

8. Barnes M.R.,
   Explicit Dynamic Analysis of Tension Structures, Int. Symp. on Wide Span Surface Structures, Stuttgart, 1976.

9. Barnes M.R.,
   Form Finding and Analysis of Tension Space Structures by Dynamic Relaxation, PhD Thesis, The City University, London, 1977.

10. Barnes M.R., Topping B.H., Wakefield D.S.,
    Aspects of Form-Finding by Dynamic Relaxation, Int. Conf. On Slender Structures, 1977.

11. Barnes M.R.,
    Explicit Dynamic Analysis of an Impulsively Loaded Pneumatic Dome, Symposium on Air-Supported Structures: the State of the Art, London, 1980.

12. Barnes M.R.,
Non-linear Numerical Solution Methods for Static and Dynamic Analysis of Tension Structures, Symposium on Air-Supported Structures: the State of the Art, London, 1980.

13. Barnes M.R., Wakefield D.,
Dynamic Relaxation Applied to Interactive Form Finding and Analysis of Air-Supported Structures, Conf. on the Design of Air-Supported Structures, Bristol, 1984.

14. Barnes M.R.,
Review of Solution Methods for Static and Dynamic Analysis of Tension Structures, Conf. on the Design of Air-Supported Structures, Bristol, 1984.

15. Barnes M.R.,
Form-Finding and Analysis of Prestressed Nets and Membranes, Proc. of the Int. Conf. on the Design and Construction of Non-Conventional Structures, London, 1987.

16. Barnes M.R.,
Private correspondence, 1988.

17. Bathe K.J., Wilson E.L.,
Numerical Methods in Finite Element Analysis, Prentice-Hall, Inc., 1976.

18. Bearman P.W.,
Wind Loads on Structures in Turbulent Flow, Seminar on the Modern Design of Wind-Sensitive Structures, CIRIA, London, 1971.

19. Bearman P.W.,
Aerodynamic Loads on Buildings and Structures, Proc. Conf. on Wind Engineering in the Eighties, CIRIA, 1980.

20. Bearman P.W.,
Wind Induced Oscillations of Class E Buildings and Structures, Proc. Conf. on Wind Engineering in the Eighties, CIRIA, 1980.

21. Beger G., Macher E.,
Results of Wind Tunnel Tests on Some Pneumatic Structures, Proc - 1st Int. Colloquium on Pneumatic Structures (IASS), 1967.

22. Bell M.H., Shears M.,
The Assessment of Wind Effects in Design Practice, Proc. Conf. on Wind Engineering in the Eighties, CIRIA, 1980.

23. Belytschko T., Hughes T.J.R., (Editor),
Computational Methods for Transient Analysis, Chapter 5, Dynamic Relaxation, Elsevier Science Publishers, 1983.

24. Benzley S.E., Key S.W.,
Dynamic Response of Membranes with Finite Elements, Journal of the Eng. Mech. Division, Proc., ASCE, Vol. 102, No. EM 3, June 1976.

25. Beutler J.,
Beitrag Zur Statistischen Windlasten von Seilnetzwerken-Ergebnisse von Windkanaluntersuchungen, Proc. of the IASS Col. on Hanging Roofs, Paris, 1962.

26. Birkhoff G.,
Hydrodynamics, Princeton University Press, 1950.

27. Bisplinghoff R.L., et al,
Aeroelasticity, Addison-Wesley Publishing Company, Inc. Massachusetts, 1957.

28. Blum R.,
Tensile Membrane Structures Symposium on Air-Supported Structures: the State of the Art, London, 1980.

29. Bowes W.H., Russell L.T.,
Stress Analysis by the Finite Element Method for Practising Engineers, Lexington Books, D.C. Heath and Company, 1975.

30. Bristow D.R., Grose G.G.,
Modification of the Douglas Neumann Program to Improve the Efficiency of Predicting Component Interference and High Lift Characteristics, NASA CR 3020, 1978.

31. Bristow D.R.,
Development of Panel Methods for Subsonic Analysis and Design, NASA CR 3234, 1980.

32. BS 3424 Testing Coated Fabric
Part 2: 1982 Conditioning and selection of Test Specimen
Part 3: 1982 Determination of Mass per Unit Area
Part 4: 1982 Determination of Breaking Strength and Elongation at Break
Part 21:1987 Method for Determination of Elongation and Tension Set

33. Buchholdt H.A.,
The Configuration of Prestressed Cable Nets, Acta Polytechnica Scandinavia, Civil Eng and Building Construction Series, No. 54, Trondheim, Norway, 1968.

34. Buchholdt H.A.,
Introduction to Cable Roof Structures, Cambridge University Press, 1985.

35. Campbell W.F.,
The Added Mass of some Rectangular and Circular Flat Plates and Diaphragms, National Research Council, Canada, Laboratory Technical Report, LTR-LA-223, 1982.

36. Cassell A.C.,
Shells of Revolution under Arbitrary Loading and the use of fictitious Densities in Dynamic Relaxation, Proc. Inst. Civil Engrs, Jan, 1970.

37. Cassell A.C., Hobbs R.E.,
Numerical Stability of Dynamic Relaxation Analysis of Non-linear Structures, Int. J. for Num. Meth. in Engrg 10, 1976 pp 1407 - 1410.

38. Cebeci T., Bradshaw,
Momentum Transfer in Boundary Layer, McGraw-Hill Book Company, 1977.

39. Cermack J.E.,
Physical Modelling of the Atmospheric Boundary Layer in Long Boundary - Wind Tunnels, Wind Tunnel Modelling for Civil Engineering Applications, Proceedings of the Int. Workshop, USA, 1982.

40. Christensen R.M.,
Theory of Viscoelasticity, Second Edition, Academic Press, 1982.

41. Chuen-Yen Chow,
An Introduction to Computational Fluid Mechanics, John Wiley & Sons, 1979.

42. Clough R.W., Penzien J.,
Dynamics of Structures, McGraw-Hill Ltd., 1975.

43. Cook M.,
The use of Physical Models in the Design of Air-Supported Structures, Conf. on the Design of Air-Supported Structures, Bristol, 1984.

44. Cook N.J.,

Simulation Techniques for Short Test-Section Wind Tunnels, Roughness, Barrier and Mixing-Device Method, Wind Tunnel Modelling for Civil Engineering Applications, Proceedings of the Int. Workshop, USA, 1982.

45. Cook N.J.,
The Designer's Guide to Wind Loading of Building Structures, Part 1, BRER, Butterworths, 1985.

46. Cook R.D.,
Concepts and Applications of Finite Element Analysis, John Wiley and Sons, 1981.

47. Craig R.R.,
Structural Dynamics; An Introduction to Computer Methods, John Wiley and Sons, 1981.

48. Cundall P.A.,
Explicit Finite - Difference Methods in Geomechanics, Proc. E.F. Conf. Numerical Methods in Geomechanics, Blacksbung, Va., 1976.

49. Davenport A.G.,
The Application of Statistical Concepts to the Wind Loading of Structures, Proc. of the Inst. of Civil Engrs. Vol. 19, 1961.

50. Davenport, A.G.,
Note on the Distribution of the Largest Value of a Random Function with Application to Gust Loading, Proc. of Inst. of Civil Engrs., Vol. 28, 1964.

51. Davenport, A.G.,
Gust Loading Factors, Journal of Structural Division, Proc. of ASCE, June 1967.

52. Davenport A.G.,
The Dependence of Wind Loads on Meteorological Parameters, Int. Research Seminar, Wind Effects on Buildings and Structures, Ottawa, Canada, 1967.

53. Davenport A.G., Holm E., Surry D.,
A report of the Wind Tunnel Measurements on the Olympic Coliseum, Calgary, Alberta, BLWT-SS11-1981.

54. Davenport A.G., Surry D.,
Turbulent Wind Forces on a Large Span Roof and their Representation by Equivalent Static Load, Canadian Journal of Civil Eng., 11 (4), 1984.

55. Day A.S.,
An Introduction to Dynamic Relaxation, The Engineer, Jan., 1965.

56. De La Salle R.F.,
Pneumatic Structures, A Report Nr 813, The City University, London, 1976.

57. Dent R.N.,
Principles of Pneumatic Architecture, The Architectural Press, London, 1971.

58. Dowell, E.H.,
Aeroelasticity of Plates and Shells, Noordhoff Int. Publishing, Leyden, 1975.

59. Dowell E.H., et al.,
A Modern Course in Aeroelasticity, Sijthoff and Noordhoff, 1978.

60. Dugundji J., Dowell E., Perkin B.,
Subsonic Flutter of Panels on Continuous Elastic Foundation, AIAA Journal, May, 1963.

61. Elashkar I., Novak M.,
Wind Tunnel Studies of Cable Roofs, Proc. of the Sixth Int. Conf. on Wind Eng., 1983, Part A.

62. Ellen C.H.,
The Stability of an Isolated Rectangular Surface Embedded in Uniform Subsonic Flow, Journal of Applied Mechanics, June 1977.

63. ESDU Engineering Data Vol 1c.,
Item Number 74030, 1974, Characteristics of Atmospheric Turbulence Near Ground, Part 1: Definitions and General Information.

64. ESDU Engineering Data Vol 1c.,
Item Number 85020, 1985, Characteristics of Atmospheric Turbulence near the Ground, Part II: Single Point Data for Strong Winds.

65. ESDU Engineering Data Vol 1c.,
Item Number 86010, 1986, Characteristics of Atmospheric Turbulence near the Ground, Part III: Variations in Space and Time for Strong Wind.

66. ESDU Engineering Data Vol 1c.,
Item Number 82026, 1982, Strong Winds in the Atmospheric Boundary Layer, Part 1: Mean-Hourly Wind Speed.

67. ESDU Engineering Data Vol 1c.,
Item Number 83045, 1983, Strong Winds in the Atmospheric Boundary Layer, Part 2: Discrete Gust Speeds.

68. Falkner V.M.,
The Calculation of Aerodynamic Loading on Surfaces of any Shape, R and M No. 1910, Aug 1943.

69. Firt V.,
Statics, Form-finding and Dynamics of Air-supported Membrane Structures, Martinus Nijhoff Publishers, Prague, 1983.

70. Flüge W.,
Stresses in Shells, Springer-Verlag, Berlin, 1960.

71. Flüge W.,
Viscoelasticity, Springer-Verlag, Second Edition, 1975.

72. Forrester T.J.,
A General Panel Method for the Analysis and Design of Arbitrary Configurations in Incompressible Flows, NASA CR 3079, 1980.

73. Glockner P.G., Vishwanath T.,
On the Analysis of Nonlinear Membranes; Department of Civil Eng., Report, University of Calgary, Calgary, Canada, Feb 1971.

74. Goetz A.,
Introduction to Differential Geometry, Addison Wesley Publishing Company, 1968.

75. Goland D.,
Two-Dimensional Inflated Buildings in a Cross Wind, M.Eng thesis, McGill University, Montreal, Canada, 1980.

76. Gould P.L., Abu-Sitta S.H.,
Dynamic Response of Structures to Wind and Earthquake Loading, Pentech Press, 1980.

77. Gow M.M.,
A Course in Pure Mathematics, The English University Press Ltd, 1960.

78. Green A.E., Adkins J.E.,
Large Elastic Deformations, Oxford University Press, London, 1960.

79. Grigorlev A.E.,
Equilibrium of a Membrane Shell of Revolution at Large Deformation, Prokladnaya Matematika i Mekhanika, Journal of Applied Mathematics and Mechanics, Vol 25, Vol 6, 1961, pp 1618-1626.

80. Habashi W.G., (Editor),
Computational Methods in Viscous Flows, Vol 3 in Series Recent Advances in Num. Methods in Fluids, Pineridge Press Ltd., 1984.

81. Harris B.,
Engineering Materials for Airhouses, Conf. on the Design of Air-Supported Structures, Bristol, 1984.

82. Harris R.I.,
The Nature of the Wind, Seminar on the Modern Design of Wind-Sensitive Structures, CIRIA, London, 1971.

83. Harris R.I.,
The Classification of Structures for Wind Effects, Proc. Conf. on Wind Engineering in the Eighties, CIRIA, 1980.

84. Harris R.I., Deaves D.M.,
The Structure of Strong Wind, Proc. Conf. on Wind

Engineering in the Eighties, CIRIA, 1980.

85. Haug E., Powell G.H.,
Finite Element Analysis of Non-linear Membrane Structures, IASS Pacific Symposium on Tension Structures and Space Frames, Tokyo and Kyoto, 1971.

86. Haug E.,
Remarks on Unsymmetric Coefficient Matrices in Implicit Non-linear Finite Element Membrane and Cable Analysis, Int. Symposium on Wide Span Surface Structures, Stuttgart, 1976.

87. Haug E.,
Numerical Design and Analysis of Lightweight Structures, Symposium on Air-Supported Structures: The State of the Art, London, 1980.

88. Hedman S.G.,
Vortex-Lattice Method for Calculation of Quasi-Steady State Loadings on Thin Elastic Wings in Subsonic Flow, The Aeronautical Research Institute of Sweden, Report 105, Oct 1965.

89. Herzog T.,
Pneumatic Structures, Verlag Gerd Hatje, Stuttgart, 1976.

90. Hess J.L., Smith A.M.O.,
Calculations of Potential Flow about Arbitrary Bodies, Progress in Aeronautical Sciences, Vol 8, 1967, Pergamon Press.

91. Horder A., (Editor)
The Manual of Photography, Focal Press 1973.

92. Houghton E.L.,
Wind Forces on Buildings and Structures: An Introduction, Edward Arnold Ltd, 1976.

93. Houghton E.L., Carruthers N.B., Aerodynamics for Engineering Students, Edward Arnold Ltd, 1982.

94. Howell J.F.,
Definition of External Forces, Symposium on Air-Supported Structures: The State of the Art, London, 1980.

95. Howson W.P., Wooton L.R.,
Some Aspects of the Aerodynamics and Dynamics of Tension Roof Structures, Int. Conf. on Tension Roof Structures, London, 1974.

96. Irons B.M., Anmad S.,
Finite Element Techniques, 1980. Ellis Horwood, Chichester.

97. Irwin H.P.A.H., et al.,
A Wind Tunnel Investigation of the Montreal Olympic Stadium Roof, National Research Council of Canada, LTR-LA-228, May 1979.

98. Isaacson E., Keller H.B.,
Analysis of Numerical Methods, J Wiley and Sons, 1966.

99. Jensen J.J.,
Das Dynamische Verhalten Eines Vorgespannten Kabelnetzes, 9th Congress IABSE, Amsterdam, 1972.

100. Jensen J.J.,
Dynamics of Tension Roof Structures, Int. Conf. on Tension Roof Structures, Int. Conf. on Tension Roof Structures, London, April, 1974.

101. Johnson D.E., Grief R.,
Dynamic Response of Cylindrical Shell: Two Numerical Methods, AIAA Journal, Vol.4 N.3, 1965.

102. Jones R.E., Strome O.R.,
Direct Stiffness Method Analysis of Shells of Revolution Utilizing Curved Elements, AIAA Journal, Vol.4, 1966.

103. Kalman T.P., Rodden W.P.,
Application of the Doublet-Lattice Method to Nonplanar Configurations in Subsonic Flow, J Aircraft, Vol.8, No.6, 1971.

104. Kellogg O.D.,
Foundations of Potential Theory, Dover Publications, 1954.

105. Kind R.J.,
Aeroelastic Modelling of Membrane Structures, Proc. of the Int. Workshop on Wind Tunnel Modelling Criteria and Technics in Civil Eng. App., USA, 1982.

106. Kind R.J.,
Pneumatic Stiffness and Damping in Air-Supported Structures, J. Wind Eng. Aerodyn, Sept, 1984, pp 295-304.

107. Knudson W.C.,
Response of Cable-Net Structures under Dynamic Loads, Symp. on Tension Structures and Space Frames, Toky & Kyoto, 1971.

108. Knudson W.C.,
Some Aspects of the Response of Cable Nets to Wind Loadings, Int. Symp. on Wide Span Surface Structures, Stuttgart, 1976.

109. Kornecki A., Dowell E.H., O'Brien J.,
On the Aeroelastic Instability of Two-Dimensional Panels in Uniform Incompressible Flow, Journal of Sound and Vibration, 1976, 47(2).

110. Kraus H.,
Thin Elastic Shells, John Wiley and Sons Inc., 1967.

111. Krieg R.D., Key S.W.,
Transient Shell Response by Numerical Time Integration, Int. J. for Num. Meth. in Engng, Vol 7, 1973.

112. Krishna P.,
Cable Suspended Roofs, McGraw-Hill, 1978, USA.

113. Kunieda H.,
Flutter of Hanging Roofs and Curved Membrane Roofs, Int. J. Solids Struct., 1975, Vol 11.

114. Kunieda H., et al.,
Cylindrical Pneumatic Membrane Structures Subject to Wind, ASCE Proc., Eng. Mech. Division Journal, Vol 107, 1981.

115. Kunita J., et al.,
An Interactive Shape Finding Analysis for Cable Membrane Structures, Shells, Membrane and Space Frames, Proceedings of the IASS Symposium, Osaka, 1986, Vol 2.

116. Lamb M.A.,
Hydrodynamics, Cambridge University Press, Sixth Edition 1932.

117. Landahl M.T., Stark V.J.E.,
Numerical Lifting - Surface Theory - Problems and Progress AIAA, Vol 6, Number 11, Nov 1968.

118. Langford M.J.,
Advanced Photography, Fourth Edition, Focal Press, 1983.

119. Langford M.J.,
Basic Photography, Focal Press, London, 1984.

120. Leonard J.W., et al.,
Structural Considerations of Inflatable Re-Entry Vehicles, NASA TN D-457, 1960.

121. Leonard J.W., et al.,
Analysis of Inflated Re-Entry and Space Structures, Proc. of Recovery of Space Vehicles, Symposium, Los Angeles, 1960.

122. Leonard J.W.,
Inflatable Shells: Pressurization Phase, Journal of the Engineering Mechanics Division, ASCE, Vol 93, No. EM2, Proc, Ap 1967, pp 207-221.

123. Leonard, J.W.,
Inflatable Shells: In Service Phase, Journal of the Engineering Mechanics Division, ASCE, Vol 93, No. EM6, Proc, Dec 1967, pp 67-81.

124. Leonard J.W.,
Inflatable Shells: No-Symmetric In-Service Loads, Journal of the Engineering Mechanics Division, ASCE, Vol 94, No. EM5, Proc, 1968, pp 1231-1248.

125. Leonard J.W.,
Inflatable Shells in the Fluid Environment, Proc, IASS Pacific Symposium on Hydrodynamically Loaded-Shells, Part 7, Honolulu, Hawaii, 1971.

126. Leonard J.W.,
Use of Pressurized Membrane as a Low-Cost Erection Scheme for Concrete Structures, Proc, second Int. Symp. on Lower Cost Housing Problems Related to Urban Renewal and Developments, University of Missouri-Rolla, Mo, 1972.

127. Leonard J.W., Li C.T.,
An Interpolated Geometry for Shell Elements, Sixth South Eastern Conf. on Theoretical and Applied Mechanics, University of South Florida, Taropa, Fla, Mar 1972.

128. Leonard J.W.,
State-of-the-Art in Inflatable Shell Research, Journal of the Engineering Mechanics Division, ASCE, Vol 100, No. EM1, Proc, 1974, pp 17-25.

129. Leonard J.W.,
Tension Structures, McGraw-Hill Book Company, 1988.

130. Lewis W.J.,
A Comparative Study of Numerical Methods for the Solution of Pretensioned Cable Network, Proc. of the Int. Conf. on the Design and Construction of Non-Conventional Structures, London, 1987.

131. Li C.T.,
Analysis of Inflatable Shell by Finite Element Method, PhD Thesis, State University of New York at Buffalo, Buffalo, N.Y., 1971.

132. Li C.T., Leonard J.W.,
Non-Linear Response of a General Inflatable Shell to In-Service Loads, Proc. IASS Conf. on Shell Structures and Climatic Influences, Calgary,

Canada, 1972.

133. Li C.T., Leonard J.W.,
Finite Element Analysis of Inflatable Shells, Journal of the Eng. Mechanical Division, ASCE, Vol 99, 1973, pp 495-514.

134. Liddell I.,
Review of Current Fabrics and Laminates for Airhouse Construction, Conf. on the Design of Air-Supported Structures, Bristol, 1984.

135. Liddel I.,
A Covered City in the Arctic, Conf. Non-Conventional Structures, London, 1987.

136. Linkwitz K., Gründing L.,
Strategies of Form-finding and Design of Cutting Patterns for Large Sensitive Membrane Structures, Proc. of the Int. Conf. on the Design and Construction of Non-Conventional Structures, London, 1987.

137. Lo A.,
Non-Linear Dynamic Analysis of Cable and Membrane Structures, PhD, Oregon State University, Covvallis, USA, 1981.

138. Love A.E.H.,
A Treatise on the Mathematical Theory of Elasticity, 4th ed., New York, Dover Publications, 1944.

139. Maskew B.,
Calculation of the Three-Dimensional Potential Flow around Lifting Non-Planar Wings and Wing-Bodies Using a Surface Distribution of Quadrilateral Vortex-Rings, TT 7009, Loughborough University of Technology, Dep. of Transport Technology, Leicestershire, U.K., 1970.

140. Mayne J.R., Cook N.J.,
Extreme Wind Analysis, Proc. Conf. on Wind Engineering in the Eighties, CIRIA, 1980.

141. Mayne J.R.,
Statistical Background, Proc. Conf. on Wind Engineering in the Eighties, CIRIA, 1980.

142. McComb H.G., et al.,
A Linear Theory of Inflatable Plates of Arbitrary Shape, NASA TN D-930, Washington, 1961.

143. McComb H.G., Leonard J.W.,
Slanted Drop Cords in Inflatable Airmat Beams; Journal of the Aerospace Sciences, Vol 29, No. 4, April, 1962.

144. Melbourne W.H.,
Wind Tunnel Blockage Effects and Corrections, Proc. of the Int. Workshop on Wind Tunnel Modelling and Technics in Civil Eng; USA, 1982.

145. Miles J.W.,
On the Aerodynamic Instability of Thin Panels, Journal of the Aeronautical Science, Aug, 1956.

146. Mills I., Webster R., Happold E.,
Cost and Comparisons and Markets, Conf. on the Design of Air-Supported Structures, Bristol, 1984.

147. Milne L.M., Thomson C.B.E.,
Theoretical Hydrodynamics, MacMillan Press Ltd., 5th Edition, 1968.

148. Mooney,
A Theory of Large Elastic Deformation, Journal of Applied Physics, Vol 11, 1940, pp 582-592.

149. Moran J.,
An Introduction to Theoretical and Computational Aerodynamics, New York, Chichester, Willen 1984.

150. Morris N.F.,
Wind-Structure Interaction of Flexible Roofs, Proc of a Symp on Long Span Roof Structures, 1981, St Louis, Missouri.

151. Müler R.K.,
Model Tests as an Aid to Design and Construction of Membrane Structures, Shells, Membranes and Space Frames, Proceedings of the IASS Symposium, Osaka 1986.

152. Murray T.M.,
Application of Direct Energy Minimalization to the static Analysis of Cable Supported Structures, Ph.D Thesis, Univ of Kansas, Lawrence, KA(1970).

153. Newland D.E.,
An Introduction to Random Vibration and Spectral Analysis, Longman Group Ltd, London, 1975.

154. Newman B.G.,
Flow Past on Thin, Inflated Lenticular Aerofoil, Journal of Fluid Mechanics, Vol 100, Part 3, 1980.

155. Newman B.G., Goland D.,
Two-Dimensional Inflated Buildings in a Cross Wind, J Fluid Mech, Vol 117, 1982 pp 507-530.

156. Newman B.G., et al.,
Flow over Spherical Inflated Buildings, J. Wind Eng. Ind. Aerodyn. Sept 1984, 305-327.

157. Nicholas F., Morris M.,
Wind Structures Interaction of Flexible Roofs, Proc of a Symp on Long Span Roof Structures, St Louis, Missouri, 1981.

158. Niemann H.J.,
Wind Tunnel Experiments on Aeroelastic Models of Air-Supported Structures, Procs-Int IASS Symp. on Pneumatic Structures, 1972.

159. Nishimura T., et al.,
Membrane Structural Analysis using the Finite Element Technique, IASS symp. on Membrane Structures and Space Frames, Japan, 1986.

160. Oden J.T., Kubitza W.K.,
Numerical Analysis of Nonlinear Pneumatic Structures, IASS Colloquium on Pneumatic Structures, Stuttgart, 1967.

161. Oden J.T., Sato T.,
Finite Strains and Displacements of Elastic Membranes by the Finite Element Method, Int. J Solids Structures, 1967, Vol 3.

162. Oden J.T.,
Finite Elements of Nonlinear Continua, McGraw-Hill, New York, 1972.

163. Oden J.T., et al.,
A Note on the Analysis of Nonlinear Dynamics of Elastic Membranes by the Finite Element Method, Computers and Structures, Vol 4, 1974.

164. Otter J.R.H.,
Dynamic Relaxation Compared with Other Interactive Finite Difference Methods, Nuclear Eng and Design, 3, 1966.

165. Otto Frei.,
Tensile Structures - Vol I, M.I.T., Press Cambridge, Mass, 1967.

166. Owen D.R.J., Hinton E.,
Finite Elements in Plasticity, Theory and Practice, 1980 Pineridge Press Ltd.

167. Papadrakakis E.M.,
Discrete Statical-Analysis of Structural Mechanisms, PhD Thesis, The City University, London, 1978.

168. Patankar S.V.,
Numerical Heat Transfer and Fluid Flow, Hemisphere Publishing Corporation, USA, 1980.

169. Pipes L.S., Harrill L.R.,
Applied Mathematics for Engineers and Physicists, McGraw-Hill, 1983.

170. Prager W.,
Introduction to Mechanics of Continua, Dover, New York, 1961.

171. Pucher A.,
Uber der Spannung Szutand in Gerkrümnten Flachen, Beton und Eisen, Vol 33, 1934, pp 298-304.

172. Rae W.H., Pope A.,
Low-Speed Wind Tunnel Testing, John Willey & Sons, Second Edition, 1984.

173. Rivlin R.S.,
The Deformation of Membrane by Inextensible Cords, Archive for Rational Mechanics and Analysis, Vol 2, No.5, 1959, pp 447-476.

174. Rodden W.P., Giesing, et al.,
New Developments and Applications of the Subsonic Doublet-Lattice Method for Nonplanar Configuration, AGARD, Sym on Unsteady Aerodynamics for Aeroelastic Analyses of Interfering Surfaces.

175. Rubert P.E.,
Theoretical Characteristic of Arbitrary Wings by a Nonplanar Vortex-Lattice Method, D6-9244, The Boeing Co., 1964.

176. Rubert P.E., Saaris G.R.,
Review and Evaluation of a Three-Dimensional Lifting Potential Flow Computational Method for Arbitrary Configurations, AIAA Paper 72-188, San Diego, Calif., 1972.

177. Schlichting H.,
Boundary-Layer Theory, McGraw-Hill Book Company, Sixth Edition, 1968.

178. Schmit L.A., Mallett R.H.,
Nonlinear Structural Analysis by Energy Search, J Structural Div. ASCE, 93, pp 221-234, 1967.

179. Shahrokh K., Ellen C.H.,
The Stability of Partially Rigid Two-Dimensional Surfaces in Uniform Incompressible Flow, Journal of Sound and Vibration, 1979 65(3).

180. Shield R.T., Fosdick R.L.,
Extremum Principles in the Theory of Small Elastic Deformations Superimposed on Large Elastic Deformations, Progress in Applied Mechanics, The Prager Anniversary Volume, 1963, pp 107-125.

181. Siev A.,
Experimental Study of Flutter in Suspended Roofs, Int. J. Solids Struc, 11(4), 1975.

182. Simiu E., Scanlan R.H.,
Wind Effects on Structures, A Wiley - Interscience Publication, USA, 1978.

183. Simmonds J.G.,
The General Equations of Equilibrium of Rotationally Symmetric Membranes and some Solutions for Uniform Centrifugal Loading, NASA TND-816, 1961.

184. Spinelli P.,
Dynamic Response under Wind of a Cylindrical Air-Supported Structure, Journal of Wind Eng and Industrial Aerodynamics, 1983.

185. Szabo J., Kollar L.,
Structural Design of Cable-Suspended Roofs, Ellis Horwood, Series in Eng Science, 1984.

186. Tan K.Y.,
Dynamic Analysis of a Model Pneumatic Dome, MSc Thesis, The City University, 1983.

187. Tan K.Y., Barnes M.,
Numerical Representation of Stress/Strain Relations for Coated Fabrics, Conf. on the Design of Air-Supported Structures, Bristol, 1984.

188. Timoshenko S.P., Goodier J.N.,
Theory of Elasticity, Third Edition, McGraw-Hill Int Book Company, 1982.

189. Tryggvason B.V., Isyumov N.,
Similarity Requirements for Inflatable Structures, 3rd US Wind Eng Conf., Florida 1978.

190. Tsze C Tai.,
Determination of Three-Dimensional Flow Separation by a Streamline Method, AIAA Journal, 1981, pp 1264-1271.

191. Tuan H.,
Cable Dynamics in an Ocean Environment, PhD, Oregon State University, Covvallis, USA, 1983.

192. Vellozzi J., Cohen E.,
Gust Response Factors, Journal of the Structural Division, ASce, 1968.

193. Vennard J.K., Street R.L.,
Elementary Fluid Mechanics, Sixth Edition, John Wiley & Sons, 1982.

194. Vinogradov O.G.,
Structural Analysis of Cable-Reinforced Inflatables, Computer and Structures, Vol 20, No.4, pp 759-766, 1985.

195. Vishwanath T., Glockner P.G.,
On the Nonlinear Membrane Displacement Problem, Department of Civil Eng Report, University of Calgary, Calgary, Canada, 1971.

196. Vishwanath T.,
Effect of Temperature on Inflatable Shells, Proc IASS Conference on Shell Structures and Climatic Influences, Calgary, Canada, 1972.

197. Wakefield D.S.,
Pretensioned Networks Supported by Compression Arches, PhD Thesis, The City University, London, 1980.

198. Wayner P.,
Modelling Chaos, Byte, May 1988.

199. Weber J.A., et al.,
Three-Dimensional Solution of Flows over Wings with Leading-Edge Vortex Separation, AIAA Journal, Vol 14, No. 4, April 1976, pp 519-525.

200. Webster R.L.,
On the Static Analysis of Structures with Strong Geometric Nonlinearities, Computer and Structures, Vol 11, 1980.

201. Whitbread R.E.,
The Application of Wind-Tunnel Techniques to Wind-Load Prediction, Proc. Conf. on Wind Engineering in the Eighties, CIRIA, 1980.

202. Williams Ch. J.K.,
Form-Finding and Cutting Patterns for Air-Supported Structures, Symposium on Air-Supported Structures: the State of The Art, London, 1980.

203. Williams Ch. J.K.,
The Integration of Wind Tunnel Testing and Structural Analysis of Air-Supported Structures, Conf. on the Design of Air-Supported Structures, Bristol, 1984.

204. Williams Ch. J.K.,
Methods of Including the Effect of the Surrounding Air in the Dynamic Analysis of Air-Supported Structures, Conf. on the Design of Air-Supported Structures, Bristol, 1984.

205. Wootton L.R., Scrutton C.,
Aerodynamic Stability, Seminar on the Modern Design of Wind-Sensitive Structures, CIRIA, London, 1971.

206. Wyatt T.A.,
The Calculation of Structural Response, Seminar on the Modern Design of Wind-Sensitive Structures, CIRIA, London, 1971.

207. Younis B.,
Private Correspondence, 1988.

208. Zieniewicz O.C., et al.,
A Numerical Method of Visco-Elastic Stress Analysis, Int. J. Mech. Sci. Vol 10, 1968.

209. Zieniewicz O.C., Valliappan S., King I.P.,
Stress Analysis of Rock as a 'No Tension' Material, Geotechnique 18, 1968.

210. Zieniewicz O.C.,
The Finite Element Method in Engineering Science, McGraw-Hill, London, 1971.

211. Sykes D.M.,
A New Wind Tunnel for Industrial Aerodynamics, Journal of Industrial Aerodynamics, 2 (1974) 65-78.

212. Paterson D.A., Apelt C.J.,
Computation of Wind Flows Over Three-Dimensional Buildings; Journal of Wind Engineering and Industrial Aerodynamics, 24 (1986) 193-213.

213. Haggkvist K., Taesler R.,
Pressure Distribution on a Small-Scale House-Numerical Simulations of Wind Tunnel Experiments; 2nd International Phoenics User Conference, Nov 1987.

214. Anderson D.A., Tannehill J.C., Pletcher R.H.,
Computational Fluid Mechanics and Heat Transfer, Hemisphere Publishing Corporation, McGraw-Hill Book Company, 1984.